# Improved System Models for Building-Integrated Hybrid Renewable Energy Systems with Advanced Storage: A Combined Experimental and Simulation Approach

Dipl.-Ing. (FH) Lars Baumann, M.Sc.

A thesis submitted in partial fulfilment of the requirements of
De Montfort University for the degree of
Doctor of Philosophy

**Institute of Energy and Sustainable Development**
**De Montfort University, Leicester, UK**

**Faculty of Supply Engineering – Energy, Environment, Facility Management**
**Ostfalia University of Applied Sciences, Wolfenbüttel, Germany**

**Submission Date: December 2014**
**Viva Voce Date: February 2015**
**Final Submission Date: March 2015**

# Abstract

The domestic sector will play an important role in the decarbonisation and decentralisation of the energy sector in the future. Installation numbers of building-integrated small-scale energy systems such as photovoltaics (PV), wind turbines and micro-combined heat and power (CHP) have significantly increased. However, the power output of PV and wind turbines is inherently linked to weather conditions; thus, the injected power into the public grid can be highly intermittent. With the increasing share of renewable energy at all voltage levels challenges arise in terms of power stability and quality. To overcome the volatility of such energy sources, storage technologies can be applied to temporarily decouple power generation from power consumption. Two emerging storage technologies which can be applied at residential level are hydrogen systems and vanadium-redox-flow-batteries (VRFB). In addition, the building-integrated energy sources and storage system can be combined to form a hybrid renewable energy system (HRES) to manage the energy flow more efficiently.

The main focus of this thesis is to investigate the dynamic performance of two emerging energy storage technologies, a hydrogen loop composed of alkaline electrolyser, gas storage and proton exchange membrane (PEM) fuel cell, and a VRFB. In addition, the application of building-integrated HRES at customer level to increase the self-consumption of the onsite generated electricity and to lower the grid interaction of the building has been analysed.

The first part deals with the development of a research test-bed known as the Hybrid Renewable Energy Park (HREP). The HREP is a residential-scale distributed energy system that comprises photovoltaic, wind turbine, CHP, lead acid batteries, PEM fuel cell, alkaline electrolyser and VRFB. In addition, it is equipped with programmable electronic loads to emulate different energy consumption patterns and a charging point for electric vehicles. Because of its modular structure different combinations of energy systems can be investigated and it can be easily extended. A unified communication channel based on the local operating network (LON) has been established to coordinate and control the HREP. Information from the energy systems is gathered with a temporal resolution of one second. Integration issues encountered during the integration process have been addressed.

The second part presents an experimental methodology to assess the steady state and dynamic performance of the electrolyser, the fuel cell and the VRFB. Operational constrains such as minimum input/output power or start-up times were extracted from the experiments. The response of the energy systems to single and multiple dynamic events was analysed, too. The results show that there

are temporal limits for each energy system, which affect its response to a sudden load change or the ability to follow a load profile. Obstacles arise in terms of temporal delays mainly caused by the distributed communication system and should be considered when operating or simulating a HRES at system level.

The third part shows how improved system models of each component can be developed using the findings from the experiments. System models presented in the literature have the shortcoming that operational aspects are not adequately addressed. For example, it is commonly assumed that energy systems at system level can respond to load variations almost instantaneously. Thus, component models were developed in an integrated manner to combine theoretical and operational aspects. A generic model layout was defined containing several subsystems, which enables an easy implementation into an overall simulation model in MATLAB®/Simulink®. Experimental methods were explained to extract the new parameters of the semi-empirical models and discrete operational aspects were modelled using Stateflow®, a graphical tool to formulate statechart diagrams. All system models were validated using measured data from the experimental analysis. The results show a low mean-absolute-percentage-error (<3%). Furthermore, an advanced energy management strategy has been developed to coordinate and to control the energy systems by combining three mechanisms; statechart diagrams, double exponential smoothing and frequency decoupling.

The last part deals with the evaluation, operation and control of HRES in the light of the improved system models and the energy management strategy. Various simulated case studies were defined to assess a building-integrated HRES on an annual basis. Results show that the overall performance of the hydrogen loop can be improved by limiting the operational window and by reducing the dynamic operation. The capability to capture the waste heat from the electrolyser to supply hot water to the residence as a means of increasing the overall system efficiency was also determined. Finally, the energy management strategy was demonstrated by real-time experiments with the HREP and the dynamic performance of the combined operation has been evaluated.

The presented results of the detailed experimental study to characterise the hydrogen loop and the VRFB as well as the developed system models revealed valuable information about their dynamic operation at system level. These findings have relevance to the future application and for simulation studies of building-integrated HRES. There are still integration aspects which need to be addressed in the future to overcome the proprietary problem of the control systems. The innovations in the HREP provide an advanced platform for future investigations such as electric-vehicles as decentralised mobile storage and the development of more advanced control approaches.

# Acknowledgement

This research was conducted at the Institute of Energy and Sustainable Development, De Montfort University, Leicester, UK in cooperation with the Laboratory of Electrical Engineering and Renewable Energy Systems, Faculty of Supply Engineering, Ostfalia University of Applied Sciences, Wolfenbüttel, Germany. The research formed part of the "*Dezentrale Speicher für Gebäude DeSG-Projekt*" funded by the German Federal Ministry of Education and Research (BMBF) under grant FKZ 17N1611. I also gratefully acknowledge the financial support of the *Rud. Otto Meyer-Umwelt-Stiftung* during the last months of this research.

I would like to thank my supervisor team for their dedicated support and guidance throughout my entire PhD study. They are Professor Mark Richard Rylatt and Dr Andrew Wright at De Montfort University, and Professor Ekkehard Boggasch at Ostfalia University. Particular thanks go to Professor Ekkehard Boggasch who has always encouraged me during the process of completing this thesis.

My thanks also go to my colleagues at the Laboratory of Electrical Engineering and Renewable Energy Systems at Ostfalia University and the students who accompanied me during these years. Special thanks go to Jonas Grahn and Yifan Zhang who programmed the LabVIEW based data acquisition systems, which I have used for my research. I would also like to thank Alice Oppermann and Stamatia Dimoupolou for their support during the final stage of finishing this thesis.

I am also very grateful to my dear friend Dr Florian Albert for his critical feedback and his encouragement to keep going. I would also like to thank Richard Snape for his time to enjoy coffee during my stays at De Montfort University and his helpful comments.

My thanks go to my parents who have supported and encouraged me to make the decision to go on this journey.

Finally, but definitely not least, I would like to thank my beloved wife Jessi for being there, supporting me, her patience and understanding that it was necessary to sacrifice lots of weekends to complete this thesis.

## Declaration

I declare that the content of this submission is my own work. The material included in this thesis has not been submitted, wholly or in part, for any award or qualification other than that for which it is submitted. I acknowledge that this thesis is submitted according to the conditions laid down in the regulations. Furthermore, I declare that the work was conducted as part of the part-time PhD programme, for which I was registered at De Montfort University, United Kingdom. I draw attention to any relevant considerations of rights of third parties.

Braunschweig, December 2014

# Table of contents

# List of Figures

# List of Tables

# Abbreviations

| | |
|---|---|
| AS | Automation Server |
| BOP | Balance-Of-Plant |
| CAN | Controller Area Network |
| CHP | Combined Heat and Power |
| $CO_2$ | Carbon Dioxide |
| COV | Change-Of-Value |
| CR | Control Room |
| CS | Charging Station |
| DAQ | Data Acquisition |
| DeOxo | De-oxidation |
| DHW | Domestic Hot Water |
| DSM | Demand Side Management |
| DSR | Demand Side Response |
| EEG | Erneuerbare-Energien-Gesetz |
| EU | European Union |
| FC | Fuel Cell |
| genset | Generator set |
| GL | Gas Laboratory |
| HES | Hybrid Energy System |
| HREP | Hybrid Renewable Energy Park |
| HRES | Hybrid Renewable Energy System |
| HHV | Higher Heating Value |
| ICT | Information and Communication Technology |
| IP | Internet Protocol |
| KOH | Potassium hydroxide |
| LHV | Lower Heating Value |
| Li-ion | Lithium ion |
| LMTD | Logarithmic Mean Temperature Difference |
| LON | Local Operating Network |
| MAPE | Mean Absolute Percentage Error |
| NiCd | Nickel Cadmium |
| Ni-Cr | Nicke Chrom |
| NiMH | Nickel Metal Hydride |
| NTP | Normal Temperature and Pressure |
| OPC | OLE for Process Control |
| OpenADR | Open Automated Demand Response |

| | |
|---|---|
| PEM | Proton Exchange Membrane |
| PV | Photovoltaic |
| PCC | Point of Common Coupling |
| PI | Proportional Integral |
| PLC | Programmable Logic Controller |
| PR | Production Rate |
| RMS | Root Mean Square |
| RMSE | Root Mean Square Error |
| rpm | Revolutions per minute |
| SCDA | Supervisory Control and Data Acquisition |
| SOC | State-Of-Charge |
| SQL | Structured Query Language |
| UK | United Kingdom |
| USV | Uninterruptible Power Supply |
| VRFB | Vanadium-Redox-Flow-Battery |

# Nomenclature

| ***Symbol*** | ***Parameter*** |
|---|---|
| $\alpha$ | Smoothing value of the level |
| $A$ | Area |
| $A_{hx}$ | Surface area of the heat exchanger |
| $A_{1,2}, B_{1,2}, C_n,$ $D_{1,2}, E_{1,2}, F$ | VRFB: Empiric coefficients |
| $a_{1,2,3,4}$ | Polynomial coefficients |
| $\beta$ | Smoothing parameter of the trend |
| $b$ | Fuel Cell: Empiric coefficient to calculate the activation losses |
| $A_{hx}$ | Surface of the heat exchanger |
| $C_{p,i}$ | Molar heat capacity |
| $C_{ele}$ | Electrolyser: Thermal heat capacity |
| $C_{FC}$ | Fuel Cell: Thermal heat capacity |
| $C_{ele,eff.}$ | Electrolyser: Effective thermal heat capacity |
| $c_{cw}$ | Specific heat capacity of cooling water |
| $c_{KOH,30\%}$ | Specific heat capacity of KOH 30 wt% |
| $c_{steel,1.4404}$ | Specific heat capacity of stainless steel 1.4404 |
| $d_1$, $d_2$, $d_3$ | Fuel Cell: Empirc parameters to calculate the peripheral current. |
| $\Delta_R H_m^0$ | Enthalpy of reactants at standard temperature and pressure |
| $\Delta_f H_{m,i}^0$ | Enthalpy of formation at standard temperature and pressure |

| | |
|---|---|
| $\Delta_{vap}H$ | Heat of vaporisation |
| $\Delta_R G_m^0$ | Gibbs free energy at standard temperature and pressure |
| $\Delta_R S_m^0$ | Entropy of reactants at standard temperature and pressure |
| $E_{capacity}$ | VRFB: Energy capacity |
| $E$ | Energy |
| $E_{ele/FC,AC}$ | Electrolyser/Fuel cell AC energy |
| $E_{H_2,HHV/LHV}$ | Accumulated energy of the generated hydrogen (HHV/LHV) |
| $E_{ele/FC,useable\ Heat}$ | Electrolyser/Fuel cell utilised heat |
| $F_t$ | Smoothed level of process value |
| $FTPV$ | Forecast of the process value |
| $f_c$ | Cut-off frequency |
| $h_{FC}$ | Fuel Cell: Overall heat transfer coefficient |
| $I$ | Current |
| $I_{stack}$ | Fuel Cell: Stack current |
| $I_{peripheral}$ | Fuel Cell: Current of the peripherals |
| $I_{aux}$ | VRFB: Auxiliary current |
| $I_{sh}$ | VRFB: Shunt current |
| $I_{stack,eff}$ | VRFB: Effective stack current |
| $I_{system}$ | VRFB: System current |
| $kR_0$ | Fuel Cell: Empiric coefficient of the internal resistance |
| $kR_1$ | Fuel Cell: Empiric coefficient of the internal resistance |
| $kR_2$ | Fuel Cell: Empiric coefficient of the internal resistance |
| $M$ | Molar mass |
| $m$ | Fuel Cell: Empiric coefficient to calculate the concentration losses |
| $\dot{m}_{cw}$ | Mass flow rate of the cooling water |
| $n$ | Fuel Cell: Empiric coefficient to calculate the concentration losses |
| $\dot{n}_{H_2}$ | Hydrogen molar flux |
| $\dot{n}_{measured}$ | Measured molar flux |
| $\dot{n}_{theo}$ | Theoretical molar flux |
| $\dot{n}_{stoi}$ | Stoichiometric molar flux |
| $n_{cells}$ | Number of cells |
| $\eta$ | Efficiency |
| $\eta_{coulombic}$ | Coulombic efficiency |
| $\eta_{electr.\ energy,HHV}$ | Energy efficiency based on HHV |
| $\eta_{Faraday}$ | Faraday/Current efficiency |
| $\eta_U$ | Voltage efficiency |

| | |
|---|---|
| $P_{AC/DC}$ | AC/DC Power |
| $P_{diff}$ | Power difference |
| $P_{electric}$ | Electric power |
| $P_{ex}$ | Exported power |
| $P_{gen}$ | On-site generated power |
| $P_{grid}$ | Power exchanged with the grid |
| $P_{load}$ | Electric load |
| $P_{renewables}$ | Power generation of the renewable energy sources |
| $P_{ref,PCC}$ | Power reference signal at PCC |
| $P_{store,charge/discharge}$ | Charge/Discharge power |
| $\mathrm{PV}_{\mathrm{mean}}$ | Mean of the process value |
| $p_{system}$ | Electrolyser system pressure |
| $p_0$ | Pressure at standard conditions |
| $\dot{Q}_{cool}$ | Heat removed by cooling system |
| $\dot{Q}_{gen}$ | Generated heat flow |
| $\dot{Q}_{loss}$ | Heat losses |
| $R$ | Ohmic resistance |
| $R_i$ | Fuel Cell: Internal resistance |
| $R_{eq,charge/discharge}$ | VRFB: Equivalent resistance charge/discharge |
| $R_{sh}$ | VRFB: Shunt resistance |
| $R_{s,i}$ | VRFB: Empiric coefficients of the shunt resistance |
| $R_{th}$ | Total thermal resistance |
| $R_{th,dyn.}$ | Dynamic thermal resistance |
| $r_{1,2}$ | Electrolyser: parameters of the ohmic voltage losses |
| $S_{m,i}^0$ | Standard entropy |
| $T$ | Temperature |
| $T_0$ | Temperature at standard conditions |
| $T_{amb}$ | Ambient temperature |
| $T_{cw,in/out}$ | Cooling water inlet/outlet temperature |
| $T_{ele}$ | Electrolyser temperature |
| $T_{FC}$ | Fuel cell temperature |
| $T_t$ | Trend value |
| $t_2 - t_1$ | Time period |
| $t_{1,2,3}$ | Electrolyser: parameters of the over voltage losses |
| $\tau$ | Time constant |
| $U_{cell}$ | Cell voltage |
| $U_{eq}$ | VRFB: Open circuit voltage |

| | |
|---|---|
| $U_{th}$ | Thermo neutral voltage |
| $U_{rev}$ | Reversible voltage |
| $U_{stack}$ | Stack voltage |
| $U_{OCV}$ | Open circuit voltage |
| $U_{hx}$ | Overall heat transfer coefficient |
| $U$ | Voltage |
| $V$ | Volume |
| $\dot{V}_{H_2}$ | Volumetric Flow rate of hydrogen |
| $v_i$ | Stoichiometric coefficient |
| $\gamma_{FS}$ | Grid interaction index |
| $\gamma_{load}$ | Load cover factor |
| $\gamma_{supply}$ | Supply cover factor |
| $z$ | Number of electrons |

# Constants

| *Symbol* | *Parameter* | *Value/Unit* |
|---|---|---|
| $e$ | Elementary charge | $1.6022*10^{-19}$ As |
| $F$ | Faraday Constant | 96485 As |
| $R$ | Universal gas constant | 8.31446 J/(mol*K) |
| $R_{H_2}$ | Specific gas constant of hydrogen | 4124.5 J/(kg*K) |

# 1 Introduction

Moving from a fossil fuel and nuclear dominated energy era to a sustainable energy supply is one of the most ambitious targets which the European Union (EU) has committed itself to achieve. Motivated by the threat of global warming and the depletion of fossil energy resources, the EU intends to reduce greenhouse gas emission by 80-95% below 1990 levels by 2050 (EU-DGE 2011). In 2008 the EU defined an interim target that there should be at least 20% reduction in emissions by 2020 (EU-EC 2008). All members of the EU have made significant progress to fulfil these commitments collectively. Recently, the EU has agreed on an energy and climate policy framework beyond 2020. By 2030 the greenhouse gas emissions have to be reduced by 40% compared to 1990 levels, 27% of the consumed energy has to be supplied by renewable energy sources and energy efficiency has to be improved by 27% (EU-ECO 2014). Some EU member states have always been proactive in this context and have formulated their own climate policies. The United Kingdom (UK) has set a road-map towards a low carbon society (DECE 2009). This involves higher emission cuts (more than 30% of 1990 levels) and that 40% of the electricity is generated from low carbon sources by 2020. Furthermore, around 30% of the electricity should come from renewable energy sources. However, on this road-map the application of nuclear power is still considered as a clean energy resource. Recent history has shown that the utilisation of nuclear energy can be a threat to mankind and the environment. Another important aspect to be kept in mind is that one of the key issues of using nuclear energy, the final disposal of the nuclear waste, has not been solved so far. Germany, on the other hand, has committed to transform its energy sector to a post-nuclear era characterised by a high share of renewable energy by 2022. This decision, which is commonly known as the "Energiewende", has made Germany the subject of world-wide interest as a highly industrialised country attempting to substitute the traditional base load generators with preferential use of renewable energy sources without decreasing the energy security and reliability. In addition, issues arise with respect to how it can be ensured that the energy prices will be kept at affordable levels to guarantee Germany's international competitiveness. Thus, Germany's energy policy is even more ambitious than the policies of other EU members. Greenhouse gas emissions have to be reduced by 40% by 2020 compared to 1990 levels, the electric energy supplied by renewables has to be increased to 40-45% by 2025 and has to reach a share of the total electric energy consumption of 80% by 2050; and the primary energy consumption has to be reduced by 50% compared to 1990 levels (DE-BMWIU 2012). Without doubt the consistent utilisation of renewable energy resources such as wind and solar power along with increasing the energy efficiency in all sectors are the key elements to successfully achieve the transition to a sustainable energy sector.

In Germany the legislative introduction of the “Erneuerbare-Energien-Gesetz” (EEG) with its defined feed-in-tariffs has accelerated the installation of renewable energy sources since 2000. In 2013 almost 26% of the total electricity demand in Germany was supplied by renewable energy sources including onshore and offshore wind farms, hydropower, biomass, bio-waste and photovoltaic (PV) (AG-En 2014). The highest proportion was provided by wind energy with 7.3%, which is predominantly installed in the northern regions of Germany. In addition, the share of PV power has reached a level of 4.5%. The power output of both technologies is linked to inherently variable weather conditions, which challenges both the grid capacity and the established operation of conventional power production units in balancing the electricity demand and supply. In Germany, the penetration of solar and wind power sources have reached levels which become a true technical problem such that at times with low electric demand and with high wind or high solar radiation the power output of the wind farms or PV needs to be reduced. In 2012 this aggregated loss of production caused by grid congestion was 384.8 GWh (Bundesnetzagentur 2014). Similar developments of the evolution of the increasing share of renewables can be seen in the UK, where the Government has introduced a feed-in-tariff scheme in 2010. The installed total capacity of PV systems has exponentially increased from less than 50 MW in 2010 to 4.2 GW in 08/2014 (DECC 2014a). From the total capacity approximately 86% are eligible for the feed-in-tariffs (DECC 2014b).

As outlined above, the need to transform our current energy system to a sustainable one implies the introduction of renewable energy sources and the improvement of the energy efficiency in all sectors. Challenges arise in how the integration of renewable sources can be achieved without compromising our secure and reliable electricity supply. This thesis is motivated by these issues and concerns innovative technologies to convert, store and release electric energy to buffer the volatile power output of renewable energy sources.

## 1.1 Managing the electricity at distribution level

To manage the increasing share of renewable energy sources, the traditional energy system may transform from a centralised system with large power plants to a decentralised one with high share of medium to small scale distributed energy generators. In addition, information and communication technologies (ICT) need to be introduced to coordinate and to manage the distributed generators (Wissner 2011). Furthermore, mechanisms such as demand side management and demand side response need to be established to support the integration of volatile renewable energy sources. Due to the massive integration of renewables the traditional energy system faces challenges of power balancing and demand side management/response; therefore, it needs to be transformed to an active system composed of interacting smart grids (EU-DGR 2006). In this future energy scenario

the introduction of energy storage will be another important mechanism to temporarily decouple the electricity supply from the demand.

Applying energy storage seems to be the perfect solution buffering the uncontrolled power generation of renewable sources. Surplus electricity is stored and will be released again at times when needed. Introducing electrical storage is also one of the key elements in achieving a low carbon energy system (EU-DGE 2013). Its application can be beneficial at all levels of the electricity network (Strbac et al. 2012). Various technologies can be applied to store renewable energy. It has already been demonstrated that traditional and mature technologies, for instance, pumped hydroelectric and lead-acid batteries can be utilised for power applications. However, each technology has its own limitations and no storage technology can currently provide all the desirable characteristics of high energy and high power density (Bhuiyan & Yazdani 2012). Due to the desirability of energy storage and the immaturity of some technologies, research in the field of energy storage technologies has been recently promoted by many countries.

In this frame the attention on the EU domestic building sector, responsible for approximately 25% of the primary energy usage and 29% of the total electric demand (Paolo, Labanca & Hirl 2012), has been increased (EeB 2010). Buildings have a high potential for improving energy efficiency, thus, they are of great importance to achieve a sustainable energy future. In addition, most of the PV capacity and micro combined heat and power (CHP) systems are installed at distribution level. The increasing penetration of small scale PV systems challenges the grid stability at the low-voltage level. It can be anticipated that the increasing share of these PV systems may cause overvoltage not only at the low-voltage level, but in certain circumstances also at the next mid-voltage level (Eftekharnejad et al. 2013). There is a growing need to establish mechanisms to actively control the power flow at this level. In addition, the electricity costs of PV have reached grid parity in some EU countries (Pérez et al. 2013) and some countries have already started to reduce the incentives of the renewables. For instance, Germany has cut the feed-in-tariffs below the retail prices of electricity. Utilising the on-site generated renewable energy has become attractive for building owners. The introduction of electric storage technologies at this level can be deployed to maintain grid stability by giving an additional degree of flexibility. Electricity can be generated, stored, distributed and consumed locally to provide added value for both the electricity grid and the building owner. Similar to the electricity grid itself, buildings may transform to an active energy consumer and provider composed of energy sources such as PV, electrical storages and energy management systems forming building-integrated hybrid renewable energy systems (HRES).

## 1.2 Scope of thesis

The main motivation for this thesis is the need to investigate the potential of the following two promising emerging storage technologies to enable building-integrated HRES to support the local utilisation of on-site generated PV energy more effectively.

Hydrogen can be used, if generated from renewables by water electrolysis, as a clean and sustainable energy carrier. It can play an important role to store surplus renewable energy and it facilitates a link between the electricity, heat and transport sector by offering a flexible usage as fuel (Ball & Wietschel 2009). The technical feasibility of hydrogen systems composed of an electrolyser, a gas storage and a fuel cell buffering renewable energy has been demonstrated since 1990 (Yilanci, Dincer & Ozturk 2009). It is believed that hydrogen systems have a high potential for the decentralised market if the system reliability can be improved (IEA-HIA 2010). Although technological progress has been made, there are still research challenges in terms of improving the system efficiency, system integration and to reduce the costs of the components (Gahleitner 2013).

Another emerging energy storage technology is the vanadium-redox-flow-battery (VRFB). It has the potential to be applied at the distribution and customer level providing energy management services. Compared to traditional battery systems, VRFB have the advantages that the power rate can be independently scaled from the energy capacity and that the entire working range of the state-of-charge (SOC) can be used without reducing its lifetime. However, VRFB is a relatively new technology which is only recently commercially available. It was found that the commercial production and the availability of such systems have increased faster than fundamental knowledge about the underlying process (Weber et al. 2011). On-going research is focused on all aspects, for example on new component materials, electrolyte, electrochemical reactions, optimising flow distribution, optimising flow rates, system integration and reducing the costs (Alotto, Guarnieri & Moro 2014).

Although both technologies are already available in suitable sizes for buildings, relatively little is known about practical aspects and their performance in building-integrated HRES. System integration issues associated with the development of a building-integrated HRES composed of hydrogen systems or VRFB are not adequately reported or documented in the literature. More importantly, their dynamic performance integrated in a standardised building automation system has not been analysed. In addition, general challenges arise in terms of defining and testing of appropriate control strategies for HRES (Ulleberg et al. 2007). Practical experience has to be made to gain a better understanding of the emerging technologies, their dynamic performance and how they can be effectively integrated into a domestic scale HRES application. There is still a need for practical

demonstration projects, to analyse and document the performance of such storage technologies (IEA 2014).

The application of HRES at the low-voltage level seems to be a good solution to effectively manage the energy flow; however, design, control and operational aspects involved with HRES are rather complex. Computer simulations can be used to design the system, to assess the performance and to develop control strategies for a specific application. With regard to hydrogen systems there is a need for validated system models which can be used in commonly available simulation software to design HRES and to define operational strategies (Ulleberg et al. 2007). In addition, most of the existing modelling studies of VRFB cover specific aspects of the technology itself rather than investigating the overall system behaviour. Although various research studies have been presented with a focus on developing models of hydrogen systems and VRFB, they neglected potentially important operational aspects at system level.

In this regard, this thesis seeks to make a further contribution towards the application of building-integrated HRES by developing system models in an integrated manner. Experimental investigations are carried out alongside with the development of system models and control strategies.

## 1.3 Research aim, objectives and methodology

The overall aim of this thesis is to provide a better understanding of the integration of hydrogen systems and VRFB into a building automation system and how the system performance is influenced by operational conditions. In addition, it seeks to develop models of an electrolyser, a fuel cell and a VRFB by combining theoretical and operational aspects to build an integrated system model applicable for annual simulations using high resolution temporal data and to assess their performance for residential application.

To address these aims, the research objective is threefold:

1) Development of an experimental platform to investigate systematically the steady state and the dynamic performance of energy systems under real world conditions.
2) Development of system models of the energy systems considering theoretical and operational aspects, and the development of a suitable energy management strategy.
3) Evaluation of the hydrogen system and the vanadium-redox-flow-battery as decentralised storage for buildings.

To accomplish the three research objectives several practical issues had to be tackled. An experimental platform was developed from individual energy systems. A unified communication channel among all energy systems was established and control structures were implemented to

investigate the dynamic interaction of the energy systems. Furthermore, each energy system was equipped with additional measurements to perform the detailed component characterisation. The integration process presented in this thesis provides important insights and will help system integrators to design a building-integrated HRES.

To evaluate the dynamic performance of the hydrogen system and the VRFB at system level, a generally applicable experimental method had to be defined to systematically characterise their behaviour. The first set of experiments investigated the steady state performance, the second set focused on the response to a single dynamic event and a third set of experiments characterised the response to multiple dynamic events. The systematic approach revealed important information about the real performance of the energy systems and identified transient limitations at system level. These findings were required to develop the system models and the energy management strategy of the HRES. In addition, the systematically characterisation provided important information about the capability of the systems to balance the volatile power output of renewable energy sources integrated in multivendor HRES, which is valuable for system integrators to design appropriate control strategies.

The model development was carried out in an integrated manner. Based on the experimental characterisation a generic model layout was defined. The modelling process was carried out within the MATLAB®/Simulink®/Stateflow® environment. Each developed semi-empirical model combines theoretical and operational aspects to reflect the real behaviour of the energy systems. Furthermore, the developed models were improved compared to models presented in the literature. Moreover, experimental methods were designed to extract the parameters of the developed empirical functions of the models. The cross-validation technique was applied to find the parameters and to validate the models against measured data. The detailed presentation of the model development process and the experimental data gathered from the hydrogen system and the VRFB provide valuable information, which can be applied for system model analysis by other researchers in the field of HRES.

To investigate the performance of building-integrated hydrogen systems and VRFB it was necessary to establish an overall energy management strategy, which ideally can be applied to conduct the annual simulations and to control the experimental platform in real-time. In this regard, an advanced energy management strategy was also developed in MATLAB®/Simulink®/Stateflow®. A combination of three mechanisms was applied to manage the HRES. The application of a standardised software interface established a communication method between the simulation environment and the experimental platform.

The annual performance of a building-integrated hydrogen system and VRFB was analysed by means of different simulation scenarios. The scenarios were modelled to represent a grid-connected HRES integrated in a residential building. The objectives of the energy management strategy were to improve the on-site utilisation of the PV energy, to reduce the grid interaction of the building and to operate the energy systems efficiently. Each individual simulation scenario was carried out for a time period of one year with a high temporal resolution. The performance was assessed by calculation of three performance indices. Furthermore, sensitivity analyses were performed to find optimised control parameters and to establish the impact of the PV size and the load on the annual performance. Moreover, the application of the building-integrated HRES as deferrable load in smart grid environment was evaluated. The conducted simulation studies revealed important insights to better understand the performance and the interaction of a building-integrated hydrogen systems and VRFB, which are essential for the design HRES.

Finally, the developed energy management strategy was applied to control the experimental platform and the dynamic performance of the energy systems integrated in a building automation system was analysed. The real-time management of the experimental platform provided valuable information of the dynamic performance of such energy systems in a real world application. The presented findings are relevant to understand the factors which influence the performance of hydrogen systems and VRFB associated with renewable energy sources and can be used for further developments.

## 1.4 Research limitations

The research carried out in this thesis applied a combined experimental and simulation approach to develop system models of two emerging storage technologies. Due to the complexity of each individual energy system and the overall complexity of the integrated experimental platform, some boundaries were defined.

The developed models are based on the systems installed at Ostfalia University. To achieve comparability between the simulations and experimental investigations, these models were used for annual simulations to assess building-integrated hydrogen systems and VRFB. An overall optimisation of the system sizes was not performed.

Since the focus was the development of system models useable for annual simulations, transient effects occurring within the energy conversions systems, for example, double layer effects at the electrodes were not considered due to the significantly increasing computational time and the minor impact on the overall performance.

The defined simulation scenarios were focused on the domestic application. The applied electric load data and the domestic hot water profile were generated by load models presented in the literature with a temporal resolution of one minute.

Hydrogen systems and VRFB are still emerging and not broadly applied technologies; thus, they are not cost competitive compared to other energy storage technologies such as lead-acid batteries, in particular for small scale applications. Therefore, a techno-economic analysis was not conducted.

Due to the complexity of the processes involved to understand the ageing of alkaline electrolyser, PEM fuel cell and VRFB, component degradation was not considered in the developed system models. The investigation of ageing processes is time consuming and requires more specialised measuring equipment if an overall model validation is desired.

## 1.5 Outline of the thesis

The thesis is organised in the following manner:

**Chapter two** presents a literature review to provide a more detailed context. First, a brief introduction to hybrid energy systems and their different system topologies is presented. It is followed by a discussion on the relevance of buildings and the application of storage technologies. Different energy management approaches are reviewed and their characteristics are outlined. The key section of this chapter presents a review of hybrid renewable energy systems with a particular focus on experimental and simulation studies at residential level.

**Chapter three** presents in detail the developed experimental platform. It describes the electrical and communication topology of the experimental platform and the individual experimental set-up of each energy system. In addition, the layout of the control structure to coordinate the energy systems and to manage the energy flow is outlined.

**Chapter four** introduces methods to systematically characterise the performance of the alkaline electrolyser, the fuel cell and the vanadium-redox-flow-battery. In addition, experimental results of each system characterisation are presented.

**Chapter five** presents the development of system models based on the operational aspect identified in the previous chapter. A general model layout composed of several sub-models is proposed, that considers theoretical and operational aspects. In addition, experimental methods are defined to extract parameters for the semi-empirical models. Furthermore, the validation of the developed sub-models and the integrated system models are outlined. This chapter closes with the development of an energy management strategy that considers the findings of chapter 4.

**Chapter six** presents as a continuation of the previous chapters the application of the system models and the energy management strategy. Different domestic simulation scenarios are defined to determine the annual performance of the electric storage systems, the local utilisation of the PV energy and the grid interaction of the building. Finally, the functionality of the developed energy management system is demonstrated and the dynamic interaction of the energy systems is investigated by means of experiments.

**Chapter seven** closes the thesis by giving conclusions, recommendations for future work and the major contributions.

# 2 Background and related work

This chapter provides the context of this PhD thesis. Section 2.1 introduces and clarifies the term of hybrid renewable energy systems. In addition, the relevance of buildings and the need for electrical storage are discussed. An overview of energy management approaches is followed. Section 2.2 reviews the application of hybrid energy systems with main focus on hydrogen systems. Modelling of hybrid energy systems is discussed in section 2.3.

## 2.1 Introduction to hybrid energy systems

The term Hybrid Energy System (HES) defines a combination of different energy sources and energy storages to cover a certain demand. A general definition was formulated by Manwell (2004, p 215): *"Hybrid energy systems are combinations of two or more energy conversion devices (e.g., electricity generators or storage devices), or two or more fuels for the same device, that when integrated, overcome limitations that may be inherent in either."*

This definition is not precise about the scale and can be applied quite general. From a macro level perspective, the public electricity grid itself can be defined as hybrid energy system composed of a portfolio of different power plants with certain characteristics (nuclear and coal power plants to satisfy the base load, gas power plants for load following and pumped hydro storages to meet the peak load) to guarantee a stable and reliable power supply. A small scale application is, for instance, a hybrid electric vehicle that combines a combustion engine with an electric motor to increase the efficiency and the performance of the vehicle. Therefore, the combination or the hybridisation of energy systems compensates the limitation of the individual component and leads to a higher degree of supply reliability and/or a performance increase.

The most typical application of HES is rural electrification supplying individual systems such as buildings or telecommunication stations or to power an aggregation of single systems, for example a village. In addition to the conventional HES typically composed of a diesel generator or a CHP unit, the utilisation of renewable power becomes more important in terms of providing pollution free energy as well as minimising fuel costs. This improvement can be achieved by adding renewable power generators such as PV and wind turbines to a HES, which then is generally defined as hybrid renewable energy system (HRES) (Wichert 1997; Manwell 2004). Apart from reducing fuel costs and carbon dioxide emission, the integration of renewable power sources into conventional HES is also promising to increase the efficiency and the supply reliability. Recently, the general interest in HRES has been significantly increased. A variety of HRES are presented in the literature (Deshmukh & Deshmukh 2008; Nema, Nema & Rangnekar 2009; Bajpai & Dash 2012). Hybrid energy systems can

be classified into stand-alone (aka off-grid), which has been the most discussed to date, and grid-connected systems.

In stand-alone systems it is obvious that the utilisation of solar and wind power cannot be done by simply adding PV or wind turbines to the system due to the fact that the power output of the renewables is linked to weather conditions. Thus, renewable energy will not exactly match the local demand which may cause operational problems in terms of voltage and frequency variations. To overcome this limitation, storage technology is very important within stand-alone applications to balance electric power output and electric demand.

Grid-connected systems, on the other hand, are part of the public electricity grid and are installed at the distribution level. Electricity is generated near to where it is consumed; consequently, distribution losses could be reduced and the electricity grid of rural areas, which tend to have a weak network with long radial branches, could be stabilised (Kaundinya, Balachandra & Ravindranath 2009). The volatile characteristic of renewable power sources plays a minor role because the grid can provide the deficit power as long as the penetration of renewable power is low. As discussed in the previous chapter, there is a growing interest for manageable decentralised energy sources to provide added-value to the public grid. Hence, storage technologies at this level may become necessary to provide a higher degree of flexibility. In the literature only a few studies have been published with focus on grid-connected utility interactive HRES (Deshmukh & Deshmukh 2008; Nema, Nema & Rangnekar 2009).

The work presented in this thesis is relevant to the general class of HRES installed at the distribution level. Introducing HRES combined with electric storage at this level will provide a mechanism to actively manage the power flow; therefore, it will help to equalise electric demand and the volatile power injection of the renewable. In addition, it may reduce the risk that the increasing share of renewables destabilises the grid.

### 2.1.1 System topologies

HES/HRES can be classified as DC or AC coupled electric systems (Abd El-Aal 2005). Figure 2-1 illustrates the two topologies, which can be applied either for hybrid energy systems or for micro-grids. In DC coupled systems all electric energy sources and storages are connected via DC/DC converter or AC/DC inverter to a common DC bus with a defined voltage level. Although PV arrays and batteries generate a DC voltage, it is necessary to adopt the varying output voltage of each device to a defined voltage level of the DC bus via DC/DC converters. The connection to AC loads and/or the public grid is realised by a single AC/DC inverter. Advantages of the DC topology are its simplicity and the direct coupling of components independent of frequency (Nehrir et al. 2011).

Drawbacks are that no standardised DC voltage level exists, system extension may cause difficulties and the overall efficiency in case of serving AC loads is low (Abd El-Aal 2005). In AC coupled systems the electric energy sources and storages are connected through an AC/DC inverter to standardised AC bus (e.g. 230 V/400 V 50 Hz).

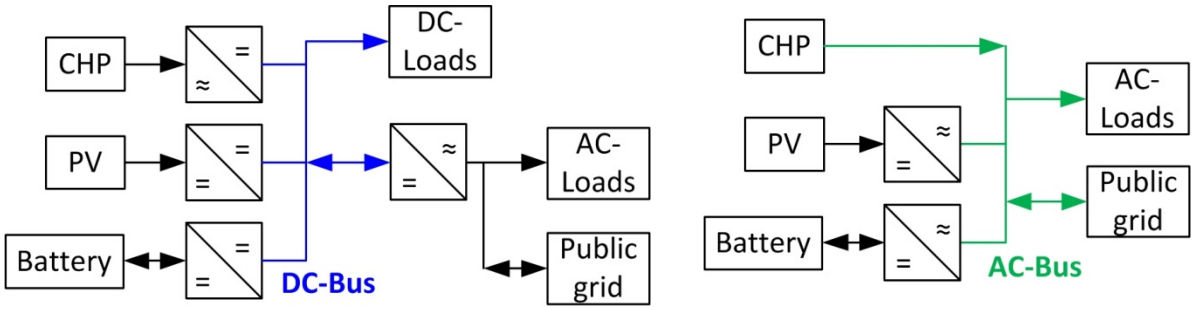


**Figure 2-1: DC coupled (left) and AC coupled (right) HRES.**

This system configuration has several advantages, for example, electric generators can be directly connected to the AC bus, AC loads can be served directly and the system can be easily extended (Abd El-Aal 2005; Nehrir et al. 2011). Drawbacks are that the different electric energy sources and storages need to be synchronised with the AC bus and the voltage and frequency should be well controlled in stand-alone operation.

Instead of using strictly one of the above described system topologies combined solutions also exist. For instance, it could be beneficial to group localised DC energy sources, storages or loads with similar voltage level to form a DC bus with a single connection via an AC/DC inverter to an AC bus. In such configuration the conversion losses could be reduced leading to a higher overall energy efficiency.

The HRES developed in the thesis is based on the AC topology which can be typical found in European households. The scale of the applied technologies is in the range of a few kilowatts, thus, they can be considered for residential applications.

### 2.1.2 Relevance of buildings

As approximately 40% of the primary energy usage in the EU applies to the building sector the EU has focused on increasing the energy efficiency in buildings (EeB 2010). It is expected that buildings will be transformed from passive energy consumers into active energy providers/consumers (prosumers). Recently, net zero- and positive-energy buildings have gained a lot of interest in the research community (Milo et al. 2011; Kolokotsa et al. 2011; Renau et al. 2014). The EU has issued a directive that after 31$^{st}$ January 2021 all new buildings have to be nearly zero-energy buildings, which means

that the building has a very high energy efficiency, an almost zero or at least very low annual energy balance and the energy is preferably supplied by renewable energy sources either generated on-site or nearby (EU-Directive 2010).

The transition of the electricity supply system from a centralised to a decentralised system puts the building sector into focus in the on-going discussion about the introduction of smart grids. Buildings can play a significant role in realising the future distributed electricity grid composed of interacting smart grids if the energy usage within buildings is understood and the energy flow can be controlled (Agarwal, Weng & Gupta 2011). In electricity networks the power generation and the demand needs to be always in equilibrium, otherwise the grid can become unstable. Therefore, to provide added value to the electricity grid, the energy consumption and generation in buildings needs to be considered not only on an annual basis but on a temporal resolution of hours, minutes or even seconds. Therefore, nearly net-zero energy buildings should be improved to be grid-friendly by providing grid services such as peak-shaving, reactive power compensation and back-up power to local loads (Milo et al. 2011).

In this regard, the roll-out of smart metering devices along with the introduction of ICT will help to establish mechanisms to actively manage electrical energy flow within the grid and buildings (VDE 2010). From a technical feasibility perspective, the amount of energy from the German domestic sector that could be time shifted in 2020 has been predicted to be 3.8 GW (ETG Task Force DSM 2012). However, this potential will remain unused, if smart meters and mechanisms to control the demand are not introduced. Such mechanisms are commonly referred to as Demand Side Management (DSM) and Demand Side Response (DSR). DSM describes the management of appliances within the building, for instance, to reduce the peak load. On the other hand, DSR includes the active response of the building to an external signal, for instance, a price signal to manage the demand. In addition, the application of electric storage provides more flexibility. DSR will not only be restricted to demand shift, but It can also be used to release energy at certain times (ENA/EnergyUK 2012).

In this context the introduction of HRES composed of renewable power sources and electrical storages into the built environment is of utmost importance. Recently, the application of HRES in buildings has gained more attention in the literature (Kanchev et al. 2011; Sechilariu, Wang & Locment 2013; Wang 2013; Zeng, Zhao & Yang 2013). Kanchev et al. (2011) discussed the interaction between building-integrated micro-grids and a smart grid without a particular focus on the applied technologies. They highlighted the need for electrical storage systems to compensate the fluctuations of the renewables and to gain the flexibility to be an active prosumer. Sechilariu et al. (2013) and Wang (2013) studied building-integrated DC micro-grids consist of PV and batteries with

focus on supervision and energy management in interaction with the smart grid. Both proposed a local energy management system that considers time variable electric energy tariffs and limits the grid injection of the renewables. In all these reviewed research articles it was found that the communication within the building was the key to establish a local energy management.

Introducing smart grid communication poses several new challenges which have to be addressed. Especially, aspects such as privacy of the end-user, data security, communication infrastructure, standardisation and interoperability need to be considered and clarified (Fan et al. 2013). Standards need to be introduced to establish a secure, reliable and interoperable communication between the building and the grid operator as well as among the appliances in the building. An emerging standard in this frame is the Open Automated Demand Response (OpenADR) standard, it defines an open communication between grid operators and end-users to exchange demand response signals (OpenADR 2010). In this regard, the adaption of established building automation standards should be considered to achieve a high degree of interoperability (Noga et al. 2013). Among others, the Local Operating Network (LON) (EN 14908 2005) has been identified as standard which can be used at the end-user side due to its interoperability and maturity. Therefore, it may be relevant for the deployment of smart grids (Greer et al. 2014).

Tremendous effort has been put into research, standardisation, harmonisation and legalisation to facilitate the introduction of smart grids world-wide (Fan et al. 2013). It is unlikely that a timely solution will be found that adequately addresses all aspects because of the complexity of smart grids. In addition, the variety of different requirements in national grid codes increases the difficulty to implement broadly applied DSR mechanisms. Understanding the application of HRES at the level chosen in this thesis is an important contribution which could underline advances in smart demand response but the details regarding the communication between the HRES and the grid operator are outside the scope of this thesis. However, the developed experimental platform applies a standardised building automation protocol, LON, to coordinate and to control the energy systems to improve the local consumption of the renewable energy. Therefore, the presented experimental analysis provides important insights about the dynamic performance of HRES at the end-user side.

### 2.1.3 Electric energy storage

The introduction of electric energy storage technologies is a necessary step towards a low carbon electric energy system in the EU: *"In a low-carbon energy system, storage will be needed at all points of the electricity system" (EU-DGE 2013, p 6)*.

Energy storage technologies can be applied at power generation level (large scale storage, GWh), at transition level (medium to large scale storage, MWh), at distribution level (medium scale storage,

kWh-MWh) and customer level (small scale storage, kWh). Although energy storage will become necessary in the future electricity system with a high share of renewable power, the introduction faces a lot of barriers. Taylor et al. (2013) conducted a qualitative analysis of three different pathways – user led, decentralised and centralised – for energy storage in the UK. Among others they have identified that the introduction of storage at decentralised and centralised level requires new institutional and business arrangements. At customer level barriers arise in terms of energy efficiency, affordability, controllability, performance and integration into the built environment. A recently published report (Hollinger et al. 2013) analysed the benefits of applying PV-battery systems at customer level. They concluded that the introduction of electric storage can significantly reduce the grid peak injection of PV leading to an overall improvement of the electric grid capacity and thus more PV can be installed. However, it would be only beneficial if the energy flow can be controlled. Besides the positive effects, the major challenge to introduce electric energy storage still remains, its application needs to be economically feasible (EU-DGE 2013; Taylor et al. 2013).

Electric energy can be stored directly (electric/magnetic field) or it can be converted into another energy form (mechanical (potential/kinetic), thermo-electric or chemical) (ETG Task Force ES 2009). The simplest approach to store electricity is to convert it into heat (power-to-heat) and use the energy, for example to produce domestic hot water. A drawback of this method is that the stored energy cannot be converted back into electricity. Ideally, an electric energy storage technology involves the accumulation and the storage of energy to release electricity at certain times when it is needed. Each form of storage has its own characteristic and can be deployed for power quality/reliability or for energy management purposes. The requirements in terms of response time and power density are high for power quality/reliability applications. In energy management applications the main focus is to shift energy in times where it is required or to reduce peaks in the power profile.

Figure 2-2 illustrates the issue of matching the electric energy demand with the generated electricity from renewable energy sources. A daily typical domestic load profile is shown to the left and the daily supply profile of a combined PV and wind generation system to the right. Both profiles are strongly variable and there is only a small overlap between the two profiles. To improve the match, electric storage can be applied, for example to level the power to avoid peaks (a), to shift the generated electric energy in times when demand exceeds the generated energy of the renewables (b) or to compensate the fluctuations of both the power output of the renewable sources or the power demand of the loads (c).

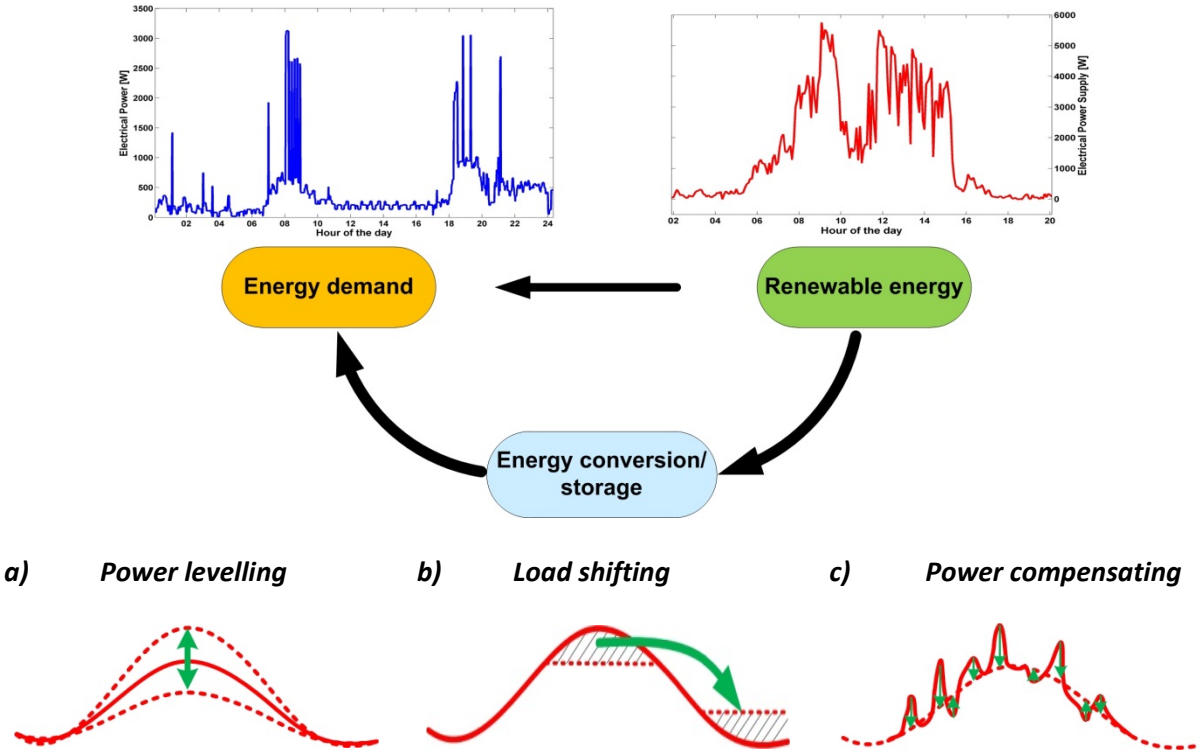


**Figure 2-2: Matching energy demand and energy supply**

An extensive overview of various energy storage technologies and their different functionality and performances can be found e.g. in (Ibrahim, Ilinca & Perron 2008; IEC 2011). What type of electric energy storage can be deployed depends strongly on the application, operational constraints and spatial requirements. Nair and Garimella (2010) conducted an assessment of small scale electric storage technologies for buildings. They focused on a comparison between lead-acid, nickel cadmium (NiCd), nickel metal hydride (NiMH) and lithium ion (Li-ion) batteries. Their results show that NiCd have the highest potential for small-scale application in renewable energy systems. They also stated that Li-ion batteries have the greatest potential to enter the renewable energy sector with its high energy density, high lifetime, stable voltage level and fast response times. An overview of commercially available small scale battery systems is presented by the German PV-magazine (PVMD 2014). It states that nowadays the dominant technologies are lead-acid and lithium batteries for small scale domestic application with PV. Chatzivasileiadi et al. (2013) discussed more generally suitable electric storage technologies for buildings. Among others they discussed emerging technologies such as vanadium-redox-flow-batteries (VRFB) and the usage of hydrogen. They identified that VRFB have high potential for load-shifting applications at distribution and customer level.

One advantage of VRFB is the independent scalability of power and energy capacity. The power is defined by the size of the energy converter (the cell stack), whereas the energy is defined by the

amount of positive and negative charged electrolyte stored in two tanks. In general, the interest in VRFB has been significantly increased over the past ten years and several installations from a few kW/kWh to MW/MWh have been realised worldwide (Shigematsu T. 2011; Alotto, Guarnieri & Moro 2014). It ranges from off-grid and emergency power supply to grid services such as load levelling and power output stabilisation of renewables. Schreiber et al. (2012) have shown that VRFB could be cost competitive compared to lead-acid and lithium-ion batteries for small scale application, if the manufacturing costs can be reduced. However, only a few manufacturers exist world-wide and their focus is currently the application of VRFB at distribution level.

The introduction of hydrogen as energy carrier gives a high degree of flexibility in terms of its utilisation. It can be used for stationary applications to provide power and heat as well as for transport applications. Hydrogen can be a key technology to decarbonise both the heating and transport sector. However, its usage would only be environmentally beneficial, if the hydrogen is sustainably generated from renewable energy sources (Ball & Wietschel 2009). Hydrogen can be sustainably produced by water electrolysis using excess renewable energy and it can be easily stored, for example in compressed gas cylinders. It can be converted back into electricity in fuel cell systems or it can be used in combustion processes substituting hydrocarbon fuels. The complete electric conversion cycle is often called “hydrogen loop”. In the future energy supply system hydrogen may be important to store large amounts of energy at centralised and distributed level (ETG Task Force ES 2009; EU-DGE 2013). The introduction of small scale on-site hydrogen production units is arguable due to the high component costs and the low efficiency of the hydrogen loop. However, small-scale decentralised systems may play an important role in achieving a hydrogen economy in the future, for instance, as part of a domestic or office building (Yilanci, Dincer & Ozturk 2009), if the manufacturing costs can be reduced and the technology can be improved in terms of efficiency and reliability. A detailed summary of world-wide hydrogen projects (large and small scale) are given by Yilancy et al. (2009) and Gahleitner (2013). Most of the projects were motivated by substituting fossil fuels especially in remote applications and by the need to have a reliable and scalable option to store renewable energy at the distribution level. Nevertheless, hydrogen systems are still an emerging technology and research challenges remain with respect to improving the system efficiency, system integration and to reduce - overall - the costs of the components (Gahleitner 2013).

This thesis focuses on the system integration of the two emerging energy storage technologies: the hydrogen loop and the VRFB applied at customer level. The electrical and the communicational integration into a hybrid energy system are presented. In addition, technical barriers are addressed and operational aspects are discussed aiming to improve the energetic efficiency. The presented

findings provide a better understanding about the application of hydrogen systems and VRFB system as a controllable energy source or sink associated with DSR.

### 2.1.4 Energy management of hybrid energy systems

The management of the energy flows within HRES is a key issue to achieve an efficient and reliable operation (Nehrir et al. 2011). Each component has its own characteristics and constraints, which needs to be considered within the overall energy management strategy. For example, in chapter 4 it is shown that the fuel cell system has a certain start-up time, a limited load following capability and an optimal operational range.

A detailed review of energy management approaches for HES are presented by Salmasi (2007) and Erdinc and Uzunoglu (2010). The approaches can be classified as rule-based strategies and optimisation based strategies. Rule-based energy management approaches can be sub-categorised into deterministic methods and intelligent methods. Deterministic methods manage the energy flow according to defined rules, e.g. simple relay (on/off) strategy, a flow chart (Uzunoglu, Onar & Alam 2009; Ipsakis et al. 2009) or petri-nets/statecharts (Lu et al. 2010) strategy. More advanced rule-based approaches are intelligent methods such as fuzzy logic (Bilodeau & Agbossou 2006; Stewart et al. 2009) or multi-agent modelling (Lagorse, Paire & Miraoui 2010; Jun et al. 2011). One advantage of rule-based strategies are that they can be implemented for real-time or on-line application as demonstrated e.g. by Caux et al. (Caux et al. 2010) and Erdinc et al. (2012). Optimisation based energy management strategies are often applied to find an optimal operational strategy or optimal system design by applying mathematical optimisation techniques such as neural networks (Al-Alawi, M Al-Alawi & M Islam 2007), linear programming (Chedid & Rahman 1997), dynamic programming (Riffonneau et al. 2011), and genetic algorithms (Bernal-Agustín & Dufo-López 2009). In addition, they are also used to minimise costs by optimising the control set-points or by optimal sizing of individual components (Salmasi 2007). Drawbacks of the optimisation based strategies are that they cannot be deployed directly online, that historical data about energy supply and demand are required, and that high computational resources are necessary (Erdinc & Uzunoglu 2010). Another important challenge arises in considering different dynamic characteristics of the installed energy systems in the energy management strategy. According to the load following capability of each energy system, the power set-point transitions need to be restricted. For instance, Bilodeau and Agbossou (2006) applied a low-pass filter to reduce the on/off switching of the energy systems. Therefore, frequency decoupling techniques should be implemented into the energy management system to reduce the dynamic stress on certain energy systems such as fuel cells (Erdinc & Uzunoglu 2010; Etxeberria et al. 2010).

Each energy management approach has its own advantages and weaknesses. When developing energy management systems it should always be to find the right balance between the application and the available computational resources. Since the focus of this thesis is to demonstrate the principle operation of a HRES, a rule-based approach is applied to manage the energy flow in real-time because of its simplicity and robustness. The overall control strategy is composed of a strategic supervisory level, a local supervisory control level and a local control level, which is also referred to as multilevel control approach (Nehrir et al. 2011). Based on the experimental study presented in chapter 4, operational limits are extracted from each component. The development of an energy management strategy is outlined in section 5.4. In chapter 6 the energy management strategy is evaluated by means of simulations and real-time tests conducted with the experimental platform.

## 2.2 Application of hybrid energy systems

There has been continuing interest in many countries in research, demonstration and promotion of HRES for stand-alone and grid-connected applications. The following literature survey provides an overview of research activities in this field with a particular focus on hydrogen systems and small scale residential projects in the range of some kilowatts. In addition, the application of VRFB is reviewed. Although, VRFB research activities have been increased lately, the available literature in the frame of HRES, especially at customer level, is restricted.

### 2.2.1 Hydrogen hybrid renewable energy systems at distribution level

During the last decade there has been increasing focus on larger grid-connected wind hydrogen systems at distributed level (Gahleitner 2013). For instance, one of the larger demonstration projects is located on the Ustria Island in Norway (Ulleberg, Nakken & Eté 2010). This project has demonstrated that wind hydrogen energy systems can provide a reliable supply of electricity to an island with a small settlement. In 2012 the MYRTE project has been started in France to demonstrate a large scale PV hydrogen energy system with the objective to provide controlled peak-shaving power (power levelling) (Darras et al. 2012). Furthermore, the MYRTE project is one of the few projects which utilises the waste heat of the hydrogen loop, in this case for the air-conditioning unit of the facility.

### 2.2.2 Hydrogen hybrid renewable energy system at customer level

Although, the applicability of hydrogen at customer level is questionable due to the high component costs and low overall efficiency, the energy carrier hydrogen has motivated many researchers to demonstrate the technical feasibility at customer level. An early demonstration project was the

Freiburger self-sufficient solar-hydrogen house designed by the Fraunhofer Institute of Solar Energy Systems; it was in operation for 3 years (Voss et al. 1996). The produced hydrogen was used to supply an oven and to power a fuel cell system. In addition to the electrolyser and fuel cell, a battery system was added as short-term storage. Waste heat of the fuel cell was utilised for hot water supply. During three years of operation reliability issues of the hydrogen components had occurred due to their early stage of development. The PHOEBUS project (Barthels et al. 1998) demonstrated the integration of a hydrogen loop and PV into the energy supply of a library to achieve an autonomous operation. Hollmuller et al. (2000) evaluated a privately owned grid-connected dwelling in Switzerland, equipped with photovoltaic, battery, electrolyser and hydrogen storage. The on-site produced hydrogen was used by domestic appliances (cooking and heating) and for transport. The energy system of the dwelling was manually controlled and it was successfully operated for several years. The HaRI project (Gammon et al. 2006) has utilised both solar and wind to power a farm and an office building. Furthermore, it has been demonstrated the multifaceted application of hydrogen for stationary energy storage and for transport to power fuel cell vehicle. Recently, a self-sustainable and zero-$CO_2$-emitting HRES integrated into a medium-sized office building has been developed within the H2SusBuild project (H2SusBuild 2010; Paspaliaris et al. 2013). Paspaliaris et al. (2013) have summarised the results of the H2SusBuild project and they highlighted that a zero-$CO_2$-emission of the building has been achieved.

Experimental studies of residential scale stand-alone HRES have emerged focusing particularly on demonstrating and evaluating of operational and dynamic issues of the hydrogen systems. Bergen et al. (2009) and Maclay et al. (2011) presented detailed experimental studies of a laboratory hydrogen/solar test-bed in stand-alone and grid-connected operation, respectively. Both test-beds consist of an electrolyser and fuel cell system as long-term storage, and a battery system as short-term storage to cope with power transients. Bergen et al. (2009) highlighted the need of sufficient short-term storage to maintain the minimum input power of the electrolyser; thus, unnecessary operational transitions of the electrolyser can be avoided leading to a stabilised operating temperature. Maclay et al. (2011) experimentally identified that combining a fuel cell and battery improves the system performance. They found that batteries can compensate high power fluctuations; in addition, the batteries can provide balancing power to operate the fuel cell more continuously during periods of low power demand. Lutz et al. (2010) presented a report about a wind/solar/battery/hydrogen small-scale stand-alone system installed at the Kahua Ranch Hawaii. The main objective of the project was to validate the hydrogen system's functionality in real world application. They reported that operational aspects such as warm-up periods and dynamic operation influence the energy efficiency of hydrogen systems. The project outcomes underline the necessity of

applying an appropriate control strategy to minimise the operational stress on the hydrogen system. Furthermore, they suggest utilising the waste heat of both the fuel cell and electrolyser especially when supplying homes.

In her comprehensive review article about hydrogen HRES, Gahleitner (2013) concluded that the system integration process remains a challenging task due to the lack of standards and the early stage of development of the components. However, as discussed previously an overall energy management strategy is important for ensuring an energy efficient operation of HRES. Apart from the electrical connection of the energy systems, information, for instance, the current operational state needs to be exchanged among the energy management system and the energy systems. Thus, the introduction of a common communication channel is important to coordinate HRES. Bergen et al. (2007) and Little et al. (2007) conducted research studies on a residential hydrogen HRES. Both reported difficulties to achieve overall controllability of the HRES. The authors also stated that they have underestimated the effort to integrate the different interfaces of the components into a central data acquisition and control system. Ziogou et al. (2011; 2012) presented a more innovative system integration approach of a stand-alone hydrogen HRES. They have integrated different industrial communication protocols by transferring them into the standardised software interface OLE for Process Control (OPC) (OPC 2014). Based on this open system architecture an interconnection between the different subsystems and the control system can be easily achieved. A similar method was demonstrated by Figueiredo and Martins (2010). They integrated the control system of a HRES into the building and demand side management system of the Experimental Park of Renewable Energies in Évora, Spain. They proposed a system architecture that was based on an industrial communication protocol.

From the reviewed literature it can be concluded that little research has been carried out to investigate the dynamic performance of HRES integrated into building automation systems. Therefore, the system integration and the operation of HRES in buildings need to be evaluated. Such building-integrated HRES can either operate most of the time autonomously from the grid or they are able to provide grid-services such as load-levelling or peak-shaving. Autonomous or zero emitting operation of hydrogen based HRES was demonstrated, for instance, by Stewart et al. (2009), Figueiredo and Martins (2010) and Paspaliaris et al. (2013). Bocklisch et al. (2014) have recently presented an experimental study on a laboratory solar/hydrogen/battery test-bed for domestic application. They have focused on the development of a control algorithm to improve the PV self-consumption rate and to smooth the power output of the photovoltaic system to contribute the low voltage grid stabilisation.

Although a considerable amount of experimental studies on HRES with hydrogen for residential application have been carried out, there has been little discussion about the utilisation of the thermal energy of the hydrogen systems. The utilisation of the waste heat of both the electrolyser and the fuel cell may be beneficial in terms of increasing the overall energy efficiency. A field experiment conducted by Hamada et al. (2011) evaluates a photovoltaic/solar thermal collector/fuel cell system to provide both electricity and heat to a residential building. Their results show that a combination of solar thermal system and fuel cell can help to save primary energy compared to conventional heating system.

### 2.2.3 Hybrid renewable energy system with vanadium-redox-flow-battery

The VRFB is a technology which has recently become commercially available and has experienced an increasing interest. In the following experimental studies of VRFB systems are reviewed with focus on small scale application associated with renewable energy.

The on-going research project SmartRegion Pellworm (Wasowicz 2012) has demonstrated the grid integration of a hybrid storage system composed of a commercially available 200 kW/1.6 MWh VRFB and a 1 MW/560 kWh lithium-ion battery on a German island. The project aims to optimise the self-consumption of generated renewable energy from PV and wind on the island, thus, to minimise the power exchange with the public grid (mainland). At a test-facility of the Technical University of Denmark the integration of a 15 kW/120 kWh VRFB (advanced prototype) into a micro-grid has been demonstrated and tested to balance wind energy (Bindner et al. 2011). The focus of the experimental analysis was on long-term continuously operation of the VRFB. Sterrer and Prüggler (2013) have experimentally analysed the integration of a commercially available 10 kW / 100 kWh VRFB into a grid-connected HRES composed of PV and small-scale wind turbine. In addition, they have developed a central battery management system and demonstrated the capability of the VRFB to provide grid services such as load-levelling and power compensation. The Alaska Center for Energy and Power conducted an experimental analysis of a small-scale commercially available 5 kW/20 kWh VRFB (an earlier model of the same VRFB deployed in this thesis) to evaluate the performance for stand-alone operation in wind-diesel hybrid energy systems (Muhando & Johnson 2012). They conducted a performance analysis at different constant charge/discharge power levels in a laboratory environment without the physical integration of the VRFB into a HRES. At customer level the on-going research project “Multi-source Energy Storage System Integrated in Buildings” has published first results about the development and integration of small-scale VRFB. They have integrated a 1 kW/6 kWh prototype of a VRFB into the Freiburger solar house and developed a smart redox-flow-battery management (MESSIB 2014).

### 2.2.4 Scope of experimental investigations

A particular focus of this thesis is on the system integration of two emerging energy storage technologies, namely the hydrogen loop and the VRFB. The electrical and the communicational integration into a residential scale hybrid energy system are presented. In addition, technical barriers are addressed. In chapter 4 an experimental methodology is introduced to systematically analyse the dynamic performance of the components at system level. Based on this analysis, operational constrains are identified and the system performance is discussed. Furthermore, the dynamic interaction of hydrogen systems and VRFB integrated in a building automation system is experimentally analysed in chapter 6. The research carried out in this thesis provides a better understanding how the intermittent operation influences the system performance. In addition, it illustrates the potential of hydrogen systems and VRFB to be employed as deferrable energy source or sink.

## 2.3 Modelling of hybrid energy systems

A considerable number of theoretical models have been reported in the literature. Depending on research purposes models can be applied from macro level (e.g. national) to component level. Usually high level models focus on annual energy prediction and could be used for feasibility, economic and system evaluation studies. Low level models or individual component models, on the other hand, are more specific and are often applied to address dynamic aspects. The following section 2.3.1 discusses what temporal resolution is suitable for simulation studies to investigate the performance of HRES. Section 2.3.2 summarises modelling studies presented in the literature.

### 2.3.1 Understanding the need for high resolution data

Feasibility of a hybrid energy system could be determined from techno-economic simulation studies. Such studies normally apply low temporal resolution – several minutes to one hour – data and simplified models. Techno-economic studies are focused on optimising the component size and operating costs, to estimate the basic operational strategy and demonstrating feasibility of HRES (Ashok 2007; Gupta, Saini & Sharma 2011; Hongfeng Li & Hennessy 2013). Some studies also apply low temporal resolution data to discuss the influence of the applied energy management strategy onto the system performance (Dursun & Kilic 2012). However, these studies neglect system dynamics such as power fluctuations and transitions between operating states of components.

How time averaging influences the behaviour of energy systems is illustrated in Figure 2-3. This graph shows measured data of PV power with a temporal resolution of one second. The data is taken from one PV system of the experimental platform which is introduced in chapter 3. For comparison,

averaged data with a temporal resolution of one hour, five minutes and one minute is drawn in Figure 2-3. As can be clearly seen, the larger the averaging time interval, the smoother the power profile of the PV is. Higher power gradients are smoothed out at time intervals larger than five minutes. It is evident that data used in simulation studies with a low temporal resolution will underestimate the impact of the dynamics on the overall energy system.

These findings agree well with an analysis of domestic load profiles presented by Wright and Firth (2007). They investigated the effect of different time averaging intervals from one minute to 30 minutes on the supply and demand matching process. They showed that temporal resolution of less than 5 minutes is necessary to reveal short power peaks. A study conducted by Erdinc und Uzunoglu (2011) underlines the need to apply high resolution data for energy management analysis of HRES. They examined a PV/wind/battery/hydrogen system and carried out two simulations based on hourly data and on minutely data. They showed that the averaging process leads to a considerable underestimation of the power variations which needs to be compensated by the hydrogen system. Thus, they suggest the usage of minutely or even secondly data for energy management system analysis.

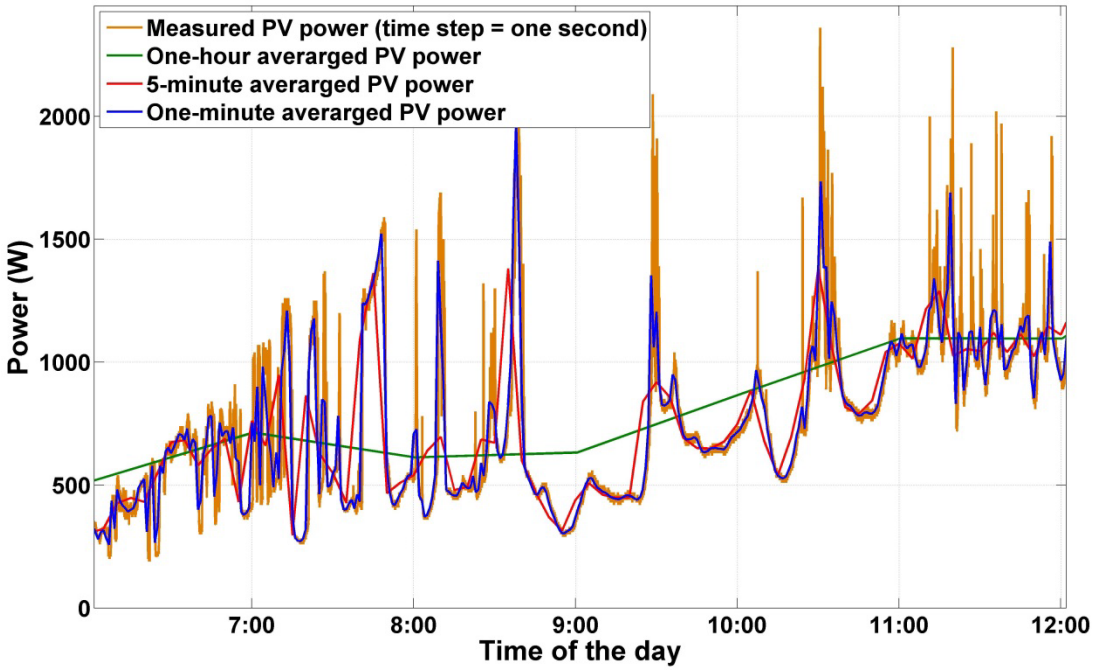


**Figure 2-3: Photovoltaic power at different temporal resolutions based on measured data taken from the Ostfalia Hybrid Renewable Energy Park.**

### 2.3.2 Modelling of hybrid renewable energy system at customer level

Numerous modelling studies on autonomous residential scale HRES have been presented in the literature, e.g. by Hatti et al. (2011), Cau et al. (2014), Kahn and Iqbal (2009) and Tesfahunegn et al.

(2011). Different energy management strategies are discussed by Hatti et al. (2011) and Cau et al. (2014). Hatti et al. (2011) present a simulation study on a PV/hydrogen system focusing on control and management. They deployed a rule-based energy flow management algorithm to control the fuel cell and electrolyser. A simulation study over one day based on five minutes weather data was carried out. Cau et al. (2014) analysed three different energy management strategies for a PV/wind/battery/hydrogen system. Meteorological data with a temporal resolution of 30 seconds was used to predict the power output of the photovoltaic array and the wind turbine. Both studies neglect temporal transitions of the hydrogen loop and the presented models are not validated against measured data. Dynamic aspects were analysed by Khan and Iqbal (2009) and Tesfahunegn et al. (2011). Khan and Iqbal (2009) discussed the dynamic behaviour of a wind/hydrogen stand-alone system for residential application. They conducted a simulation study with a high sampling time of milliseconds but with a limited time period of only 15 seconds. Their results indicate that the modelled control system can successfully operate under such dynamic conditions. Tesfahunegn et al. (2011) focused on operation of a hydrogen loop integrated in a PV/battery stand-alone system. They highlighted the need of short-term storage to compensate power fluctuation and to operate the electrolyser and fuel cell more smoothly. A moving-average filter was applied to calculate the set-point of either the electrolyser or fuel cell. The results show that the proposed control method is able to reduce the dynamic stress onto the hydrogen systems, thus, the component lifetime will be increased and operating costs can be reduced.

Research related to grid-connected HRES is presented by Maclay et al. (2006), Stewart et al. (2009), Milo et al. (2011) and Para et al. (2014a; 2014b). Maclay et al. (2006) developed a model of PV/battery/hydrogen system to analyse the efficiency, load sharing and energy storage capacity. They proposed a rule-based energy management strategy that operates the battery and the hydrogen loop sequentially, first the battery is used until fully charged/discharged then the hydrogen loop is activated. An instantaneous switching between the energy systems was assumed. The presented analysis was based on low temporal resolution data of five minutes and 15 minutes for the residential load and photovoltaic power, respectively. Stewart et al. (2009) proposed a parallel operation of battery and fuel cell, where the electrolyser was directly powered by PV. A fuzzy logic power management was developed with the objective to minimise the electricity import from the grid. Milo et al. (2011) developed an adaptive rule-based control strategy for a zero energy building. The proposed energy management strategy considers minimum operation times for both the fuel cell and the electrolyser. The simulation results indicate that an appropriate control strategy can enhance a zero energy building to a grid-friendly building by providing auxiliary services such as peak-shaving or back-services. In addition, they have validated the proposed energy management strategy by

means of a real-time controller-in-the-loop simulation. A validation with a physical HRES was not performed. Parra et al. (2014a) have modelled a grid-connected dwelling equipped with PV, battery and hydrogen loop. The two storage technologies were compared with regard to their ability to utilise the local generated PV energy. In addition, an annual simulation study based on minutely data (weather and electric load) has been conducted. Parra, Gilliot and Walker (2014b) extended their study to analyse the role of fuel cells in the domestic sector and the application of a lithium battery/electrolyser hybrid storage system for a single dwelling and small community of 7 houses. Results show that the fuel cell - functioning as combined heat and power unit - can help to reduce carbon dioxide emission and that the hybrid storage system can significantly improve the local use of PV energy. In both presented studies operational aspects are not addressed. An experimental platform is currently under construction at Nottingham University to investigate different renewable energy technologies and electric storages (Parra, Gillott & Walker 2014b).

While waste heat utilisation of building-integrated fuel cell systems has been broadly discussed in the literature e.g. (Staffell 2009; Hamada et al. 2011), only a few studies have considered utilising the waste heat of electrolysers. Sossan et al. (2014) have presented an analysis about a smart building focusing on model predictive control to provide space heating according to dynamic electricity price. Space heat is supplied by conventional electric heater and a CHP unit composed of a fuel cell and an electrolyser. Lacko et al. (2014) analysed a stand-alone HRES for residential application considering both electricity and heat. A conventional system (small wind turbine, PV and oil boiler) was compared with an alternative energy system consist of wind/PV/hydrogen including waste heat utilisation. An annual simulation study with simplified component models was conducted. Their results demonstrate the waste heat utilisation can totally eliminate the need of a boiler.

System analysis of HRES composed of VRFB at customer level has not been thoroughly reported in the literature. An economic performance analysis was presented by Chen et al. (2013b) considering a grid-connected building integrated with a VRFB and PV. They conducted a spread sheet analysis and concluded that power peaks can be reduced and that the power output of the PV can be stabilised. Nguyen et al. (2011) present a simulation study on a PV/wind/VRFB/diesel hybrid energy system to supply a military base. They proposed a power management strategy to minimise the diesel consumption and to maximise the utilisation of the renewable energy sources. Qiu et al. (2014) extended this simulation study by means of validation of the proposed VRFB model against experimental data and discussion about the charge/discharge of the VRFB.

### 2.3.3 Scope of model development

Although extensive research has been carried out on residential HRES for both, stand-alone and grid-connected application, none of the studies apply high resolution data for annual simulation and adequately addresses operational aspects within the models. An important issue is the temporal resolution of the data used in the simulation. As stated previously high power peaks, which are typical in renewable energy application, are significantly underestimated in data with a temporal resolution lower than five minutes. The most notable gap in current understanding relates to the operational behaviour of energy systems. A common simplification in modelling energy systems such as fuel cells or electrolysers is that they can respond instantaneously to power variations. Operational transitions are often neglected; thus, simulation studies at system level tend to overestimate the response time and load following capability. In addition, applying hydrogen systems in conjunction with renewable energy sources will lead to a more transient operation. Furthermore, from the reviewed literature, it can be concluded that the evaluation of waste heat of the electrolyser has not well analysed so far. Moreover, little is known about the application of HRES with VRFB at customer level.

The simulation models developed in this thesis aim to integrate the electrical, thermal and operational behaviour of the experimentally characterised energy systems. Hence, a generic model layout is introduced in chapter 5. The developed system models are applied for annual simulations with a temporal resolution of one-minute to assess the performance of hydrogen systems and VRFB for domestic application. Furthermore, the useable amount of waste heat of the electrolyser is quantified.

# 3 Development of a research test bed for hybrid renewable energy systems

The Hybrid Renewable Energy Park (HREP) at the Laboratory of Electrical and Renewable Energy Engineering, Ostfalia University Wolfenbüttel, is a test facility to investigate the operation and the interaction of small scale decentralised energy systems for domestic applications (LabERT 2014). The overall goal of the HREP is to provide an experimental platform to demonstrate the practical operation of commercially available or nearly market ready microgeneration and energy storage technologies which can be used for educational, industrial and research studies.

At the start of this PhD, the existing HREP consisted of three PV arrays, a wind turbine, a CHP unit and a weather station. Every power device was separately connected to the university's electric grid. Additionally, they were wired to a building communication system, the LON protocol.

One of the objectives of this thesis was to develop the HREP further to transform it to an easily expandable modular system structure. In the framework of this research several new energy systems have been integrated into the HREP; besides the integration of a conventional lead-acid battery system, less mature technologies have been incorporated, a hydrogen loop and a VRFB. This plant expansion forms the basis for a detailed study of a subset of components configured as a hybrid energy system within the HREP as a whole. The experimental results will probe the current state of technologies and will expose obstacles when introducing new technologies for the domestic energy sector. Furthermore, data obtained from each component have been applied to develop semi-empirical models using a simulation environment. Based on computer simulations energy management strategies have been developed and have finally been applied to the experimental platform. It was very important for this thesis to develop ideas based on a combined experimental and simulation approach to gain practical and realistic understanding of the domestic application of HRES.

The following section gives an overview of the HREP including the presentation of the electric and communication system design. In addition, the experimental setup of the main components, the hydrogen loop and the VRFB, is described in detail. The control structure followed and the objectives of the energy management strategy are defined. Finally, the used programmable electric AC loads are presented. All other relevant components of the HREP are outlined in the appendix A-2.

## 3.1 Experimental system overview

The HREP power and energy capacity was designed to emulate typically installed energy systems in residential applications. This emulated scenario can be a single household equipped, for example with PV and battery storage, a house equipped with the whole setup, or a small settlement which aggregates to the HREP. Normally, a house in Germany is connected to the electric distribution grid via a three phase AC cable. Other European countries, for instance the UK, a household usually has a single-phase connection. Power capacities of electric energy systems are typically in the range of one to ten kilowatts. Energy sources such as PV and fuel cells are connected to the grid via DC to AC inverters. Consequently, the design for the HREP is based on an AC coupled system topology. Besides the availability of electronic devices, the AC coupled system has the advantage that it is highly flexible in terms of system configurations and expandability, which meets another design criterion of the test bed.

All components are commercially available and have been assembled to a hybrid energy system composed of renewable energy sources, power sources as well as energy storage devices. It has to be emphasised that the intention of this PhD thesis was to use the HREP for exploring integration and operational issues of decentralised energy systems, not for developing core components. However, the HREP can be used as a perfectly designed environment for early market testing of individual devices. The energy systems discussed are being far from broadly used or ready to enter the domestic market. Nevertheless, all of them have such a potential if costs and reliable issues can be solved. Therefore, the use of nearly market-ready products was considered to demonstrate that such a system could in principle be developed for a real world scenario.

A simplified schematic of the HREP is shown in Figure 3-1. The main components are two PV arrays, a wind turbine, a CHP, a fuel cell, an alkaline electrolyser, a VRFB, a lead-acid battery, three programmable electronic loads and a charging point for electric vehicles. All devices are linked via an electric three phase connection, the AC-bus (the black line in Figure 3-1). The electric design is discussed in chapter 3.2. The blue line represents the local hydrogen distribution network which links the electrolyser and the fuel cell to the gas storage.

Table 3-1 presents the chronological order of the installations and provides the main technical information. The first system that was implemented during this PhD project was the battery system in 2009.

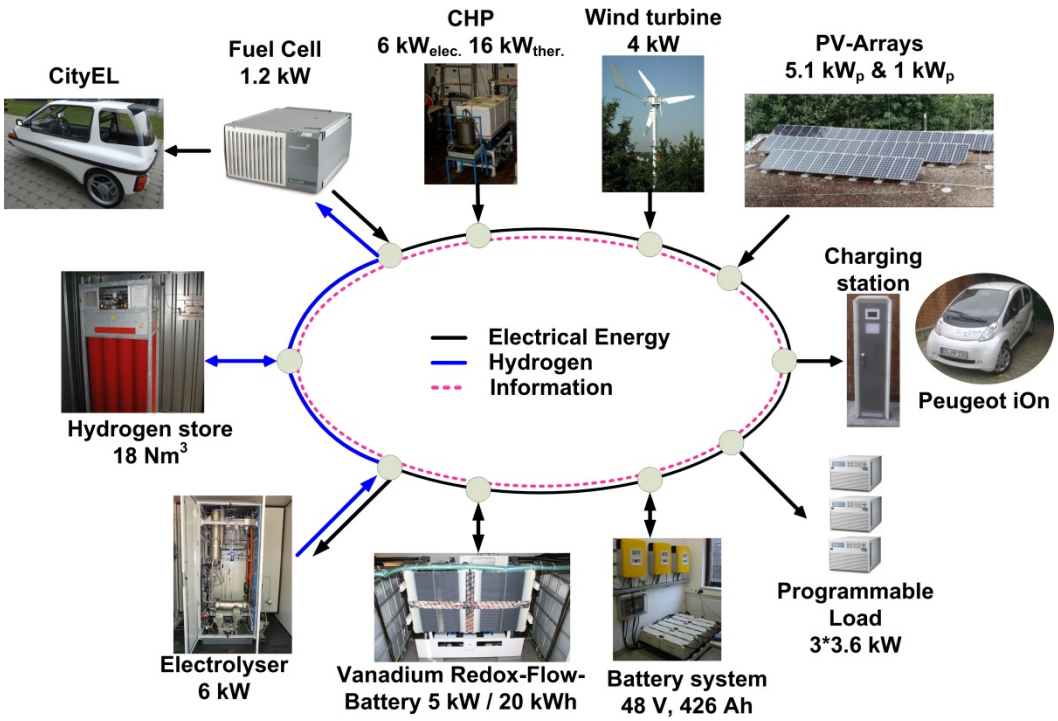


**Figure 3-1: Schematic of the HREP test facility**

**Table 3-1: An overview of the HREP components (details are given in chapter 3.2)**

| Component | Manufacturer | Power/Energy | Year of installation |
|---|---|---|---|
| CHP | Fischer Panda | 6kW$_{electric}$/16 kW$_{thermal}$ | 1995 |
| PV array | BP solar / SMA inverter | 5.1 kW$_p$ (2*2.55 kW$_p$) / 2 kW | 2002 |
| PV array | BP solar / SMA inverter | 1 kW$_p$ / 1.1 kW | 2003 |
| Wind turbine | Geiger SG 500/ ASP inverter | 4 kW / 3.6 kW | 2003 |
| Battery System | SMA | 3*5 kW (inverter)<br>48V/ 423 Ah (lead acid batteries) | 2009 |
| Electrolyser (alkaline, KOH) | Accagen SA | 6 kW / 1.1 Nm³/h $H_2$ | 2009 |
| Compressed gas cylinders | | 12*0.05 m³ | 2009 |
| Fuel Cell (PEM) | Heliocentris / SMA inverter | 1.2 kW / 1.2 kW | 2010 |
| Programmable electronic loads | Chroma | 3*3.6 kW | 2010 |
| Vanadium-Redox-Flow-Battery | Prudent Energy / SMA | 5 kW, 20 kWh / 2*5 kW | 2012 |
| Charging Point for electric vehicles | WAGO (charge controller) | 3~400V,6/10/16/32 A | 2012 |

As stated previously, an important aspect of operating distributed systems is the availability of information (dashed magenta line) from each installed component. Only consistent communication architecture assures an efficient supervisory control of the whole system. This architecture is presented in section 3.3 and section 3.6.

## 3.2 Electric system design

Prior to this PhD study, the grid connection points of the PV-arrays, the wind turbine and the CHP to the electric distribution system were scattered around the faculty building. Since the focus of the proposed thesis is on residential buildings connected to the main electric distribution network, a comparable electric configuration should be realised. Therefore, all devices were reassembled and finally connected to a single point of common coupling (PCC). The PCC connects the HREP to the electric grid of the faculty building, which itself is connected to the public electric distribution grid. Figure 3-2 shows a simplified schematic of the realised electric system configuration.

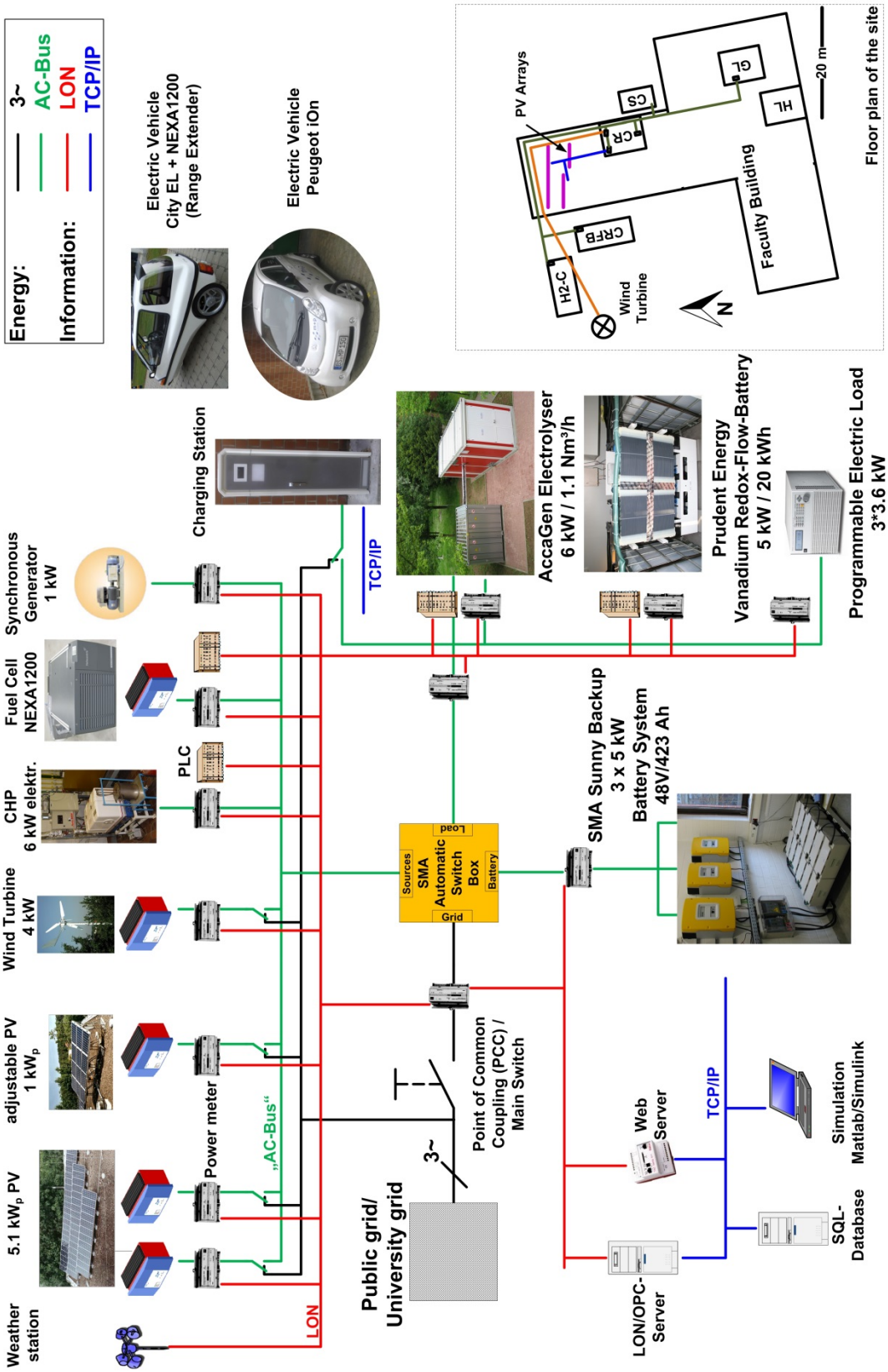


**Figure 3-2: Simplified electric drawing of the HREP.**

The small sketch on the right side illustrates the floor plan of the site and marks the location of the energy systems. The hydrogen loop and the VRFB are integrated into two containers H2-C and CVRFB, respectively. The two containers, the wind-turbine and the charging station (CS) are located close to the building. The PV arrays are mounted on the roof. The battery system, the inverter of the PVs, wind turbine and the lead-acid battery system are installed in the control room (CR) on the 1st floor. The CHP unit is installed in the Gas laboratory (GL) on the ground floor. All connection cables are routed to the CR where the HREP is connected to the university's three phase electric grid (400V/230V) via a three pole main switch. This point is the PCC and would represent, for instance, the junction box of a dwelling. Each renewable power source can be either connected directly to the university electric grid or can be selectively connected to one of the three phases (AC-Bus) of the HREP by switches. The other power sources, the storage devices and the loads are directly connected to the AC-bus. Depending on the device, either the power output or the power consumption can be controlled. This modular approach gives the opportunity to investigate different hybrid system configurations.

The test-facility is fully instrumented with digital power meters which measure the active and reactive power, voltage, current, power factor, frequency and imported/exported energy. In addition, weather conditions such as temperature, solar radiation and wind speed are continuously monitored. More details on the installed measurement devices and their accuracy is given in section 3.3.

The HREP can operate in two different modes: grid-parallel mode and island mode. Normally the HREP operates as a grid-parallel system. By opening the main switch at the PCC, the HREP can be transferred into the island mode. During this mode the controller of the installed battery system regulates the AC voltage and the frequency. Such a system configuration is classified as single switching master mini-grid architecture (Lopes et al. 2012). A single master system is formed by several AC power sources, but, only one device is responsible for the regulation of the grid frequency and voltage. This device can either be a generator set (genset) or a battery system. Other AC sources connected to the mini-grid are slaves following the voltage and frequency control of the master. Such architecture is typically used in single residences, small buildings and smaller settlements. In principal three different operation modes are possible (Lopes et al. 2012):

1) autonomous operation with the inverter as the grid forming master,

2) autonomous operation with the genset as the grid forming master,

3) grid-parallel mode with the utility grid as master.

The installed CHP system consists of an electric asynchronous (induction) generator. Such kind of generator requires an external reactive power source to magnetise and is normally not able to form an electrical AC grid on its own. Consequently, the HREP supports the modes “1” and “3”.

In HREP like systems with several additional power sources and storage devices it is necessary to implement a supervisory control that manages the energy flows between the components. This supervisory control will not directly regulate the voltage or the frequency but it will support the master device to keep control of the mini-grid.

## 3.3 Communication topology and data acquisition system of the main components

As discussed in the previous chapter buildings may play an important role in the future smart grid development. They may evolve from a simple passive entity to an interactive partner of the grid itself. For this purpose energy flows exchanged with a building’s environment must be manageable, either from inside the building or from high level management systems operated by a smart grid operator. The building itself becomes a system of systems where information between the participants need to be exchanged. Therefore, the introduction of communication protocols is essential to link the different energy components of a building to an integrated system. Over the last three decades several building automation protocols have emerged, whereby some are proprietary and some have been accepted as world-wide standard e.g. KNX (EN 50090 2005; KNX-Assoc 2014) and LON (EN 14908 2005; LonMark 2014).

Although such standards exist, real world installations may contain several different protocols depending on the manufacturer and the application. Challenges still remain with respect to integrating each subsystem consistently into energy management systems (Kastner et al. 2005; Balta-Ozkan et al. 2013). The HREP demonstrates the challenges involved in assembling an integrated system with commercially available decentralised energy systems using different communication protocols. To ensure that the proposed concepts of an energy management strategy are comparable to real world installations it was necessary to develop a system based on communication networks which may adoptable to buildings.

In general, building automation systems are hierarchically organised (DIN EN ISO 16484-2 2004). At the lowest level, the field level, digital/analogue inputs and outputs are installed. The field devices communicate to the next higher level, the automation level, where control units are installed and information between those units are exchanged. At the top level, the management level, usually

supervisory control and data acquisition (SCADA) systems are implemented with the aim to coordinate the sub-levels and to enable the analyses of data.

The HREP's realised communication and control topology is illustrated in Figure 3-3. At the field and automation level the main information carrier is based on the LON protocol. Due to the diversity of manufactures it was necessary to integrate different protocols to achieve interoperability. For instance, the inverter of the fuel cell provides a Controller Area Network (CAN) interface and the controller of the VRFB communicates via Modbus. The latter protocol is also used to communicate with the charging station and with the bidirectional inverter of the VRFB.

The LON network is scattered throughout the facility and consists of four subsystems, see the red lines in Figure 3-3. Within the subsystems a twisted-pair cable is used to connect every device, called a LON node, to the physical layer and a bit rate of 78.13 kbps is supported. In addition, network infrastructure components, LOYTEC L-LINX™ 101 Automation Server (AS) and LOYTEC L-IP™ LON/IP routers, are used to connect the four twisted pair network segments via the University's Ethernet to a LON domain. The configuration and commissioning of the LON network was carried out with the LonMaker® integration tool.

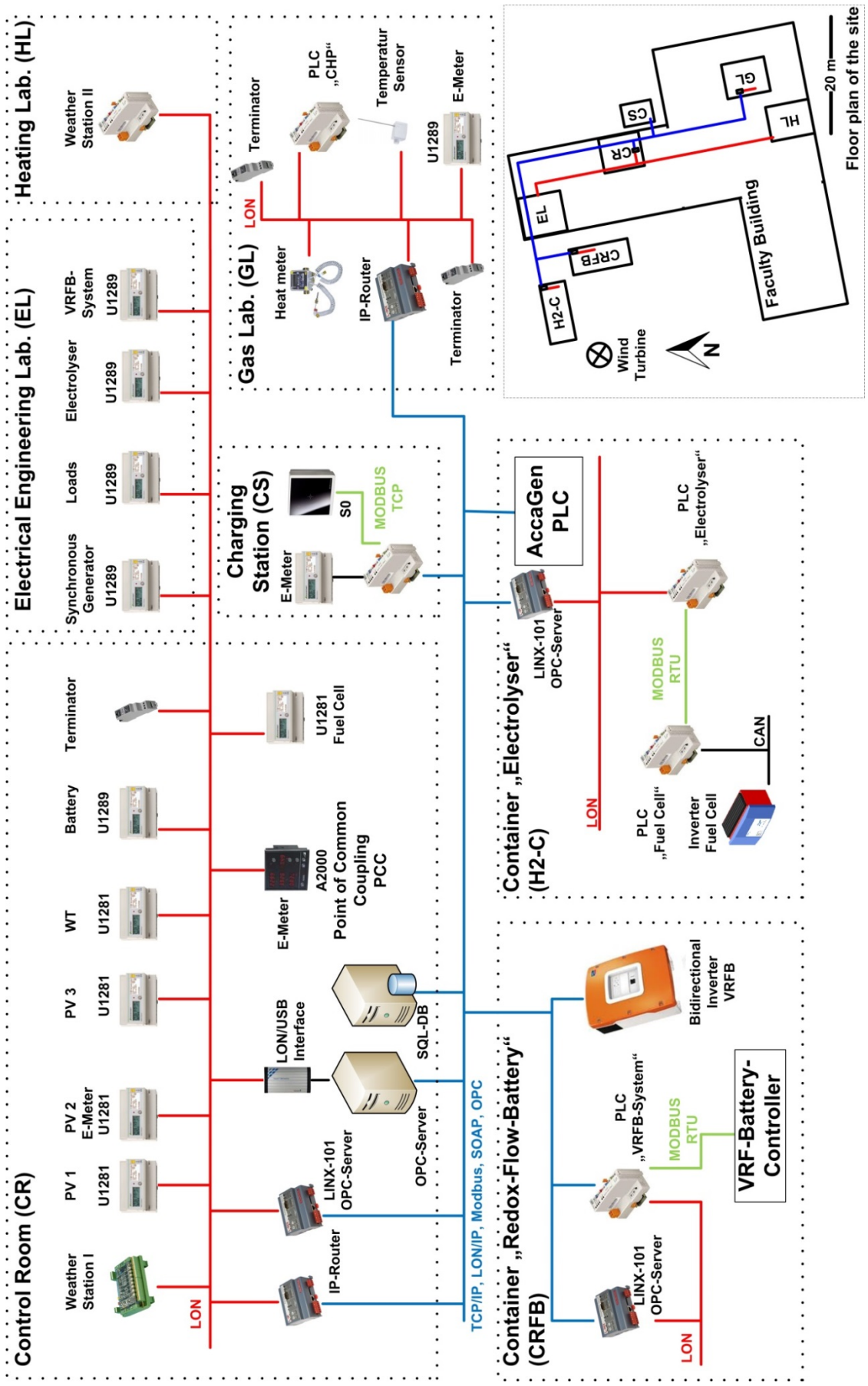


**Figure 3-3: Distributed communication and control topology of the HREP.**

Measuring the power flow accurately within the HREP is an important aspect of the presented investigations. Thus, the power flow of every energy system is separately measured by LON based power meters. Table 3-2 gives an overview of the meters used for this study. The listed accuracy of the gauges is provided by the manufacturer. In addition to the active power the meters measure the voltage, current, power factor, frequency and the imported/exported energy. Weather conditions are also measured by sensors installed on the roof of the faculty building. The analogue signals of the weather sensors are wired to LON-input modules. Table 3-3 lists the monitored weather data.

**Table 3-2: Power meters**

| Manufacturer, device type | Nr. of phases | Accuracy of power measurement | Installation point |
|---|---|---|---|
| Gossen-Metrawatt, U1281 | 1 | 1% ± 1 digit | PV-1, PV-2, PV-3, WT and Fuel Cell |
| Gossen-Metrawatt, U1289 | 3 | 1% ± 1 digit | Battery, CHP, Electrolyser, Generator, Loads and VRFB |
| Gossen-Metrawatt, A2000 | 3 | ±0.5% + 1 digit | Point of Common Coupling |

**Table 3-3: Monitored weather data**

| Parameter | Accuracy | Parameter | Accuracy |
|---|---|---|---|
| Air pressure | ± 1 hPa | Temperature | ±0.15K at 0°C |
| Global Radiation | ±2% | Wind Direction | ± 2.5° |
| Humidity | ± 3 % | Wind Speed | ±0.3 m/s |

The data exchange in the installed LON network is based on the Change-Of-Value (COV) mechanism. Every measured parameter is automatically sent to the receivers if its value changes by a defined amount. Compared to the polling mode, the COV mechanism significantly reduces the bus load. However, the threshold for the COV is normally set to the lowest value so that nearly every change is registered by the data acquisition (DAQ). The typical temporal resolution of the gathered data is one second. At management level all measured parameters are translated into the OPC Data Access format by means of a LON/OPC-Server. OPC is a standardised software interface to connect DAQ or supervisory controls programs with the automation systems (OPC 2014). All data from the renewables and the weather station are permanently logged via a commercial OPC data logger program into a SQL database. The stored values can be analysed, for instance, by MATLAB® (MATLAB 2012) or by other data analysis programs. In addition, in-house LabVIEW programs are used to visualise and collect the relevant data from the energy systems.

## 3.4 Hydrogen loop

The hydrogen loop is composed of the hydrogen generation unit, the alkaline electrolyser, including the gas distribution and the fuel cell system. As a consequence of safety requirements, available space in the laboratory, length of the gas plumbing system and accessibility to the equipment during maintenance and service work the hydrogen loop was purchased as containerised system and was placed in front of the faculty building. Afterwards, the fuel cell system, its inverter and the additional equipment were integrated into the electrolyser container. The enclosure of the gas storage is located beside the electrolyser container at a safety distance of 3 m. Figure 3-4 shows the installation at Ostfalia University.

**Figure 3-4: The two enclosures of the electrolyser (right) and the gas storage (left).**

The following section presents in detail the layout of the hydrogen generation unit, the additional installed control systems and the fuel system.

### 3.4.1 Hydrogen generation unit

The hydrogen generation unit was purchased from Accagen SA and it is an alkaline water electrolyser (Accagen AGE 1.0). According to technical system specification provided by Accagen SA (Accagen SA 2011) the maximum power consumption of the system is about 6 kW (DC) with a maximum hydrogen production of 1.1 $Nm^3/h$ (at Normal Temperature and Pressure, NTP). An advantage of this electrolyser is its operating pressure of 30 bar. Hence, the produced hydrogen can be delivered at a relatively high pressure without any need for an additional compressor. The applied electrolysis technology is based on the classical alkali electrolytic process using potassium hydroxide solution

(30 wt% KOH) as electrolyte. Accagen SA has introduced a unique cell stack design, the zero-pressure stack. The sealed cell stack is embedded into a cylinder which is filled with demineralised water. During operation the pressure of the chamber filled with demineralised water is always greater than the pressure inside of the cell stack. Accagen SA claims that this unique design is an improvement with respect to the prevention of KOH leakage (Dall'ara 2009). In fact, according to Accagen SA the hydrogen generation unit installed at Ostfalia is the first small scale system with this stack design.

A detailed schematic of the hydrogen loop is given in Figure 3-5. The process diagram shows all important components and measure points of the hydrogen generation unit (purple dashed line), the fuel cell system (green dashed line), and of the additional installed equipment (brown dashed line) serving to control the systems and to measure more accurately the hydrogen streams. Figure 3-6 shows the process cabinet of the electrolyser installed within the container (shown in Figure 3-4) and highlights the important parts of the process diagram. The electric integration of the hydrogen generation unit and the fuel cell system was realised according to Figure 3-2.

The hydrogen generation unit is powered by a three-phase rectifier with maximum DC current of 56 A at a voltage of approximately 112 V. A water treatment unit (not shown in the process diagram) supplies the stack with demineralised water with electric conductivity of < 5µS/cm. The electrolyser cell stack composed of 50 cells which are connected in series to the cell stack. Each cell has a diameter of 116 mm consequently a surface area of 105.68 cm². Accagen SA uses special coated electrodes made of a Ni-Cr alloy for the two main electrodes and the electrodes of the bipolar plates are coated with pure nickel. The operating pressure is regulated by a back pressure valve (PCV01) at the outlet of the electrolyser system and by two water pumps. The electrolysis process takes place under a minimum pressure of approximately 25 bar and can reach a maximum pressure of 30 bar. During operation the electrolyte temperature increases to 75°C before a two-point temperature control starts to cool the electrolyte. Cooling water with an inlet temperature of approximately 10°C is supplied to two heat exchangers (HO and HH) integrated in the electrolyte vessels (OV and HV), see Figure 3-5. Both the oxygen and hydrogen produced may contain traces of water and KOH. The oxygen is cooled down by a heat exchanger (OC01) before it is sent to the environment via a fluid trap (not shown in the process diagram). For safety reasons, a small amount of the produced raw hydrogen is guided through an oxygen gas analyser to monitor the percentage of oxygen. The remaining stream of raw hydrogen flows to a gas purification unit, where remaining traces of KOH, $O_2$ and water are removed to achieve a hydrogen gas quality of 99.99 vol% and a dew point of -50°C. First the hydrogen flows through a de-oxidation (DeOxo) unit filled with palladium as catalyst. The remaining oxygen reacts with the hydrogen to form vaporous water. Then the hydrogen is cooled down by a heat exchanger (HC02) and is routed through a fluid trap (not shown in the process

diagram) to the dryer unit where finally the remaining moisture is removed from the gas stream. The hydrogen produced is finally routed to the gas storage composed of 12 compressed gas cylinders each with a capacity of 50 l. Approximately 18 $m^3$ (≈1.6 kg) of hydrogen can be stored at a maximum pressure of 30 bars.

The Accagen AGE 1.0 system employs a Siemens programmable logic controller (PLC) to monitor continuously the whole system and control the pressure regulation and the temperature. In addition, the PLC offers a communication interface, the Simple Object Access Protocol, to collect every measurement point from the hydrogen generation unit with a data acquisition program. For this purpose an in-house LabVIEW based DAQ program is used. Due to the warranty and safety agreement, Accagen SA provides only a 4-20 mA analogue input signal of the Siemens PLC to control the hydrogen generation unit remotely. By regulating this input signal it is possible to start/stop the system and according to Accagen SA to control the production rate between 10% and 100%, which corresponds to a current set point for the rectifier of 18 A and 56 A, respectively. In addition to the gauges provided by Accagen SA, a mass flow meter, power meter, DC voltage transducer, DC current meter, pressure and temperature sensors are installed. The details of the additional installed sensors of the hydrogen loop are listed in Table 3-4. The accuracy values listed below are taken from the technical datasheets of the sensors.

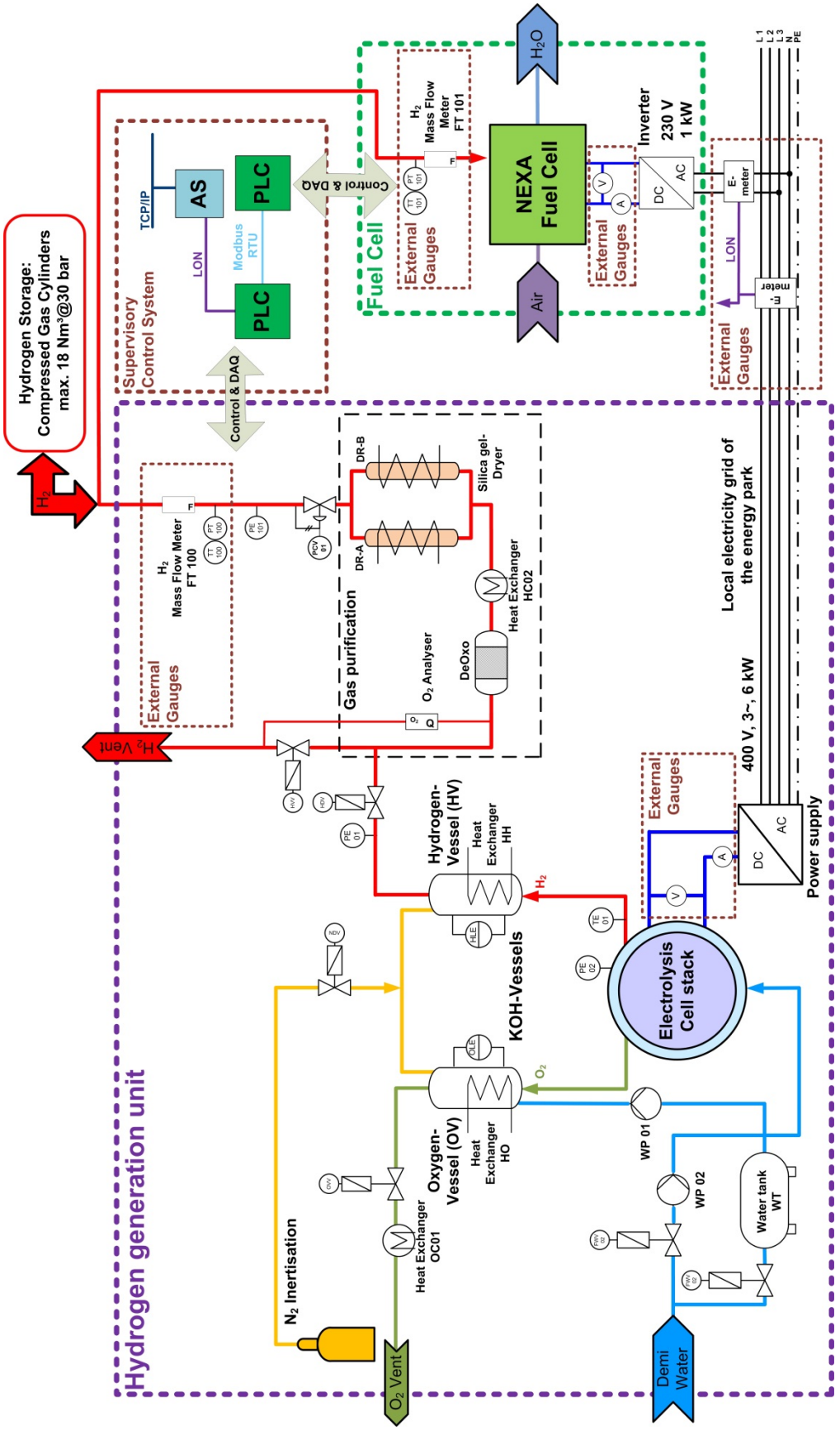


**Figure 3-5: Schematic of the hydrogen loop showing the electrolyser system (dashed purple line), the fuel cell system including the inverter (dashed green line), and the installed PLC systems to control both the electrolyser as well as fuel cell and to collect additional data from external gauges (brown dashed line).**

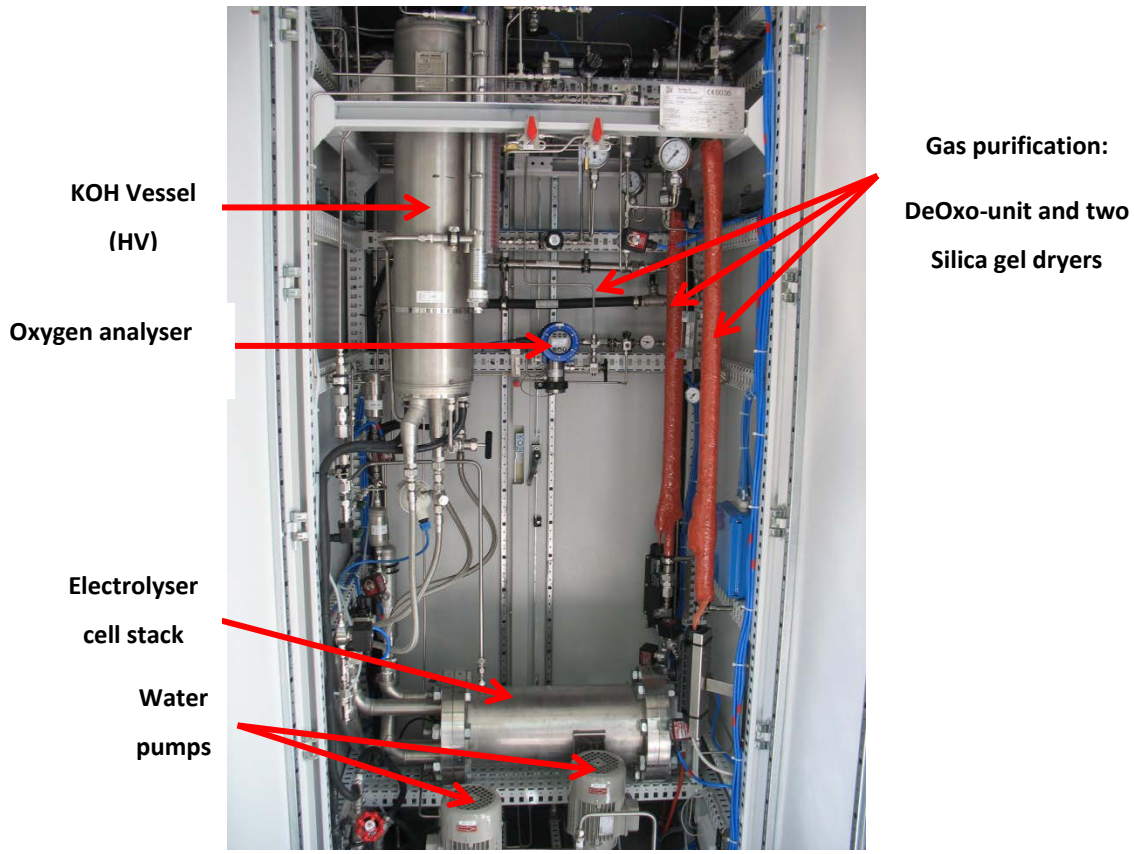


**Figure 3-6: Picture of the Accagen AGE 1.0 electrolyser.**

All measuring points and the analogue signal to control the hydrogen generation unit are processed by a WAGO 750-819 PLC. Moreover, all data are integrated into the LON network and are available for the DAQ and the simulation software. Detailed technical specification is given in the appendix A-2-1.

**Table 3-4: Additionally installed sensors of the hydrogen loop.**

| Sensor | Location | Manufacturer / Type | Accuracy |
|---|---|---|---|
| Mass flow meter | Electrolyser | Bronkhorst F-111AI-50K-AFD-33-V (0-2 m³/h) | ± (0.8%Rd+0.2%FS) |
| Voltage transducer | Electrolyser | Ziehl MU1001K (0-140V) | ± 0.3% |
| DC current meter | Electrolyser | LEM DHR 100 C420 (0-100A) | <±1.0 % |
| Pressure | Electrolyser/ Fuel Cell | WIKAI IS-21 | ≤0.5% |
| Temperature | Electrolyser/ Fuel Cell | WIKAI TR30 | ± 0.2% |
| Mass flow meter | Fuel Cell | Bronkhorst F-111BI-20K-AGD-33-V (0-1m³/h) | ± (0.8%Rd+0.2%FS) |
| Voltage transducer | Fuel Cell | Ziehl MU1001K (0-40V) | ± 0.3% |
| DC current meter | Fuel Cell | LEM DHR 100 C420 (0-100A) | <±1.0 % |

### 3.4.2 Fuel cell system

The integration of the fuel cell system (dashed green line) into the hydrogen loop is illustrated in Figure 3-5. The fuel cell is supplied with hydrogen coming from the gas storage. A Heliocentris NEXA® 1200 Proton Exchange Membrane (PEM) fuel cell system is installed to convert the hydrogen back to electricity. The NEXA® 1200 is a compact fuel cell system based on the FCgen™-1020ACS fuel cell stack supplied by Ballard Power Systems Incorporation. In addition, this system is equipped with a balance-of-plant (BOP) that includes an air fan to supply the oxidant and a control system regulating the operating conditions. The stack composed of 36 cells with a maximum power of 1.2 kW at a DC voltage of 20 V and a DC current of 60 A. According to the operational manual (NEXA 2011), the fuel cell consumes 0.9 $m^3/h$ (NTP) of hydrogen at full load. This value corresponds approximately to the hydrogen generation capacity of the electrolyser. Oxygen is provided by the air fan with a maximum volume flow rate of 335 $m^3/h$. Heliocentris integrated an interface for monitoring the fuel cell using a DAQ program. The whole system is self-controlled and depends on the load and environmental conditions. Temperature is regulated by the inlet air fan to keep the system temperature within defined operational limits. Only the fuel cell activation can be controlled remotely by an on/off signal coming from the PLC. The fuel cell is wired to a single phase 1.2 kW inverter supplied by SMA. The SMA Hydroboy™ has been especially developed for the operation with fuel cells. A CAN interface enables the control of the inverter's power output by adjusting the DC current set-point. The NEXA® 1200 automatically follows the load and regulates the fuel consumption. Figure 3-7 shows the installation of the fuel cell system and the inverter.

**Figure 3-7: Heliocentris NEXA™ 1200 fuel cell system (left) and SMA Hydroboy fuel cell inverter.**

The integration of the fuel cell system and inverter is reported in Figure 3-8. Hydrogen flows from the gas storage tank through a distribution system into a pressure regulator (not shown in the figure). The inlet pressure of the fuel cell is adjusted to 5 bar. Additional measurement equipment namely a

pressure sensor, temperature sensor, DC voltage transducer, DC current sensor and mass flow meter are installed and wired to the WAGO 750-819 PLC, listed in Table 3-4, and are accessible via the LON network.

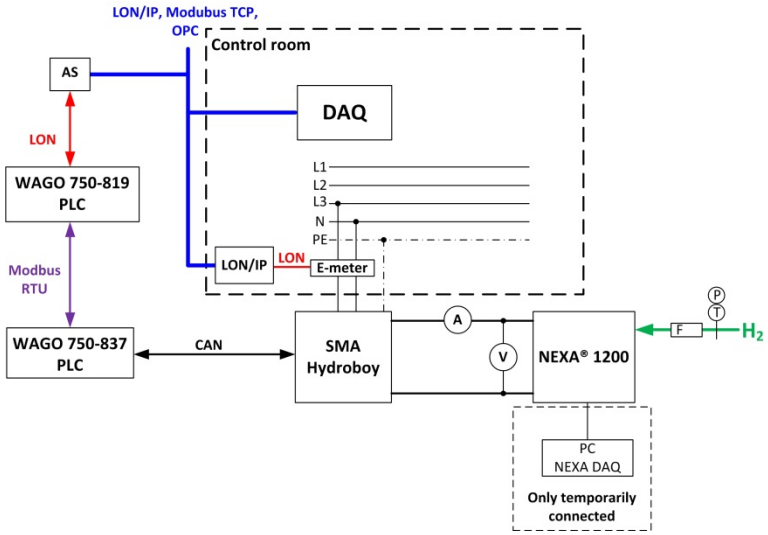


**Figure 3-8: System integration of the NEXA® 1200 and SMA Hydroboy.**

To integrate the SMA Hydroboy™ into the LON network of the HREP it was necessary to establish communication between LON and CAN. A WAGO 750-837 PLC with CAN interface was directly connected to the SMA Hydroboy™. The inverter sends every 500 ms several CAN messages with information about the electric measurements of both, the AC and DC side. The PLC program processes the received data and sends it via the serial interface to the LON based WAGO 750-819 PLC of the electrolyser and vice versa. The LON PLC is connected to the communication network of the HREP via a LOYTEC L-LINX™ 101 Automation Server (AS).

Technical data of the fuel cell is outlined in the appendix A-2-2.

## 3.5 Vanadium-redox-flow-battery system

In January 2012 a VRFB system purchased from Prudent Energy™ was set up in a container next to hydrogen loop. Figure 3-9 shows the placement of the VRFB-container (left) and the power module of the battery (right). The weight of the container is about 5,000 kg whereby the battery system itself weights approximately 3,000 kg. The overall electric and communicational integration into the HREP can be found in Figure 3-2 and Figure 3-3, respectively.

A redox-flow-battery uses a liquid electrolyte to store electricity by a chemical reaction taking place in an energy conversion unit. In case of the VRFB the electrolyte is based on a sulphuric acid solution

containing vanadium at different oxidation states namely $VO_2^+/VO^{2+}$ and $V^{2+}/V^{3+}$ dissolved in the positive and negative electrolyte, respectively. The electrolyte is stored in two tanks with a total amount of about 1,800 l, which roughly corresponds to 20 kWh of useable electric energy.

**Figure 3-9: Placement of the VRFB container (left). The right hand shows the power module (energy conversion unit, pumps, controller, heat exchanger, etc.) installed inside of the container between the two electrolyte tanks.**

Figure 3-10 illustrates a simplified process schematic (black dashed line) of the VRFB. From the tanks the electrolyte is fed by two pumps to the energy conversion unit, the cell stack, where the chemical reaction takes place and electricity is converted into chemical energy and vice versa. The cell stack contains 36 single cells, which are electrically connected in series (nominal voltage = 48 V, max. current 130 A), whereas they are hydraulically connected in parallel. The whole process is controlled by a battery controller. Depending on the applied DC power rate the battery controller regulates the speed of the two pumps and gathers data from the plant. To determine the SOC of the electrolyte, a single reference cell is hydraulically connected in parallel to the cell stack and continuously measures the open circuit voltage. The internal battery controller predicts the SOC based on this value.

To integrate the battery into an application the VRFB system has two user interfaces; the electric DC connection and a communicational serial interface (Modbus RTU) to collect process data from the battery controller. The DC output of the battery is coupled to two bidirectional SMA Sunny Island™ inverters with a nominal power rate of 5 kW (DC). Each inverter is connected individually to a single AC phase but they are operating as a master/slave system. Normally those inverters are used in combination with standard battery types such as lead-acid. To make them compatible to VRFB the internal battery management system was deactivated. In addition, a remote access gateway supplied by SMA was installed that directly communicates with the master inverter. The charge/discharge

process of the VRFB can be controlled by manipulating the AC current set-point of the inverter via the remote access gateway. This gateway also allows the modification of parameters of the inverter such as the maximum charging voltage, maximum charge/discharge current or minimum discharge voltage.

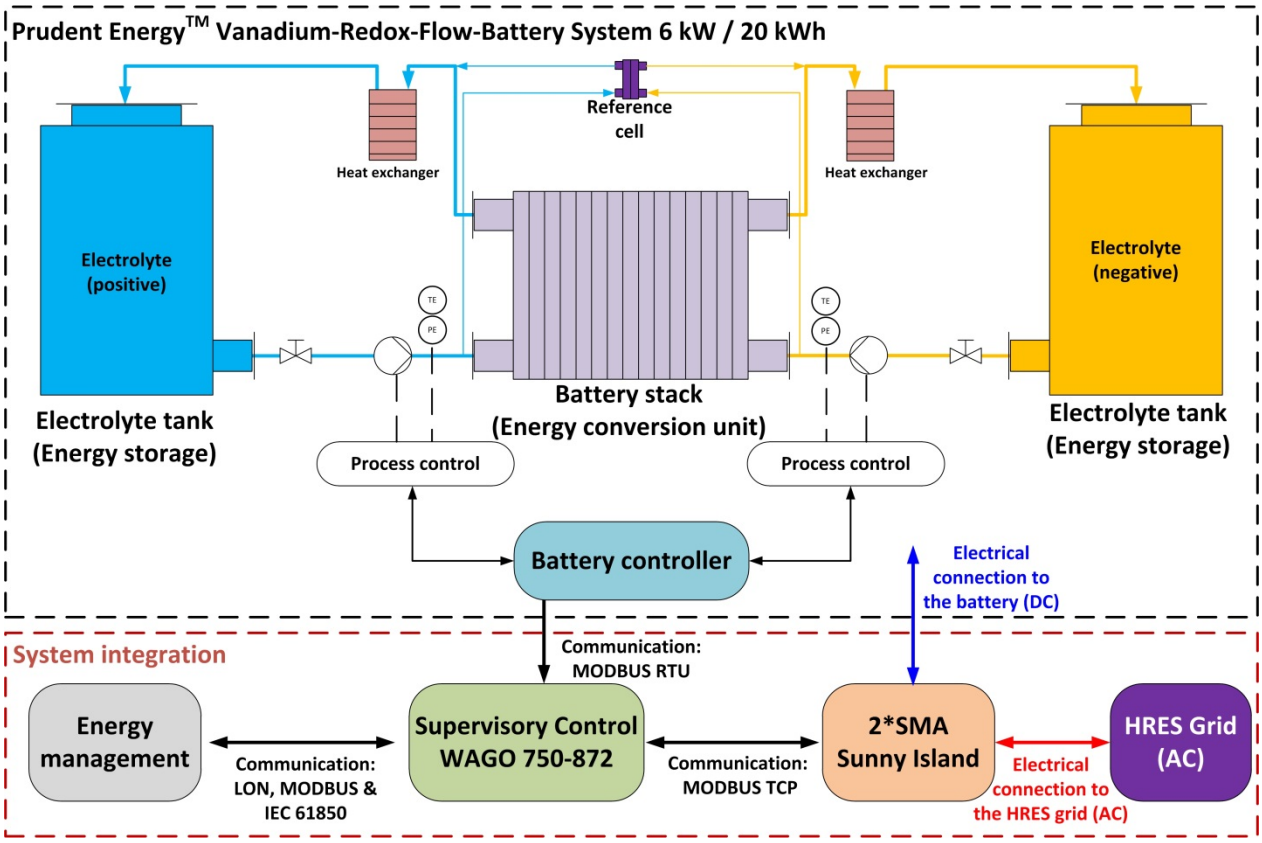


**Figure 3-10: Schematic of the VRFB (black dashed line) and the necessary additionally equipment to integrate the system into the HREP (red dashed line, System integration).**

Figure 3-11 shows the additionally installed two inverters, the PLC and the LON network interface (AS) inside of the VRFB container. The overall system integration was achieved by installing and programming a supervisory and control unit. This task is fulfilled by a WAGO 750-872 PLC, which communicates via a serial interface module directly with the Prudent Energy™ battery controller using the Modbus RTU protocol. In addition, the PLC communicates via an Ethernet connection with the SMA remote access gateway and with an in-house LabVIEW based DAQ program. The PLC is also equipped with a LON interface module that connects the VRFB system to the prime communication network of the HREP.

**Figure 3-11: The left picture shows the two SMA Sunny Island 5048 inverter. To the right the picture shows the WAGO PLC and the LON Network Interface. Both installations are inside of the VRFB container.**

The control of the charge and discharge process of the battery, the acquisition of all process data coming from the battery controller, the inverter and the LON energy meter are implemented in the PLC program. All relevant process data are converted to LON network variables. Figure 3-12 illustrates the electric layout of the VRFB system including the additional installed gauges. The Prudent Energy™ battery controller measures the battery voltage and the DC current (CSP) exchanged with the inverters. To get more accurate data from the DC voltage side, the battery is additionally equipped with two current sensors (CS1 and CS2) and a voltage transducer (VS1).

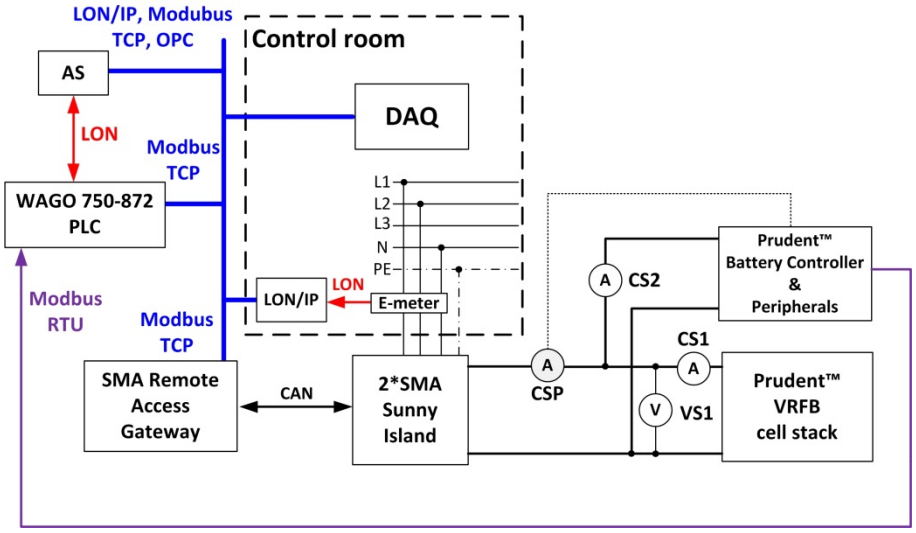


**Figure 3-12: Schematic of the VRFB system integration.**

The first current sensor (CS1) measures only the stack current, while the second current sensor (CS2) measures the current flow to the battery controller and the auxiliary devices of the battery (pumps

and sensors).The voltage transducer (VS1) is used to measure the DC voltage directly at the cell stack connection. All three sensors are connected to analogue inputs of the WAGO 750-872 PLC. Table 3-5 reports the technical details of the sensors provided by the manufacturer. Technical information of the Prudent Energy™ VRFB can be found in the appendix A-2-3.

**Table 3-5: Additionally installed gauges of the VRFB.**

| Sensor | Location | Manufacturer/Type | Accuracy |
|---|---|---|---|
| DC current meter | Stack current (CS1) | LEM DK 200 B10 (0-200A) | ± 2 % |
| DC current meter | Auxiliary current (CS2) | LEM DK 20 C10 U (0-20A) | ± 1 % |
| Voltage transducer | Stack voltage (VS1) | Ziehl MU1001K (0-60V) | ± 0.3% |

## 3.6 Control structure of the HREP

As outlined in section 3.3, the HREP is composed of a complex communication system to gather all the measurements from the installed energy systems. To coordinate and to control the individual energy systems it is important to establish a unified communication bus among the devices. Several integration issues were encountered during the system integration process due to the variety of communication standards used by the manufactures. Integration aspects of the hydrogen loop and the VRFB are presented in detail in section 3.4 and 3.5. In Table 3-5 an overview of the energy systems with their corresponding PLC is given. In addition, the manipulated variables of the energy systems are reported. For instance, the production rate (PR) of the electrolyser can be controlled via the PLC 750-819 by adjusting a 4-20 mA analogue input signal of the electrolyser's internal control unit, see Figure 3-5. From the table it can also be seen, that none of the energy systems offers a direct control of the AC power. Therefore, it was necessary to implement a local power control loop in each PLC to regulate the power flow in the HREP.

**Table 3-6: Overview of the installed PLCs and the control parameters.**

| Device | PLC model | Communication | Description | Manipulated variable |
|---|---|---|---|---|
| CHP | WAGO 750-819 | LON | Collects data from the CHP test-stand | CHP On/Off → Digital output |
| Electrolyser | WAGO 750-819 | LON | Collects and processes data from the electrolyser and Fuel cell | Production Rate 10-100 % → Analogue signal 4-20 mA. |
| Fuel Cell | WAGO 750-837 | CAN | Data exchange with the Fuel Cell inverter via CAN | Fuel Cell On/Off → Digital output Inverter On/Off → CAN message DC current set-point → CAN Message |
| VRFB | WAGO 750-872 | Ethernet, Modbus/TCP/RTU, LON, (IEC 61850) | Data Exchange with the bidirectional inverter of VRFB via Modbus/TCP and collects data from VRFB controller via Modbus/RTU | VRFB On/Off → digital output, Inverter active current set point → Modbus message, inverter reactive current set point → Modbus message, Inverter max. charge voltage |

The power control applies the classical proportional integral (PI) control algorithm. The process variable, the AC active power, is provided by the LON power meters. The reference value can be adjusted through a LON input variable of the PLC. Regarding the controller parameters, the main objective of this thesis was not to find the optimum values, but to achieve a nearly optimum behaviour in a simple and robust manner. Therefore, the control parameters were tuned by applying heuristic methods as presented e.g. by Åström and Hägglund (1995) and Cooper (2008). The experimentally determined parameters are listed in Table A-4, Table A-5 and Table A-6.

In addition, the PLCs communicate with the corresponding energy systems to collect data. As described in the previous sections each energy system is equipped with an internal control unit, which supervises the process and transfers the energy systems in different operational states such as start-up, operating or standby. For each PLC an individual program is developed using the CoDeSys programming environment (CoDeSys 2014) based on IEC 61131-3 (DIN EN 61131 2004). The programs are composed of a power controller and supervisory controller to determine the operational state of the energy system. All information is accessible via the LON communication network.

In analogy to the organisation of building automation systems, the control structure of the HREP is hierarchical organised. Figure 3-13 illustrates the implemented control structure of the HREP. The third level is the local control level and it is responsible to regulate the AC power. The second level, the local supervisory level, coordinates the energy system itself and it includes the internal control

unit of the BOP. To coordinate the energy systems and to manage the power flow in the HREP, a first level, the strategic supervisory level, is introduced. This level communicates via OPC with the LON network infrastructure components, the automation servers (AS).

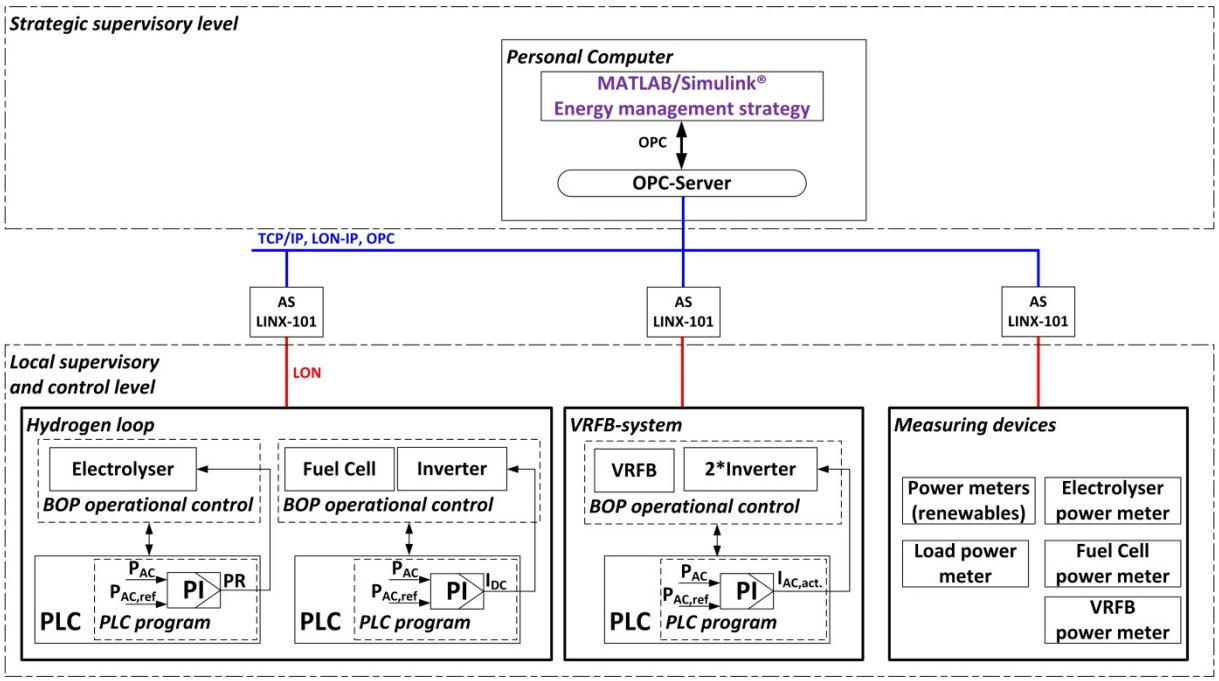


**Figure 3-13: Simplified schematic of the control structure of the HREP.**

Since the focus of this thesis was on the experimental investigation of the dynamic performance of the HREP along with the development of system models to run annual simulations, it was necessary to define an energy management strategy which can ideally be used in both the experimental and the simulation part. Several energy management approaches were reviewed in chapter 2.1.4 and it was found that deterministic methods can be easily implemented. They may not have found the optimal operating strategy; however, they provide a good performance and they can be used for real-time applications. The MATLAB®/Simulink® simulation software was applied to develop an overall energy management strategy. Furthermore, by using the Simulink® OPC toolbox (OPC Toolbox 2012) it is possible to connect the developed energy management strategy model directly to the LON communication network as described previously. The energy management strategy can be tested initially by simulations and then it can be applied to manage the real devices.

Before developing an energy management unit, it is necessary to specify the objectives and to determine the required input and output variables (Courtecuisse et al. 2010; Robyns, Davigny & Saudemont 2013). In this thesis the overall objective of the energy management strategy is to increase the amount of renewable energy used locally.

From the literature review several further objectives were identified, which should be implemented:

- to coordinate the hydrogen loop and the VRFB,
- to reduce power fluctuations of the renewable energy sources injected into the public grid,
- to limit the dynamic stress of the energy systems.

In order to fulfill these objectives information from the energy systems needs to be gathered. The compulsory input variables are:

- the generated renewable power,
- the actual electric demand,
- the operational state of the energy systems,
- the SOC of the energy storage systems.

Based on the collected input variables, the energy management unit makes decisions, which need to be communicated to the lower levels of the control hierarchy. The defined output variables are the control signals to activate the energy systems and the reference power signals.

The development and application of the energy management strategy was a key aspect to the work described in this thesis. In chapter 4 experimental results of the electrolyser, the fuel cell and the VRFB are presented. From these results the basic operation is understood and dynamic constraint are identified. In chapter 5.4 the energy management strategy is developed based on the defined objectives and the experimental investigations. In chapter 6 the energy management strategy is used to assess the annual performance of a building-integrated hydrogen loop and VRFB. In addition, the functionality is demonstrated by means of experiments for both a single storage configuration (hydrogen loop) and multi-storage configuration (VRFB and hydrogen loop) of the HREP. Furthermore, the dynamic performance of an integrated hybrid renewable energy system is discussed.

## 3.7 Programmable electronic AC loads

**Figure 3-14: AC load bank consist of three Chroma 68306 programmable AC loads.**

Three programmable AC loads, Chroma 68306, are implemented to emulate different electric consumption patterns, at maximum power rate of 3*3.6 kW, see Figure 3-14. Commonly, such devices are used by manufactures of power electronics for system testing. The three loads can be connected in series or in parallel for testing single phase or three phase voltage networks. All parameters such as the active power set-point or the power factor, and all measurements can be accessed remotely using a parallel-interface. Chroma included a basic software tool to monitor and to control the loads. In addition, LabVIEW driver are included in the software package to develop custom control and monitor tools. An in-house developed LabVIEW based software tool is used to feed the loads with user defined load profiles created in an Excel spread sheet. Only the time step, the active power and the power factor need to be defined. To generate reasonable annual domestic electricity consumption profiles a software tool from the University of Loughborough (Richardson & Thomson 2010) was used. The load profiles have a temporal resolution of one minute.

## 3.8 Other components

The energy systems introduced so far form the core elements for the presented research carried out in this PhD thesis. Nevertheless, there are other components which were integrated or used to guarantee the overall performance of the HREP. In addition, the integration of other components demonstrates the simple expandability of the applied AC coupled system topology. The installed lead-acid battery system, the AC generators and electric vehicle charging station are presented in the appendix A-2.

## 3.9 Summary

The design of the HREP was explained in detail providing the background to understand the interaction between the components. The electrical system was reported, followed by the introduction of the communicational network. In addition, the experimental set-ups of the electrolyser, the fuel cell and the VRFB were presented. Several integration issues were addressed to establish a unified communication channel. Furthermore, the control structure of the HREP was introduced and the objectives of the energy management strategy were clarified. Finally, the used programmable electronic AC loads and other components of the HREP were briefly presented.

# 4 Component characterisation

The following chapter presents first an experimental methodology to characterise energy conversion systems during both steady-state and dynamic operation. Furthermore, it shows experimental results conducted with the hydrogen loop and the VRFB system. It examines fundamental operational modes, which each energy system would encounter on a daily basis if it is part of a HRES. The results obtained ensure that the developed models outlined in chapter 5 show a realistic operational behaviour.

Figure 4.1 illustrates the applied experimental method to characterise each component. The first set of experiments represents standard operations such as start-up and standby. Additionally, it analyses the steady state operation and assesses the system efficiency at different power rates. The second set of experiments investigates how the component can cope with a single dynamic event. A step function response test investigates how fast the system can reach a new operational point. Finally, the third series of experiments examines the system's response to dynamic power variations. For this purpose, the system follows a sinusoidal input signal with changeable period length and amplitude. Based on the results of chapter 4 the system models and the energy management strategy have been developed. This process is outlined in chapter 5. In chapter 6.3 a fourth series of experiments is presented to investigate the overall system response to a realistic power profile of renewable sources and typical loads.

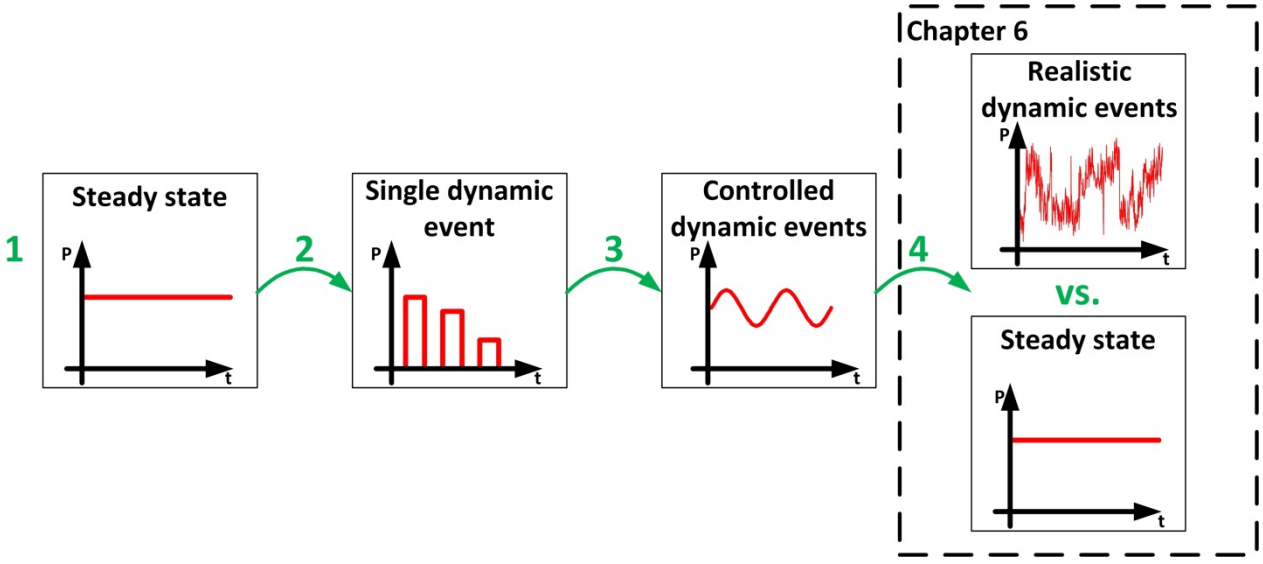


**Figure 4-1: Experimental methodology for characterisation of energy conversion systems**

## 4.1 Operational behaviour of the hydrogen generation unit

The volatility of the renewable energy sources causes transient operation of the electrolyser over its full range of power input. As a consequence the system operation is far from being steady-state as it is in industrial processes. The high degree of variability of the power input may influence the system performance. As discussed in chapter 2, system simulation studies often neglect operational aspects such as start-up, stand-by and transitional times and assume that a hydrogen system can follow the input power instantaneously. Therefore, the experimental work conducted with the installed hydrogen generation unit examines the basic and the dynamic operational behaviour how it could occur in a renewable energy system.

### 4.1.1 Electrolyser: Basic theory and steady state operation

Before the electrolyser can follow an energy supply profile or simply produce hydrogen at a fixed current value, the system needs to start up. During the off mode the pipes inside of the electrolyser plant and the KOH vessels are filled with nitrogen for safety reasons. A pre-defined start-up procedure is implemented by the manufacturer in the control system of the electrolyser (Accagen SA 2011). First, the inert gas will be removed from the plant by producing hydrogen and oxygen at minimal current. The KOH vessels and the pipes will be gently purged and the nitrogen will be removed by venting the gases to the environment. Figure 4-2 illustrates a measured start-up process of the electrolyser. During the first minutes a low DC current of 10 A is applied to the system, compare Figure 4-2 area I. As soon as the nitrogen is removed the electrolyser enters the next stage of the start-up process. During start-up the electrolyser will be pressurised according to a two stage current increase as illustrated in Figure 4-2:

1. The DC current is set to 22.5 A for 2 minutes,
2. the DC current is set to 49 A until the minimum operating pressure of 25 bar is reached, see Figure 4-2 area II.

On average it takes about 15 minutes before the electrolyser enters finally the normal operation mode (area III in Figure 4-2). The total electrical energy needed to start-up is approximately 1.2 kWh. In addition, it can be seen from the diagram that at certain times the pressure decreases (Time 34 min, 44 min, etc. in Figure 4-2). This is caused by the pressure balancing mechanism of the two electrolyte vessels. While during normal operation the hydrogen produced flows from the electrolyser to the gas storage, the oxygen only leaves the electrolyser when the oxygen venting valve (OVV, see Figure 3-5) opens. Thus, the pressure in the KOH vessel of the oxygen side is steadily increasing leading to an imbalance of the liquid levels between both vessels. If a certain threshold is

reached, OVV opens and the level will be equalised. The gas production rate can be derived from the chemical reactions of water electrolysis in an alkali electrolyser:

Cathode: $$2H_2O + 2e^- \rightarrow H_2 \uparrow + 2OH^- \quad \textbf{(4-1)}$$

Anode: $$2OH^- \rightarrow \frac{1}{2}O_2 \uparrow + H_2O + 2e^- \quad \textbf{(4-2)}$$

According to equation (4-1) and (4-2) hydrogen at the cathode is produced at twice the rate of oxygen at the anode. Following this, the pressure increases differently in both vessels. This also affects the start-up process. While the liquid level in the hydrogen vessel decreases due to the higher gas production rate, the level in the oxygen vessel increases during pressurisation. To equalise both levels, the pressure in the hydrogen side needs to be reduced by opening a hydrogen venting valve (HVV, see Figure 3-5).

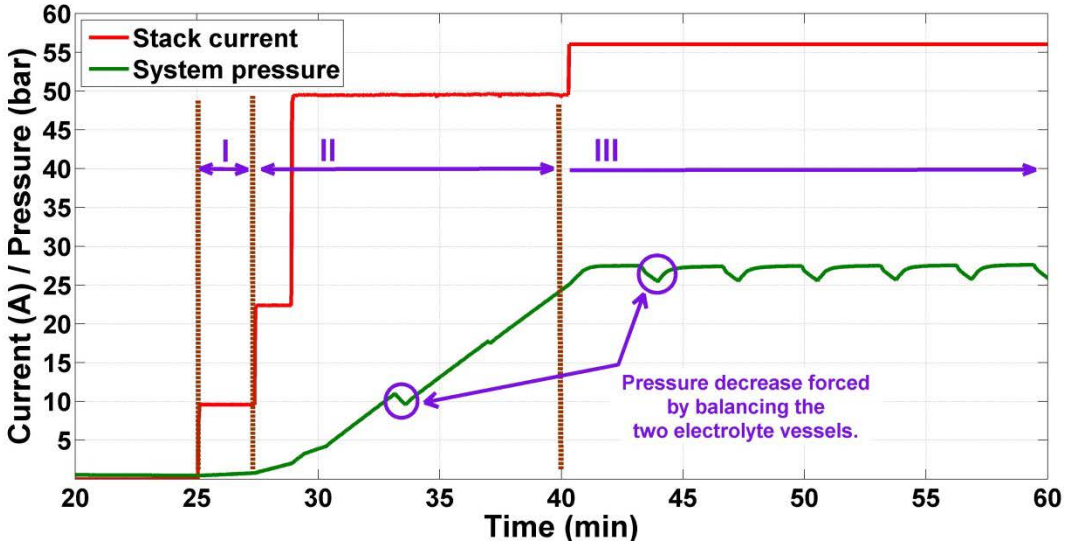


**Figure 4-2: Start-up of the electrolyser unit. The red line shows the DC current and the green line the system pressure. Area I marks the venting phase to remove the nitrogen. Area II illustrates the pressurisation phase before the electrolyser enters the normal operating phase (III).**

Another important parameter which needs to be considered is the system's temperature and how it affects the process performance. Figure 4-3 shows the measured electrolyte temperature, stack current and voltage during a start-up and steady state operation at 56A. The electrolyte temperature is steadily increasing while the stack voltage decreases. With a fixed DC current rate of 56 A, the warm-up period starting from a container indoor temperature of 13°C to reach normal operating temperature of 72°C-78°C takes approximately 80 minutes. The voltage decline can be explained by the increasing conductivity of the electrolyte. It is apparent from this diagram that the temperature significantly impacts the energy consumption of the electrolysis process. In general, the required

energy for the process can be found by considering the overall reaction of water decomposition by combining equation (4-1) and (4-2).

$$H_2O + Energy\ (thermal\ energy + electricial\ energy) \rightarrow H_2 \uparrow + \frac{1}{2} O_2 \uparrow \qquad \textbf{(4-3)}$$

The total energy is composed of both thermal and electrical energy, which represents the enthalpy change due to the reaction. Under standard conditions ($10^5$ Pa and 25°C) this value is equal to the reaction enthalpy for liquid water electrolysis $\Delta_R H_m^0 = 285.84 \frac{\text{kJ}}{\text{mol}}$ and can be calculated by:

$$\Delta_R H_m^0 = \Delta_R G_m^0 + T \Delta_R S_m^0 \qquad \textbf{(4-4)}$$

The Gibbs free energy $\Delta_R G_m^0 = 237.21 \frac{\text{kJ}}{\text{mol}}$ is the required electrical energy for water decomposition and the required heat amounts to $\Delta_R S_m^0 = 48.6 \frac{\text{kJK}}{\text{mol}}$. It is well known that water electrolysis is an endothermic ($\Delta H >0$) and a nonspontaneous ($\Delta G > 0$) reaction and it needs both electrical and thermal energy to occur. In normal electrolyser systems the required heat is generated by internal electrical resistances; accordingly, the electrical energy demand is increasing. If no extra heat is generated the minimum required electrochemical potential, the thermal neutral voltage $U_{th}$, can be calculated by applying Faraday's Law:

$$U_{th} = \frac{\Delta_R H_m^0}{z * F} = \frac{285.84\ {}^{\text{kJ}}/_{\text{mol}}}{2 * 96485\ {}^{\text{As}}/_{\text{mol}}} = 1.481\ \text{V} \qquad \textbf{(4-5)}$$

where, $z$ is number of participating electrons to create one mole of hydrogen and *F* is the Faraday constant (96485 As/mol).

According to equation (4-5) the minimal required voltage is 1.481 V for splitting liquid water at standard conditions in a single electrolysis cell without generating excess heat. Thus, the minimal voltage of the 50 cell stack of the Accagen SA electrolyser is 74.05 V. Comparing this result with Figure 4-3 it can be noticed that the voltage is around 108 V, indicating that higher losses occur at normal operating temperature and pressure.

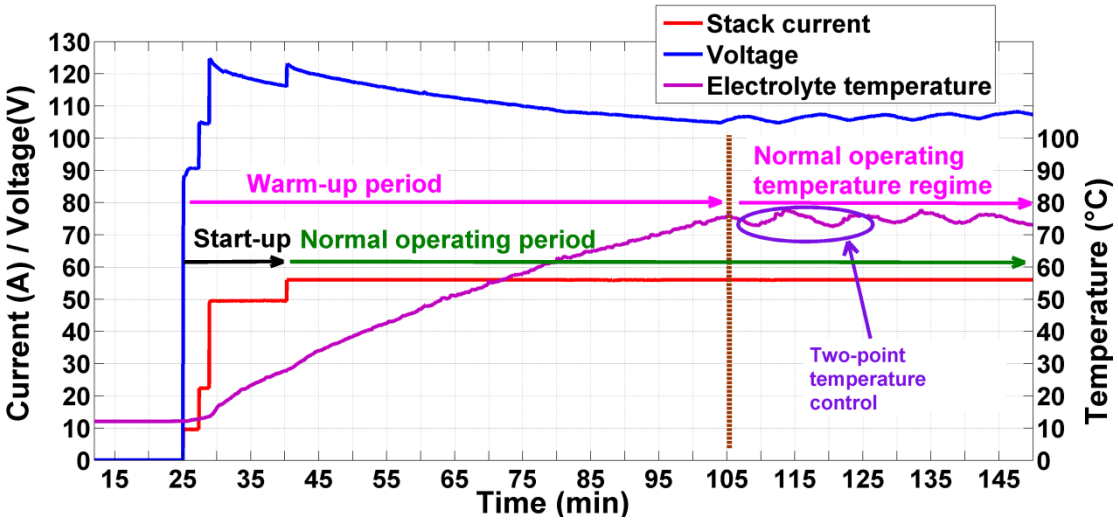


**Figure 4-3: Temperature (magenta line), stack current (red line) and voltage (blue line) as a function of time.**

The difference between the actual cell voltage and the stack voltage is an aggregation of voltage losses due to required activation potentials at the electrodes and the ohmic resistances in the cells. As a result, the temperature is increasing steadily; thus, during the electrolysis process heat is generated.

This heat flow rate is proportional to the difference between the operational cell voltage and the thermal neutral voltage and can be calculated by (Ulleberg 2003):

$$\dot{Q}_{gen} = n_{cells} * I * (U_{cell} - U_{th}) \qquad \textbf{(4-6)}$$

where, $\dot{Q}_{gen}$ is the heat flow (W) generated by the electrolyser stack with $n_{cells}$ number of cells operating at an electric current $I$ (A). As shown in Figure 4-3 the temperature rise is almost linear over time with a mean gradient of 46°C/h at a current rate of 56 A. Once the normal operating temperature of approximately 75°C is achieved, the plant's cooling system controls the temperature by a two-point regulator. The temperature oscillation also affects the voltage because of the temperature dependency of the electrical conductivity. Within the normal operating temperature the voltage alternates between 107 V and 112 V at a DC current of 56 A.

Evaluation of the electrolysis process is assessed by calculation of three indices the voltage efficiency ($\eta_U$), the Faraday efficiency ($\eta_{Faraday}$) and the energy efficiency ($\eta_{electr.\ energy,HHV}$).

The voltage efficiency is defined by the ratio of the thermal neutral voltage $U_{th}$ and the actual cell voltage $U_{cell}$:

$$\eta_U = \frac{U_{th}}{U_{cell}} \quad \textbf{(4-7)}$$

It compares the actual chemical process to the thermodynamically optimum where no extra heat is generated. The second efficiency value is the Faraday or current efficiency $\eta_{Faraday}$. This value describes the conversion of electrical charge into the chemical reaction to produce hydrogen. It takes into account the parasitic currents which occur between the gas ducts of the cells. With decreasing current density the percentage of the parasitic currents increases resulting in lower current efficiency (Ulleberg 1998). In general, it describes the relationship between the measured hydrogen molar flow rate $\dot{n}_{measured}$ and the theoretically possible hydrogen molar flow rate $\dot{n}_{theo}$:

$$\eta_{Faraday} = \frac{\dot{n}_{measured}}{\dot{n}_{theo}} \quad \textbf{(4-8)}$$

where, $\dot{n}_{theo}$ is the molar flux of hydrogen (mol/s) which can be calculated from Faraday's Law:

$$\dot{n}_{theo} = \frac{n_{cells} * I}{z * F} \quad \textbf{(4-9)}$$

The released hydrogen can be measured at the output of the electrolyser by a mass flow meter.

Technically, the Faraday efficiency can reach values between 90%-95% (Ursua, Gandia & Sanchis 2012) at normal operating conditions. However, this can be assumed for the electrolysis process at cell or stack level. As aforementioned the produced hydrogen stream is reduced due to internal processes. Firstly, some hydrogen is used for gas analyses. Secondly, hydrogen is used in the gas purification to reduce oxygen to water. Finally, some hydrogen is required to regenerate the two silica-gel-dryer units one at a time. The Faraday efficiency value in this thesis corresponds to the ratio of the useful hydrogen, measured at the output, and the theoretically possible hydrogen at system level.

From an energy perspective, the most important parameter to characterise an electrolyser is the third performance indicator, the electrical energy efficiency $\eta_{electr.\ energy,HHV}$. This indicator takes into account the consumed electric power $P_{electric}$ within a time period ($t_2$-$t_1$) to produce hydrogen. As recommended in a report of the US National Renewable Energy Laboratory (Harrison, Remick & Martin 2010) the higher heating value (HHV) is used to calculate the energy of the produced hydrogen. Thus, the energetic efficiency is calculated by:

$$\eta_{electr.\ energy,HHV} = \frac{HHV\ of\ produced\ hydrogen}{\int_{t_1}^{t_2} P_{electric} dt} \quad \textbf{(4-10)}$$

Derived from measured data Figure 4-4 shows the calculated efficiencies for different current densities at nominal temperature and pressure conditions of 72-78°C and 25-30 bar. The values are calculated by averaging voltage, current, electrical power and mass flow over one hour based on a sample rate of one second at an average temperature 75°C.

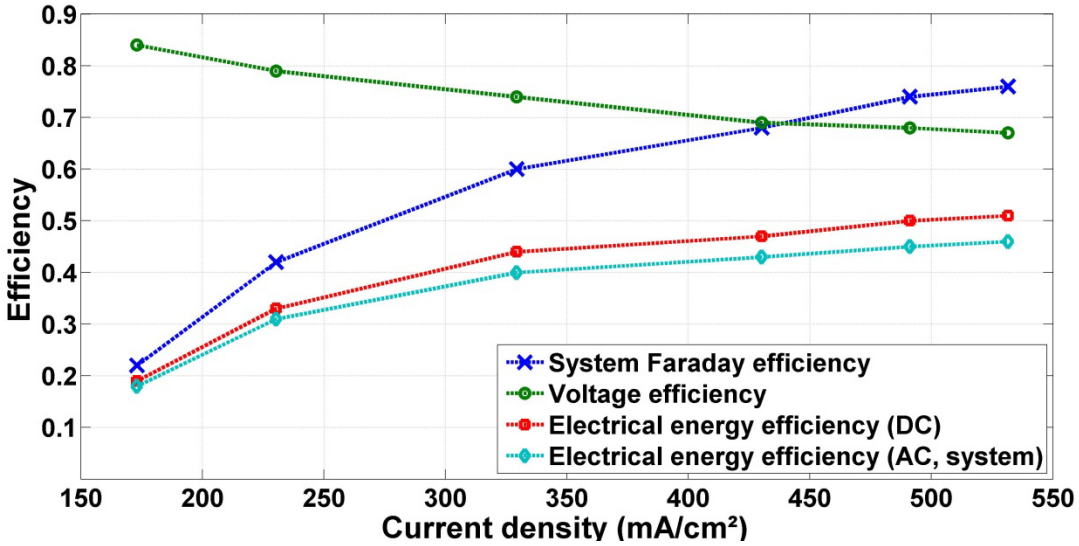


**Figure 4-4: Efficiencies at a current density of 173.1 mA/cm², 230.3 mA/cm², 329.3 mA/cm², 430.2 mA/cm², 491.2 mA/cm² and 529.9 mA/cm².**

The voltage efficiency decreases with increasing current density due to increasing over-potential and ohmic losses, whereas the other efficiencies increase. The maximum AC energy efficiency can be found at maximum DC current (56 A, 529.9 mA/cm²) with 47% and the minimum AC energy efficiency is about 18% at 18.3 A (173.05 mA/cm²). Typical energy efficiency values found in literature, for example in the review articles (Ursua, Gandia & Sanchis 2012; Gahleitner 2013), are in the region of 47-78%. In the literature the efficiency is often calculated at the best operating point of the electrolyser, in addition, the definition of the system boundary to calculate the efficiency is often imprecise. It is also often unclear whether the efficiency is referred to the higher or lower heating value of hydrogen. In a technical report presented by Harrison et al. (2009) the performance of an alkaline electrolyser was analysed. It was found that the AC energy efficiency (HHV) varies from 0% to 41% at the lowest and the rated current rate, respectively. From an operational point of view electrolysers should operate near the nominal power rates so that the energy efficiency is in the region of its optimum.

Another basic characteristic of an energy storage device is its standby behaviour. Particularly with respect to its applications associated with volatile renewable energy sources. At times where the renewable power is not high enough to maintain the minimum production rate the electrolyser enters the standby phase. The DC current is set to 0 A and the voltage declines likewise. During standby the system pressure decreases continuously due to the internal gas losses until a certain threshold is reached. The system pressure can usually be maintained above this value for 30-60 minutes before the gases will be released to the environment and the system will be filled again with nitrogen for safety reasons. If the renewable power sources recover during this standby period, the electrolyser can instantaneously enter the production phase.

### 4.1.2 Electrolyser test: Single dynamic event

Temporary interruption of renewable energy sources would occur during normal operation and the electrolyser will be subjected to a dynamic input power profile. For instance, the power output of a PV array can rapidly decrease if clouds are passing by. To emulate such single events two experiments were conducted. The first experiment (step response A) investigates the response to a sudden on/off switching with different power rates and the second experiment (step response B) examined the temporal power reduction to different power levels. The production rate of the electrolyser can be varied between 10% and 100% by a 4-20 mA analogue input signal which corresponds to a current set-point of about 18 A and 56 A, respectively. If the input signal is set to a value below 10% the electrolyser enters the standby mode.

Prior to the step response experiments, the electrolyser operated for more than two hours at maximum power to ensure that optimal operating temperature of 75 °C was reached. Figure 4-5 shows the DC current (red), DC voltage (blue) the electrolyte temperature (magenta). During the first experiment the electrolyser operated for 10 minutes at the defined set-point followed by 5 minutes standby period where the control signal was set to 0%. Then the next value for the control signal was applied. In total five steps were performed with a control signal value of 100%, 90%, 75%, 50% and 25%. The second step response test investigated a sudden power reduction from 100% to four different production rates (10%, 25%, 50% and 75%). The electrolyser operated for five minutes at a set-point of 100% followed by 10 minutes operation at the reduced set-point. Since the response of the electrolyser to each step shows similar characteristics, only the two extremist cases are discussed below. The step response of the first emulated event, a sudden change from 0% to 100% (0 A to 56 A) at 8540 seconds is illustrated in Figure 4-6. The diagram shows the control signal, the measured DC voltage and DC current with a sample rate of one second. It can be noticed that there is a dead time of one second before the electrolyser starts to follow the control signal.

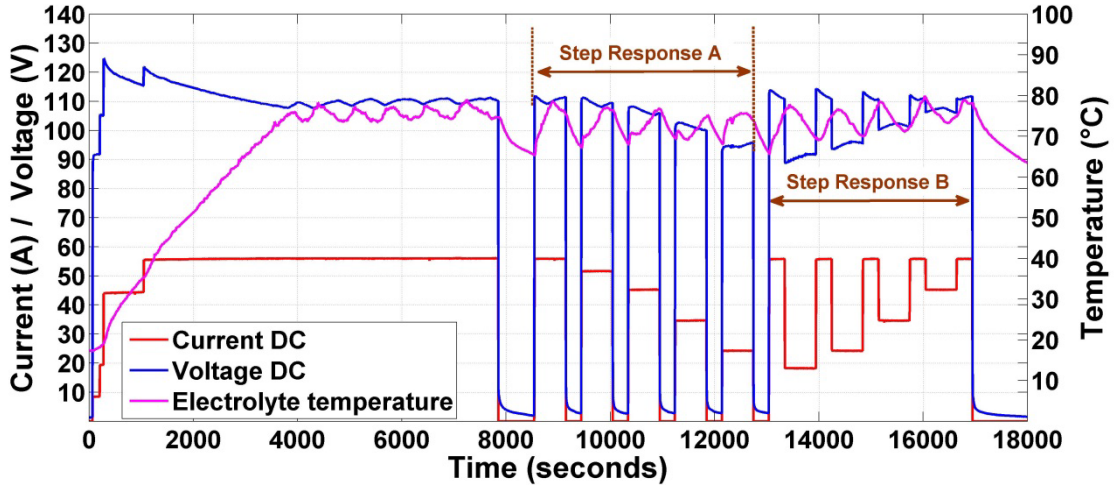


**Figure 4-5: Step response experiment.**

This time delay is mainly caused by the processing time of the electrolyser's PLC which controls the rectifier. The current rises from 0 A to 56 A at second 8541 and stabilises at 56 A at 8545 seconds. In total the settling time amounts to 5 seconds. The voltage changed from nearly 0 V to 110 V. A change from 0% to 100% represents the most extreme case of step response and the electrolyser can follow such an impulse within 5 seconds. Consequently, the system can follow a single dynamic event with a power gradient of about 1200 W/s. Figure 4-7 presents the result of the first sudden set-point reduction of the second experiment.

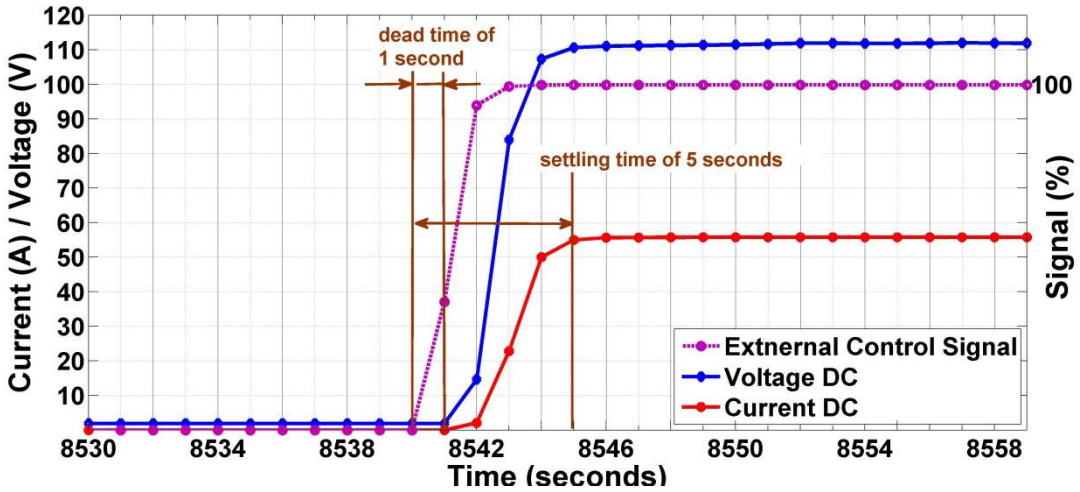


**Figure 4-6: Step response test A: The external control (magenta) signal is suddenly set from 0% to 100%.**

At the time of 13342 seconds, the production rate drops from 100% to the minimal production rate of 10%. As with the step-up experiment, the DC current starts to follow the set-point change with a dead time of one second and declines from 56 A to 18.3 A. The voltage changed likewise from 110 V

to 89.2 V. In total the settling time accounts for 4 seconds before both the DC current and the voltage are stabilised. The corresponding power gradient is 1132 W/s.

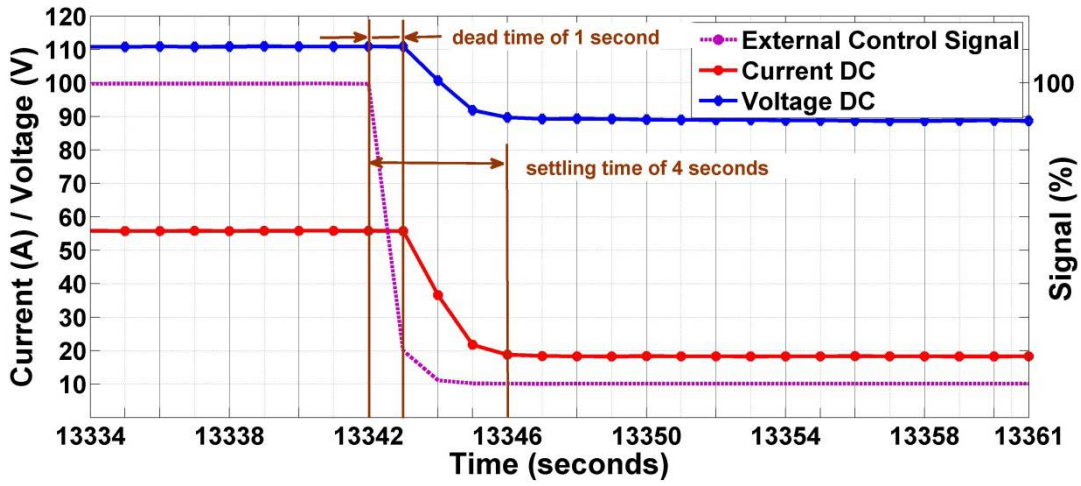


**Figure 4-7: Step response test B: The external control signal (magenta) is temporarily reduced from 100% to 10%.**

### 4.1.3 Electrolyser test: Controlled dynamic events

Single dynamic events such as shown in the previous section of course occur during normal operating conditions, for instance, if electrolysers start from standby. But to be part of a renewable energy system an electrolyser would be stressed to follow a profile with multiple dynamic events. The following results are based on an experiment that was designed to investigate limitations of electrolyser to follow a dynamic profile.

From the observations of the steady-state operation and the response to single dynamic events it is known that the energy efficiency is higher in the region of the rated power and that the installed electrolyser can cope with power gradients of about 1200 W/s Therefore, in this experiment the electrolyser was forced to operate at energy efficiencies between 30% and close to its maximum. In addition, the power was changed between approximately ±1500 W over a certain period of time. This power cycling was achieved by generating a sinusoidal control signal in the WAGO 750-819 PLC (see Table 3-6) which controls the electrolyser's PLC by a 4-20 mA analogue input signal. Figure 4-8 illustrates the experimental set-up. The amplitude and period time of sinusoidal signal can be adjusted within the PLC program. The signal represents the production rate set-point for the electrolyser's PLC going from 0-100%. The minimum production rate is equal to 10%. A value below 10% forces the electrolyser to enter the standby mode. Before the experiments were carried out the electrolyser operated over a longer period at maximum power. After a standby period of 10 minutes

three dynamic experiments (“Sinus A”, “Sinus B” and “Sinus C”) were conducted starting at second 10626.

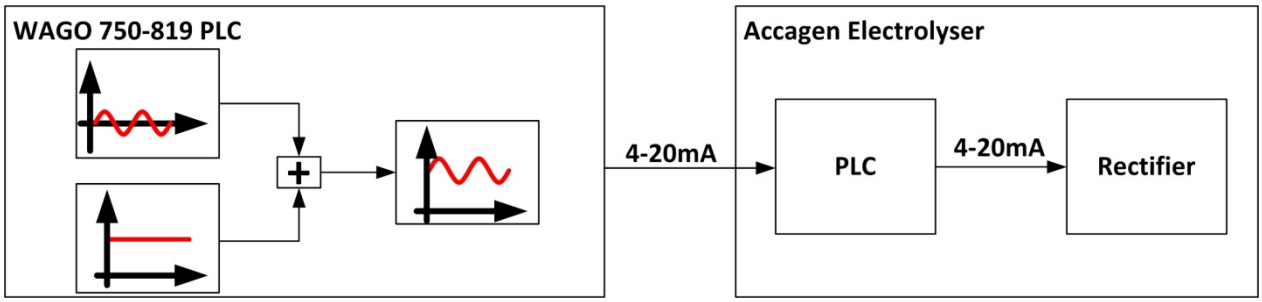


**Figure 4-8: Controlled dynamic events experiment.**

The control signal was composed of a constant value and sinusoidal signal; it was oscillating around a production rate of approximately 67% with amplitude of 28%. Accordingly, the production rate was varying between 39% and 95%. Amplitude change of 28% corresponds to a power change of approximately ±1500 W at normal operating temperature. During the experiments only the period duration was changed. The first experiment “Sinus A” was carried out for 40 minutes with a period of 40 seconds. Then the operation was interrupted at second 12996 and the period duration was halved to 20 seconds. The second experiment “Sinus B” took about 12 minutes before the period duration was finally set to 10 seconds in the last experiment “Sinus C”. Figure 4-9 depicts the DC current, the DC voltage and the electrolyte temperature as a function of time. The data sample rate of the DAQ was set to one second.

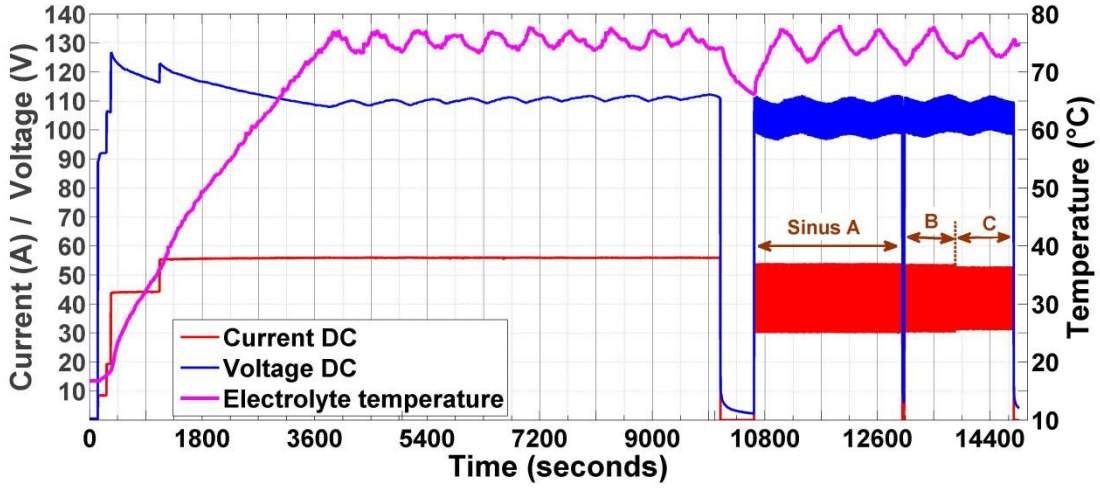


**Figure 4-9: Controlled dynamic events experiment: The diagram shows the DC current (red), the DC voltage (blue) and the electrolyte temperature (magenta).**

A 60 seconds long snapshot of experiment “Sinus A” is shown in Figure 4-10. The control signal (purple) oscillates between approximately 38% and 95% with a period of 40 seconds. The DC current (red) and DC voltage (blue) are able to follow that signal but with a time delay of two seconds. Data analyses revealed a maximum power gradient at 10822 seconds with 260 W/s.

Figure 4-11 illustrates a snapshot of the “Sinus B” and “Sinus C” experiment. During the “Sinus B” and the “Sinus C” experiment the period duration was set to 20 seconds and 10 seconds, respectively. Reviewing the measured data confirms that the electrolyser was able to follow the signal with a time delay of two seconds.

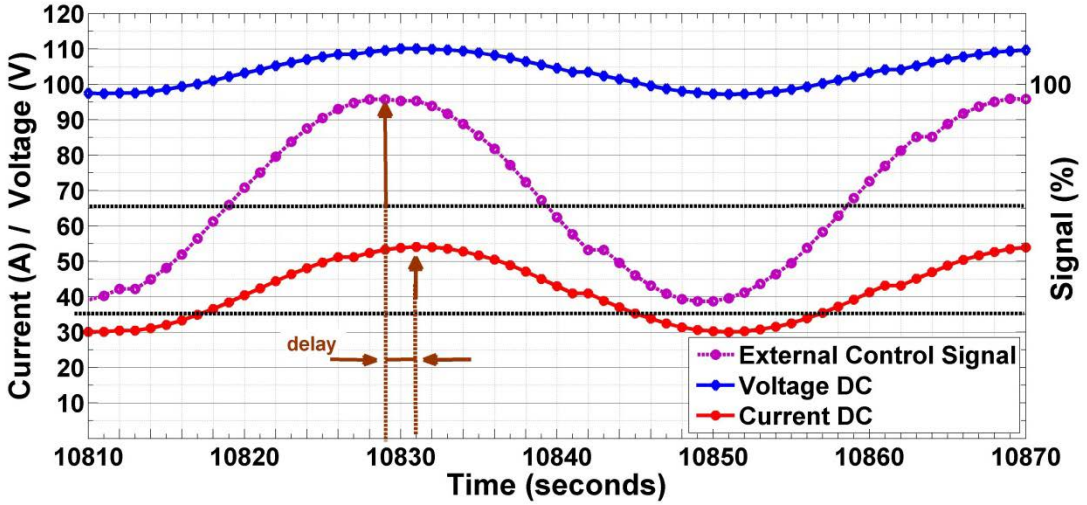


**Figure 4-10: Sinus A: The diagram illustrates the resulting control signal (magenta), the DC current (red) and the DC voltage.**

The maximum power gradient was about 527 W/s and 930 W/s in experiment “Sinus B” and “Sinus C”, respectively. Comparing the DC current of both experiments, it can be seen that the current sufficiently followed the control signal during the “Sinus B” experiment, while the current amplitude was cut off in the last experiment “Sinus C”. It is apparent that an information loss occurred; the electrolyser was not able to follow the applied control signal. Reasons for this can be found in signal propagation delays within the electrolyser’s control system. Therefore, the power gradients should be kept around 600 W/s to achieve that the control system can follow the employed operating profile.

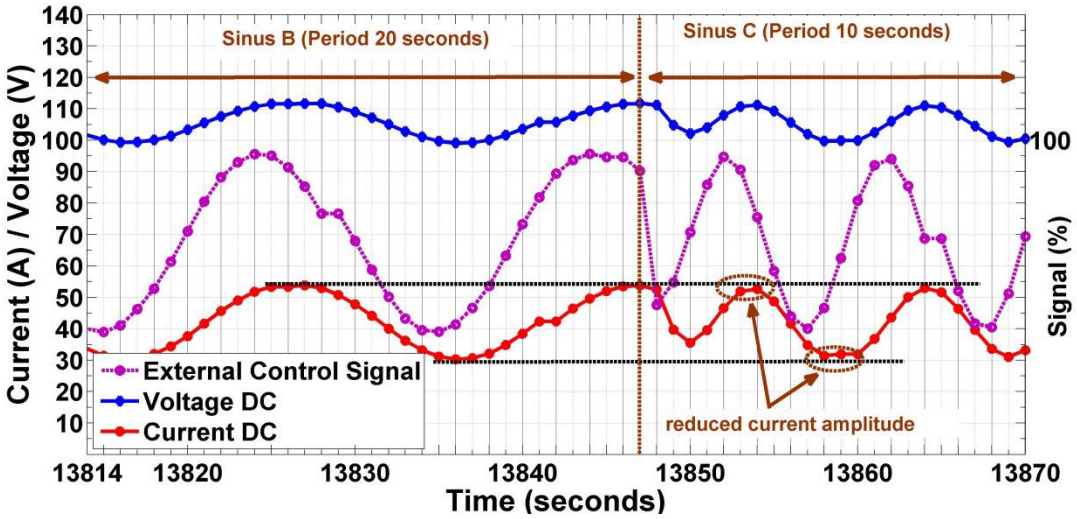


**Figure 4-11: Sinus B and Sinus C: Between 13815 s and 13847 s the period of the sinusoidal signal was 20 s, after this the period was changed to 10 s.**

## 4.2 Operational behaviour of the fuel cell system

The following section discusses the operational performance of the fuel cell system of the HREP. Some theoretical basics of fuel cells are introduced, followed by results of experimental tests as proposed in Figure 4.1.

### 4.2.1 Fuel cell: Basic theory and steady state operation

This section briefly describes some theoretical background to understand the working principle of the used fuel cell system. A more comprehensive view of the technology can be found in e.g. (Larminie & Dicks 2003) and (Williams 2004). In general a fuel cell converts directly chemical energy into electricity and heat. Basically, it is the reverse reaction of the electrolyses process presented in section 4.1.1. The chemical reaction takes place in a chamber consisting of two porous electrodes (anode and cathode). The electrodes are separated by an electrolyte that also provides ion-conductivity. The reactants are continuously supplied from the outside. In case of PEM fuel cells hydrogen catalytically oxidises at the anode to $H^+$ ions and electrons. If the two electrodes are electrical connected, the electrons travel to the cathode, while the $H^+$ ions diffuse through the proton exchange membrane to the cathode. At the cathode oxygen (typically supplied by air) reduces to water. The chemical reactions at the anode and cathode are expressed by equations (4-11), (4-12) and (4-13).

Anode: $$2H_2 \rightarrow 4H^+ + 4e^- \quad \textbf{(4-11)}$$

Cathode: $$O_2 + 4e^- + 4H^+ \rightarrow 2H_2O \quad \textbf{(4-12)}$$

Overall: $$2H_2 + O_2 \rightarrow 2H_2O + electrical\ energy + heat \quad \textbf{(4-13)}$$

The released reaction enthalpy $\Delta_R H_m^0 = -285.84 \frac{\text{kJ}}{\text{mol}}$ (under standard conditions) according to equation (4-13) will be converted into electricity and heat. If all the released enthalpy of reaction could be converted into electricity, the open circuit cell potential between the electrodes would be equal to the thermo neutral voltage $U_{th}$.

$$U_{th} = -\frac{\Delta_R H_m^0}{z * F} = -\frac{-285.84\ {}^{\text{kJ}}/_{\text{mol}}}{2 * 96485\ {}^{\text{As}}/_{\text{mol}}} = 1.481\ \text{V} \quad \textbf{(4-14)}$$

The resulting voltage value of 1.481V is only theoretical. The 2nd Law of Thermodynamics needs to be considered; accordingly, the enthalpy of reaction will be reduced by the entropy change resulting in the Gibbs free enthalpy of reaction of water formation ($\Delta_R G_m^0 = -237.21 \frac{kJ}{mol}$, in liquid form), see equation (4-4). This gives the maximum useable electrical energy and can be applied to calculate the reversible voltage $U_{rev}$ under standard conditions.

$$U_{rev} = -\frac{\Delta_R G_m^0}{z * F} = -\frac{-237.21\ {}^{\text{kJ}}/_{\text{mol}}}{2 * 96485\ {}^{\text{As}}/_{\text{mol}}} = 1.229\ \text{V} \quad \textbf{(4-15)}$$

It should be noted that the Gibbs free enthalpy depends on the temperature and the partial pressure of the reactants at the anode and electrode, thus, the reversible voltage also changes with temperature and pressure variations. In real systems the open circuit voltage is below the possible maximum of 1.23 V. This can be explained by activation and parasitic losses occurring within the cells. During operation the output voltage will be further reduced by voltage losses depending on the applied current. The output voltage of a fuel cell is shaped by four irreversibilities (Larminie & Dicks 2003):

a) activation loss caused by slowness of the reaction taking place at the electrodes,

b) fuel crossover and internal current resulting from a small amount of fuel that diffuses from the anode through the electrolyte to cathode without producing an external current,

c) mass-transfer or concentration loss due to depletion of the reactants especially at high current densities,

d) ohmic loss of the electrolyte, the electrodes and other connections.

The operating behaviour of the output voltage of a fuel cell system can be illustrated by an I-U curve. Figure 4-12 shows the measured output voltage of the fuel cell system as function of the stack current. For this experiment the current set-point of the inverter was set to 60 A with a current gradient of 0.02 A/s. This value was fixed for 3200 seconds before the set-point was set back to 0 A and the current smoothly followed with 0.02 A/s. The curves were derived from data collected with the in-house LabVIEW based DAQ of the hydrogen loop and directly from the fuel cell by using the software tool supplied by the manufacturer. Three different I-U curves are illustrated in Figure 4-12. The first curve shows the increasing DC bus current from 0 A to 60 A (blue dots). The second curve shows the decreasing DC bus current (green dots) from 60 A to 0 A. The third curve depicts the mean I-U curve (dotted magenta line) derived from both curves. In addition, the reversible voltage $U_{rev}$=1.23 V and the manually measured open circuit voltage $U_{OCV}$≈0.91 V are drawn in the diagram. For comparison the small figure beneath the legend shows the qualitative voltage curve of a fuel cell from low current to high current to highlight the non-linear voltage drop at high currents.

It is apparent from Figure 4-12 that the current-voltage relationship is non-linear in low current regions (<10 A) as a result of the dominant influence of the activation losses. Between 10 A and 60 A the current-voltage correlation is mostly influenced by the ohmic losses and shows a strong linearity between a stack current of 10 A to 60 A. In higher current regions (>60A) the current-voltage relationship would be strongly non-linear again due to the influence of the concentration losses. However, to avoid deterioration of the fuel cell the current rate was limited.

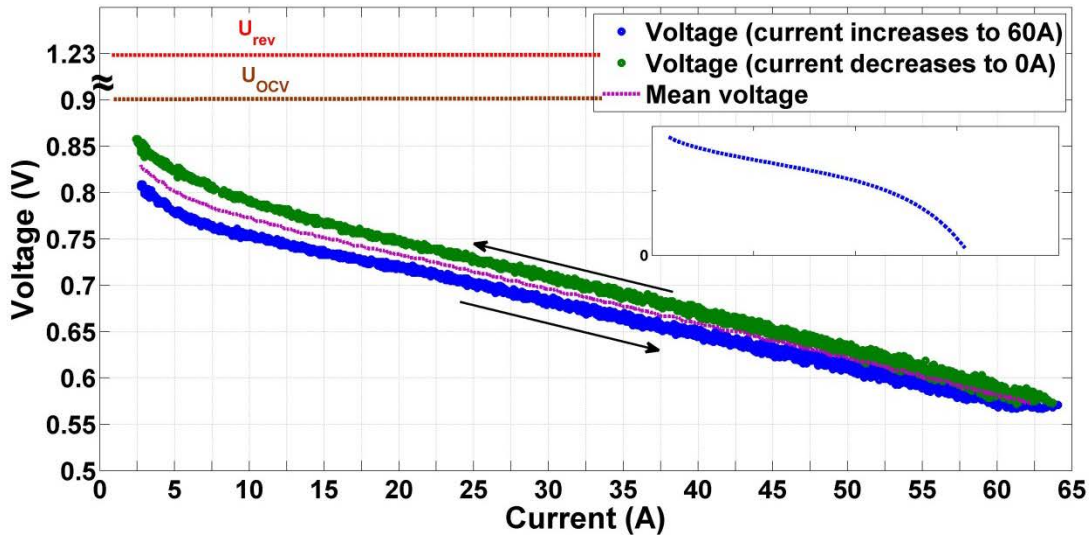


**Figure 4-12: Current-Voltage curve of the fuel cell system.**

Interesting in Figure 4-12 is the hysteresis effect between the increasing (blue line) and decreasing (green line) current-voltage curve. This can be explained by the dependency of the ionic conductivity of the membrane on the water content and the temperature (Larminie & Dicks 2003; Haubrock 2007). With increasing current, the water production increases, which leads to a better humidification and better proton conductivity of the membrane (Le Canut et al. 2009). Thus, the voltage is higher in the second curve (60 A to 0 A).

Before the fuel cell system can satisfy an electrical demand it needs to be started remotely by applying 24 V (DC) to the BOP and to close an external remote contact of the on-board controller. The PLC of the electrolyser is used for this task. In addition, the second PLC of the hydrogen loop communicates via a CAN interface with the inverter of the fuel cell system and controls the DC current to meet the demand. The start-up process is relatively fast compared to the one of the electrolyser. It takes approximately 45 seconds until the fuel cell system can follow a demand profile. First, the fuel cell system initialises itself followed by starting the duty cycle of the air supply and cooling fan. Then, a solenoid valve opens and hydrogen streams into the cell stack. At this moment the cell voltage starts to increase and the fuel cell system provides itself enough energy to maintain its operation; a load relay closes and the inverter will be activated. After approximately eight seconds the inverter synchronises itself with the electrical grid and can be finally controlled by adjusting the DC current set-point using the PLC.

Figure 4-13 shows the measured start-up of the fuel cell system with an initial stack temperature equal to room temperature. During the first two minutes the inverter was in standby mode (stack current <2A) as soon as the inverter was transited into grid-connected mode (the AC power output can be controlled by adjusting the DC current) a small increase of 1 A of the stack current was measurable, although, the DC current set-point was still at 0 A. Then the fuel cell was in operation at a DC stack current (red line) of approximately 26 A for 30 minutes. The temperature (magenta line) increased practically simultaneously and reached after a few minutes a stable value of about 50 °C. Then the DC current set-point was set back to 0 A followed by a stepwise increase of 5 A every 10 minutes to 55 A and vice versa. As the current set-point was changed from 0 to 55 A, the voltage decreased from around 30 V to 21 V at 55 A. Proportional to the current increase, the temperature climbed to 61 °C. The temperature followed a load change according to a first-order time delay. As aforementioned the fuel cell system is equipped with a BOP to regulate the stack temperature at certain current depending regions, in addition, it also regulates the fuel and oxidant supply. Therefore, load variations influence the fan speed and thus leading to an increasing or decreasing energy demand of the BOP, see Figure 4-13 peripheral current (black line). The variations of the peripheral current show the same step-up/step-down rhythm as the stack current.

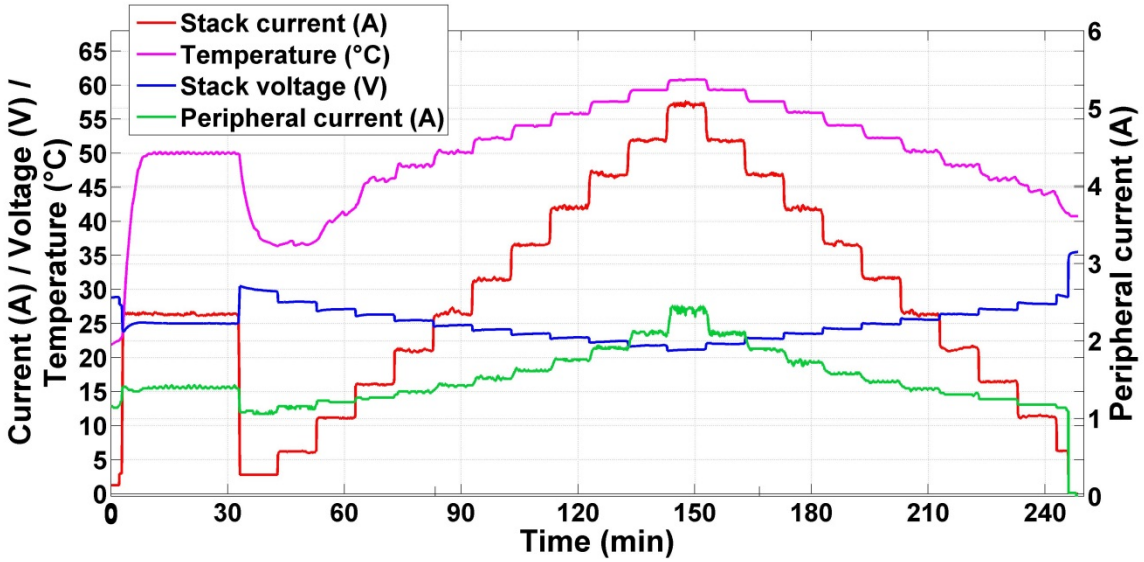


**Figure 4-13: Operational performance of the fuel cell system. The figure shows a 30 minutes operation at 25 A followed by a stepwise current increase from standby to 55 A (DC, output) and back.**

To evaluate the performance of the fuel cell system, data gathered from several step-climbing tests, as illustrated in Figure 4-13, were used to calculate the efficiency. Similar to the electrolyser different possible efficiencies can be calculated to characterise the system. At stack level the voltage efficiency is commonly used to assess the performance, which is defined by the ratio of the operating voltage to the reversible cell voltage:

$$\eta_U = \frac{U_{stack}}{U_{rev} * n_{cells}} \quad \textbf{(4-16)}$$

From a system level perspective the energetic efficiency is of great importance and can be defined as the ratio of the electrical energy supplied to the chemical energy of the consumed hydrogen within given time period ($t_2$-$t_1$):

$$\eta_{energy,DC/AC,LHV} = \frac{\int_{t_1}^{t_2} P_{DC/AC} dt}{LHV * \int_{t_1}^{t_2} \dot{V}_{H_2} dt} \quad \textbf{(4-17)}$$

where, $P_{DC/AC}$ is the electrical power on the DC or AC side, $\dot{V}_{H_2}$ the flow rate of the consumed hydrogen in normal cubic meters per second and LHV is the lower heating value under normal conditions (3 kWh/m³).

Figure 4-14 presents the calculated efficiencies (to the left) and the power output (to the right) of the FC as a function of the current. The voltage efficiency steadily decreases with increasing current due to the increase of the voltage losses. Whereas the DC and AC energy efficiency first increases to a maximum of 53% DC efficiency and 46% AC efficiency at approximately 15 A and starts then to decline. Reasons for this can be found by the higher weight of the power consumption of the peripherals at low currents to the produced electrical energy and by the efficiency of the inverter. The efficiency curve taken from the operating manual of the inverter is illustrated in Figure A-1.

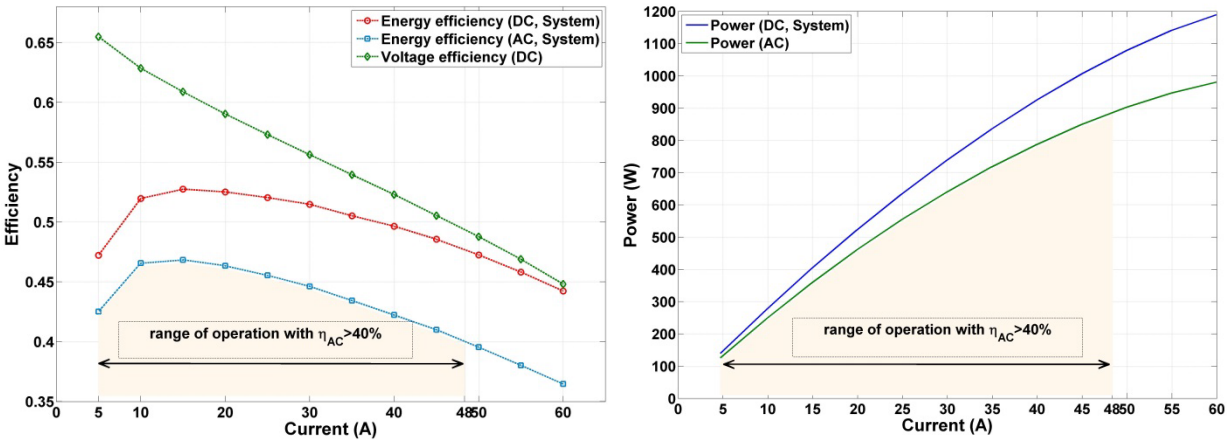


**Figure 4-14: To left the picture shows the voltage (green line), DC energy (red line) and AC energy (light blue line) efficiency as a function of the DC current. The right picture shows the DC (blue line) and AC (green line) power vs. the DC current.**

To keep the energetic AC efficiency at high levels, the minimum AC output power should be set to 120 W and the AC output power should not exceed values of 900 W. In Figure 4-14 the operating region leading to high efficiencies are indicated by the shaded area. Furthermore, by limiting the operational range the fuel consumption will be minimised and the fuel cell will be operated at moderate current densities. This limitation, in turn, helps to reduce the operating costs and improves also the life-time.

### 4.2.2 FC tests: Single dynamic event

The second set of experiments was carried out to investigate the response of the fuel cell system to sudden load changes. Starting with a maximum current ramp of 20 A/s, the profile as shown in Figure 4-15 was demanded from the fuel cell system.

After 30 minutes operation at a constant current (red line) of 25 A and the corresponding constant voltage (blue line), the current set-point (magenta dotted line) was changed every 5 minutes as illustrated in Figure 4-15. A voltage undershoot occurred when the current set-point was changed, followed by an exponential curved recovery until a stable voltage value was reached again. This can

be clearly seen during the first two steps from 0 A to 50 A and from 0 A to 40 A. On the other hand, the fuel cell output voltage was less sensitive against decreasing current steps. As shown in Figure 4-15 the voltage shows only a small overshoot after the current was set back to lower value with nearly the same height regardless of the magnitude of the current step.

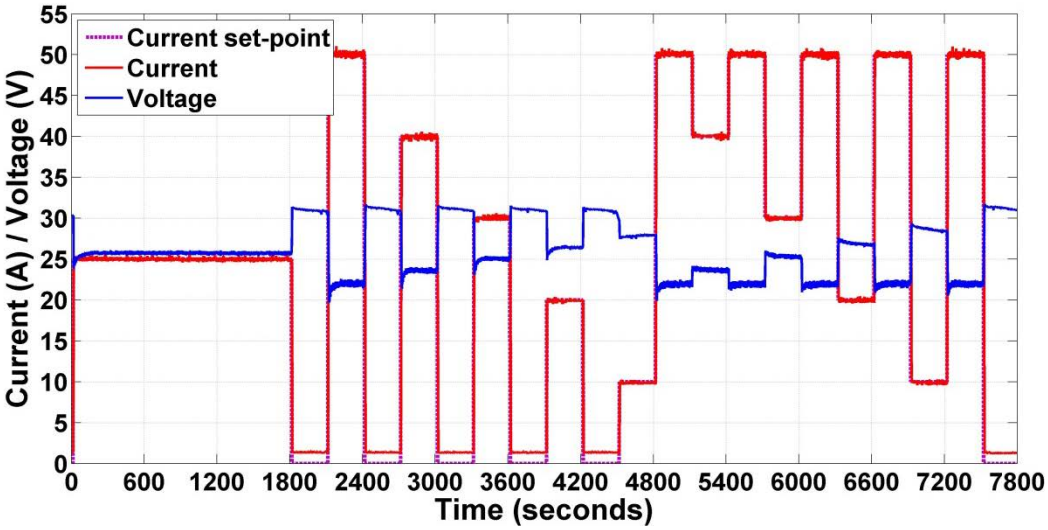


**Figure 4-15: Defined current profile for the step response test. The picture shows the results of an experiment with a current ramp of 20 A/s.**

To establish the impact of the current step gradient on the output voltage, the step response test was repeated three times at different maximum current ramps of 10 A/s, 5 A/s and 1 A/s. Figure 4-16 summarises the experiments for the highest step from 0 A to 50 A. The top graph shows the transient response of the DC current. The lower the current ramp of the inverter was, the slower the rise time. The response of the DC current with a current ramp of 20A/s (light blue line) showed the fastest rise time of two seconds, but led to a small current overshoot resulting in a settling time of 7 seconds. In comparison, the settling time of the experiment with a current ramp of 10 A/s (red line) was only 5 seconds. The lower graph of Figure 4-16 shows the corresponding transient response of the voltage. The black dotted line indicates the voltage during steady state (approx. 21.5V) at a DC current of 50 A. It can be clearly seen, the voltage undershoot increases with increasing current gradients. It took about 36 seconds until the voltage was recovered and was stabilised at the steady state voltage.

The current response to a set-point (mangenta dotted line) change from 0 A to 10 A is shown in Figure 4-17 on the left. The maximum current ramp of the inverter was changed from 1 A/s to 5, 10 and 20 A/s. The right graph shows the corresponding fuel cell voltage. Although, the height of the current step was significantly reduced there was still a minor voltage undershoot evident. The magnitude of the voltage undershoot was 1 V and of about 0.5V at a current ramp of 20 A/s and

5/10 A/s, respectively. The settling time of the current with a ramp of 5 A/s was 6 seconds compared to 4 seconds of the experiments with a current ramp of 20 A/s and 10 A/s. The recovery time of the voltage was about 24 seconds.

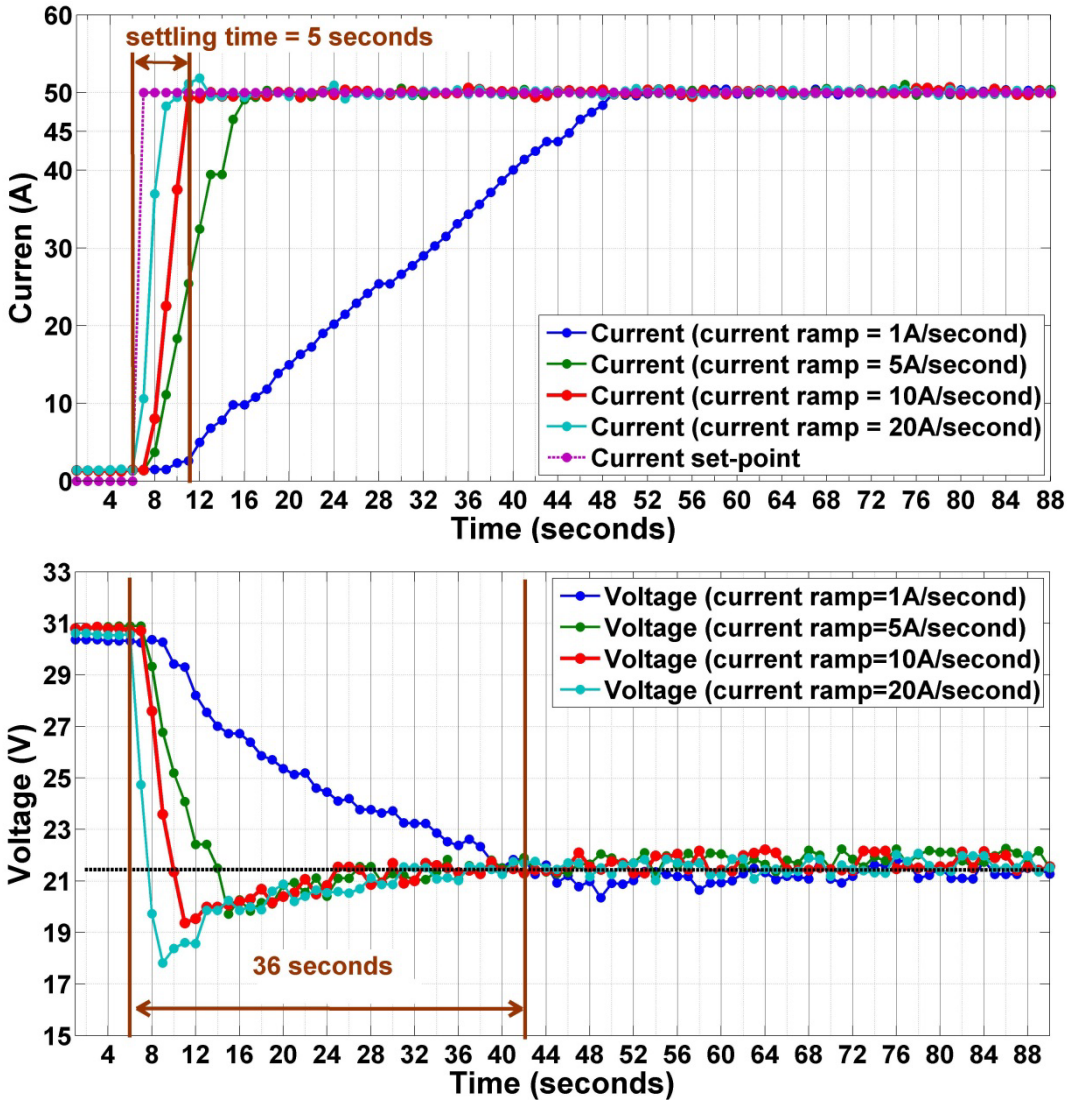


**Figure 4-16: Experimental results of current step from 0 A to 50 A with unified timestamp. The top graph shows the current response to a set-point (mangenta dotted line) change from 0 A to 50 A. The bottom graph presents the corresponding voltage response to the sudden load change.**

In general, a dynamic load change leads to sudden current change and consequently to a sudden change in the hydrogen and oxygen consumption. In addition, the supply of reactants and the water management of the membrane are influenced by dynamic load variations. Under rapid load changes fuel starvation can occur (Erdinc & Uzunoglu 2010). On the anode side the membrane can temporarily dehydrate due to electro-osmotic drag. This leads to an increase of the internal resistance resulting in a higher voltage drop (Tang et al. 2010). Moreover, the temperature also affects the performance and cannot simultaneously follow a load change. Every load transition

influences the control system of the BOP and a certain time is needed to regulate the subsystems, for instance, the air supply fan. Such unfavourable operating conditions accelerate performance degradation of fuel cells and should be avoided (Stumper & Stone 2008). Concluded from the results of the step response test it can be said that a maximum current ramp of 10 A/s provides a quite good dynamic performance without showing to high voltage undershoots. Thus, the next set of experiments was carried out with this value.

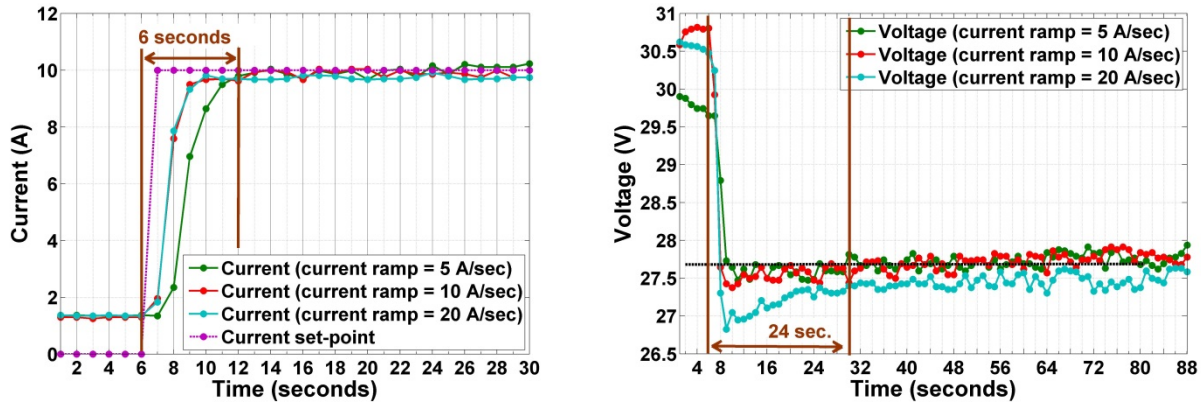


**Figure 4-17: Experimental results of current step from 0 A to 10 A with unified timestamp.**

### 4.2.3 FC tests: Controlled dynamic events

So far the steady state operation and the step response capability of the fuel cell system have been discussed. The following experiments were designed to find the operational limit under multiple dynamic events. Three experiments were carried out with a period duration of 40, 20 and 10 seconds. Figure 4-18 shows the complete current profile of the first experiment with a period of 40 seconds. The principal of the experiment is shown in Figure 4-8, but, instead of using an analogue signal to adjust the control set-point a communication protocol (CAN) is used to transmit new set-points to the fuel cell inverter. Within the PLC a sinusoidal control signal was generated with a peak-to-peak amplitude of 50 A superimposed on base current of 27 A. The current ramp of the inverter was set to 10 A/s.

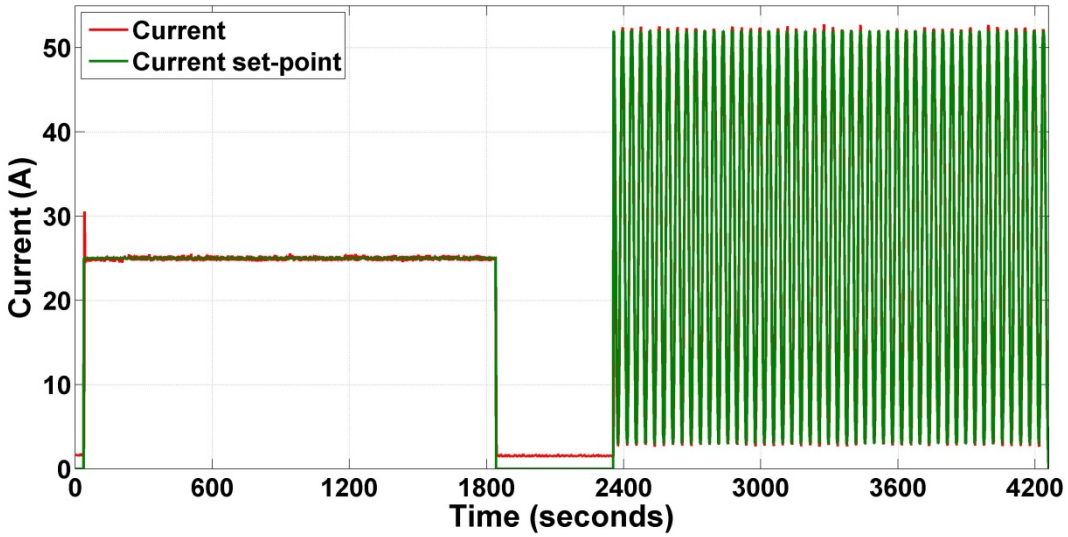


**Figure 4-18: Sinus profile: Control signal with a period duration of 40 seconds and peak-to-peak amplitude of 50 A superimposed on 27 A current. The maximum current ramp was set to 10 A/s.**

For a detailed analysis of the transient response Figure 4-19 illustrates a snapshot of the time frame from second 3926 to second 4016. The magenta line indicates the control signal of the inverter; the red line presents the measured DC current of the fuel cell. It is evident from this graph that both curves are almost identical without showing any significant time delays. The averaged current gradient was about 5 A/s.

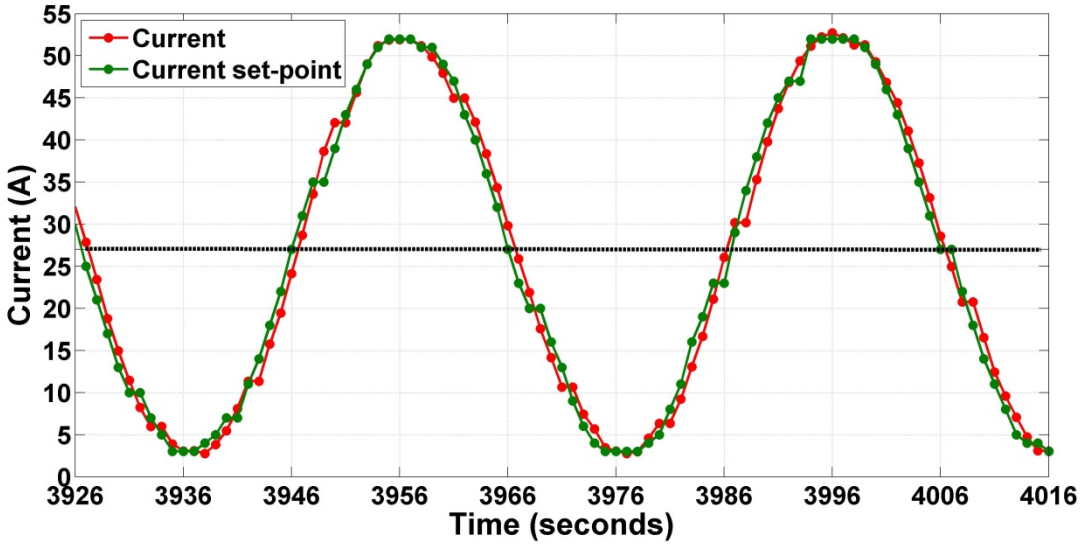


**Figure 4-19: Zoom into Figure 4-18: The magenta line shows the control signal, the black dotted line indicates the baseline of the sinusoidal control signal and the measured DC current.**

Figure 4-20 graphs the results of the experiments with period of 20 seconds (to the left) and 10 seconds (to the right). The left graph in Figure 4-20 shows that the fuel cell DC current response nearly matches the control signal with a period of 20 seconds. The right graph, on the other hand, shows the response to control signal with a period of 10 seconds. It is apparent from the graph that a phase shift occurs due to propagation delays within the control system. Further analysis of the data revealed maximum current gradients of 9 A/s and 13 A/s for a period of 20 seconds and 10 seconds, respectively.

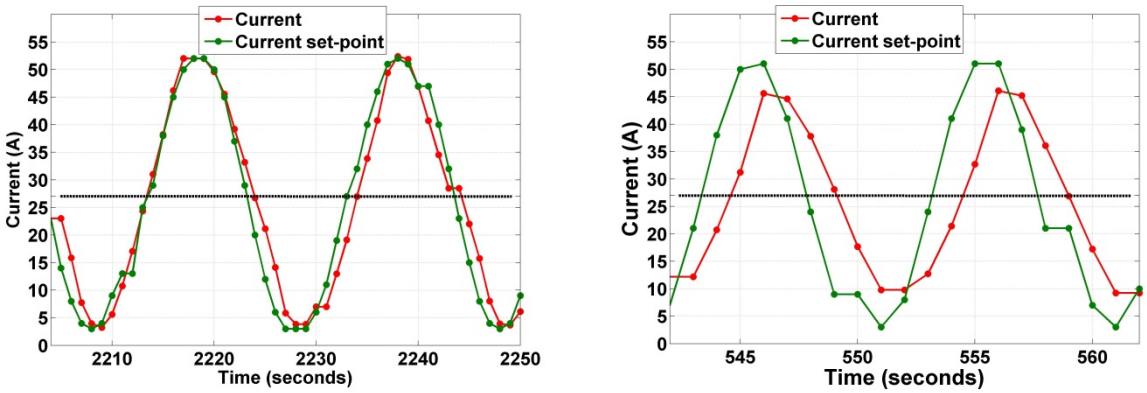


**Figure 4-20: The left graph gives results with a period of 20 seconds. The right graph shows the response to control signal with period of 10 seconds.**

The best match between the control signal and the measured DC current shows evidently the experiment with a control signal with a period of 40 seconds. Analysing the results of this experiment revealed a maximum current and power gradient of 5 A/s and 130 W/s, respectively. Therefore, the current ramp of the inverter is limited to 5 A/s for further investigations.

## 4.3 Operational behaviour of the vanadium-redox-flow-battery system

This subchapter firstly conveys basic theory on the VRFB and introduces performance indicators to evaluate the battery performance. Subsequently, experimental results are presented to characterise the steady state performance at different power rates. Finally, the dynamic operation is investigated by experiments as shown in Figure 4-1.

### 4.3.1 VRFB: Basic theory and steady state operation

VRFB are characterised by their independent scalability of power and energy capacity. The power is defined by the active area of the energy conversion unit (the cell stack), whereas the energy depends on the volume of the storage tanks of the electrolyte. In principle the process of the VRFB can be compared with the aforementioned process of the fuel cell. In both cases a redox reaction takes

place within the cells consisting of two electrodes which are separated by a proton exchange membrane. But instead of using oxygen and hydrogen for the reaction, a positive and negative electrolyte circulates from two tanks through a hydraulic system into the cell stack and back to the tanks. Figure 3-10 illustrates the process flow schematic of the used VRFB system. The VRFB can be either charged or discharged by a reversible chemical reaction between the two electrolytes. The electrolyte is based on sulphuric acid containing $VO_2^+/VO^{2+}$(positive electrolyte: catholyte) and $V^{2+}/V^{3+}$ (negative electrolyte: anoloyte) redox couples.

The chemical equations of the reaction become (Blanc & Rufer 2010):

Positive electrode (cathode):
$$VO^{2+} + H_2O - e^- \underset{discharge}{\overset{charge}{\rightleftharpoons}} VO_2^+ + 2H^+ \quad \textbf{(4-18)}$$

Negative electrode (anode):
$$V^{3+} + e^- \underset{discharge}{\overset{charge}{\rightleftharpoons}} V^{2+} \quad \textbf{(4-19)}$$

Overall reaction:
$$V^{3+} + VO^{2+} + H_2O \underset{discharge}{\overset{charge}{\rightleftharpoons}} V^{2+} + VO_2^+ + 2H^+ \quad \textbf{(4-20)}$$

During the discharge process $VO_2^+$ ions are reduced to $VO^{2+}$ ions at the positive electrode, while $V^{2+}$ ions are oxidised to $V^{3+}$ ions at the negative electrode. The open circuit voltage across the electrodes depends on the concentration of the vanadium species. Thus, the concentration indicates the SOC of the battery system: a fully charged electrolyte (SOC=100%) contains 100% $V^{2+}$ and 100% $VO_2^+$ in the negative and positive electrolyte, respectively (Sukkar & Skyllas-Kazacos 2003). Figure 4-21 illustrates the open circuit voltage as a function of the SOC. It can be seen that the behaviour is strongly nonlinear at low and high SOC regions. VRFB are very tolerant to over-discharging, however, charging the battery beyond a certain voltage can lead to side effects at the electrodes such as oxygen and hydrogen generation and should be avoided (Mohamed, Ahmad & Abu Seman 2012). In addition, high SOC values could lead to oxidation of components inside the cell (electrodes and bipolar plate) and it should not exceed values above 80% (Schreiber 2011). Therefore, the prediction of the SOC during operation is crucial for the lifetime of the battery. A commonly applied method is to use a single reference cell, which is hydraulically connected to the stack in parallel (see Figure 3-10) and to measure continuously the open circuit voltage. The useable SOC range of the installed Prudent Energy™ VRFB system is between 34% and 72% which corresponds to an open circuit voltage of 1.362 V and 1.481 V, respectively, see Figure 4-21.

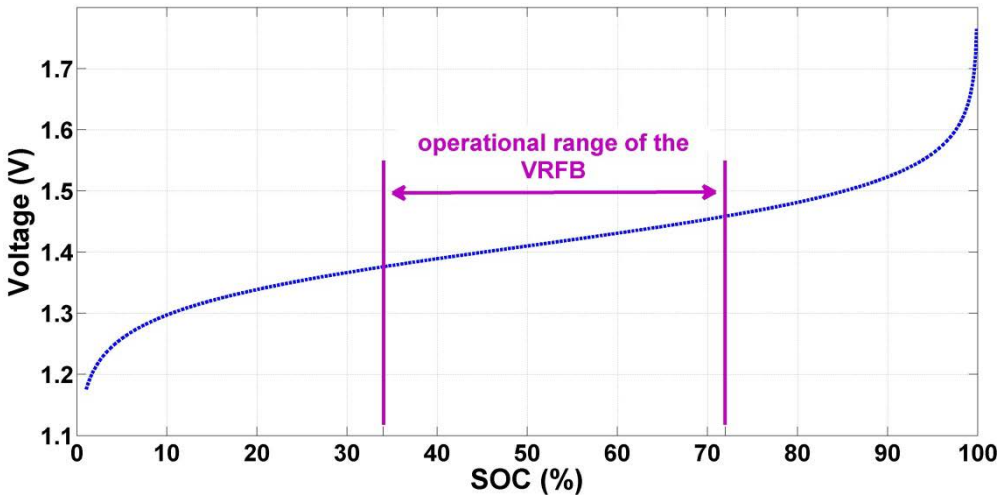


**Figure 4-21: Relationship between the open circuit voltage (dotted blue line) and SOC.**

Turning now to the experimental analysis of the VRFB system, the test set-up is illustrated in Figure 3-12. The start-up procedure of the VRFB is similar to the one of the fuel cell system. To start the battery after a long term shutdown, it is necessary to supply electrical power to the BOP. Then, the battery controller initialises itself and starts ramping up the electrolyte pumps. Fresh electrolyte will be pumped through the stack resulting in an increase of the stack voltage according to electrolyte's SOC. As soon as the voltage level is stabilised, the external power supply can be switched off. In total the start-up process takes approximately 75 seconds. Now the VRFB can be either charged or discharged by using the two inverters that are controlled by the WAGO 750-872 PLC. If no energy is exchanged with the electric grid of the HREP, the VRFB enters the standby-mode where the pumps are kept running at reduced speed. From this state the system can be instantaneously transited back into charge or discharge mode. However, it should be noted that the energy consumption of the pumps is covered by the battery leading to a self-discharge rate of approximately 280 Wh/h. Therefore, the standby time should be limited to avoid energy wasting.

To evaluate the efficiency of the VRFB system, several charge and discharge cycles were carried out at different stack current rates. During the experiments the electrolyte temperature varied between 28°C-33°C.

The performance is evaluated at three different system levels:

I. Stack level: Cell stack,

II. DC system level: Cell stack + peripheral components (controller, sensors and pumps),

III. AC system level: Cell stack + peripheral components (controller, sensors and pumps) + inverter.

The following efficiencies are defined to assess the performance (Blanc & Rufer 2010):

Coulombic efficiency: $$\eta_{coulombic} = \frac{\int I_{discharge} dt}{\int I_{charge} dt} \quad \textbf{(4-21)}$$

Energy efficiency: $$\eta_{energy} = \frac{\int P_{discharge} dt}{\int P_{charge} dt} \quad \textbf{(4-22)}$$

The Coulombic efficiency $\eta_{coulombic}$ is calculated as the ratio between the discharge and charge current within a given time period. In this thesis this efficiency is only calculated at stack level. The energetic efficiency $\eta_{energy}$ is calculated at every system level to quantify all losses of energy conversion process. Figure 4-22 presents the averaged efficiencies of several full charge-discharge cycles (34%-72% SOC). The Coulombic efficiency (blue line) increases with increasing current. With increasing current density the charge/discharge time decreases, accordingly, the effect of diffusion of electrolyte species through the membrane reduces and hence the rate of self-discharge in the stack (Zhao et al. 2006).

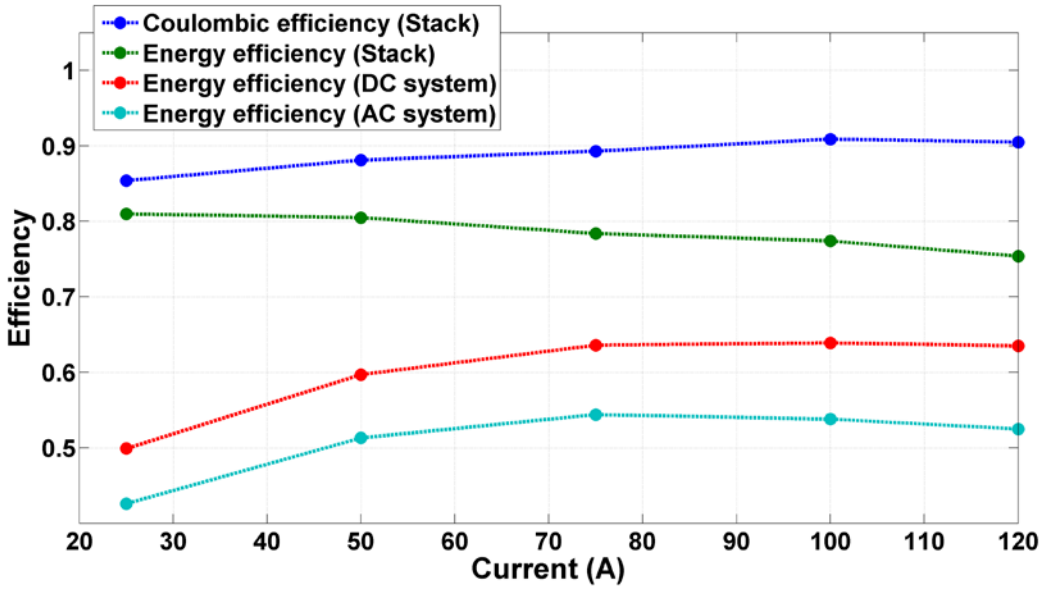


**Figure 4-22: Comparison of the calculated efficiencies as a function of the stack current.**

The stack energy efficiency (green line), on the other hand, decreases due to the higher polarisation losses at higher current densities (Chen et al. 2013a). The energy efficiency at DC system level (red line) is influenced by the energy demand of the BOB. Thus, the amount of the energy supplied to the peripherals is higher at lower current regions resulting in lower efficiencies. In addition, the AC system efficiency (light blue line) is affected by the efficiency curve of the inverter (see Figure A-2) and shows apparently the lowest values. In comparison to the hydrogen loop, the VRFB shows quite high efficiencies over the complete operation range.

### 4.3.2 VRFB tests: Single dynamic event

The single dynamic response of the VRFB system was investigated by carrying out three different current step experiments. Firstly, the capability to follow a sudden power supply change was evaluated. Secondly, the response to a sudden load change was analysed. Finally, a rapid switching between charge and discharge was investigated. During the experiments the electrolyte temperature varied between 30°C and 33°C. As described in chapter 3.5 the electrical power to charge or discharge the battery can be controlled by manipulating the AC active current set-point of the Sunny Island inverters by using the PLC. Figure 4-23 illustrates the applied active current profile to charge the battery and the measured root mean square (RMS) value of the AC current by the LON energy meter. Each set-point was kept for three minutes before it was set back to zero. It can be seen that the AC current response fairly matches the set-point. The experiments were repeated at least three times and every data set was analysed. The sample rate of the DAQ was set to 500 ms.

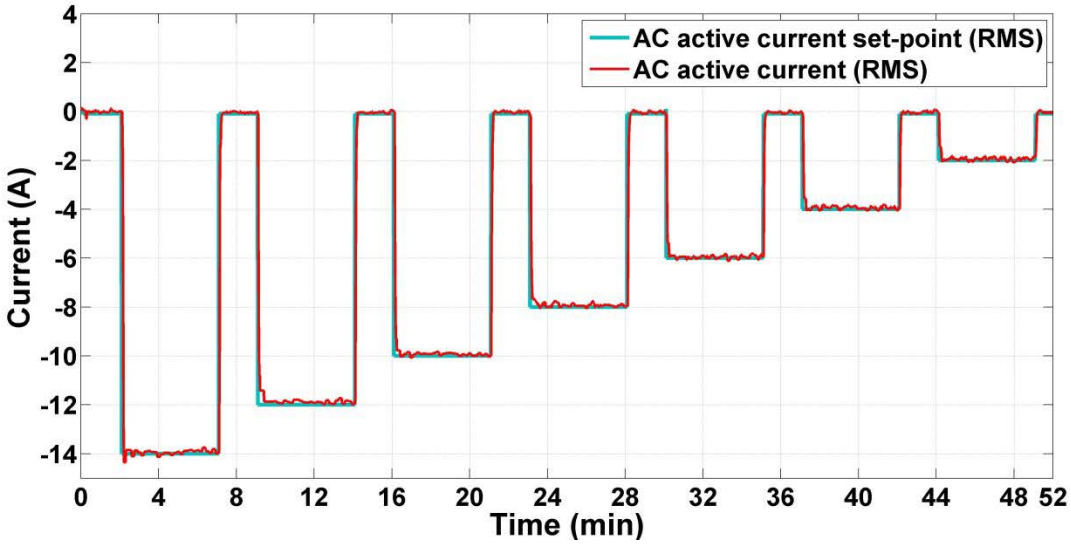


**Figure 4-23: AC active current (RMS) profile to charge the VRFB**

The response to the first current step from 0 to -14 A is shown in Figure 4-24. After the AC active current set-point (light blue line) was changed, the measured AC active current (red line) followed with a time delay of one second. An overall analysis revealed a diversity of the response time of one to two seconds. In total the AC current needed 7 seconds to settle. The maximum DC current (green line) gradient for AC active current step from 0 A to -14 A was approximately -46 A/s. On average the DC current gradient was -15 A/s which corresponds to an average power gradient of -780 W/s. The DC voltage (blue line) transited smoothly to the new value. Whereas, the current showed a small overshoot before both values the DC current and the AC current starts to settle.

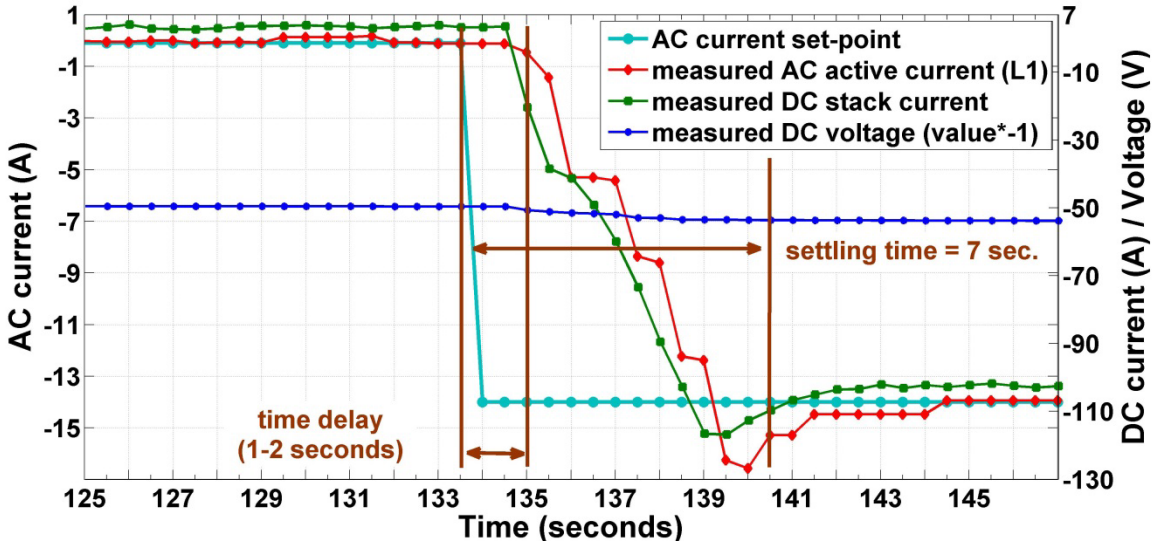


**Figure 4-24: Response to an AC current step from 0 to -14 A.**

The response of the BOP to the AC current step from 0 A to -14 A is presented in Figure 4-25. As stated in chapter 3.5 the VRFB system is equipped with a battery controller that monitors and controls the process, see Figure 3-10. The controller starts to ramp-up the pumps a few seconds after the current step occurred. It takes approximately 70 seconds until a new stable value is reached. Along with the pump speed increase, the energy consumption of the BOP correspondingly increases (see peripheral current (orange line) in Figure 4-25). Consequently, the current supplied to the stack will be reduced with increasing peripheral current. It was also found that the pump speed will be ramped up to approximately 2600 rpm during charge process regardless of the applied current.

The power consumption of the BOP reduces the system's energy efficiency especially at lower charge current regions, as shown in Figure 4-22. Thus, there may exist a conflict between the electrolyte flow rate, pump power consumption and efficiency.

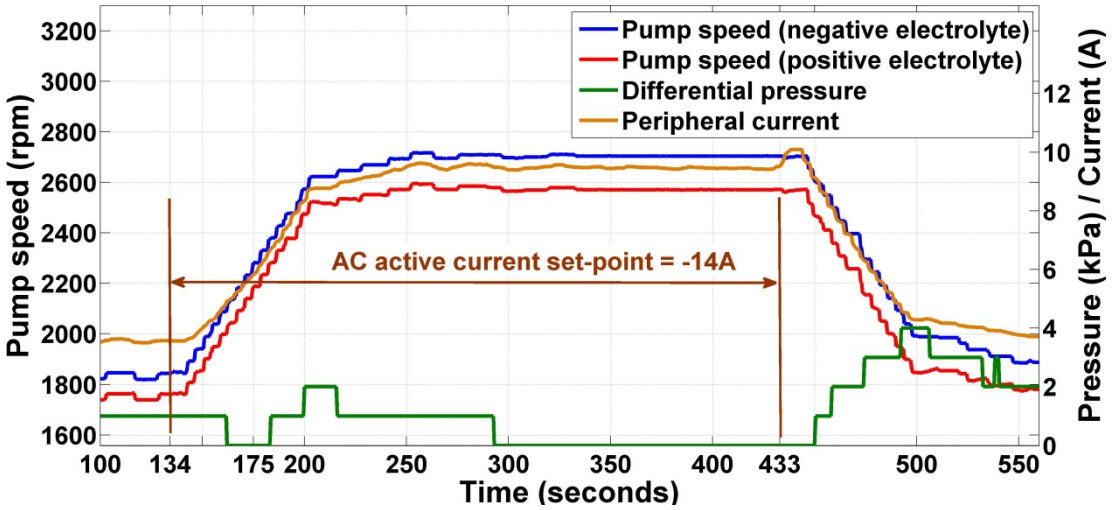


**Figure 4-25: Response of the BOP to current step from 0 to -14 A.**

Recently, the investigation of optimal flow rate of VRFB has been studied intensively. An experimental study conducted by Ma et al. (2012) discussed the effects of the flow rate with respect to the system efficiency. They demonstrated that the energy capacity increases with increasing electrolyte flow rate. Furthermore, they showed that the concentration over-potential will be reduced with higher electrolyte flow rates due to the higher supply of reactants, which leads to a better facilitation of the redox reactions. They propose to operate the VRFB at a constant flow rate over a large operating area until the flow rate will be stepped up at high and low SOC during charge and discharge, respectively. With this operating strategy they demonstrated that the system efficiency can be improved up to 8% compared to constant high flow rate during charge and discharge. Tang et al. (2014) has linked the concentration over-potential and the pressure losses to the electrolyte flow rate. They carried out a simulation study and their results show that a variable flow control can lead to higher overall efficiencies during charge and discharge. In addition, they highlight that the electrolyte flow rate is an important factor for the thermal management to remove heat from the stack to avoid potential thermal precipitation within the cells. The battery controller of the Prudent Energy™ VRFB system, however, operates the pumps during charge at the maximum flow rate resulting in higher energy capacity and higher Coulombic efficiency, but, with the drawback of lower system energy efficiency.

The second set of experiments was carried out to analyse the behaviour of VRFB during discharge. By comparing the results of the charge and discharge experiments it was found that the response time and the settling time were almost the same. The maximum and the average DC current gradient were about 50 A/s and 17 A/s, respectively. The implemented pump control, however, shows a different behaviour. The battery controller regulates the pump speed as function of SOC and DC

current during discharge. Between a SOC of 38% and 66% the pump speed depends only on the current withdrawn from battery. Within this area the results revealed that there are three different pump speeds:

I. High currents (>80 A): 2300 rpm

II. Mid currents (30 A -80 A): 2000 rpm

III. Low currents (<30 A): 1800 rpm

At the end of charge or discharge the pump speed will be stepped up again to increase the flow rate; accordingly, the mixing time of the electrolyte in the tanks will be reduced. In addition, the increased flow rate helps to monitor the SOC to avoid an overcharge or a deep discharge, where the voltage starts to have a nonlinear behaviour due to the sharply decrease of the vanadium ions $V^{3+}/V^{4+}$ and $V^{2+}/V^{5+}$, respectively (Ma et al. 2012). The implemented pump control during discharge helps to improve the system energy efficiency, but, there is space for improvement as demonstrated by (Tang, Bao & Skyllas-Kazacos 2014).

Another aspect needs to be considered when the VRFB follows a dynamic profile is the pressure balance between the two half-cells within the cell stack. A pressure difference across the membrane facilitates the volumetric transfer of the electrolyte from one half-cell to the other which leads to capacity loss (Skyllas-Kazacos & Kazacos 2011). Moreover, over long term operation such volumetric transfer can cause flooding of the electrolyte reservoir (Sukkar & Skyllas-Kazacos 2003). Figure 4-25 shows that the differential pressure (green line) increases after a load change occurs. Consequently, this will promote the fluidic transfer leading to a capacity loss and an electrolyte level imbalance in the reservoirs. To take the latter effect into account, the Prudent Energy™ VRFB system is equipped with a rebalancing mechanism that automatically equalises the tank levels over time. However, the amount of fluid exchanged between the two sides is small compared to the total volume of the tanks.

The last set of experiments examined the system's capability to switch between charge and discharge. Figure 4-26 shows the applied current profile, the set-point was first changed from 0 A to 5 A followed by periodically switching from 5 A to -5 A and vice versa every 120 seconds. From the data it can be seen that the system is capable following the first set-point change from 0 A to 5 A quite fast. But, if the set-point is directly changed from discharge to charge, the AC current response shows a relatively high overshoot. On the DC side a stack current overshoot of about 20 A was measured. Furthermore, a deeper analysis showed that the response time has significantly increased to 10 seconds. This experiment has revealed limitations of the internal control logic of the inverter to deal with sudden changes from discharge to charge and vice versa. Therefore, the transition from

one state to the other should be controlled so that high current peaks will be avoided. Of course this is a plant specific problem and cannot be generalised for all VRFB. But it highlights the need to examine the operational limits of multivendor system designs.

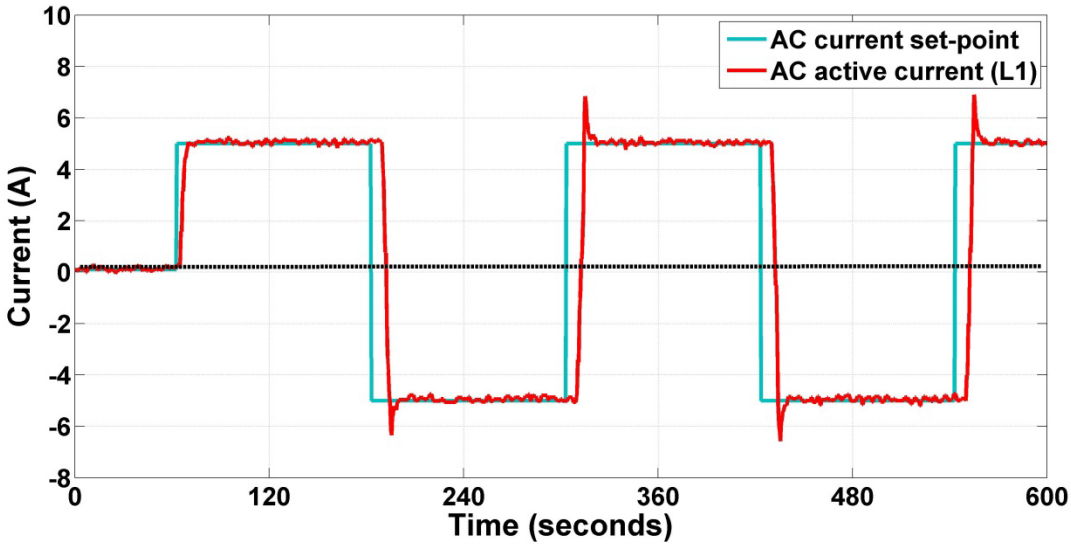


**Figure 4-26: Applied current profile to analyse the switching between discharge and charge.**

### 4.3.3 VRFB tests: Controlled dynamic events

In the next section the load/supply following capability of the VRFB system is assessed. Figure 4-8 illustrates the principle of the applied experiment. The sinusoidal control signal is generated by the PLC and then transmitted via Modbus TCP connection to the remote access gateway of the inverter, see Figure 3-12. Three set of experiments were conducted for each discharge and charge. Each set had the same current basis and peak-to-peak amplitude. The period duration was halved after every experiment starting with a value of 80 seconds. As discussed in the previous chapter the transient response to a single dynamic event shows the same temporal behaviour whether the system is charged or discharged. Only the pump control is different in both situations. While the pump speed is constant at maximum flow rate during charge, the pump speed is a function of SOC and DC current during discharge. The dynamic pump control leads to more frequently imbalanced pressures between the two sides of the cell stack. Therefore, the following paragraphs discuss the transient response during discharge.

Figure 4-27 presents the data of the first experiment with a peak-to-peak amplitude of 10 A around mean of 6 A. The time duration of the sinusoidal control signal was 80 seconds. The measured AC active current (red line) and DC stack current (greed line) followed the AC active current set-point (light blue line) with a time delay of about 2 seconds. This agrees well with the findings of the single dynamic event experiment. However, the progression of the measured AC active current (red line) is

similar to the control signal with the same peak-to-peak amplitude and period length. The maximum set-point gradient was 0.4 A/s resulting in an averaged power gradient of 160 W/s.

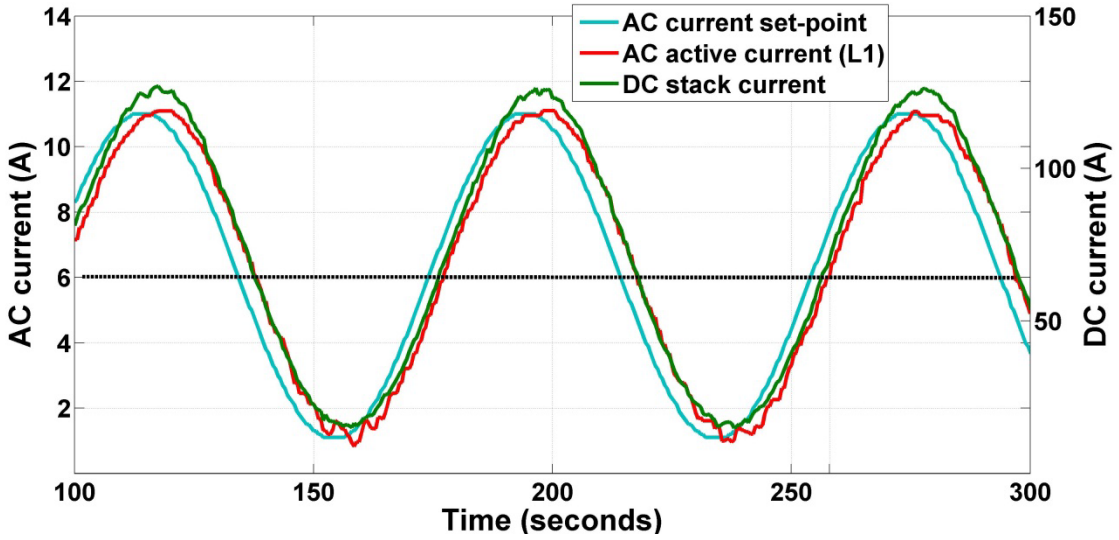


**Figure 4-27: Transient response of the VRFB system to sinusoidal AC current control signal (magenta line) with peak-to-peak amplitude of 5 A superimposed on 6 A.**

Figure 4-28 shows the results of the experiments with period duration of 40 seconds (left graph) and 20 seconds (right graph). The left graph indicates that the VRFB system can follow the control signal without showing any disturbance of the progression of the measured current. Whereas, the right graph evidently shows that the system cannot follow a sinusoidal signal with period length of 20 seconds. The AC active current curve is reduced by 1 A compared to the control signal. This indicates that the communication and control system has reached a limit. The maximum set-point gradient during the experiment with 40 seconds was 0.8 A/s and the averaged power gradient was 260W/s.

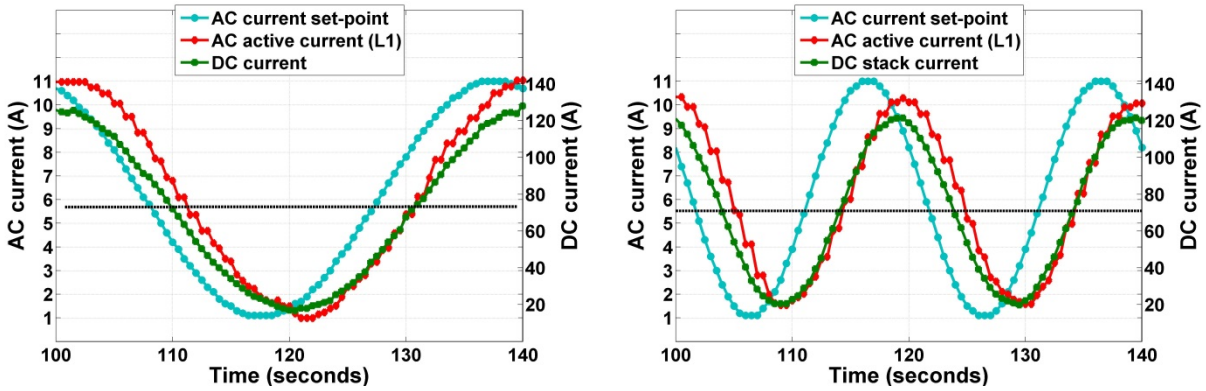


**Figure 4-28: Transient response to sinusoidal signal with period duration of 40 seconds and 20 seconds presented on the left and on the right, respectively.**

Regarding the differential pressure the data showed that the pressure difference significantly increased during the last discharge experiment with a time period of 20 seconds. During charge the differential pressure was hardly affected by the dynamic operation due to the constant pump speed strategy. As aforementioned the research on electrolyte flow optimisation has recently increased and it is important to investigate the effects of the flow rate and the differential pressure on the overall performance of VRFB systems. However, such investigations are outside the scope of this thesis.

## 4.4 Summary

The experiments outlined in this chapter addressed steady and dynamic operation of the energy conversion systems. In a HRES, the energy conversion system plays an important role to equalise the power output of the renewable energy sources and the actual electricity demand. It is necessary to understand the individual system's behaviour before defining a suitable operational strategy. To extract the relevant information from each energy system, an experimental method was defined to characterise the components of the HREP. The experimental study has identified crucial parameters, for instance, the temperature, which influence the performance and it has revealed operational limitations at system level.

The first set of experiments has analysed operational states such as start-up and steady-state performance of each energy conversion system. The electrolyser needs about 15 minutes to start-up before it can follow a power supply profile. The fuel cell and the VRFB can be transferred into operation mode within less than two minutes. All systems are affected by the operational temperature. Especially the electrolyser's efficiency is significantly influenced by the temperature. At maximum current rate it takes approximately 80 minutes to reach the nominal operating temperature where the efficiency shows higher values. The internal resistance of the VRFB is also temperature dependent. The lower the electrolyte temperature, the higher the internal resistance is. However, if the VRFB was to be installed within an insulated enclosure where the ambient temperature is normally around 25°C, the electrolyte temperature would be stabilised around 30°C during operation.

To characterise the dynamic operation of the electrolyser, the fuel cell and the VRFB two set of experiments have been carried out to investigate the response to single dynamic and multiple dynamic events. Based on the experiments operational limitations are identified which need to be considered within the control system. Table 4-1 summarises the main outcomes of the conducted experiments.

**Table 4-1: Characteristics of the energy conversion units on system level.**

| | Electrolyser | Fuel Cell | VRFB |
|---|---|---|---|
| **Start-up time /warm-up time** | 15 min. / 80 min. | 45 sec. / 10 min | 75 sec. |
| **Standby time** | max. 60 min. | User defined | User defined |
| **Averaged electrical energy consumption during standby:** | 350 Wh/h | 50 Wh/h | 280 Wh/h |
| **Operational range** | 24-56 A (DC current) | 5-50 A (DC current) | 25-120 A (DC current) |
| **Single dynamic event: Max. power gradient** | 1132 W/s | 120 W/s | 780 W/s. |
| **System response time** | 2 seconds | 0-1 seconds | 1-2 seconds |
| **System settling time** | 4 seconds | 5 seconds | 7 seconds |
| **Multiple dynamic events: Max. power gradient** | 600 W/s (approx. 10% of the rated power) | 110 W/s (approx. 10% of the rated power) | 260 W/s (approx. 5% of the rated power) |

In addition, the conducted experiments revealed unfavourable operational situations, for example, voltage undershoot phenomena, which occur if the fuel cell has to follow high current variations. Furthermore, the experiments establish the importance of considering the dynamics not only on component level, but on system level including the BOP, the inverter and the communication system.

# 5 Development of system level models of the HREP

A model is the approximation of a real system and can be based on mathematical equations, on relationships derived from measurements or from both to describe, for instance, physical or chemical processes. In general, a model can be categorised as white-box-model (purely theoretical), black-box-model (only based on experimental data) or grey-box-model (a combination of theoretical and experimental relations) (Isermann 2008). The latter is also known as semi-empirical-model and this model approach is broadly used for various engineering applications. Once the model is defined it can be used as the basis for simulation studies. The model detail depends on the purpose of the simulation study. Focused on the development and optimisation of core components, the level of detail would increase along with required computational power. However, the objective of this thesis is to analyse energy conversion systems at system level to evaluate the performance of the components and their interaction as well as to draw operational strategies from the conducted experiments. Derived from this objective, the following requirements should be met by the proposed models of the hydrogen loop and the VRFB system:

- Simple integration of the models to investigate different configurations,
- Reflecting physical correlations with sufficient precision,
- Practical adaption of parameters of the models,
- Linking operational constraints to the models.

Figure 5-1 presents the applied methodology of the modelling process. The conducted experiments presented in the previous chapter 4 provide information about the physical correlations and the operational behaviour. Based on the gathered data parameters for the mathematical description were extracted to model, for instance, the electrical, thermal or the energy capacity behaviour. In addition, operational modes and constraints were identified from the experimental results and implemented into a sub-model. Furthermore, the semi-empirical sub-models to describe the physical process and the sub-model to describe the operational behaviour were integrated into an overall system model. Finally, the system models were fully validated against measured data.

To describe an existing system properly a comprehensive understanding of the theoretical problem and a good knowledge about the material properties are necessary. In most cases this cannot be fully achieved and parameters are introduced to approximate the unknown variables from measured data. As illustrated in the previous chapter, the discussed energy conversion systems show some non-linearities. In this regard, a non-linear regression analyses was conducted to estimate the unknown parameters.

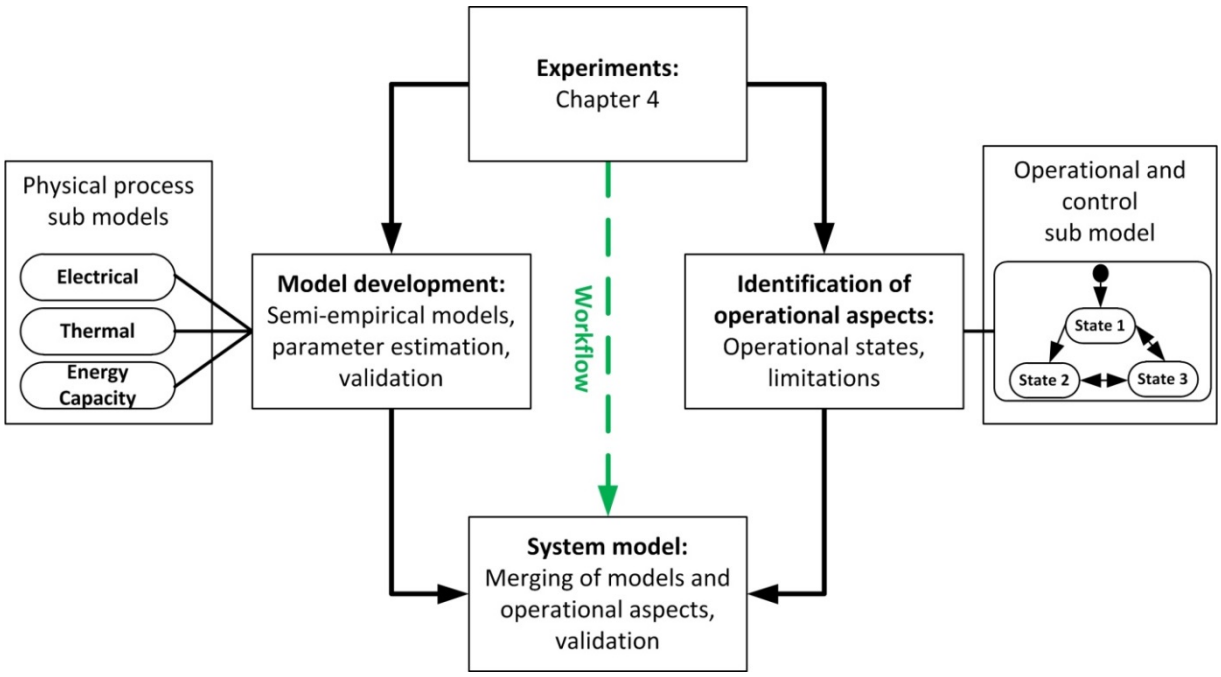


**Figure 5-1: Methodology of the model development.**

The analysis was carried out off-line (this means the model was fitted to a set of prior measured data). The unknown variables are the decision variables and a function minimises the least-squares between measured values and the predictions based on the employed model equations. To assess the fitted models the cross-validation technique was applied (Livingstone 2009). The parameters were estimated with data from one set of experiments and the validation was carried out with another set of measured data.

The models have been developed in the MATLAB® software environment (MATLAB 2012). For the parameter estimation the MATLAB Optimization toolbox was used. Individual MATLAB-script files were written containing the *lsqcurvefit*-function which is part of this toolbox. The function applies the method of least-squares for non-linear problems (Optimization Toolbox 2012). Following this, the model was developed in Simulink® (Simulink 2012), which is a block oriented simulation interface integrated in MATLAB. Operational aspects such as operational states were modelled using the Stateflow® (Stateflow 2012) toolbox. Stateflow® is a graphical interface to design event-driven systems using the statechart approach formulated by Harel (1987).

The following sections present the development of the system models of the electrolyser, the fuel cell and the VRFB. The last section describes the energy management strategy to coordinate and to control the HRES.

## 5.1 General model layout

Each developed system model has the same structure so that it can be easily applied to different simulation scenarios. The system model is divided into various sub-models, for example, the system control or the electrical model. Figure 5-2 illustrates the proposed generic layout of the developed models. The model input is at least the AC power set-point and the on/off signal. The outputs are the AC power (consumed/withdrawn), if applicable the released heat and the state of charge of the storage. In addition, several internal values such as DC voltage or DC current can be added to the output if necessary. Every system model contains a set of parameters that describe the physical system. For instance, the electrolyser is characterised by the active cell area and the number of cells. In addition, the estimated parameters for mathematical representation of the process need to be defined.

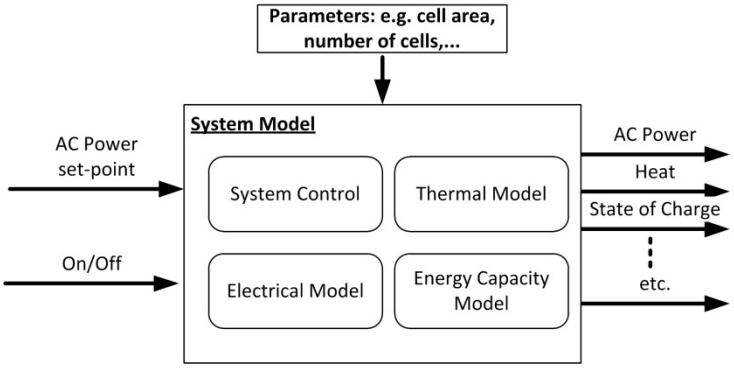


**Figure 5-2: General model layout**

The system model combines the physical continuous elements of the process with the discrete event elements derived from the implemented control logic and system constraints of the concerned component. In general, a model that integrates the continuous and the discrete behaviour of a physical system is referred to as hybrid system (Schaft, A. J. van der & Schumacher 2000). A graphical approach to describe the discrete part of a hybrid system is the statechart formalism proposed by Harrel (1987). Statecharts are composed of states, transitions, events and conditions. Discrete states of a physical system are, for instance, the start-up or the standby mode. Depending on defined thresholds or timers the physical system is transited from one state to another. In addition, statecharts can be hierarchical organised and parallel states can be introduced.

## 5.2 Modelling of the hydrogen loop

In this section models of the hydrogen loop will be developed and validated. Section 5.2.1 deals with the system model of the electrolyser and the hydrogen storage. Section 5.2.2 shows the model formulation and validation of the fuel cell system.

### 5.2.1 System model of the electrolyser

Several model approaches of electrolysers can be found in the literature. In recent years, the work on multi-physics models has been increased. Roy (2006), Agbli et al. (2011) and Henao et al. (2014) presented multi-physics models for alkaline, PEM and alkaline electrolyser, respectively. However, each model requires detailed knowledge about the used materials and about the geometry such as the membrane thickness or the distance between the electrodes. Such in-depth information is normally not provided by the manufacturer. Therefore, this thesis considers models which provide a balance between practical application and theoretical complexity. Semi-empirical models to describe the electrical behaviour have been presented by Ulleberg (1998; 2003) and Kélouwani et al. (2005). Both models were initially applied to simulate I-U characteristic of the Accagen SA electrolyser and the results indicated that the latter model was not sufficiently able to predict the current-voltage behaviour. The Ulleberg model, on the other hand, showed a quite good accuracy. Thus, this thesis presents a model that is primarily based on this modelling approach. The following section introduces the thermodynamic and the electrical model of the electrolyser. Subsequently, the thermal model and the system control model are developed. Finally, all sub-models are integrated to the overall system model.

#### *5.2.1.1 Electrolyser: Thermodynamic and electrical model*

As described in section 4.1.1 decomposition of water into hydrogen and oxygen requires both electrical and thermal energy. Equation (4-4) defines the relation of the electrical and thermal energy. By rearranging of equation (4-4) the minimum electrical energy demand for the reversible reaction which is equal to the Gibbs free energy can be calculated by:

$$\Delta_R G_m^0 = \Delta_R H_m^0 - T\Delta_R S_m^0 \qquad \textbf{(5-1)}$$

Equation (5-1) refers to the standard conditions (1 bar and 25°C). To adapt it to the working temperature and pressure it is necessary to calculate the enthalpy and the entropy of reaction:

$$\Delta_R H_m = \sum v_i * \left\{ \Delta_f H^0_{m,i} + C_{p,i}|^T_{T_0} * (T - T_0) \right\} \quad \textbf{(5-2)}$$

$$\Delta_R S_m = \sum v_i * \left\{ S^0_{m,i} + C_{p,i}|^T_{T_0} * ln\left(\frac{T}{T_0}\right) - R * ln\left(\frac{p}{p_0}\right) \right\} \quad \textbf{(5-3)}$$

where, $v_i$ is stoichiometric coefficient (reactants = negative and products = positive, for example see equation (4-3): $v_{H_2O} = -1$, $v_{H_2} = 1$ and $v_{O_2} = 1/2$), $\Delta_f H^0_{m,i}$ is the heat of formation (kJ/mol), $C_{p,i}$ is molar heat capacity (J/(mol*K)), $S^0_{m,i}$ standard entropy (J/mol*K), $R$ is the universal gas constant (8.31446 J/(mol*K), and $T_0$ and $p_0$ are the temperature (K) and pressure (bar) at standard conditions, respectively.

Since the electrical energy demand for the reversible reaction is equal to $\Delta_R G_m$, the reversible cell voltage $U_{rev}$ for a given temperature and pressure can be calculated by substituting equation (5-2) and (5-3) into (5-1) and applying Faraday's Law:

$$U_{rev} = \frac{\Delta_R G_m}{z * F} \quad \textbf{(5-4)}$$

Along with thermodynamic properties of the substances taken from (Cerbe & Wilhelms 2013) and (Lide 2006), equations (4-5) and (5-1)-(5-4) are implemented into Simulink to calculate the thermo neutral and reversible voltage. The values of the thermodynamic properties are given in Table A-7. Table 5-1 compares the calculated reversible voltage with values reported in literature for alkaline water electrolysis (30wt% KOH). It has to be noticed that the molar heat capacity of the substances is taken as constant and the presence of KOH in the aqueous solution is neglected in the model. As can be seen from the table below, the adopted simplification leads only to small deviations.

**Table 5-1: Comparison between calculated values for $U_{rev}$ and values found in literature:**

| $U_{rev,T,p}$ | (LeRoy, Bowen & LeRoy 1980) | (Onda et al. 2004) | (Roy 2006) | This study |
|---|---|---|---|---|
| $\boldsymbol{U_{rev,25°C,1\ bar}}$ | **1.229 V** | **1.229 V** | **1.229 V** | **1.229 V** |
| $\boldsymbol{U_{rev,25°C,25\ bar}}$ | **1.3 V** | **1.290 V** | **1.299 V** | **1.291 V** |
| $\boldsymbol{U_{rev,46.85°C,1\ bar}}$ | **1.211 V** | **not reported** | **1.211 V** | **1.211 V** |
| $\boldsymbol{U_{rev,75°C,25\ bar}}$ | **1.268 V** | **not reported** | **1.268 V** | **1.260 V** |

The minimum required voltage for the reversible reaction would be the reversible voltage if heat is supplied externally. As shown in section 4.1.1 the measured cell voltage is much higher due to an aggregation of voltage losses namely the activation potentials at the electrodes and the ohmic

resistance in the cells. Ulleberg (1998; 2003) introduced an empirical current-voltage relationship (5-5) to model the electrode kinetics that takes into account the temperature dependency of both the ohmic resistance and the over potentials.

$$U_{cell} = U_{rev} + \frac{r_1 + r_2 * T_{ele}}{A} * I + s * \log\left(\frac{t_1 + \frac{t_2}{T_{ele}} + \frac{t_3}{T_{ele}^2}}{A} * I + 1\right) \qquad \textbf{(5-5)}$$

The coefficients $r_i$ are the parameters of the ohmic voltage losses, $s$ and $t_i$ are the parameters to describe the overvoltage behaviour. $T_{ele}$ is the temperature of the electrolyser (°C) and *A* is the active cell area of the Accagen SA electrolyser (105.68 cm²).

A flow-chart of the proposed procedure to estimate the parameters can be found in the appendix, see Figure A-5, and is briefly described below. First, nine experiments were conducted to collect operational data of the voltage and current at electrolyte temperatures of 40°C, 45°C, 50°C, 55°C, 60°C, 65°C, 70°C, 75°C and 80°C. As explained in section 4.1.1, the operating temperature of the electrolyser oscillates due to a two-point controller. In addition, the liquid levels of the KOH accumulators vary due to pressure differences and are periodically equalised during operation. Consequently, both the temperature and the pressure vary. Therefore, each set of data (sample rate = one second) was organised with respect to limit temperature and pressure variations to ±1 K and 28 bar ±0.5 bar, respectively. Then, eight sets of data were generated where each time one of the nine sets of measured data was left out, for example the first set contains the data of the experiments 45°C-80°C and the last set contains the data from 40°C-75°C. In addition, a ninth set was merged containing all data (1519 data points). Subsequently, the data sets were passed to a programmed MATLAB® script; for each data set the parameters were estimated by employing the *lsqcurvefit*-function and the cell voltages for the missing data were calculated, for instance, 40°C for the first set. To assess the accuracy of the estimated parameters, the root-mean-square-derivation (RMSE), see equation (A-1), was calculated for all nine data sets. Finally, the parameters of the minimum RMSE (second data set) was chosen to calculate the cell voltage and the RMSE of the entire data set. Figure 5-3 shows the results of the applied procedure to assess the estimated parameters of equation (5-5). The second set gives the best results (red circle) and was finally used to predict the voltage over the entire data set.

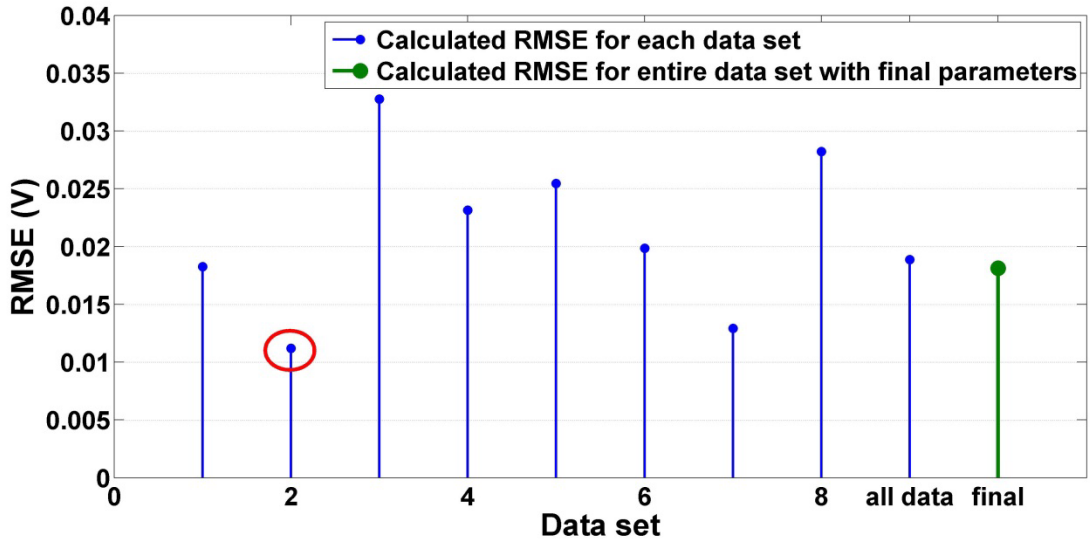


**Figure 5-3: Comparison of the calculated RMSE based on the nine data sets**

Table 5-2 presents the parameters based on the second set of data, which gave the most accurate result (RMSE=18.1 mV) and were consequently used for the further study.

**Table 5-2: Parameters to calculate the cell voltage of the electrolyser**

| Parameter | Value | Description |
|---|---|---|
| $r_1$ | $1.0862*10^{-4}$ Ωm² | related to the ohmic resistance |
| $r_2$ | $-3.8508*10^{-8}$ Ωm²/°C | |
| $s$ | 0.3469 V | related to the overvoltage at the electrodes |
| $t_1$ | 0.0024 m²/A | |
| $t_2$ | -0.1898 m²°C/A | |
| $t_3$ | 38.4971 m²°C²/A | |

Figure 5-4 compares the predicted cell voltage with measured data at two different temperatures. The blue curve shows the predicted cell voltage at a temperature of 40°C and 28 bar; the measured data are illustrated by blue circles. In addition, the results of the three terms of equation (5-5) are visualised for 40°C and 28 bar. The green, red and magenta line presents the reversible voltage, ohmic overvoltage and electrode overvoltage, respectively. For comparison the black dotted line shows the predicted voltage at a temperature of 80°C and 28 bar; the black rhombus mark the measured data. As expected the cell voltage at 80°C is much lower due to the lower internal resistance.

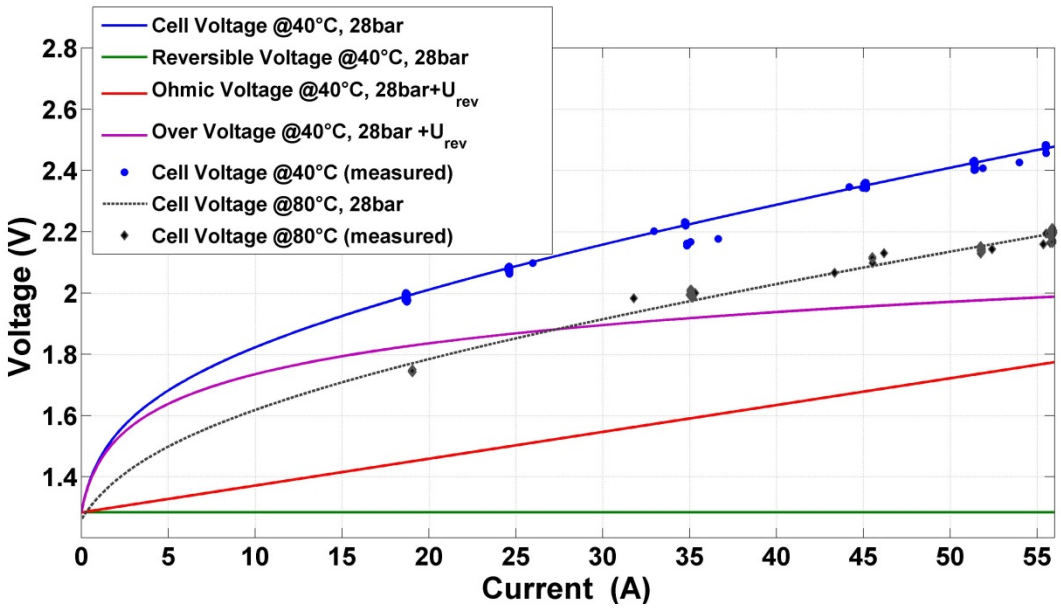


**Figure 5-4: Electrolysis voltage of a single cell at 40°C and 80°C.**

The stack voltage is easily calculated by multiplying the cell voltage by the number of cells $n_{cells}$ of the electrolyser ($n_{cells} = 50$):

$$U_{Stack} = n_{cells} * U_{cell} \quad \textbf{(5-6)}$$

The thermodynamic and electrical model is composed of equations (5-1), (5-2), (5-3), (5-4), (5-5) and (5-6).

### *5.2.1.2 Electrolyser: Thermal model*

As shown in chapter 4.1.1 the performance of electrolyser is significantly influenced by the temperature. The prediction of the electrolysis voltage, equation (5-5), is directly connected to the temperature. For the overall model an accurate prediction of the electrolysis temperature is very important. Heat is generated inside of the cell stack due to inefficiencies of the electrolysis process caused by the over-potentials. The heat is accumulated within the thermal mass of the system; mainly in the volume of electrolyte resulting in a temperature increase. At the same time heat is partly transferred to the ambient by heat conduction and convection, and by the two gas streams leaving the system. In addition, heat is also removed by the cooling system to maintain the defined operating temperature.

Figure 5-5 illustrates to the left the basic process layout of the electrolyser. The cell stack consists of two chambers. The inner chamber contains the electrolysis cells and is connected by a piping system

to the electrolyte vessels. This chamber is surrounded by an outer chamber filled with demineralised water. The pressure of the outer chamber is always greater than that in the inner chamber. During operation the gases produced flow through the pipes into the KOH vessels. The electrolyte outlet is located in both KOH vessels at the middle. The electrolyte streams from the vessels through the pipes (outlet at the bottom of the vessel) into the cell stack. One heat exchanger is installed within each vessel to cool the electrolyte as described in section 4.1.1. The electrolyte temperature sensor (T) is installed at the stack outlet pipe of the hydrogen side. During operation electrolyte circulates between the cell stack and the two vessels. The electrolyte flow depends on the temperature difference of the electrolyte between the cell stack and vessels (buoyancy force) and on the gas production rate. The higher the gas production, the more amount of electrolyte is dragged with the gas bubbles to the vessel where the gas is separated from the liquid. Both effects cause a natural circulation of the electrolyte without any need of pumps. Taking into account all physical phenomena in the thermal and hydraulic electrolyser system, the mathematical model would include a complex energy and mass balance to describe the spatial and temporal distribution of the temperature with many unknown parameters.

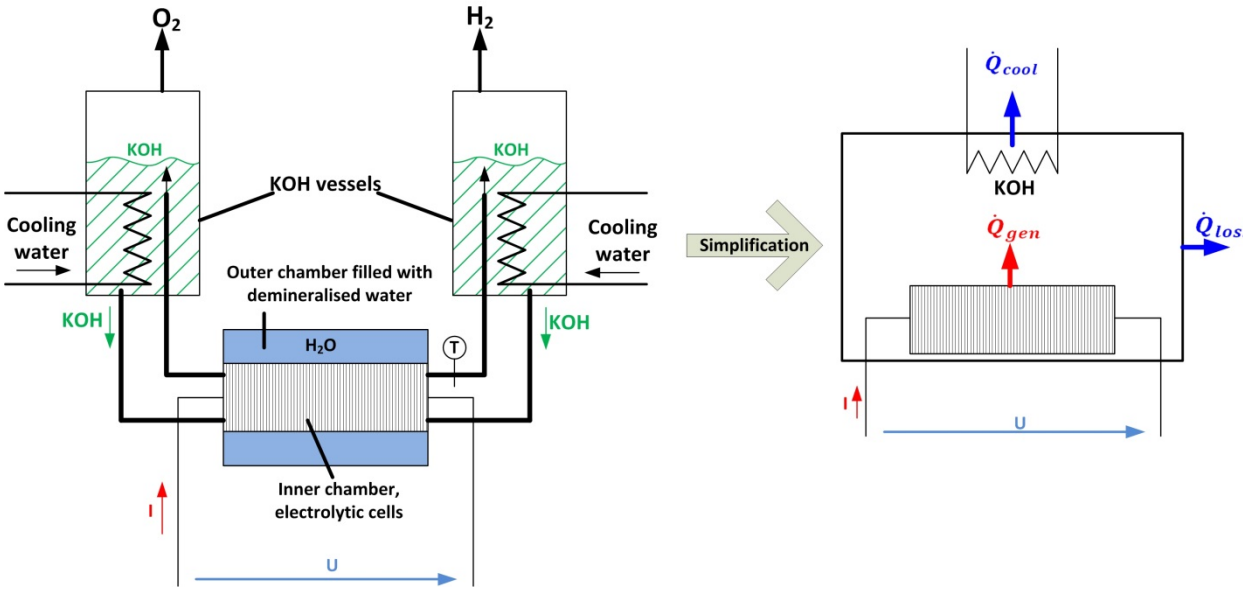


**Figure 5-5: Basic schematic of the electrolyser (left) including cell stack, electrolyte vessels with integrated heat exchangers and temperature sensor (T); simplified layout of the thermal model (right).**

For instance, the amount of electrolyte pushed from the cell stack into the vessels due to the generated gas bubbles is difficult to determine. Therefore, as a first approximation of the thermal system, a lumped thermal capacity model (Çengel 2003) is introduced. This simplification is illustrated on the right side of Figure 5-5. In this model, the electrolyser is assumed to be one body with uniform temperature distribution and the temperature is only a function of time. Similar

approaches have already been presented in previous works by Ulleberg (1998; 2003), Roy (2006) and Dieguez et al. (2008).

The system boundary around the process as illustrated in Figure 5-5 gives the thermodynamic control volume containing the cell stack, the two electrolyte vessels and the piping system. A calculation of the enthalpy streams of the two gases leaving the electrolyser amounts to an aggregated heat loss of less than 2% of total generated heat at maximum DC current. Thus, the gas streams leaving the system are neglected in the thermal analysis. The equation of the heat balance of the unsteady process can be written as:

$$C_{ele} * \frac{dT}{dt} = \dot{Q}_{gen} - \dot{Q}_{cool} - \dot{Q}_{loss} \quad \textbf{(5-7)}$$

where, $C_{ele}$ is the accumulated heat capacity (J/K) of the electrolyser system, $\dot{Q}_{gen}$ is the generated heat (W) according to equation (4-6), $\dot{Q}_{cool}$ is the heat (W) removed by the cooling system and $\dot{Q}_{loss}$ summarises the heat losses (W) to the ambient. The thermal energy stored in the mass of the electrolyser corresponds to the temporal derivative of the temperature (*dT/dt*) multiplied by the heat capacity.

If the electrolyte exceeds the maximum temperature (=75°C), heat will be removed by the cooling system. The cooling rate of the two heat exchanger installed inside of the vessels can be calculated by:

$$\dot{Q}_{cool} = U_{hx} * A_{hx} * LMTD = \dot{m}_{cw} * c_{cw} * (T_{cw,out} - T_{cw,in}) \quad \textbf{(5-8)}$$

where, $U_{hx}$ is the overall heat transfer coefficient of the heat exchanger $(\mathrm{W}/(\mathrm{m}^2 * \mathrm{K}))$, $A_{hx}$ is the surface area of the heat exchanger (m²), *LMTD* is the logarithmic mean temperature difference in K (Çengel 2003), $\dot{m}_{cw}$ is the mass flow rate (kg/s) of the cooling water, $c_{cw}$ is the specific heat capacity $(\mathrm{J}/(\mathrm{kg} * \mathrm{K}))$ of the cooling water, $T_{cw,out}$ and $T_{cw,in}$ is the outlet and inlet temperature of the cooling water (°C), respectively.

The heat loss $\dot{Q}_{loss}$ comprises all heat transfer mechanisms to the ambient such as convection and conduction from the inside of the electrolyser through the walls to the surrounding air, the enthalpy streams of the gases as well as possible heat losses due to radiation. Heat losses to the ambient can be expressed by:

$$\dot{Q}_{loss} = \frac{1}{R_{th}} * (T_{ele} - T_{amb}) \quad \textbf{(5-9)}$$

where, $R_{th}$ is the total thermal resistance (K/W) of the electrolyser, $T_{ele}$ is the temperature inside (°C) of the control volume and $T_{amb}$ is the ambient temperature (°C).

To estimate the total thermal resistance $R_{th}$ several experiments were conducted at low DC currents to obtain a steady state temperature without any need of cooling water. A steady state was only reached during experiments where the operational parameters were modified. It was necessary to extend the operational limits by modifying parameters of the electrolyser control system. The minimum DC current was set from 18 A to 13 A and the maximum operating temperature was set from 75°C to 86°C.

At steady state equation (5-7) can be simplified to:

$$\dot{Q}_{gen} = \dot{Q}_{loss} = \frac{1}{R_{th}} * (T_{ele} - T_{amb}) \quad \textbf{(5-10)}$$

Accordingly, the generated heat and the heat loss to the ambient are in equilibrium at steady state. Then the total thermal resistance can be calculated dividing the temperature difference by the generated heat. Figure 5-6 shows the measured heating curve and DC current. As explained in section 4.1.1 the electrolyser follows a starting sequence before the DC current can be controlled. It can be seen from Figure 5-6 that the temperature rapidly raises from 25°C to 42°C at high DC currents and slowly increases with lower currents. Steady state operation was assumed after 9.2 hours of operation. The total thermal resistance was calculated by averaging the measured stack voltage, DC current, electrolyte temperature and ambient temperature over a period of 2 hours. Average heat generation at steady state was approximately 100 W calculated by equation (4-6) and the average temperature difference was 62.7 K. This gives an average total thermal resistance of 0.627 K/W.

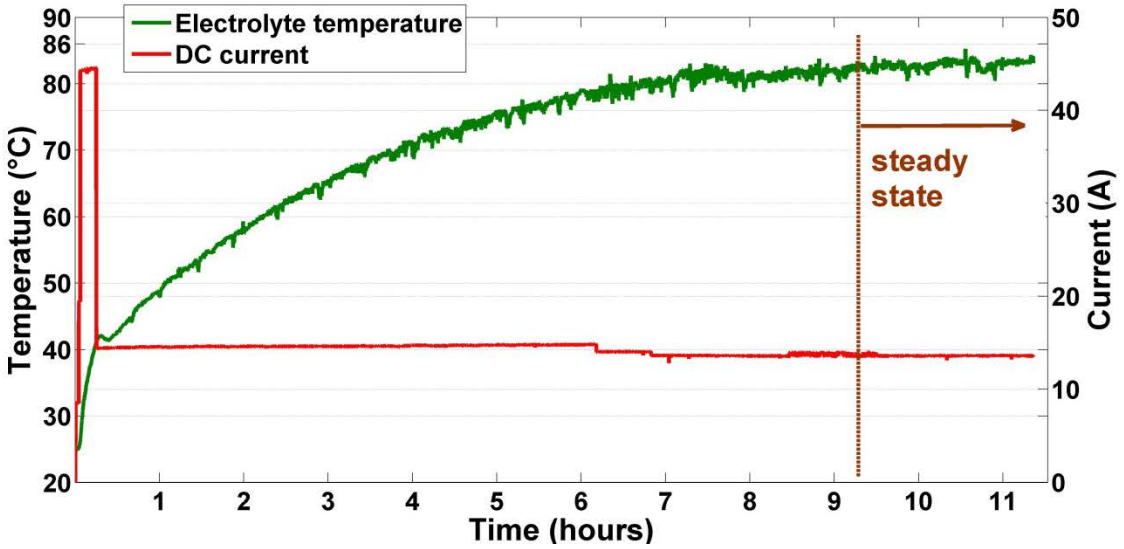


**Figure 5-6: Measured electrolyte temperature (green line) at low DC current (red line). Steady state was assumed after 9.2 hours.**

Once the total thermal resistance is calculated, the lumped thermal capacity $C_{ele}$ can be derived from the measured data by rearranging equation (5-7) to

$$\frac{dT}{dt} = \frac{\dot{Q}_{gen} - \dot{Q}_{loss}}{C_{ele}} \quad \textbf{(5-11)}$$

and using the Euler method to calculate the temperature inside of the electrolyser (initial value = $T_{measured}(1)$) for the next time step from values of the actual time step:

$$T_{ele}(i+1) = T_{ele}(i) + \frac{time\ step}{C_{ele}} * \left(\dot{Q}_{gen}(i) - \dot{Q}_{loss}(i)\right) =$$

$$T_{ele}(i) + \frac{time\ step}{C_{ele}} * \left(\left(U_{stack}(i) - n_{cells} * U_{th}(i)\right) * I(i) - \frac{1}{R_{th}} * \left(T_{ele}(i) - T_{amb}(i)\right)\right) \quad \textbf{(5-12)}$$

Based on the measured data (time step = 1 second) of the steady state experiment a regression analysis was carried out with MATLAB to approximate the value of $C_{ele}$ and was found to be 66 kJ/K. To validate the findings of $R_{th}$ and $C_{ele}$, another set of measured data (stack voltage, DC current and ambient temperature) of a heating experiment at maximum DC current (56 A) was used to predict the temperature inside of the electrolyser system. The results revealed that the model over predicts the temperature increase; the calculated mean absolute percentage error (MAPE), see equation A-2 in the appendix, was 20%. Hence, either the approximated values are imprecise or other dependencies need to be considered when evaluating $R_{th}$ and $C_{ele}$ for a simplified modelling approach. In particular difficulties arise in considering the spatial and temporal distribution of the temperature within the electrolyser system during dynamic operation, for example start-up and load changes. Analysing the temperature profile distribution and the associated heat flux density in more detail would require a more complex experimental set-up. However, such in-depth thermal analysis was out of scope of this thesis. Nevertheless, to consider the temperature evolution during dynamic operation the following experimental methodology is proposed.

A series of heating curves at different DC current rates were conducted to analyse the thermal behaviour in more detail. Figure 5-7 illustrates the heating curves of six experiments at constant current rates (13 A, 18 A, 24 A, 36 A, 45 A and 56A). The graph only depicts the temperature evolution between the time instant when the electrolyser transited into operation (constant DC current) and it reached the maximum operating temperature of 75°C.

As illustrated in Figure 5-7 the temperature gradient (*dT/dt*) decreases with decreasing DC current. Moreover, it can be recognised that after the DC current is set from 45 A (fixed start sequence of the electrolyser, see Figure 4-2) to lower production rates (34 A, 24 A, 18 A and 13 A) at t=0, a time delay occurs before the temperature increases again. An explanation for this can be the higher electrolyte flow rate due to the higher DC current at the end of the start sequence and the momentum of the hydraulic circle. A certain period of time elapses before the mass flow rate is slowed down to a steady value. Furthermore, the lower the mass flow rate of the electrolyte, the lower the mixture of the fluidic system and less electrolyte enters the cell stack. Moreover, the variable flow rate inside of the electrolyser also affects the heat convection from the electrolyte to the inner surface of the cell stack, the pipes and the two vessels. A higher flow rate and higher gas production will result in a higher heat convection coefficient at the inner surface.

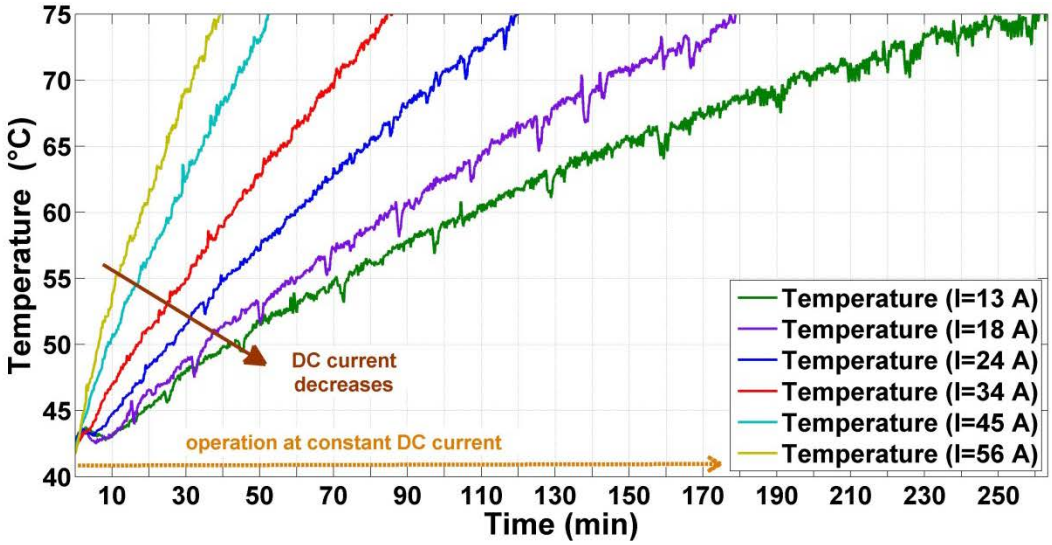


**Figure 5-7: Heating curves obtained from experiments at different constant current rates as a function of time.**

Since the aim of the electrolyser system is to store electrical energy produced from renewable energy systems, the operation is more dynamic. It is therefore crucial to consider the above described effects in the thermal model to accurately predict the temperature evolution. Empiric parameters, namely the effective thermal capacity $C_{ele,eff.}$ and the dynamic total thermal resistance $R_{th,dyn.}$ are introduced below aiming to take into account the spatial and temporal temperature distribution. Based on the experimental observations, the conclusion can be made that the effective thermal capacity increases and the dynamic total thermal resistance decreases with increasing DC current.

Considering the described effects and defining an upper limit of 0.627 K/W of the total thermal resistance and a lower limit of 66 kJ/K of the heat capacity derived from the steady state experiment

at the lowest DC current, a regression analysis was conducted to approximate the two parameters ($R_{th,dyn.}$ and $C_{ele,eff.}$) from a series of heating curves at constant DC current. The basic idea is to collect measured data ($U_{stack}$ and $T_{ele}$) at constant DC current from heating up experiments as shown in Figure 5-7, then $R_{th,dyn.}$ and $C_{ele,eff.}$ are estimated by using the *lsqcurvefit*-function and a MATLAB script containing equation (5-12) to predict the electrolyser temperature evolution with respect to the calculated temperature gradient derived from the data presented in Figure 5-7. The results of the analysis are presented in Figure 5-8. As shown in the left graph, the dynamic total thermal resistance (blue dotted line) declines with increasing current. The right graph illustrates the estimated effective thermal capacity (red dotted line) at constant DC current. It can be clearly noticed that the capacity first increases (transient area where the temperature profile is not fully developed) then stabilises at a value of 120 kJ/K.

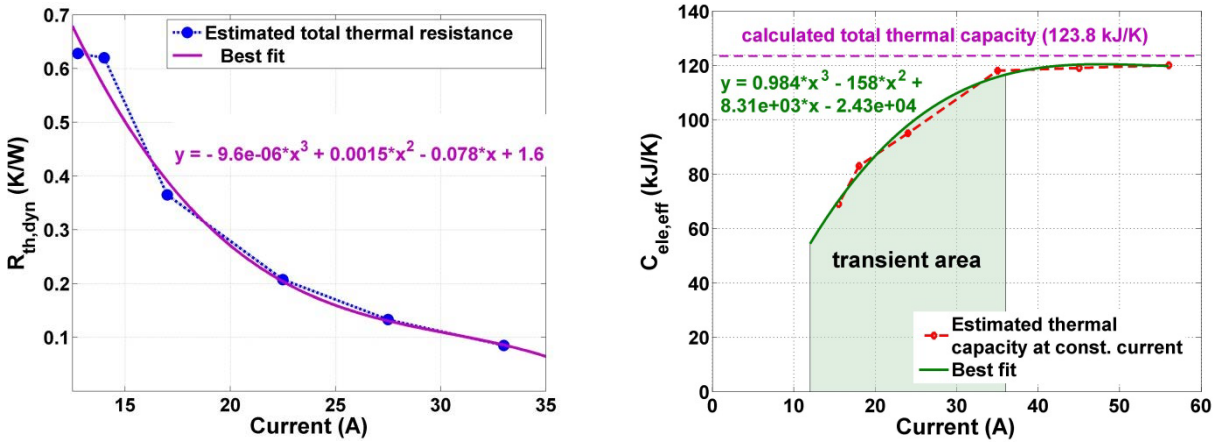


**Figure 5-8: Estimated total thermal resistance (left) and thermal capacity (right) as a function of the DC current.**

This value agrees well with the calculated total thermal capacity of 123.8 kJ/K by means of the physical data of the main components of the electrolyser: the electrolyte (approx. 30 kg of 30 wt% KOH), the two vessels and the cell stack (together approx. 70 kg of stainless steel 1.4404). The specific heat capacity of KOH ($c_{KOH,30\%} = 2.96\ \mathrm{kJ/(kgK)}$) was derived from (Poling 2008) and the specific heat capacity of stainless steel ($c_{steel,1.4404} = 0.5\ \mathrm{kJ/(kgK)}$) was taken from (DEW 2008). Both results support the above formulated hypothesis.

The DC current dependence of the dynamic total thermal resistance and the effective thermal capacity were subsequently approximated by a polynomial as shown in the two graphs of Figure 5-8:

$$R_{th,dyn.} = a_1 I^3 + a_2 I^2 + a_3 I + a_4 \qquad \textbf{(5-13)}$$

$$C_{ele,eff.} = a_1 I^3 + a_2 I^2 + a_3 I + a_4 \qquad \textbf{(5-14)}$$

The constant coefficients of the polynomials, valid within the operating range of 18 A to 56 A, are given in Table 5-3.

**Table 5-3: Approximated parameters for the calculation of $R_{th,dynamic}$ and $C_{ele,effective}$**

| Parameter | $\mathbf{a_1}$ | $\mathbf{a_2}$ | $\mathbf{a_3}$ | $\mathbf{a_4}$ |
|---|---|---|---|---|
| $R_{th,dyn.}$ | $-9.6 * 10^{-6}$ K/(WA$^3$) | $1.5 * 10^{-3}$ K/(WA$^2$) | $-0.078$ K/(WA) | 1.6 K/W |
| $C_{ele,eff.}$ | 0.984 J/(KA$^3$) | $-158$ J/(KA$^2$) | 8310 J/(KA) | $-24300$ J/K |

To validate the thermal model a comparison of the measured temperature (taken from a heating-up experiment including the start-up and then operating at constant DC current of 24.5 A) and the temperature predicted by MATLAB considering the above described findings is presented in the top diagram of Figure 5-9. As shown, the thermal model based on equation (5-7) and the polynomial approximation of $R_{th,dyn.}(I)$ and $C_{ele,eff.}(I)$ can predict the temperature of the heating-up period (T<=75°C) with good accuracy. Subsequently, the evolution of the generated heat (4-6) and the heat losses to the ambient (5-9) are illustrated.

The correlation between the DC current and both the total thermal resistance and the thermal capacity are interesting because the studies presented by Ulleberg (1998; 2003), Roy (2006) and Dieguez et al. (2008) have not considered this dependency. For instance, Ulleberg (1998; 2003) derived the value of the thermal resistance and the thermal capacity from the cooling pattern of the electrolyser. Roy (2006) introduced an empirical equation considering a constant heat transfer rate due to convection and calculated the thermal capacity from the physical data of the components. Dieguez et al. (2008) determined the thermal capacity from a heating up experiment at maximum DC current and the total thermal resistance from steady state operation at low DC currents. Consequently, the thermal performance at low DC current would be underestimated, which would negatively affect the energy efficiency of electrolyser systems.

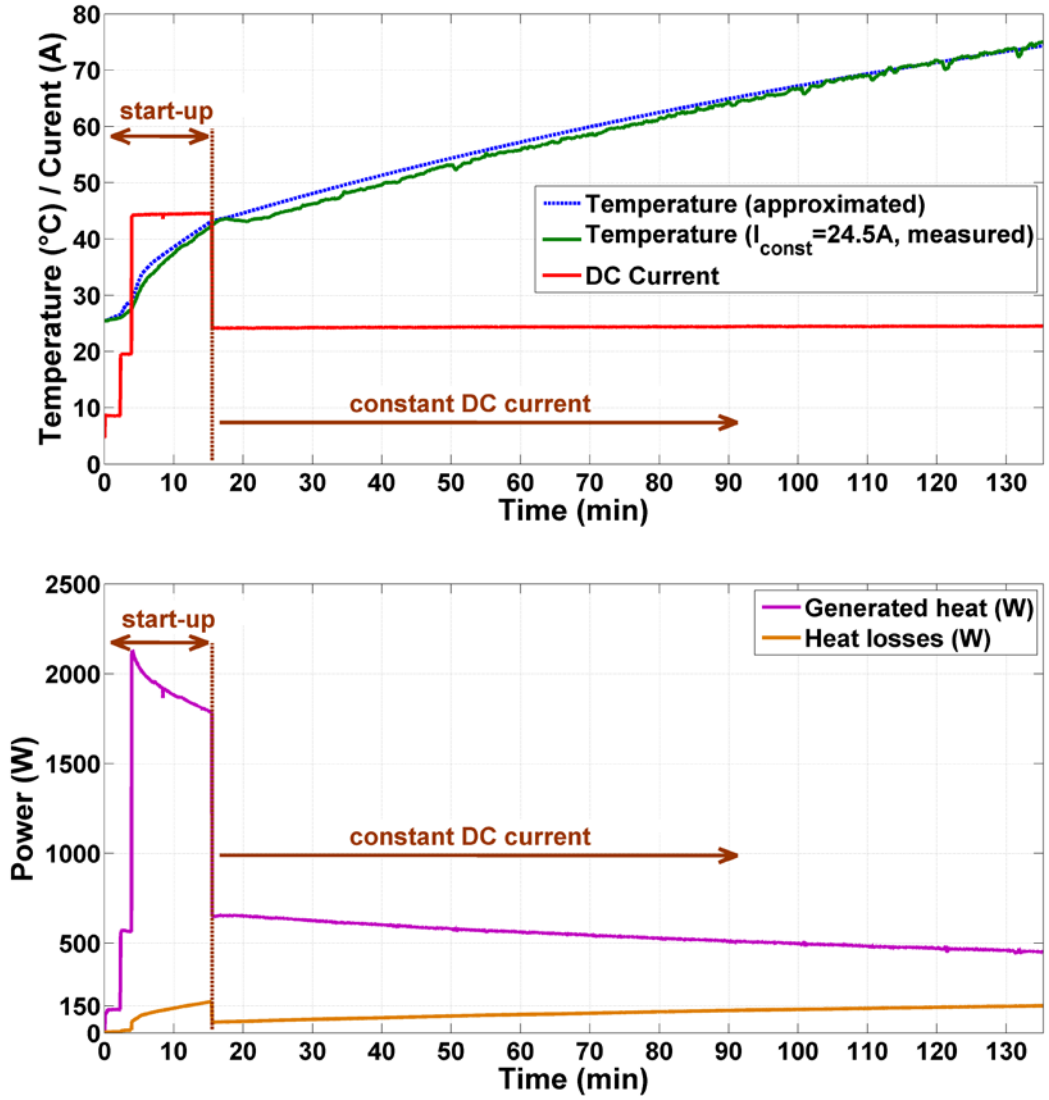


**Figure 5-9: Comparison of predicted temperature (blue dotted line) and measured temperature (green line) of the electrolyser.**

The thermal model of the electrolyser composed of equations (5-7), (5-8), (5-9), (5-13) and (5-14) are implemented in Simulink. Input variables to the model are the ambient temperature, the thermo neutral voltage, the cell voltage, the number of cells and the DC current. Output variables are the electrolyser temperature and the generated heat, the heat loss and the heat removed by the cooling system. Required parameters of the heat exchangers in equation (5-8) are derived from literature and from data provided by the manufacturer.

#### *5.2.1.3 Electrolyser: Hydrogen production and hydrogen storage model*

Based on Faraday's law of electrolysis the hydrogen and oxygen production of the electrolyser can be calculated by equation (4-8). It has been proven by Ulleberg (1998; 2003) and Roy (2006) that typical

values of the Faraday efficiency at stack level are above 90% at nominal current rates. As discussed in section 4.1.1, not all of the produced hydrogen is useable. Losses occur in the Accagen SA electrolyser system due to the analyses of the oxygen content in the hydrogen stream, the removal of oxygen traces in the de-oxidation unit, where hydrogen and oxygen react to water vapour, the regeneration process of the standby dryer and finally due to leaks in the pipes. Considering all losses the hydrogen flow rate $\dot{n}_{H_2}$ can be calculated by:

$$\dot{n}_{H_2} = \eta_{Faraday} * \dot{n}_{theo} \quad \textbf{(5-15)}$$

A function of the system Faraday efficiency $\eta_{Faraday}$ is approximated based on the data presented in Figure 4-4 and is implemented into Simulink together with equation (4-8) and (5-15).

As explained in section 4.1.1 the electrolysis takes place at a pressure above 25 bar. To predict the internal system pressure *p* of the electrolyser the ideal gas law is applied:

$$\frac{dp_{system}}{dt} = \frac{\dot{n}_{H_2} * M_{H_2} * R_i * T_{ele}}{V} \quad \textbf{(5-16)}$$

where, $R_i$ is the specific gas constant ($R_{H_2} = 4124.5\ \mathrm{J/(kgK)}$), $M_{H_2}$ is the molar mass of hydrogen (=2.0159 kg/kmol) and $V$ is the internal volume (≈0.01m³) by means of the space above the liquid level inside of the KOH separator and the pipes. The pressure balancing mechanism between the hydrogen and oxygen electrolyte vessel as illustrated in Figure 4-2 is neglected in this study. The maximum pressure in the model is set to 30 bar. The input variables of the internal pressure model based on (5-16) are the DC current and the electrolyser temperature. Output variables are the hydrogen flow rate and the internal pressure.

The external gas storage is modelled separately, thus, it is not part of the electrolyser model. However, it is also derived from the ideal gas law. Hence, the pressure inside of the gas tanks is predicted by equation (5-14). The volume of the gas storage is 0.6 m³ and the temperature is assumed to be constant at 25°C. The input variable of the storage model is the hydrogen rate produced by the electrolyser or consumed by the fuel cell. The output variable is the pressure inside of the storage (max. 30 bar).

#### *5.2.1.4 Electrolyser: System control model*

So far the electrical and thermal model of the electrolyser has been discussed in detail. Both proposed models consider the electrical and thermodynamic characteristics of the electrolysis process. However, a model applied at system level should also include operational aspects as well to

mimic the physical system behaviour. As stated previously, the electrolyser is equipped with a PLC that monitors and controls the process. System constraints such as the minimum operational DC current or operational states, for example, the start-up process of the electrolyser are predefined within the PLC program and were identified in section 4.1.1. An event driven discrete sub-model is introduced below to reflect operational aspects. In addition, this model contains a local control loop to regulate the DC current depending on the AC power set-point, which is the input variable of the overall system model. A simplified layout of the proposed sub-model is shown in Figure 5-10. The inputs to the model are the variable "System on", the AC power set-point, the DC power, the internal pressure and the storage pressure. The output variables are the DC current and the system state.

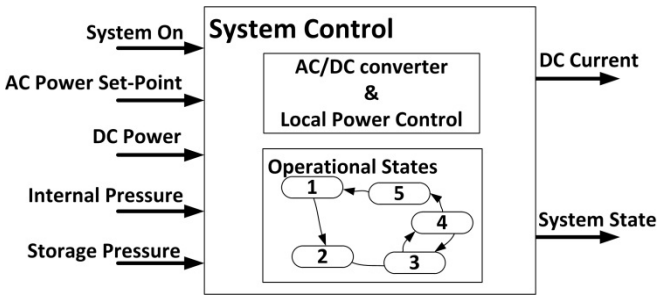


**Figure 5-10: Layout of the sub-model "system control"**

Five different system states were identified experimentally, the "off", the "startup", the "operation", the "standby" and the "blow-down" process. Together with operational constraints, for instance, the minimum DC current, the statechart, as illustrated in Figure 5-11, was developed using the MATLAB® toolbox Stateflow®. Starting from the "off" state the electrolyser can be transited into the "startup" if the external power set-point exceeds the defined minimum power and the system is switched on (variable "system on). Then the predefined sequential startup process is executed. If the internal pressure model gives a value of 25 bar the "Operation" state will be activated. This state is kept active as long as the AC power set-point is above the minimum power threshold (variable "minimum power") and the storage pressure is below 30 bar or the system is switched off (variable "SystemOn"=0). While the system stays in normal operation, the local control loop is active and the DC current can be regulated between 18 A and 56 A. The corresponding Stateflow® diagram of Figure 5-11 is shown in Figure A-6.

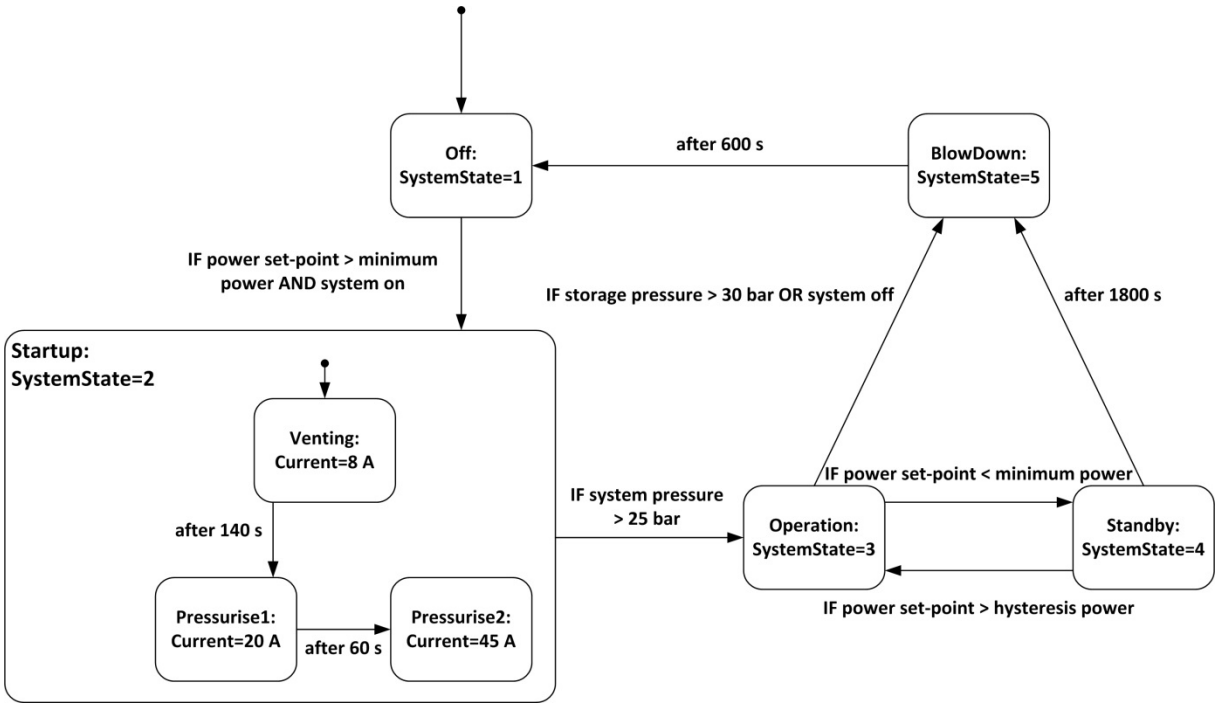


**Figure 5-11: Operational behaviour model developed in Stateflow®**

In case that the AC power set-point drops below the defined minimum power, the electrolyser enters the “standby” state. From this state the system can be instantaneously transited back into the normal operation mode if the power set-point exceeds a threshold (variable “hysteresis power”). If the system remains longer than 1800 seconds in “Standby” state, a timer elapsed and the electrolyser enters the “blowDown” process and the internal pressure is set back to atmospheric pressure. From the basic characterisation of the real system it was determined that the blow down process takes approximately 600 seconds, before the electrolyser enters the “Off” state.

In addition to the Stateflow® model, the system control sub-model contains also a local control loop. The set-point of the implemented PI controller is the AC power, the measured value is the AC power consumption of the electrolyser and the DC current is the manipulated variable. For simplification the AC power of the electrolyser is calculated by multiplying the predicted stack voltage (equations (5-5) and (5-6)) with the DC current and the reciprocal value of the averaged efficiency of the installed AC/DC converter (90%).

### *5.2.1.5 Integrated electrolyser model and validation*

Together the four sub-models form the integrated system model of the electrolyser. The inputs are the power set-point and the on/off command. The output variables are the consumed power, the system state, the generated heat, the outlet temperature of the cooling water and the mass flow rate of the produced hydrogen. As mentioned before, the sub-models are interconnected with each other. For example, the thermodynamic and electrical sub-model depends on the temperature predicted by the thermal sub-model, on the internal pressure provided by gas production and internal storage model, and the system control model. Table 5-4 gives an overview of the main variables exchanged between the four sub-models.

**Table 5-4: Variables exchanged between the four sub-models**

| Sub-model | *Variable* | Thermodynamic and electrical model | Thermal model | Gas production and internal storage model | System control model |
|---|---|---|---|---|---|
| Thermodynamic and electrical model | $U_{th}$ | | X | | |
| | $U_{stack}$ | | X | | |
| | $P_{DC}$ | | | | X |
| Thermal model | $T_{ele}$ | X | | X | |
| Gas production and internal storage model | $p_{system}$ | X | | | X |
| System control model | $I_{DC}$ | X | X | X | |
| | *SystemState* | | | X | |

To validate the continuous behaviour of the integrated electrolyser model, the system control was deactivated. The simulation inputs were the measured values (sampling time = 1 second) of the DC current and the ambient temperature. The data were taken from a DC current step-down experiment including a start-up sequence and the data were not involved in the model development process. In total, the experiment was carried out for 390 min. Figure 5-12 illustrates the response of the model. The top diagram of Figure 5-12 compares the predicted cell voltage (dotted magenta line) with the measured cell voltage (blue line). The lower graph of Figure 5-12 shows the predicted (dotted magenta line) and the measured (green line) temperature. After the start-up the DC current was set to 56 A and was kept constant for about 90 minutes before the DC current was reduced step-wise every 60 minutes to 18 A. After about 50 minutes the temperature reached the maximum operating values of 75°C and the two-point controller starts to regulate the temperature by opening and

closing the cooling water valve (cooling water inlet temperature was assumed to be constant at 10°C, the flow rate was set to 0.17 kg/s).

To assess the accuracy of the model the RMSE and the absolute MAPE were calculated, see equations (A-1) and (A-2) in the appendix. The simulated cell voltage is illustrated in the top diagram and shows a quite good agreement (RMSE=25.5 mV, MAPE=1%) with the measured voltage. At lower DC currents though the measured voltage oscillates more than in higher DC current regions. This is due to the temperature regulation as it can be seen in the lower graph. Uncertainties remain within the modelled temperature control system and the proposed simplification of the thermal model. In particular at lower DC current regions the deviation starts to increase. However, the simulated temperature shows a plausible behaviour with an acceptable accuracy (RMSE= 2.3°C, MAPE=2.7%).

If the total thermal resistance and the thermal capacity were only derived from the cooling pattern of the electrolyser or from operating at maximum DC current, the heat convection losses would be overestimated at lower DC currents and the temperature would never reach its normal operating condition again. As a result, the internal resistance would increase. For clarification Figure 5-12 shows also the temperature evolution of the electrolyser predicted with a simplified model (black dotted line in the lower diagram). The values of the thermal capacity ($C_{ele} = 123.8\,\mathrm{kJ/K}$) were derived from the physical data of the main components and the thermal resistance ($R_{th} = 0.1\,\mathrm{K/W}$) from the cooling pattern of the electrolyser. As can be seen, at lower DC currents the temperature starts to decrease, which negatively influence the performance.

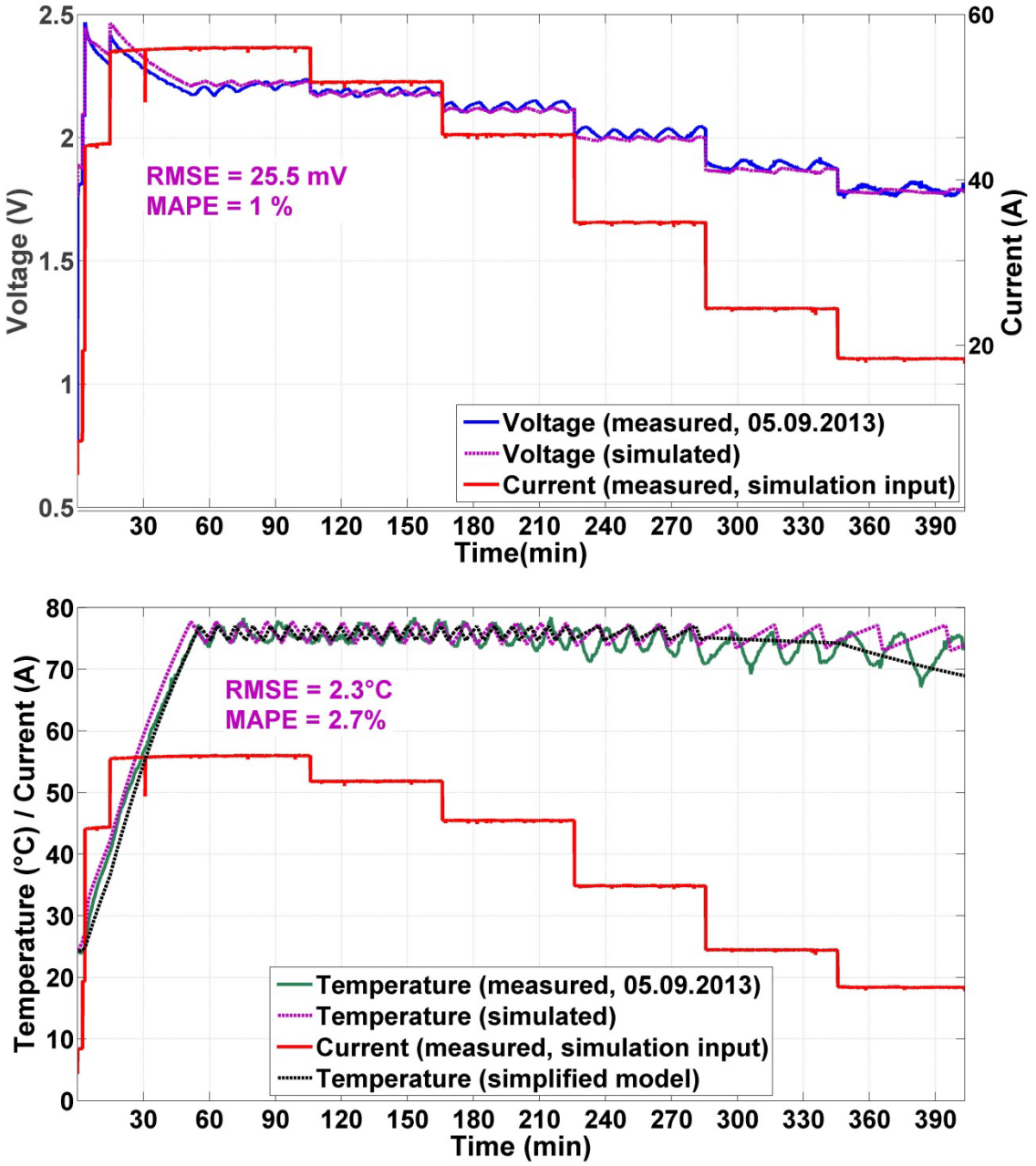


**Figure 5-12: Model response to measured DC current (red line) during a step-down experiment.**

### 5.2.2 System model of the fuel cell

The following section presents the system model of the NEXA 1200™ fuel cell. The electrical model is derived from measured data to describe the current-voltage curve of the fuel cell stack. In addition, a thermal model, a hydrogen consumption model, a system control model and an integrated model are presented.

#### *5.2.2.1 FC: Electrical model*

As shown in section 4.2.1 the output voltage of a fuel cell system depends on the applied DC current and the theoretical possible open circuit voltage is reduced due to irreversibilities. The four major irreversibilities are namely the activation losses, the fuel crossover and internal current losses, the ohmic losses and the mass transport or concentration losses (Larminie & Dicks 2003). To model the phenomena taking place in a fuel cell stack several approaches have been proposed in the literature (Cheddie & Munroe 2005). For energy system analysis semi-empirical models are typically applied to predict the operating voltage depending on the DC current. Saadi et al. (2013) compared three different static model approaches which are frequently used in simulation studies. All three approaches can be assigned to the semi-empirical models and rely on parameters derived from experimental data. One of the three discussed models was initially proposed by Kim et al. (1995) and contains the least number of parameters. It describes the steady-state fuel cell stack voltage $U_{stack}$ depending on the applied current $I_{stack}$ with only five parameters ($U_{OCV}$, *b*, *R*, *m* and *n*):

$$U_{stack} = n_{cells} * \left( \underbrace{U_{OCV}}_{open\ cicuit\ voltage} - \underbrace{b * \ln(I_{stack})}_{activation\ losses} - \underbrace{R * I}_{ohmic\ losses} - \underbrace{m * e^{(n*I_{stack})}}_{concentration\ losses} \right) \quad \textbf{(5-17)}$$

where, $n_{cells}$ is the number of cells, $U_{OCV}$ is the open circuit voltage (V), *b* is the slope in the Tafel equation (Larminie & Dicks 2003) to describe the activation voltage drop (V), *R* is the ohmic resistance (Ω) and *m*, *n* are constants considering voltage losses due to mass-transfer. As shown in Figure 4-12 the internal resistance of the fuel cell depends on the temperature and the water content of the membrane. With increasing current, the water production increases resulting in a better ionic conductivity and lower voltage losses (Jiao & Li 2011). Therefore, the internal resistance depends on the temperature, the DC current and on water management of the fuel cell. For simplification the internal resistance can be modelled as function of the DC current and the temperature (Wang, Nehrir & Shaw 2005). The following empirical equation is applied in this thesis to model the impact of the temperature on the internal resistance:

$$R_i = kR_0 + \frac{kR_1}{T_{stack} * (I_{stack} + 1)} + I_{stack} * kR_2 \quad \textbf{(5-18)}$$

where, $kR_0$, $kR_1$ and $kR_2$ are empirical constants, $T_{stack}$ is Fuel Cell temperature (°C) and $I_{stack}$ is the DC current (A).

To determine the unknown parameters of equation (5-17) and (5-18) a regression analysis was carried out using the *lsqcurvefit* function of MATLAB. The procedure to estimate the parameters was similar to the analysis presented in the previous section. Data from step-climbing experiments (2*8023 data points, 1 second interval), as illustrated in Figure 4-13, was taken to approximate the parameters. The measured stack current and temperature were passed to a coded MATLAB script to obtain the seven coefficients of the model. In low current regions the influence of the concentration losses, the fourth term in (5-17), can be neglected (Ulleberg 1998; Saadi et al. 2013). Consequently, the coded script contains a piecewise function considering a low (<35A) and a high current region (≥35A).

$$U_{stack} = \begin{cases} n_{cells} * (U_{OCV} - b * \ln(I_{stack}) - R_i * I), & I_{stack} < 35\ \text{A} \\ n_{cells} * \left(U_{OCV} - b * \ln(I_{stack}) - R_i * I - m * e^{(n * I_{stack})}\right), & I_{stack} \geq 35\ \text{A} \end{cases} \quad \textbf{(5-19)}$$

The obtained parameters of the studied PEM fuel cell are given in Table 5-5. Regarding the ohmic resistance for an operating point at 60°C/60 A the result of equation (5-18) is 0.0033 Ω. This value has a similar magnitude as findings reported by Kim et al. (2010) for a 1.2 kW Nexa power module (Ballard Power System Inc.) and San Martín et al. (2014) for a Heliocentris NEXA 1200™ PEM fuel cell.

**Table 5-5: Parameter of the steady-state electrical model.**

| $U_{OCV}$ (V) | $b$ (V) | $kR_0$ (Ω) | $kR_1$ (Ω/(°CA) | $kR_2$ (A) | $m$ (V) | $n$ ($A^{-1}$) |
|---|---|---|---|---|---|---|
| 1.05 | 0.052 | $1.6*10^{-3}$ | 5.63 | $1.69*10^{-6}$ | $4.61*10^{-5}$ | $72.6*10^{-3}$ |

The validation of the static electrical model was conducted by means of the I-U curve experiment shown in Figure 4-12. In this experiment the DC current drawn from the fuel cell was stepped from 0 A to 60 A with a ramp of 0.02 A/s and vice versa. As discussed in 4.2.1 the I-U curve shows a hysteresis effect due to the changing water content in the membrane. This effect is not considered in the model, thus, data of both I-U curves (increasing and decreasing current ramp) were averaged to get a mean current-voltage curve (magenta dotted line in Figure 4-12). The averaged data (2*2499 data points, sampling rate = 1 sec.) of the DC stack current and the fuel cell temperature were passed to the model to predict the stack voltage. Figure 5-13 compares the measured and the simulated

stack voltage. The simulation result obtained was quantified by calculating the RMSE (=127 mV) and can be considered to be satisfactory.

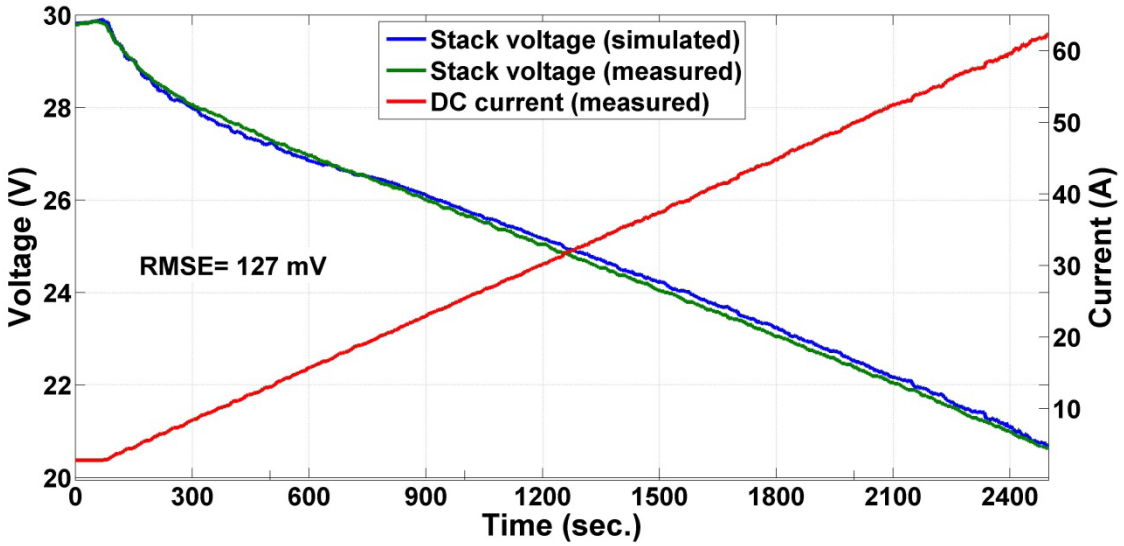


**Figure 5-13: Measured (green line) and simulated (blue line) voltage of the fuel cell. The DC stack current (red) was increased from 0-60A.**

The produced electricity is partly used to supply the BOP of the fuel cell system as described in section 4.2.1. This is modelled by means of a controlled current sink connected in parallel to the fuel cell stack. Using Kirchhoff's first law, the deliverable DC current to the loads can be calculated by subtracting the current drawn from the BOP from the generated fuel cell stack current. The power consumption of the BOP increases along with increasing DC current due to the increasing air fan speed to supply oxygen to the cells and to cool the system as graphed in Figure 4-13. A data analysis of step-climbing experiments revealed that the dependency of the peripheral current $I_{peripheral}$ to the stack current can be approximated by the following empirical equation:

$$I_{peripheral} = d_1 + d_2 * I_{stack} + d_3 * I_{stack}^2 \qquad \textbf{(5-20)}$$

where, d1, d2, d3 are empiric parameters. The calculated values of the empiric coefficients are listed in Table 5-6.

**Table 5-6: Empiric parameters to calculate the peripheral current.**

| ***d1*** **(A)** | ***d2*** **(-)** | ***d3*** **(1/A)** |
|---|---|---|
| 1.13 | $1.5*10^{-3}$ | $4*10^{-4}$ |

The electrical model implemented in Simulink® contains equations (5-18), (5-19) and (5-20).

### *5.2.2.2 FC: Thermal model*

As discussed in section 4.2.1 the fuel cell temperature is regulated by means of the DC current withdrawn from the fuel cell and the air supply fan. The simplified layout of the thermal model is illustrated in Figure 5-14. During operation the temperature increases due to the internal electrical losses. The generated heat $\dot{Q}_{gen}$ is partly stored in the thermal mass of the fuel cell and it is partly dissipated by thermal natural convection $\dot{Q}_{loss}$ and forced convection $\dot{Q}_{cool}$. The thermal modelling approach applied is also the lumped thermal capacity model.

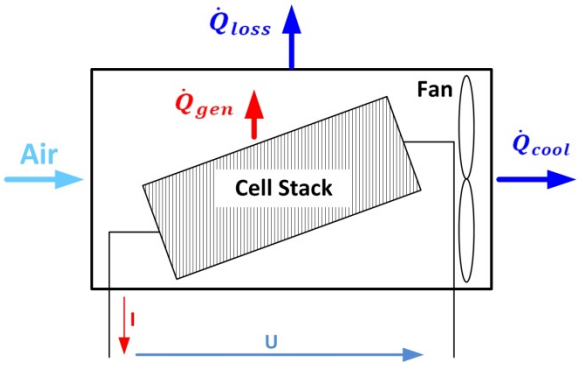


**Figure 5-14: Simplified layout of the thermal model**

The governing equation to predict the fuel cell temperature can be expressed by the following thermal energy balance:

$$C_{FC} * \frac{dT}{dt} = \dot{Q}_{gen} - \dot{Q}_{cool} - \dot{Q}_{loss}, \qquad \textbf{(5-21)}$$

where, $C_{FC}$ is the thermal capacity (W/K) of the fuel cell system. Considering that the heat removal by the air fan is dominant compared to the heat loss due to natural convection, the third term in equation (5-21) is neglected.

The generated heat can be calculated by

$$\dot{Q}_{gen} = I_{stack} * \left( n_{cells} * \left( \frac{-\Delta_f H^0 - \Delta_{vap} H}{z * F} \right) - U_{stack} \right) \qquad \textbf{(5-22)}$$

where, $\Delta_f H^0$ is the enthalpy of formation of water at standard conditions (-285.84 kJ/mol), $\Delta_{vap} H$ is the heat of vaporisation of water, *z* is the number of electrons transferred for each molecule and *F* is the Faraday constant. Water is formed at the cathode and is discharged by air streaming through the cell stack. The evaporation of water needs energy (latent heat) which is defined by the heat of vaporisation. $\Delta_{vap} H$, expressed in (kJ/mol), depends on the temperature and is approximated by a

linear function (5-23) derived from data of water steam presented, for instance, in (Cerbe & Wilhelms 2013) for a temperature range of 0-90°C:

$$\Delta_{vap}H = 45.05 - T_{FC} * 0.043 \quad \textbf{(5-23)}$$

where, $T_{FC}$ is the fuel cell temperature (°C).

Potential losses due to natural convection and radiation are considered in the second term, $\dot{Q}_{cool}$, in equation (5-21). The heat removal due to the temperature control system can be expressed by

$$\dot{Q}_{cool} = h_{FC} * (T_{FC} - T_{amb}) \quad \textbf{(5-24)}$$

where, $h_{FC}$ is the overall heat transfer coefficient (W/K) as a function of the stack current and $T_{amb}$ is the ambient temperature (°C). At steady state the generated heat is equal to the heat removed by the cooling system, consequently the overall heat transfer coefficient at different constant DC currents can be calculated by rearranging equation (5-21):

$$h_{FC} = \frac{I_{stack} * \left( n_{cells} * \left( \frac{-\Delta_f H^0 - \Delta_{vap} H}{z * F} \right) - U_{stack} \right)}{(T_{FC} - T_{amb})} \quad \textbf{(5-25)}$$

The calculation of the overall heat transfer coefficient was performed by evaluating the fuel cell temperature at different DC current rates. Experimental data from current step-climbing experiments, as illustrated in Figure 4-13, were analysed to obtain $h_{FC}$. The value of $h_{FC}$ can be determined by equation (5-25). Figure 5-15 shows the averaged values of $h_{FC}$ plotted against the DC current. Along with the increasing DC current $h_{FC}$ increases due to the increasing air fan speed. It was found that the DC current dependency of $h_{FC}$, expressed in (W/K), can be well approximated by a linear function (magenta line):

$$h_{FC}(I) = 0.59 * I_{stack} + 3.7 \quad \textbf{(5-26)}$$

The values of $h_{FC}$ are consistent with those reported by San Martín et al. (2014) for the same type of fuel cell system.

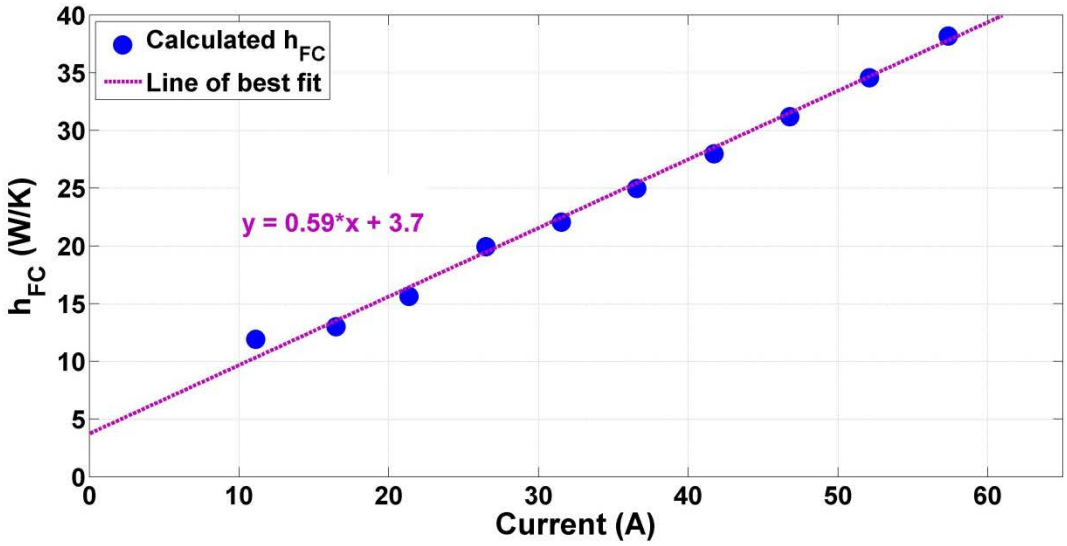


**Figure 5-15: Averaged overall heat loss coefficient (blue dots) obtained from current step-climbing experiments.**

Next, the thermal capacity of the fuel cell system needs to be determined to model the thermal behaviour. By rearranging equation (5-21) and applying the Euler method, the evolution of the fuel cell temperature can be expressed by:

$$T_{FC}(i+1) = T_{FC}(i) + \frac{time\ step}{C_{FC}} * \left(\dot{Q}_{gen}(i) - \dot{Q}_{cool}(i)\right) =$$

$$T_{FC}(i) + \frac{time\ step}{C_{FC}} * \left((n_{cells} * U_{th}(i) - U_{stack}(i)) * I_{stack}(i) - h_{FC}(i) * (T_{FC}(i) - T_{amb}(i))\right) \quad \textbf{(5-27)}$$

Data from several heating-up experiments were analysed to approximate the thermal capacity by conducting a regression analysis. Measured data (fuel temperature, stack voltage, stack current and ambient temperature) were processed by a programmed MATLAB script containing equation (5-27). On average the thermal capacity was estimated to be 3250 J/K.

To validate the thermal model data from an I-U-curve experiment was used. The DC current was slowly increased with a ramp of 0.02 A/s from 0-60 A. Figure 5-16 compares the simulated (blue) with the measured (green) fuel cell temperature. The simulated temperature evolution closely follows that obtained from experimental data. A RMSE of 0.7°C was calculated, thus, the results are considered to be satisfactory.

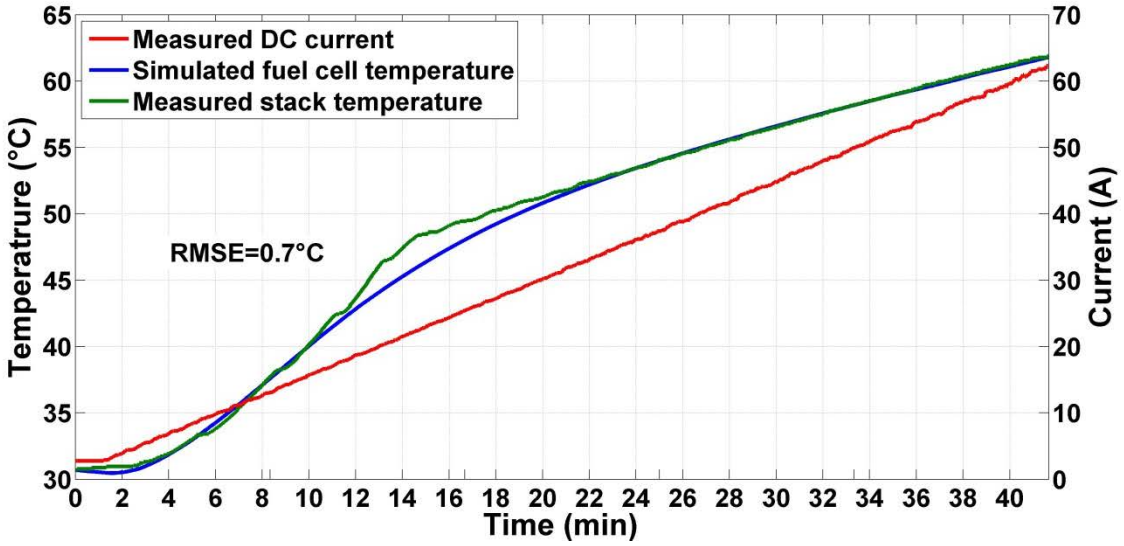


**Figure 5-16: The measured and the predicted evolution of the fuel cell temperature during a current increase from 0-60 A.**

Using equations (5-21), (5-22), (5-24) and (5-26) together with the approximated parameters the thermal model was built in Simulink. The input variables are the stack voltage and the stack current. The ambient temperature is taken as constant (25°C) for further investigations.

#### *5.2.2.3 FC: Hydrogen consumption model*

For a fuel cell stack with $n_{cells}$ cells in series, the hydrogen consumption rate is described by Faraday's Law:

$$\dot{n}_{stoi} = \frac{n_{cells} * I}{z * F} \qquad \textbf{(5-28)}$$

where, $\dot{n}_{stoi}$ is the stoichiometric molar flux of hydrogen. Since the NEXA 1200 fuel cell system operates in "dead-end" mode at the anode side, the hydrogen utilisation is almost 100% (van Nguyen & Knobbe 2003). However, during operation impurities such as water and nitrogen accumulate at the anode side. To remove these impurities the anode side is periodically purged by opening a solenoid valve depending on the DC current drawn from the fuel cell. From analysis of experimental data taken from step climbing experiments, the hydrogen loss due to purging was quantified to be approximately 2% of the total consumed hydrogen during operation. Thus, the hydrogen purge mechanism is not considered in the model. The hydrogen consumption model is composed of equation (5-28).

#### *5.2.2.4 FC: System control model*

The system control model of the fuel cell is similar to the one of the electrolyser. It is structured into a statechart representing the basic operational behaviour and a local control loop to regulate the AC power output of the inverter. Five operational states were defined for the fuel cell system the “off”, the “startup”, the “operation”, the “standby” and the “shutdown” mode. The statechart is presented in Figure A-7. Compared to the electrolyser the fuel cell system is able to start up quickly. The fuel cell system itself needs 48 seconds to initialise before the inverter can synchronise with the electric grid. The latter takes around eight seconds. In addition, some operational constraints are defined, for instance, the minimum power or the standby time before the fuel cell will be transited back to “off” mode.

The local control loop employs a PI controller to regulate the DC current according to the AC power set-point of the inverter. The efficiency of the inverter is modelled using a look-up table based on technical data derived from the operational manual, see . Depending on the power drawn from the inverter, the efficiency varies between 85-91.8%.

#### *5.2.2.5 Integrated fuel fell system model and validation*

The overall fuel cell system model integrates all four proposed sub-models into Simulink. Input variables of the model are the AC power set-point, the “system-on” signal and the gas storage pressure. Output variables are the generated AC power and the hydrogen consumption. Internal variables such as stack voltage or DC current can be simply added to the output if this is necessary. Table 5-7 summarises the variables which are exchanged between the four subsystems, for instance, the fuel cell temperature is required to predict the ohmic resistance (equation (5-18)).

**Table 5-7: Exchanged variables between the four sub-models.**

| **Sub-model** | ***Variable*** | **Electrical model** | **Thermal model** | **Gas consumption model** | **System control model** |
|---|---|---|---|---|---|
| **Electrical model** | $I_{stack}$ | | X | X | |
| | $U_{stack}$ | | X | | |
| | $P_{DC}$ | | | | X |
| **Thermal model** | $T$ | X | | | |
| **System control model** | $I_{DC,System}$ | X | | | |

The fuel cell system model was validated against measured data (not involved in the model parameter extraction) of the step-climbing experiment illustrated in Figure 5-17. The top graph shows the voltage (blue dotted=measured, green=simulated) and the stack current (light blue dotted = measured, red=simulated). The lower graph illustrates the temperature evolution (blue dotted=measured, green=simulated). During the experiment the DC system current was increased from 5 to 60 A in steps of 5A and vice versa. The simulation input variables were the initial temperature of the fuel cell and the calculated DC system power. The latter was directly given to the system control model as DC power set-point. According to the control deviation the DC system current was regulated. The predicted and the measured fuel cell stack voltage are presented in the top diagram. With increasing stack current (DC system current + peripheral current) the voltage starts, as expected, to decline. The difference between the measured and the predicted cell voltage is higher in the increasing current branch due to the simplifications assumed concerning the internal resistance and its dependence on the humidification of the membrane. On the other hand, the error between both values is smaller in the decreasing current branch. The predicted stack current agrees well with the measured value. The lower diagram shows the temperature evolution of the fuel cell system. In the decreasing current branch the deviation is higher, with a maximum difference of 2 °C between the time interval 180 min to 210 min. The simulation results were quantified by calculating the RMSE and the MAPE. Regarding the undertaken simplifications the results can be considered as satisfactory with a RMSE/MAPE of 0.66 A/2%, 0.397 V/1.4% and 0.8°C/1.3% for the stack current, stack voltage and temperature, respectively.

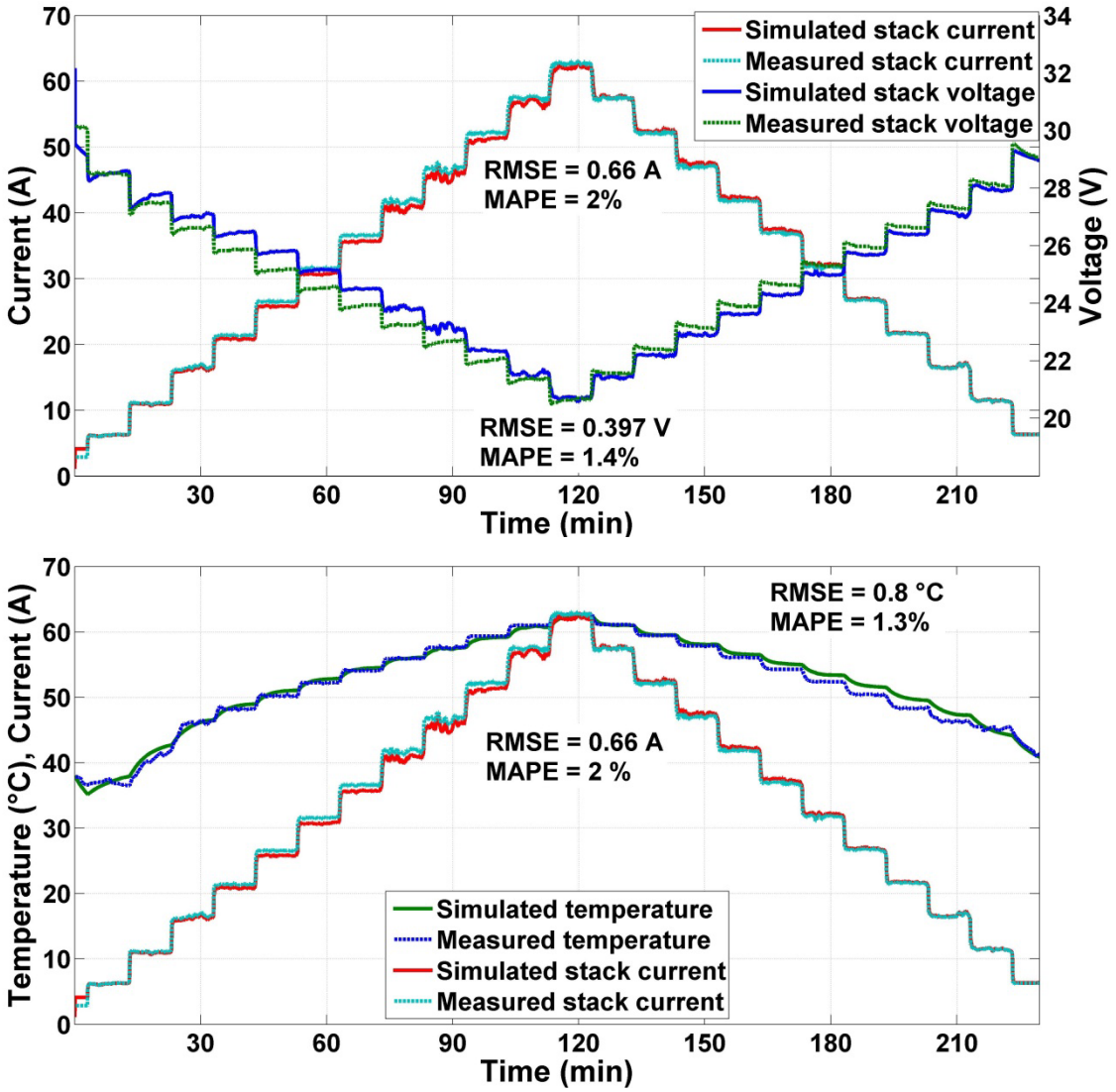


**Figure 5-17: Measured and simulated fuel cell response to a current step-climbing experiment.**

## 5.3 Modelling of the vanadium-redox-flow-battery system

Over the last years several VRFB models have been presented in literature. Depending on the research purpose the models can be applied, for example to simulate single cells to investigate the electrochemical behaviour (You, Zhang & Chen 2009), to investigate the thermal effect of self-discharge on the electrolyte temperature at system level (Tang, Bao & Skyllas-Kazacos 2012) or to focus more on the application of VRFB. Chahwan et al. (2007) proposed a model which considers battery losses such as power consumption of the BOP and internal resistance. Furthermore, the model is compared with measured data and showed reasonable results. This model is also applied by Barote et al. (Barote, Marinescu & Georgescu 2009) and Nguyen et al. (2011) to study stand-alone wind energy systems and to develop a power management for a micro-grid, respectively. A multi-physics model based on electrochemistry and fluid mechanics is proposed by Blanc and Rufer (2009).

It considers internal losses and vanadium concentrations as well as the flow rate of the electrolyte. However, Blanc and Rufer (2009) assumed a Coulombic efficiency of 100 %. The model presented by Turker et al. (2013) focuses on unit up-scaling and development of operational strategies. The model is based on experimental data taken from a commercial available kW/kWh system as presented in (Schreiber et al. 2012). Recently, Ontiveros and Mercado (2014) have published a system model that considers Coulombic losses. The model is based on efficiency curves obtained from the manufacturer or from experimental results presented in the literature. However, the model is only validated against data taken from literature.

In the following section a VRFB model is developed that considers internal voltage, Coulombic losses and the power consumption of the peripheral system. Moreover, experiments are designed to investigate the impact of the DC current and SOC on the losses. The overall system model combines the electrical model and operational aspects such as start-up and standby behaviour.

### 5.3.1 VRFB: Electrical and state-of-charge model

Figure 5-18 illustrates the proposed electrical model of the VRFB. The battery voltage can be modelled as controllable ideal voltages source in series with a resistance $R_{eq}$ that represents internal voltage losses. This resistance is different for charging and discharging. Thus, two branches are introduced containing an ideal diode to select the corresponding resistance. The Coulombic losses are modelled as a shunt resistor $R_{sh}$ in parallel to the voltage source. The power demand of the BOP is modelled as controllable current sink and is introduced in chapter 5.3.2. The following section develops the model in detail and it introduces a methodology to determine both $R_{eq}$ and $R_{sh}$ from experimental data.

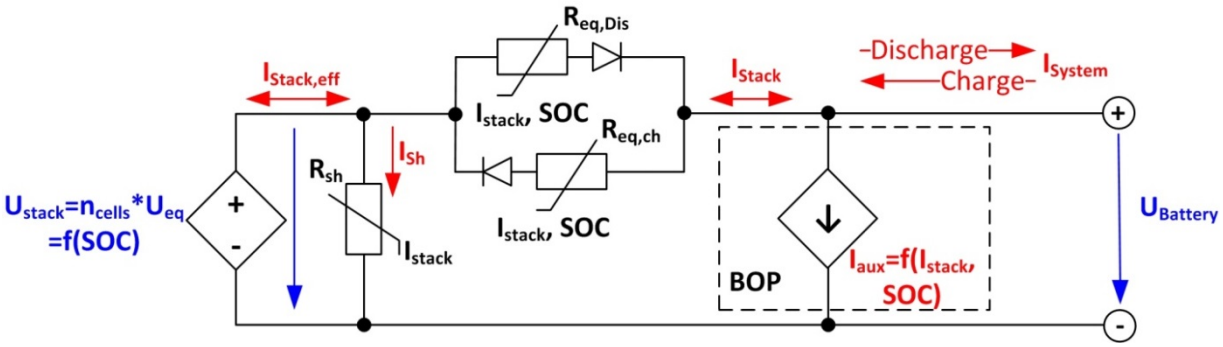


**Figure 5-18: Proposed equivalent circuit of the VRFB.**

As presented in section 4.3.1 the open circuit voltage $U_{eq}$ across the electrodes of a VRFB depends on the concentration of the ion species in the electrolyte. Sukkar and Skyllas-Kazacos (2003) have

shown that the Nernst equation, to calculate the open circuit voltage of a single cell, can be expressed as a function of the SOC of the electrolyte:

$$U_{eq} = U_{OCV,SOC=50\%} + \frac{R * T}{n * F} * ln\left(\frac{SOC^2}{(1-SOC)^2}\right) \quad \textbf{(5-29)}$$

where, $U_{OCV,SOC=50\%}$ is the measured open circuit voltage at SOC equal to 50%, *R* is the ideal gas constant (8.314 J/molK), *T* is the electrolyte temperature (K), *n* the number of electrons transferred (compare equations (4-18)-(4-20)) and *F* is the Faraday constant (96,485 As/mol).

As illustrated in Figure 3-10 the open circuit voltage is continuously monitored by a single reference cell and the battery controller predicts the SOC. To compare the measured open circuit cell voltage with the values derived from equation (5-29), it is necessary at first to determine $U_{OCV,SOC=50\%}$ from measured data. This value was found to be 1.41 V and corresponds well to data reported in (Sukkar & Skyllas-Kazacos 2003). Figure 5-19 plots the measured (blue asterisks) and the predicted (green line) open circuit voltage (5-29) as a function of SOC. As illustrated, the predicted voltage differs from the measured voltage; at SOC values below 50% the voltage is overestimated and above 50% the voltage is underestimated. Reasons for this divergence may be found in the chemical composition of the electrolyte. However, the electro-chemical analysis of the involved substances is out of scope of this thesis.

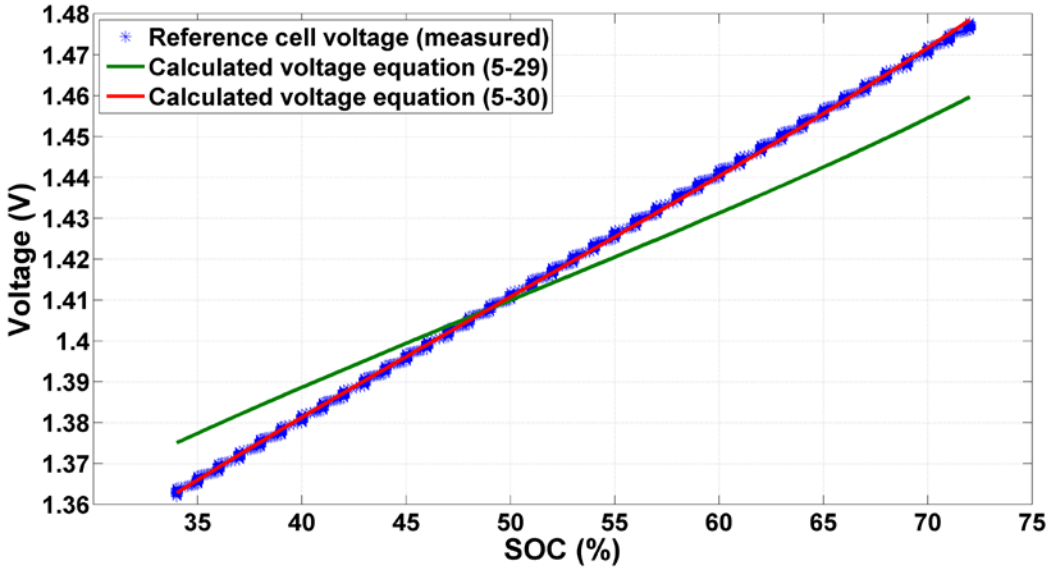


**Figure 5-19: Comparison between the measured reference cell voltage and the predicted open circuit cell voltage based on equation (5-29) and (5-30).**

Therefore, a simple regression analyses was conducted to find a correction term that adopt the slope of equation (5-29) to the measured data.

$$U_{eq} = U_{OCV,SOC=50\%} + \frac{R * T}{n * F} * ln\left(\frac{SOC^2}{(1-SOC)^2}\right) + \underbrace{(C_1 * SOC + C_2)}_{correction\ term} \quad \textbf{(5-30)}$$

The parameter $C_1$ and $C_2$ of the correction term were obtained from several charge-discharge experiments. The respective values are $C_1$= 0.0818 V and $C_2$= -0.04 V. Figure 5-19 shows the improvement of applying equation (5-30). The predicted voltage (red line) agrees well with the measured data, thus, equation (5-30) are used to determine the open circuit cell voltage using the SOC-model developed later. Since the battery contains $n_{cells}$ (=36) in series connected cells, the equilibrium voltage at stack level can be simply expressed by:

$$U_{stack} = n_{cells} * U_{eq} \quad \textbf{(5-31)}$$

Similar to the fuel cell, the internal voltage losses of the VRFB are defined as activation, concentration, ohmic and ionic over-potential. Schreiber et al. (2005) experimentally analysed the voltage losses of a VRFB system and they found out that the ohmic and ionic resistance of the electrodes, the membrane and electrolyte are dominant and that the activation and concentration over-potentials may be neglected. Thus, an equivalent resistance $R_{eq}$ is introduced to summarise the internal losses (Blanc & Rufer 2009). The battery terminal voltage can be calculated by:

$$U_{battery} = n_{cells} * U_{eq}(SOC, T) - I_{stack} * R_{eq}(I, SOC, T) \quad \textbf{(5-32)}$$

where, $n_{cells}$ is number of cells in series connected and $I_{stack}$ is the stack current (note that the current is positive during discharge and negative during charge). Both $U_{eq}$ and $R_{eq}$ depend on the temperature. In particular the ionic conductivity of the electrolyte shows a strong temperature dependency; with decreasing temperature the internal resistance increases. However, if the battery system is installed indoors, the temperature can be assumed to be constant during operation. In this study the electrolyte temperature was set to 30°C.

To investigate the characteristics of the equivalent resistance several charge/discharge experiments were conducted at a constant stack current rate (25A, 50A, 75A, 100A and 120A). Note that the installed inverters apply the “constant-current-constant-voltage” (IU) charge algorithm. This means that the battery is charged first at a constant current until the maximum charge voltage is reached; then, the current will be reduced. On the other hand, the stack current is kept constant during discharge. In each experiment, the stack voltage, the stack current and the open circuit voltage of the

reference cell were measured directly with a sample rate of two seconds, see Figure 3-12. The collected data were used to obtain the equivalent resistance by rearranging equation (5-32) to:

$$R_{eq,charge/discharge} = \left|\frac{U_{battery} - U_{stack}}{I_{stack}}\right| \quad \textbf{(5-33)}$$

It was found that the equivalent resistance is on average lower during charge than during discharge. An explanation for this difference can be found in the kinetics of the redox reactions, which are slower during discharge particular at the cathode (Blanc 2009). Zhao et al. (2007) concluded that the higher resistance during discharge can be partly attributed to the reverse flow of the $H^+$ protons through the electric field between the electrodes. Figure 5-20 depicts the relationship between the calculated equivalent resistance with variation of SOC at a constant discharge stack current of 50 A (blue) and 100 A (green). It is apparent from Figure 5-20 that $R_{eq}$ decreases with increasing stack current. This behaviour can also be seen during charge. Another interesting observation is that the resistance slightly decreases with decreasing SOC and that it starts to increase again at end of discharge. This can be explained by the variation of $H^+$ protons in the electrolyte. With decreasing SOC the concentration of $H^+$ protons reduces resulting in a lower conductivity of the electrolyte and membrane (Zhao et al. 2007).

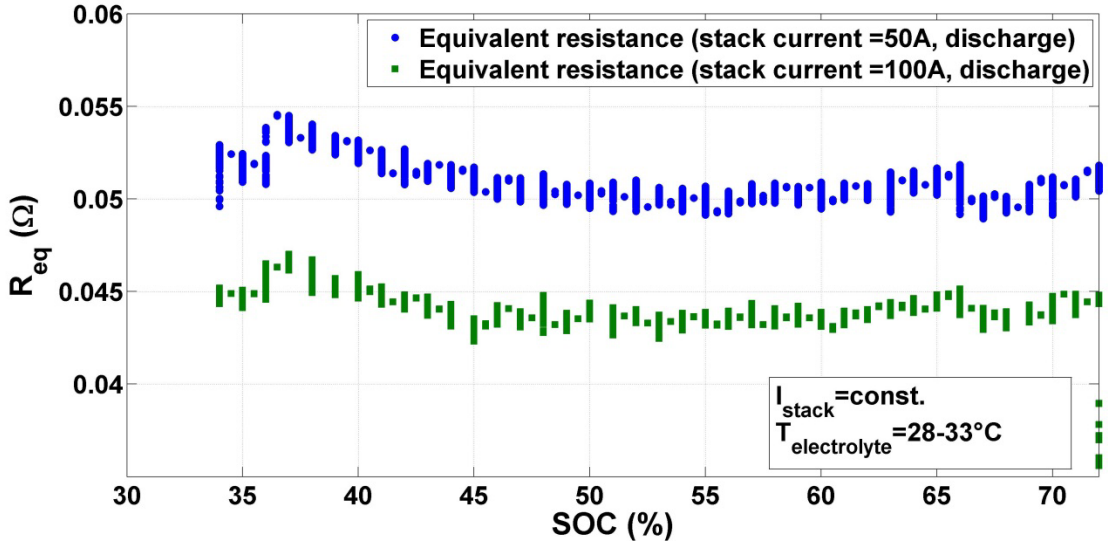


**Figure 5-20: Equivalent resistance $R_{eq}$ calculated from measured data at constant stack current of 50 A (blue) and 100 A (green).**

Instead of using constant values for the equivalent resistance, which is applied in most of the abovementioned research studies, the following two equations are proposed to take into account

the variation of the equivalent resistance during charge and discharge as a function of the stack current and SOC:

Charge: $$R_{eq,charge} = A_1 * I_{stack} + A_2 * I_{stack}^2 + B_1 * SOC^2 + B_2 * SOC + C \quad \textbf{(5-34)}$$

Discharge: $$R_{eq,discharge} = D_1 * I_{stack} + D_2 * I_{stack}^2 + E_1 * SOC^2 + E_2 * SOC + F \quad \textbf{(5-35)}$$

where, $A_1$, $A_2$, $B_1$, $B_2$ and $C$ are the empiric parameters for the charge process and $D_1$, $D_2$, $E_1$, $E_2$ and $F$ are the empiric parameters for discharge.

To extract the parameters of equations (5-34) and (5-35) from the conducted charge/discharge experiments a similar procedure as for the electrical model of the electrolyser, illustrated in Figure A-5, was applied. First, the five individual data sets (25 A, 50 A, 75 A, 100 A and 120 A) were merged into five data sets in which one constant current data set was left out, for instance, the first merged data set contains 50A, 75A, 100A and 120A. In addition, one data set was generated that contains all data. Secondly, a programmed MATLAB script was used to estimate the parameters by using the non-linear regression routine *lsqcurvefit*. A coded function including equations (5-32), (5-34) and (5-35) to calculate the battery voltage together with the measured equilibrium voltage, stack current and SOC was passed to the *lsqcurvefit* routine and the parameters were approximated with respect to the measured battery voltage. Finally, the parameter set with the lowest RMSE was chosen for further investigations. Table 5-8 presents the approximated empirical parameters of equations (5-34) and (5-35).

**Table 5-8: Experimentally estimated parameters for $R_{eq}$**

| | | | | | |
|---|---|---|---|---|---|
| **Charge** | $A_1$ | $A_2$ | $B_1$ | $B_2$ | $C$ |
| | $1.85*10^{-4}$ Ω/A | $9.36*10^{-7}$ Ω/A² | 0.0414 Ω | -0.0361 Ω | 0.0562 Ω |
| **Discharge** | $D_1$ | $D_2$ | $E_1$ | $E_2$ | $F$ |
| | $-4.097*10^{-4}$ Ω/A | $1.16*10^{-6}$ Ω/A² | 0.0592 Ω | -0.0723 Ω | 0.0913 Ω |

Figure 5-21 gives the plots of the calculated equivalent resistance (blue dots) compared to the approximated values (red line) for charge and discharge at 120 A (stack current) as a function of time on the left and on the right side, respectively. Both graphs show that the approximated values correspond very well with the experimental values.

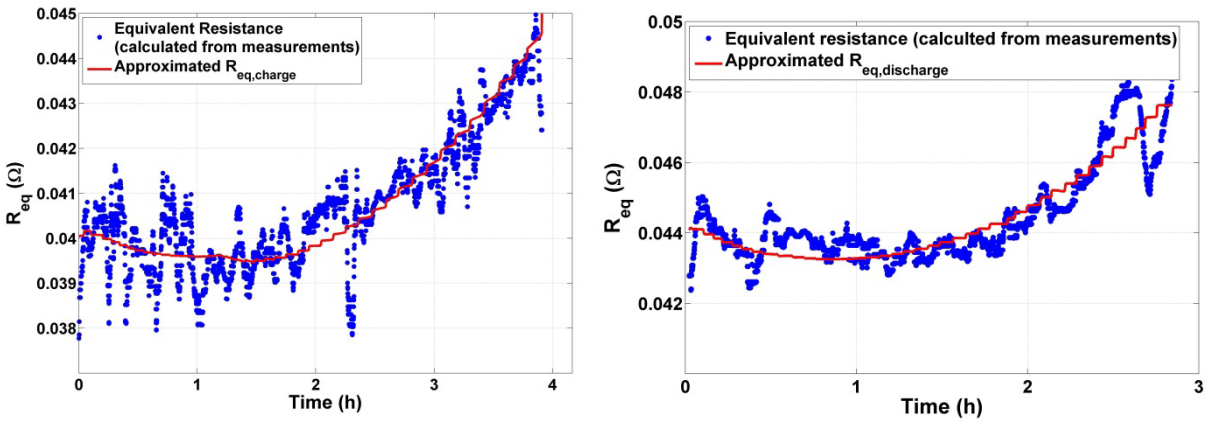


**Figure 5-21:Calculated equivalent resistance and approximated equivalent resistance for charge (left) and discharge (right) process at a constant stack current of -120 A and 120 A, respectively.**

Before the Coulombic losses can be considered, it is necessary to introduce a SOC model of the VRFB. The SOC represents the ratio of the stored energy to the maximum energy capacity of the battery. The maximum energy capacity is defined by the electrolyte volume, which is stored in the two tanks. If the initial condition of the SOC is known a capacity change can be expressed as function of time:

$$SOC_{t=n} = SOC_{t=n-1} + \Delta SOC = SOC_{t=n-1} + \int_{t=n-1}^{n} \frac{n_{cells} * U_{eq} * I_{stack,eff}}{E_{capacity}} dt \qquad \textbf{(5-36)}$$

where, $E_{capacity}$ is the theoretical storable energy in the electrolyte (kWh) and $I_{stack,eff}$ is the effective current that charges/discharges the electrolyte. Since the useable SOC range is fixed between 34% and 72% the value of $E_{capacity}$ needs to be calculated. According to the manufacturer of the battery, the rated/useable energy capacity is 20 kWh. This gives a theoretical total energy content of approximately 52 kWh. From an experimental analysis can be concluded that the useable energy of the VRFB system is lower than 20 kWh. On average only 17 kWh can be used giving a theoretical total energy capacity of 44.7 kWh. Equation (5-36) is applied in most of the reviewed studies and is only valid in an ideal continuous stirred tank. However, if the charged or discharged electrolyte leaves the battery stack and flows into the two tanks a certain time is needed to mix the electrolyte. Derived from measurements this time delay is on average six minutes.

To take this into account, a simple time delay is implemented so that equation (5-36) finally becomes to:

$$SOC_{t=n} = SOC_{t=n-1} + \Delta SOC_{t-delay} \qquad \textbf{(5-37)}$$

Due to the bipolar cell stack design, the parallel electrolyte flow through the cell stack and the conductivity of the electrolyte, a shunt current will be developed reducing the efficiency (Xing, Zhang & Ma 2011; Tang et al. 2013). Considering this, the shunt losses are modelled as a resistor in parallel with the controlled voltage source which is modelled by equations (5-30) and (5-31). The effective stack current $I_{stack,eff}$ can be simply calculated by applying Kirchhoffs' 1st Law:

$$I_{stack,eff} = I_{stack} + I_{sh} \quad \textbf{(5-38)}$$

where, $I_{sh}$ is the shunt current. During charge the effective current participating in the chemical reaction is lower than the stack current, whereas it is higher during discharge. The shunt resistance $R_{sh}$ can be calculated by:

$$R_{sh} = \frac{U_{stack}}{I_{sh}} \quad \textbf{(5-39)}$$

To explore the characteristic of the shunt resistance, a regression analysis was conducted to determine the shunt resistance from constant current charge/discharge experiments. As a first approximation it was assumed that the value of $R_{sh}$ is independent from charge/discharge and the electrolyte flow rate. Equations (5-36)-(5-39) are implemented into a MATLAB function. This function together with the measured initial SOC value, the measured stack current and the stack voltage is passed to the *lsqcurvefit* routine and $R_{sh}$ is estimated with respect to the measured SOC. Figure 5-22 illustrates the relationship between the shunt resistance and the stack current. Initially, the value of $R_{sh}$ rapidly decreases with increasing current, but, then starts to flatten out at higher current values. To take such behaviour into account, the following power function is proposed to approximate the shunt resistance.

$$R_{sh}(I_{stack}) = R_{s,1} * |I_{stack}|^{R_{s,2}} \quad \textbf{(5-40)}$$

Where, $R_{s,1}$ ($\Omega$/A) and $R_{s,2}$ (-) are empirical parameters.

The green dotted line in Figure 5-22 illustrates the result of a first curve fit based on the separately approximated values of $R_{sh}$ (blue squares). By knowing that $R_{sh}$ can be described by equation (5-40), the regression analysis was repeated.

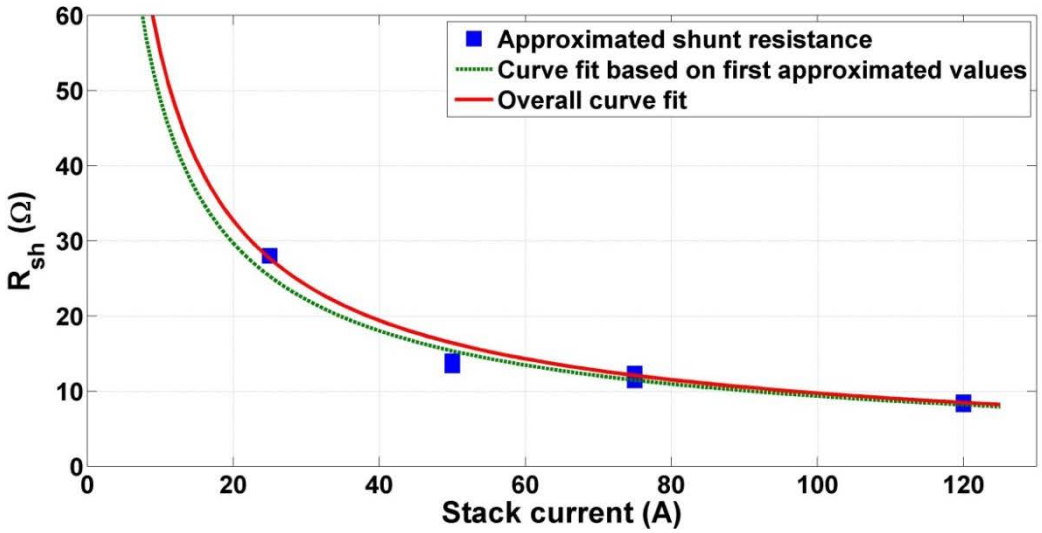


**Figure 5-22: Approximated shunt resistance as function of the stack current.**

An overall curve fit was conducted by adding equation (5-40) to the MATLAB script and by merging all data of the charge/discharge experiments into one set of data. The result of the overall curve fit is shown in Figure 5-22 as red line. The corresponding parameters of equation (5-40) are $R_{s,1}$=311.5 Ω/A and $R_{s,2}$=*-0.753*. These values are applied in the model to calculate the shunt resistance (5-40).

Based on the above described findings, the electrical model composed of equations (5-30), (5-31), (5-32), (5-34), (5-35), (5-38) and (5-40) and the SOC model (5-37) were built in Simulink. Validation was conducted by means of comparing the predicted battery voltage with measured data taken from a charge/discharge experiment at 25 A and 120 A. The input variable of the simulation was the measured stack current and the initial SOC value (34%). Figure 5-23 depicts the equilibrium voltage $U_{stack}$ and the battery voltage at a constant charge/discharge stack current at 25 A ((a) and (c)) and at a constant charge/discharge stack current of 120 A ((b) and (d)). Note that the inverter uses the IU-charge algorithm and that the current will be reduced if the maximum voltage is reached. This can be noticed in Figure 5-23 (b) and (d). The predicted equilibrium stack voltage agrees well with the measured data with an RMSE of 79.2 mV and 45.9 mV for 25 A and 120 A, respectively. Furthermore, from Figure 5-23 (b) it can be seen that although the stack current was changed from -120 A (charge) to 120 A (discharge), the $U_{stack}$ did clearly further increase due to the time delay to mix the electrolyte. It can be concluded that the model replicates this behaviour very well. The battery voltage is predicted with an RMSE of 80 mV and 92.6 mV for 25 A and 120 A, respectively.

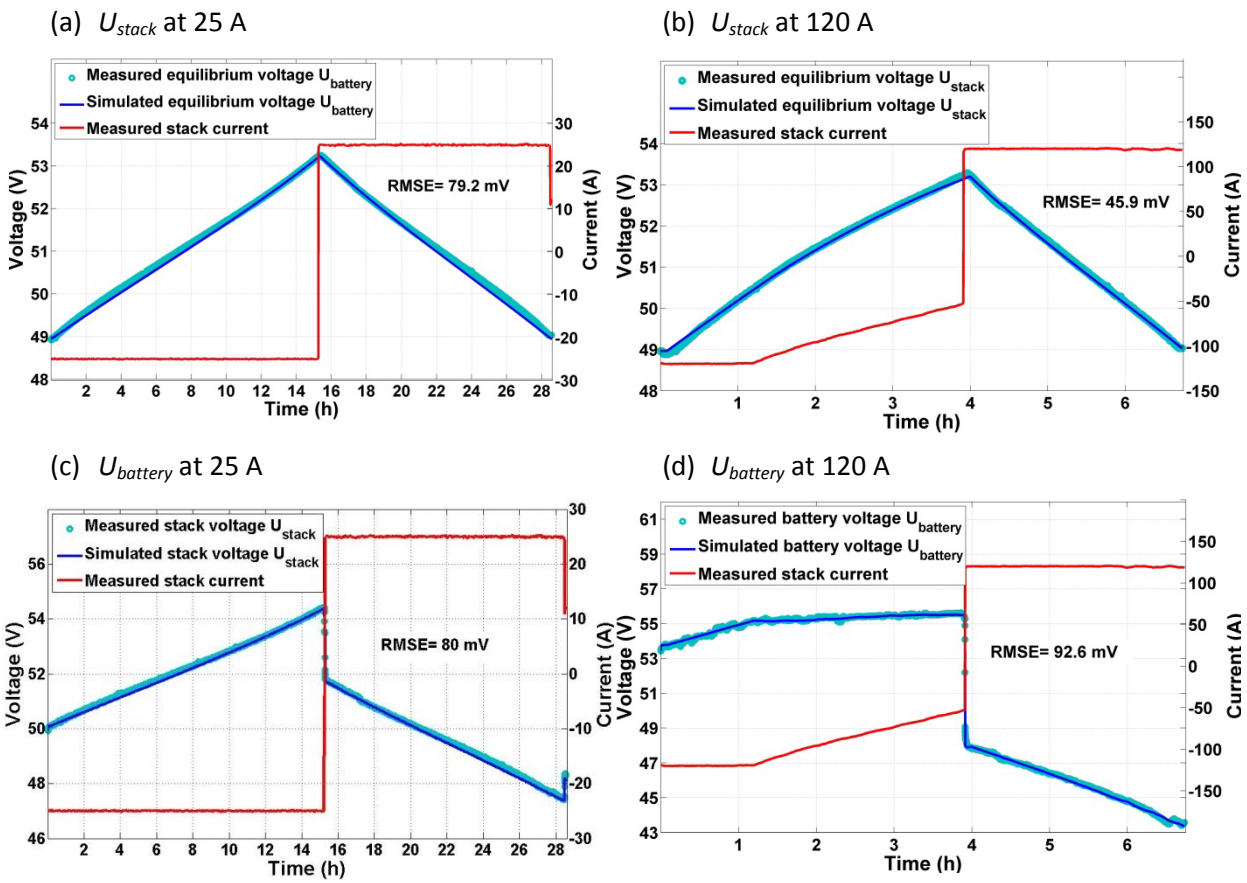


**Figure 5-23: Comparison of the measured and simulated voltages at a stack current of 25 A ((a) and (c)) and 120 A ((b) and (d)). Simulation input was the measured stack current (red).**

### 5.3.2 VRFB: Auxiliary power demand and system control model

The VRFB has one auxiliary power device, the internal battery controller. This controller supplies the installed sensors, actuators and the two electrolyte pumps. The power demand of the BOP reduces the available DC current supplied/withdrawn from the two inverters. It can be calculated by:

$$I_{system} = I_{stack} - I_{aux} \quad \textbf{(5-41)}$$

where, $I_{system}$ is the DC system current, see Figure 5-18. As described in chapter 4.3.2 the pump speed is regulated by the internal battery controller with respect to the SOC and the DC current. During charge the two pumps operate at constant pump speed, whereas during discharge the pump speed varies with SOC and DC current. Based on the experimental analysis, the power consumption of the BOP was obtained at different DC current rates and SOC. Table 5-9 summarises the averaged power values. Since a detailed model of the hydraulic part of the VRFB is not considered in this study, Table 5-9 is implemented into a Simulink subsystem, the auxiliary power demand model, as MATLAB-function block containing a set of if-rules to calculate the auxiliary current $I_{aux}$ by dividing the auxiliary power by the battery voltage.

**Table 5-9: Power consumption of the BOP**

| $I_{stack}$ | SOC | | |
|---|---|---|---|
| | $SOC < 36\%$ | $36\% < SOC \leq 66.2\%$ | $SOC > 66.2\%$ |
| $0\ A > I_{stack} > -50\ A$ | 500 W | | |
| $I_{stack} \leq -50\ A$ | 520 W | | |
| $0\ A < I_{stack} \leq 35\ A$ | 225 W | 177 W | 228 W |
| $35\ A < I_{stack} \leq 80\ A$ | 360 W | 260 W | 365 W |
| $I_{stack} > 80\ A$ | 508 W | 365 W | 518 W |

From the experimental analysis of the VRFB six operational states can be defined namely “startup”, “operation”, “charge inhibited”, “discharge inhibited”, “standby” and “off” state. Figure A-8 illustrates the implemented statechart in Stateflow®. In addition, five operational parameters are introduced the minimum charge and discharge power, minimum and maximum SOC as well as the maximum standby time. The time to initialise the system and to ramp up the pumps is set to 70 seconds.

The modelled local control system of the VRFB applies two PI-control loops; the first one regulates the DC system current to satisfy the positive or negative AC power demand and the second loop is only active during charge. If the maximum charge voltage (55.8V) is reached, the AC power set-point will be reduced to maintain the DC voltage limit. In addition, this subsystem contains a lookup table to model the two bidirectional inverters by means of the efficiency curve derived from the technical data sheet, see A-2-3. The efficiency varies between 85% and 95.2%. Figure 5-24 illustrates the basic layout of the implemented local control system.

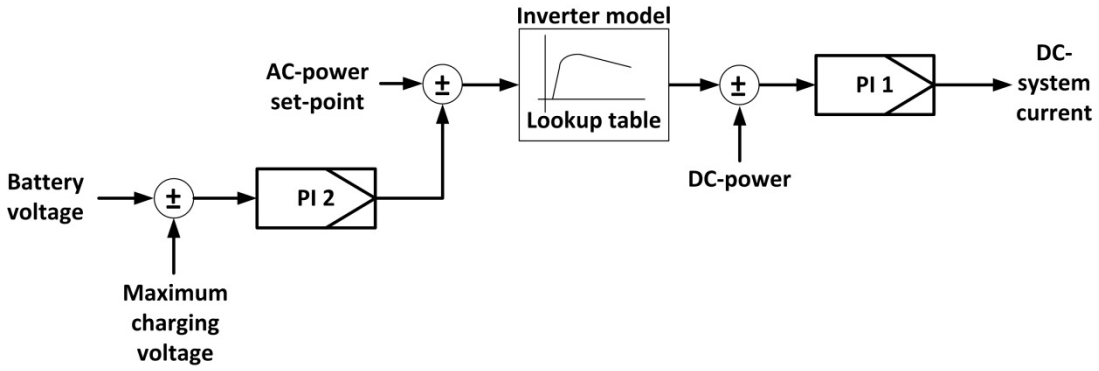


**Figure 5-24: Layout of the proposed model of the local control system of the VRFB**

The VRFB system model encompasses the statechart, the two control loops and the lookup table of the inverter and was built in Simulink.

### 5.3.3 Integrated VRFB system model

All four proposed subsystems are incorporated into one model to represent the VRFB system. The overall system model has two input variables, the AC power set-point and the on/off signal. Output variables are the AC power, SOC and the system state. In addition, internal variables, for example, the battery voltage or the stack current can be added to the output variables. Interfacing variables between the four subsystems are given in Table 5-10. For instance, the calculations carried out in the electrical sub-model depend on the predicted SOC, the DC system current provided from the system control model and the auxiliary current.

**Table 5-10: Interfacing variables between the sub-models of the VRFB-system model**

| Sub-model | *Variable* | Electrical model | SOC | Auxiliary power demand model | System control model |
|---|---|---|---|---|---|
| Electrical model | $I_{stack}$ | | | X | X |
| | $I_{stack,eff}$ | | X | | |
| | $U_{stack}$ | | X | | |
| | $U_{battery}$ | | | X | X |
| SOC Model | $SOC$ | X | | X | X |
| Auxiliary power demand model | $I_{aux}$ | X | | | X |
| System control model | $I_{DC,System}$ | X | | | |
| | *VRB-state* | | | X | |

To validate the VRFB system model, experimental data from a charge/discharge experiment at maximum 100 A stack current (14400 data points, sample time = 2 second) was used. Measured values of the AC active power were passed to the simulation input. Figure 5-25 reports the simulation result of a charge/discharge experiment. The data set used was not part of the parameter finding process.

Figure 5-25 (a) compares the measured with the simulated AC active power. Both values agree very well except at end of charge. At time values above 3.5 h the maximum charge voltage is reached and the local control loop starts to decrease the power set-point. From Figure 5-25 (b) it can be seen that the model over predicts the SOC. The reason for this can be probably found in the simplification adopted to calculate the SOC by equation (5-36) and the averaged total capacity of the battery. The higher values of the simulated SOC lead to higher values of the equilibrium voltage, equation (5-29), accordingly, the battery voltage rises faster and reaches its limit sooner. Figure 5-25 (c) and (d) depict

the battery voltage and the DC system current, respectively. The calculated MAPE for each variable are lower than 2%. Therefore, it can be concluded that the proposed VRFB system model can predict the performance of the real system with a satisfactory accuracy.

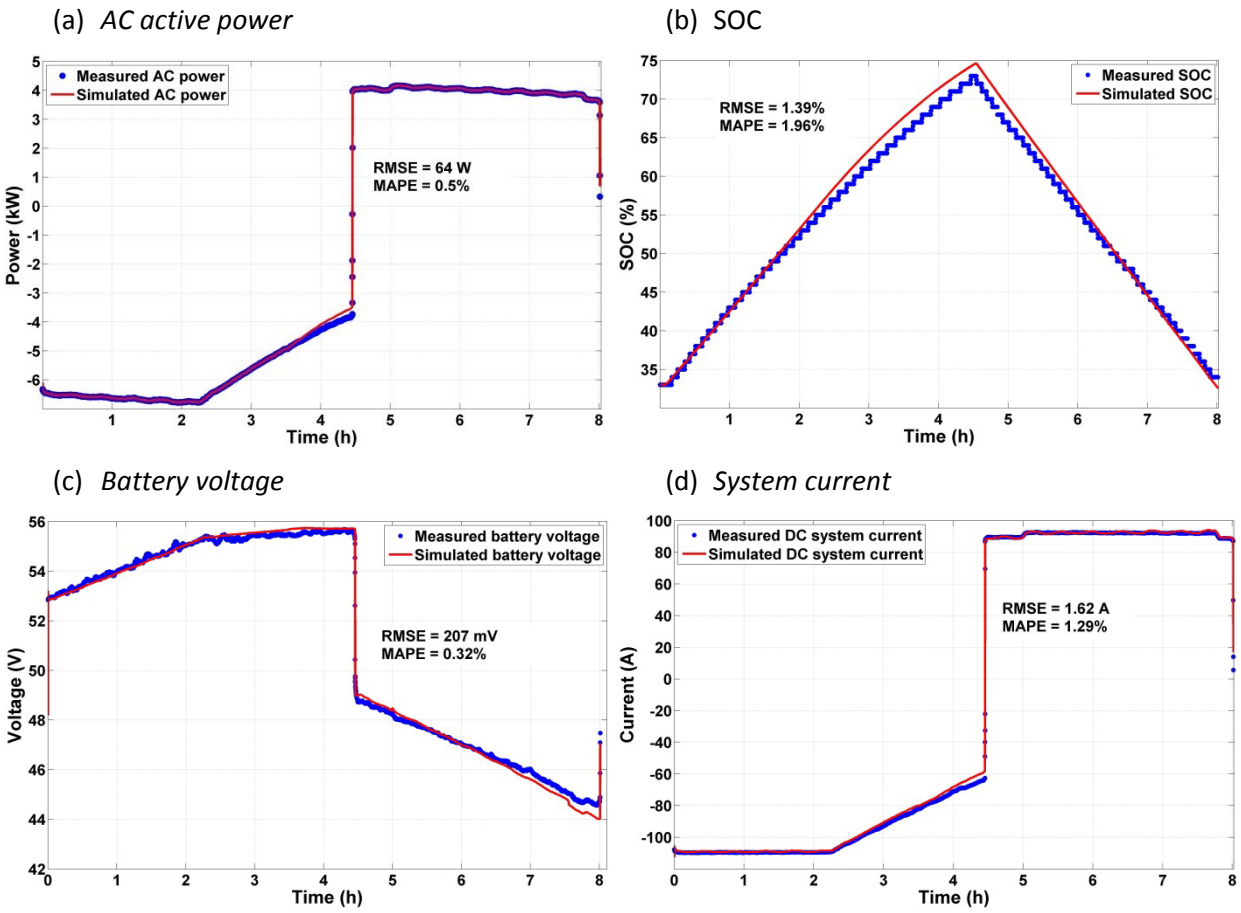


**Figure 5-25: Measured versus simulated AC active power (a), SOC (b), battery voltage (c) and DC system current (d). The measured values are the blue dots and the predicted values are given by the red line.**

## 5.4 Energy management system

The developed energy management strategy is hierarchically organised with the main objective to increase the amount of locally used renewable energy. Figure 5-26 presents the three level structure of the control strategy. The first level describes the strategic supervisory level. It is developed in Simulink®/Stateflow®, which also represents the energy management unit. The developed energy management strategy is applied for the simulation study in section 6.2 and for the experimental demonstration outlined in section 6.3. At the strategic supervisory level decisions are made regarding the operational state of the HRES, the activation of the components and the generation of the reference power signal for the corresponding energy system. The second level describes the local supervisory level of each energy system which coordinates basic operational states such as the start-up or the shut-down process. The third level contains the local control level, where the power output/input of the energy system is regulated according to the reference power signal provided by the strategic supervisory level. Both the second and third level is implemented in the control units (BOP and PLC) of the energy systems. Between the top level and the lower levels information needs to be exchanged.

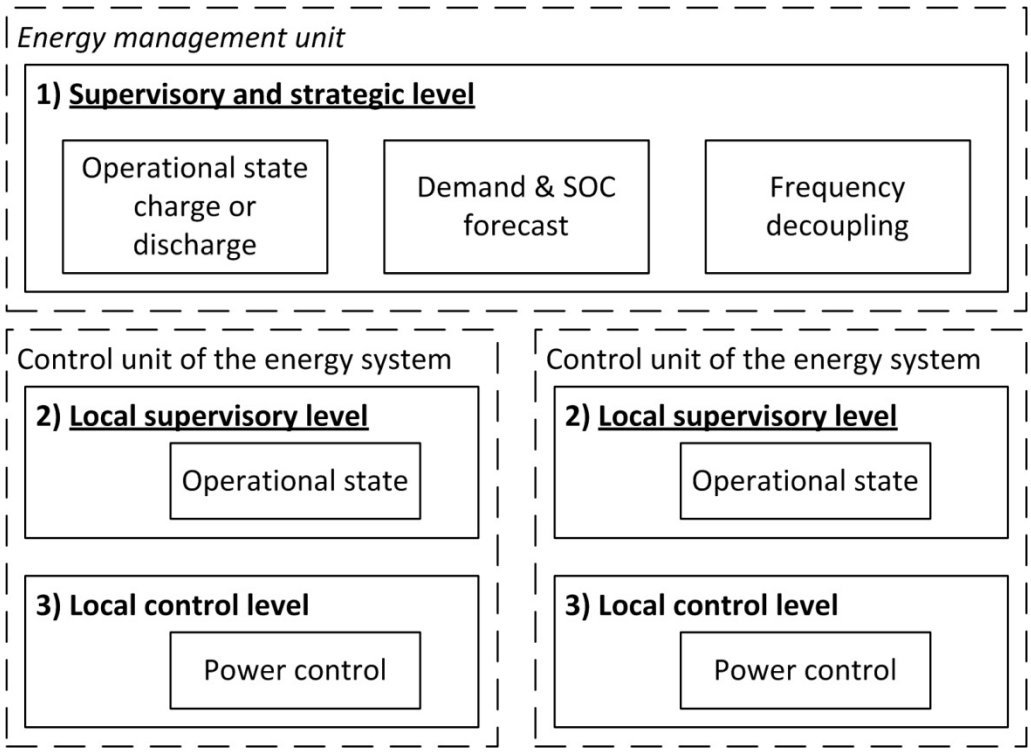


**Figure 5-26: Structure of the energy management system.**

As stated previously, the primary objective of the energy management unit is to increase the amount of locally used renewable energy. Another objective is to reduce the power fluctuations of the

renewable energy sources injected into the public grid. In addition, it should predict the optimal time to activate an energy system considering the minimum input/output power. Furthermore, the energy management unit should be configurable to control a hybrid storage system and it should estimate the instant of time to start-up the second electrical storage system. Moreover, the energy management unit calculates the reference power signal of the energy systems according to the dynamic observations carried out in chapter 4 by applying a frequency decoupling technique.

As discussed in chapter 2, buildings may transform to an active prosumer in the future smart grid. Therefore, it is assumed in the simulation study that the strategic supervisory level can process an artificial DSR signal provided from a smart grid operator. This signal, the smart grid message, is composed of a Boolean signal to activate the DSR mode of the energy management unit and of a reference signal of the power at the building's PCC. The smart grid message is treated with high priority, thus, the demand forecast algorithm is deactivated while the message is detected.

### 5.4.1 Determination of the operational state

The first task of the energy management unit is to obtain the power balance at the PCC – the connection to the public grid – to determine whether there is a power deficit or a power surplus:

$$P_{diff} = P_{load} - P_{renewables} \quad \textbf{(5-42)}$$

where, $P_{diff}$ (W) is the power difference between the electric load $P_{load}$ (W) and the aggregated power of the renewable energy sources $P_{renewables}$ (W). Based on the calculated power difference the HRES can be transited either into one of the two main states "Demand" ($P_{diff} > 0$) or the "Excess" ($P_{diff} < 0$). If the strategic supervisory level detects a smart grid signal, the power difference is calculated differently:

$$P_{diff} = P_{ref,PCC} - (P_{load} - P_{renewables}), \quad \textbf{(5-43)}$$

where, $P_{ref,PCC}$ (W) is the power reference signal at building's PCC embedded in the smart grid message.

Figure 5-27 illustrates the hierarchically organised statechart diagram of the energy management unit, which is implemented in Stateflow®.The HRES can be transited between the two main states according to the two conditions "1" and "2". For instance, if the HRES is in the "Excess" state, it can be only transferred into the "Demand" state if the power difference is positive and either the electrolyser has entered the blow-down process (operational state 5) or it is off (operational state 1), or the VRFB is in operation or off mode (operational state >2).

As aforementioned the developed strategic supervisory level can be used for both single and hybrid storage configuration. Therefore, each main state includes sub-states for the hydrogen loop and the VRFB. The hybrid storage configuration is experimentally demonstrated in section 6.3.2. Due to the higher overall efficiency the VRFB is primarily used, before the hydrogen loop will be activated. The decision when to activate the hydrogen loop depends on the SOC of the VRFB. How to predict the instant of time to start the energy systems is presented in section 5.4.2.

The sub-state "$H_2$-loop" of the main state "Excess" is also illustrated in Figure 5-27. Within this sub-state there are four states defined to control the hydrogen generation process. State "Wait" is the initial state where the strategic supervisory controller waits until one of the two conditions is fulfilled. If the demand forecast provides a start signal ("demand forecast = 1"), the hydrogen storage pressure is below 28 bar ("storage pressure < 28 bar") and the electrolyser is in operational state "Off" ("ele. op. state = 1"), the controller will be transited into the "$H_2$ Activate" state and the start signal will be sent to the electrolyser sub-model.

The electrolyser "system control" sub-model, see section 5.2.1.4, recognises the activation signal and the electrolyser is transited into the "Startup" state. When the electrolyser enters the state 2 "Operation", the sub-state "$H_2$-loop" will be moved into the "$H_2$ Charge" state. The strategic supervisory level controller stays in this state until the hydrogen store has reached its limit ("H2Store_SOC==30"), the electrolyser enters the "Off" state ("H2_Ele_SystemState==5") or the condition "2" to move into the main state "Demand" is fulfilled.

If the corresponding energy storage system is in operation, the power balance at the PCC is defined as:

$$P_{grid} = P_{load} - P_{renewables} \pm P_{storage} \qquad \textbf{(5-44)}$$

where, $P_{grid}$ (W) is the power exchanged with the public electricity grid (negative values are defined as power export and positive values as power import) and $P_{storage}$ (W) is the power consumed or released by the electrical storage system (negative values are defined as charge power and positive values as discharge power).

The Stateflow® diagrams of the strategic supervisory controller to coordinate the HRES are presented in Figure A-9, Figure A-10 and Figure A-11

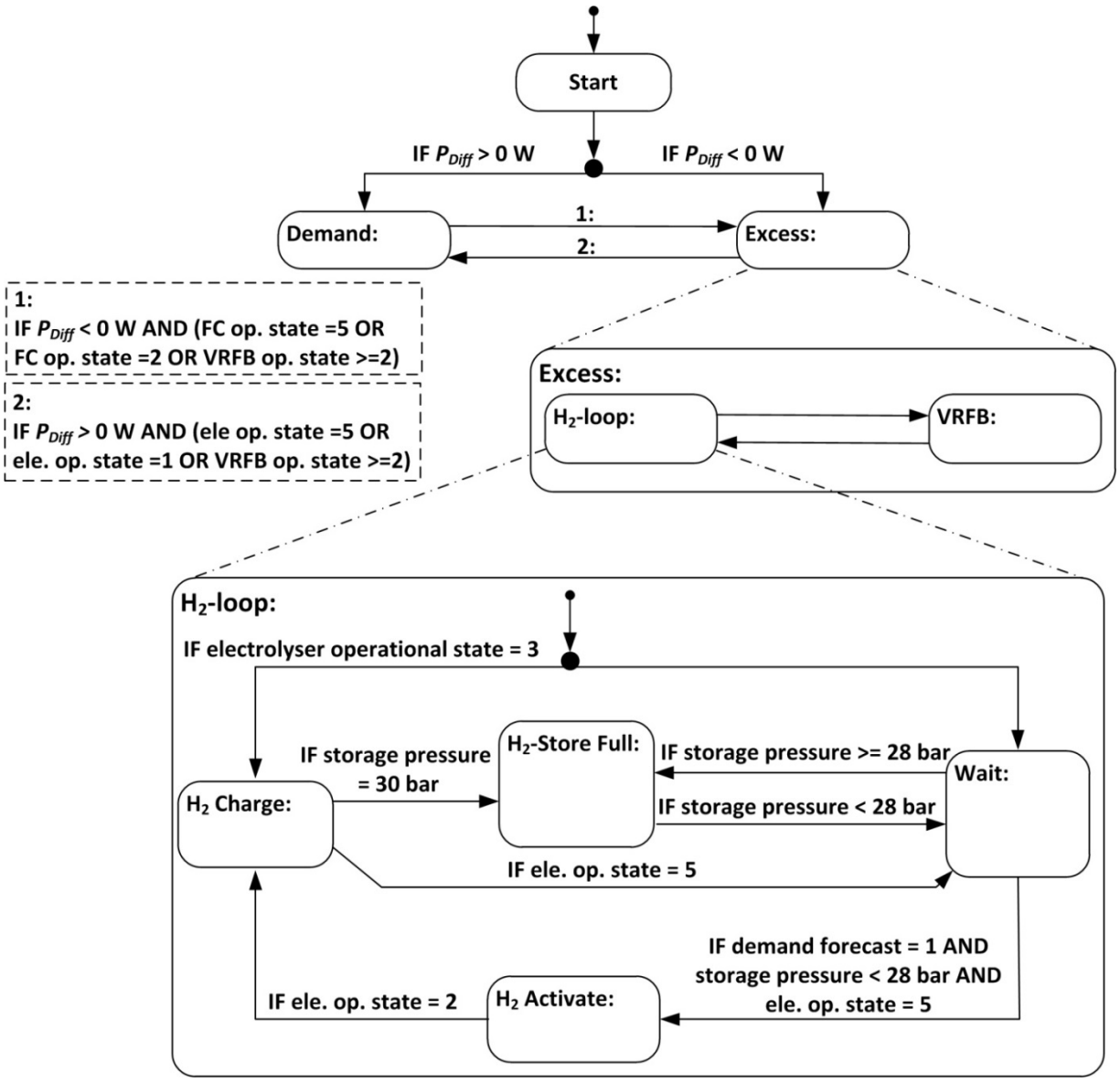


**Figure 5-27: Hierarchically organised statechart diagram to coordinate the HRES.**

### 5.4.2 Demand and SOC prediction

Since both the domestic electric load and the renewable energy sources are highly intermittent, it is difficult to predict the power difference (5-42) in the future and to determine, whether the power difference will be high enough to provide, for instance the minimum power to the electrolyser. In addition, in a HRES composed of two storage devices the time must be estimated when the second storage needs to be activated to avoid, for example an overcharging. Therefore, in this thesis a demand and SOC predictor is developed and implemented into the energy management unit. To predict the future of a time series, exponential smoothing is a widely applied method (Prins 2012). One advantage of exponential smoothing is that no large set of historic data is required and it can be applied for real-time application as demonstrated e.g. by Neusser and Canha (2013) for demand side

management. The method adopted in this thesis is based on the double exponential smoothing technique presented by Holt (2004). This allows the calculation of the forecast and the trend for the next time step. Figure 5-28 illustrates the basic structure of both the demand and SOC forecast sub-model.

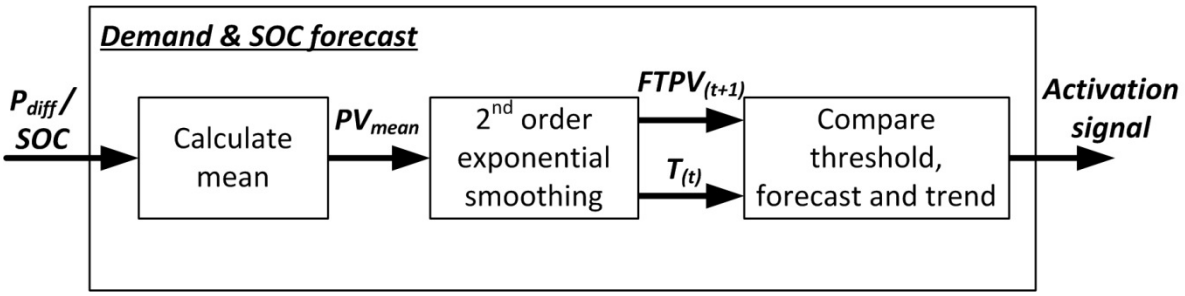


**Figure 5-28: Structure of the demand and SOC forecast sub-model.**

The input of the forecast sub-model is the power difference or the SOC. First, the moving average of the process value is calculated. Depending on the considered energy system the moving average window of the process value is defined and the calculated mean value is held constant for the time horizon of the forecast. Then, the forecast of the process value $FTPV_{(t+1)}$ (W) is calculated in three steps:

$$F_t = FTPV_{(t-1)} + \alpha * \left(PV_{mean} - FTPV_{(t-1)}\right) \quad \textbf{(5-45)}$$

$$T_t = T_{(t-1)} + \beta * \left(F_t - FTPV_{(t-1)}\right) \quad \textbf{(5-46)}$$

$$FTPV_{(t+1)} = F_t + T_t \quad \textbf{(5-47)}$$

where, $F_t$ is the smoothed level of the process value, $\alpha$ is the smoothing parameter of the level ($0<\alpha<1$), $\mathrm{PV_{mean}}$ is the actual averaged process value and $\mathrm{FTPV_{(t-1)}}$ is the forecasted value of the previous time interval. The trend value $T_t$ is calculated by equation (5-46) where $\mathrm{T_{(t-1)}}$ is the trend value of the past time period and $\beta$ is the smoothing parameter of the trend ($0<\beta<1$). The process value forecast for an averaging time period ahead is the sum of the calculated level and the trend value as stated by equation (5-47). A smoothing parameter close to 1 means that the forecast responds quicker to changes. An optimisation to find the optimal parameters for α and $\beta$ was not performed in this thesis. The values were determined experimentally and were set to $\alpha$=0.35 and $\beta$=0.15. It can be noticed from the equations above that only three values need to be stored to forecast the process value: the actual mean of the process value, the previous trend value and the forecasted value of the last period. Thus, the double exponential smoothing method is easy to implement and only low computing power is required.

Based on the calculated forecast and trend of the process value, the strategic supervisory level finally decides if the corresponding energy system will be activated. For instance, to activate the electrolyser system, the following condition must be fulfilled: the trend of the power difference must be three times in a row negative and the forecast value for the next time period has to be above the defined minimum input power. The time horizon of the forecast depends on the time to start an energy system. The electrolyser needs approximately 15 minutes to start-up. Therefore, a forecast period of 10 minutes is chosen. Consequently, the electrolyser will be activated if the trend is negative over a time period of 30 minutes and the forecast of the power difference is for example below -2000 W. Figure 5-29 illustrates the described method to activate the electrolyser. The upper diagram shows the calculated mean of the measured power difference (blue), the estimated forecast value at t-1 (magenta) and the estimated trend value (green). The lower diagram shows the signal to activate the electrolyser. Approximately at time 6:40 h the condition was fulfilled, the activation signal was set from 0 to 100 and the electrolyser was transited into the start-up mode. Note that the forecast illustrated in the graph below is shifted by one time step to show the quality of the prediction. For instance, the marked forecast value was calculated at 6:40 h.

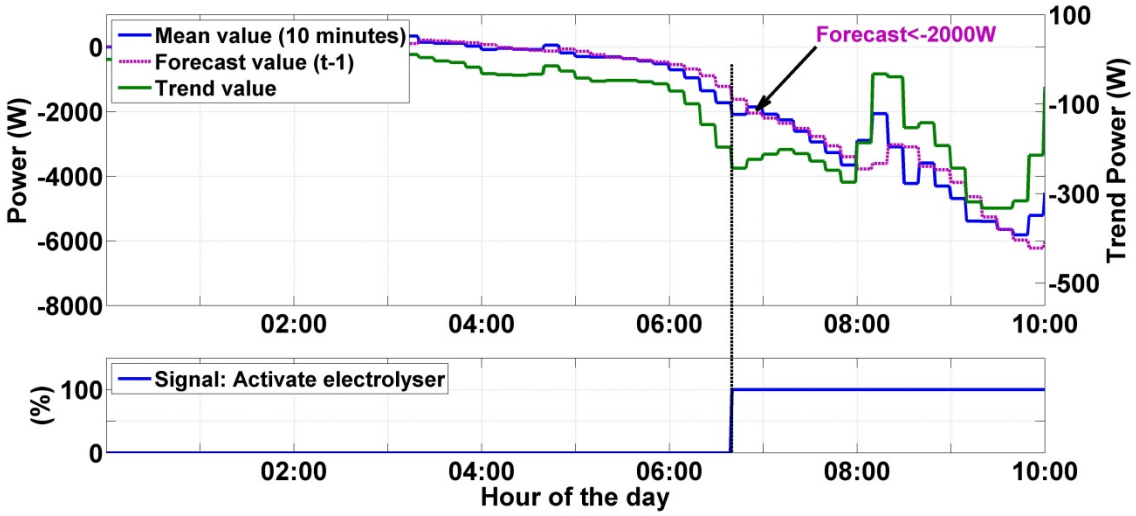


**Figure 5-29: Demonstration of the forecast algorithm to activate the electrolyser.**

The described method above is also deployed for the fuel cell and VRFB. In addition, this method is also used for the hybrid storage system to predict the SOC of the primary storage. If the SOC limit is reached the secondary storage will be activated. Considering the HREP, the primary storage device is the VRFB and the secondary storage device is the hydrogen system.

Table 5-11 summarises the defined parameters for the forecasting sub-models.

**Table 5-11: Parameters of the demand and SOC forecast sub-model.**

| | $P_{diff}$ forecast | | | SOC forecast | | |
|---|---|---|---|---|---|---|
| **Energy system** | Averaging window | Time horizon | Threshold | Averaging window | Time horizon | Threshold |
| Electrolyser | 10 minutes | 30 minutes | -2000 W | - | - | - |
| Fuel cell | 2 minutes | 6 minutes | 200 W | - | - | - |
| VRFB | 2 minutes | 6 minutes | ±500 W | 5 minutes | 15 minutes | 64 % |

### 5.4.3 Frequency decoupling

As shown in chapter 4 the capability of the energy systems to follow a dynamic load/demand is limited. Moreover, the performance of the fuel cell can be negatively influenced by highly transient operation (Erdinc & Uzunoglu 2010). To decouple high load variation from the reference power signal, a low-pass filter is implemented into the energy management. Thus, the reference signal is smoothed before it is sent to the local controller of the energy system. In Simulink® a low-pass filter (first-order filter) is simply described by a "transfer function block" (Laplace domain):

$$\frac{Output}{Input} = \frac{1}{\tau s + 1} \qquad \textbf{(5-48)}$$

where, $\tau$ is the time constant of the filter. From the results of the controlled dynamic events experiments presented in chapter 4, the time constant for the electrolyser, fuel cell and the VRFB can be estimated by applying the formula of the cut-off frequency $f_c$:

$$f_c = \frac{1}{2 * \pi * \tau} \qquad \textbf{(5-49)}$$

Table 5-12 summarises the time constants applied for the electrolyser, fuel cell and VRFB.

**Table 5-12: Filter time constants.**

| Energy system | Frequency (Hz) | Time constant (s) |
|---|---|---|
| Electrolyser | $f_c = \frac{1}{20}$ | $\tau = 3.2$ |
| Fuel Cell | $f_c = \frac{1}{40}$ | $\tau = 6.4$ |
| VRFB | $f_c = \frac{1}{40}$ | $\tau = 6.4$ |

## 5.5 Summary

In this chapter the development of mathematical models of the individual components of the HREP was presented in detail. All proposed models have the same generic layout enabling an easy integration into system level simulations of hybrid renewable energy systems in MATLAB®/Simulink®. In addition to the physical modelling of the electrical or thermal part, operational aspects such as system start-up, local control loops or operational constraints have been added to build up an integrated system model of each component. To summarise, three system models are developed namely the electrolyser, the fuel cell and the VRFB system model and they are fully validated using measured data gathered from the HREP.

The thermal model of the electrolyser is based on the lumped thermal capacity method. However, it was found that the methods proposed in the literature to derive the total thermal resistance and the thermal capacity from experimental data only provide good results at high operating power. Since the application of the electrolyser is to store power from renewable sources, it is important to develop a thermal model that also predicts the temperature at partial load with a good agreement. Therefore, a methodology is proposed to approximate those values as a function of the supplied DC current to provide an improvement over other simulation studies at system level.

The electrical model of the fuel cell system is developed from an existing semi-empirical approach. But, instead of using a constant value of the internal resistance, the value is modelled as function of the fuel cell temperature and the DC current to take the temperature dependence primarily of the membrane into account. The proposed thermal model is based on the overall thermal energy balance considering the load dependence of the temperature control system. Thus, the overall heat loss of the fuel cell system is modelled as a function of the DC current. The parameters of the proposed functions are extracted from measured data.

The electrical model of the VRFB accounts for internal losses such as voltage and current losses. An equivalent internal resistance is introduced that considers the SOC and the DC current rate. In addition, Coulombic losses are modelled by a shunt resistor in parallel with the voltage model. The shunt resistance is approximated by a function of the DC current. Furthermore, a methodology is presented to extract the parameters of the equivalent internal resistance and the shunt resistance from charge/discharge experiments.

Each system model is validated with measured data by means of the cross validation technique. To assess the accuracy of the proposed models the RMSE and the MAPE are calculated. The calculated values of MAPE are less than 3% for each proposed model. Therefore, the validation results can be considered as satisfactory for the further investigations.

The last part of this chapter develops an energy management strategy to coordinate and to control the HRES. The energy management strategy combines three different mechanisms to achieve an overall controllability. A statechart diagram is developed in Simulink®/Stateflow® that coordinates the HRES either in single storage or hybrid storage configuration. The charge/discharge operation is coordinated with respect to the power difference and information gathered from the energy systems. The second mechanism provides a forecast and trend of the calculated power difference. Based on defined thresholds to activate the energy systems and on the evolution of the trend, the strategic supervisory level decides to activate the corresponding energy system. The third mechanism takes into account the findings of the dynamic observations presented in the previous chapter. A low-pass filter is implemented to reduce the variations of the power reference signals, which are sent to the energy systems.

# 6 Performance investigation

In this chapter, the evaluation of the hydrogen loop and the VRFB is presented for both, a simulation and experimental study. In section 6.1 the simulation inputs and the defined performance indices to assess the simulations studies are introduced. Section 6.2 describes two residential use-cases to evaluate building-integrated HRES. Section 6.2.1 presents the results of the hydrogen use-case and section 6.2.2 shows the results of the residential application of the VRFB. A comparison between both use-cases is presented in section 6.2.3. Finally, section 6.3 demonstrates the real-time application of the energy management strategy and discusses the dynamic performance of the hydrogen loop and the VRFB.

## 6.1 Simulation inputs and definition of performance indices

In section 6.1.1 the data sets provided to the simulation environment are introduced. To evaluate the annual simulation results several indices are defined in section 6.1.2.

### 6.1.1 Simulation inputs

The considered electric load profile was generated by using the electric load model presented by Richardson et al. (2010). The model can be parameterised by using a software tool developed by Richardson and Thomson (2010). This model takes into account occupancy patterns and site specific minutely data of the solar radiation. In addition, it covers a wide range of domestic appliances. The parameters applied in this thesis are presented in the appendix A-4-2. Site specific data of the solar radiation, for the year 2013 in Wolfenbüttel, was taken from the database of the HREP. From the raw data an annual data set was generated and passed to the software tool. Afterwards an annual load profile for a typical 4-person household was generated with an annual electric energy consumption of 4707.4 kWh with a temporal resolution of one minute. This load profile was used as reference for all conducted simulations. Figure 6-1 depicts the annual load distribution as a carpet plot (top graph) and the daily load profile of the day 201 (lower diagram). By applying the carpet plot as graphical representation of the annual data a lot of information can be condensed and consumption patterns can be easily identified. The abscissa in the graphs represents the day of the year and the ordinate shows the hour of the day. The different colours indicate the magnitude of the electric demand. The main activity in the dwelling was during the morning and the evening. In addition, the carpet plot illustrates the stochastic behaviour of the demand of a dwelling varying from a few hundred watts over most of the time to several thousand watts for short periods with very fast transient change. A typical daily load profile is presented in the lower diagram. This diagram shows the electrical demand of the 20$^{th}$ July of 2013 (weekend day). During the morning the demand was relatively low. The base-

load was around 50 W with periodically spikes of a few hundred watts. Between 10:50 h and 11:10 h the electric demand rose quickly from 720 W to 7000 W within a few minutes. During the evening the electric consumption increased again with a higher demand period around 21:00 h with a power level above 3000 W.

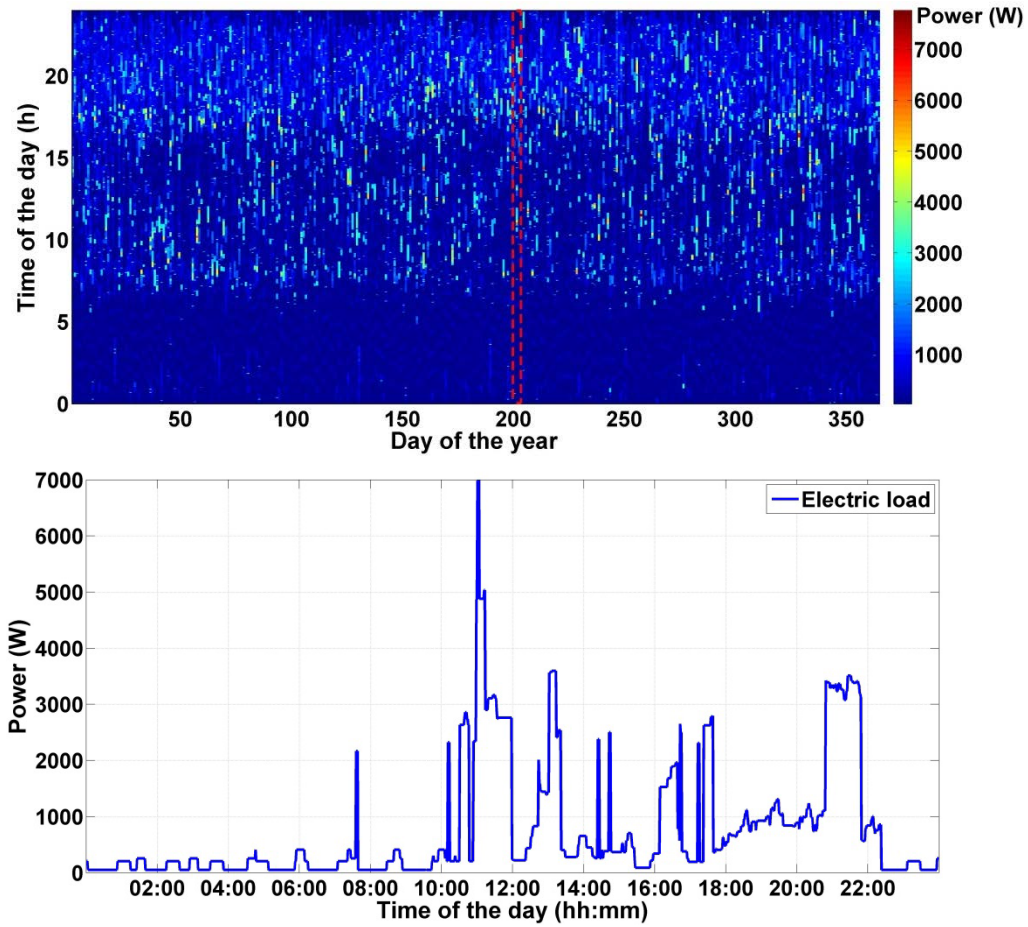


**Figure 6-1: Annual load profile (top diagram) and daily load profile of the 20th July 2013 (day 201).**

To analyse the capability of the hydrogen system, especially of the electrolyser, to supply additional heat for domestic hot water (DHW), a hot water demand profile was generated using an interactive tool developed by Jordan and Vajen (2005). This tool creates an annual domestic hot water profile with a temporal resolution of one minute. The average daily hot water consumption was assumed to be 200 l/day for a four-person household. Figure A-14 shows the generated annual daily hot water consumption.

The power output of the renewable energy sources of the HREP was measured with a temporal resolution of one second. This data was processed to generate annual power profiles of three installed PV arrays with a temporal resolution of one minute. Figure 6-2, for instance, presents the annual power generation of one 2.5 $kW_p$ PV system of the HREP installed at Ostfalia University

Wolfenbüttel in the year 2013. In total, the annual energy yield of the PV system amounts to 1991 kWh. The power output of PV was extremely stochastic throughout the year with high production periods during the summer and low to zero production periods during the winter season. Compared to other years the intercepted PV energy was relatively low, for instance, in 2011 the annual energy yield was 2364 kWh. A detailed view on the PV profile of day 201, the 20th July 2013, is given in the lower diagram.

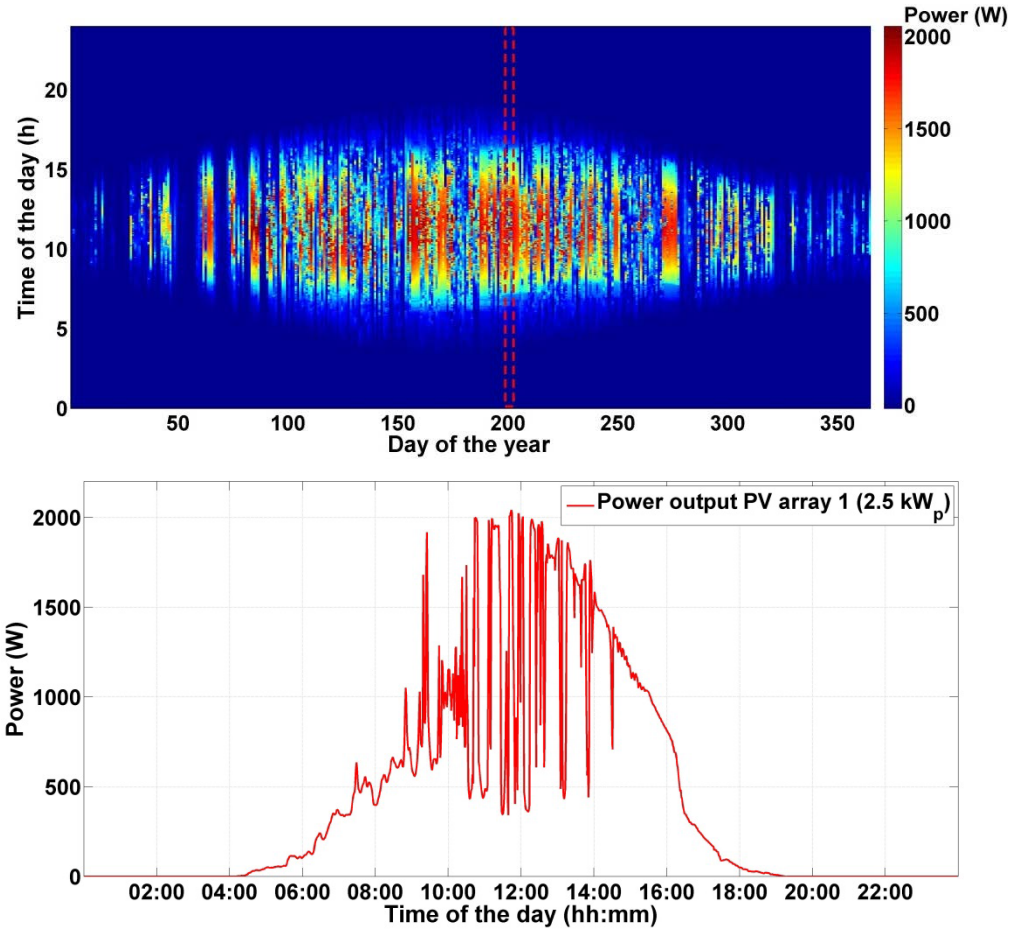


**Figure 6-2: Annual PV power profile (top diagram) and daily PV generation of the 20th July 2013 (day 201).**

During the early morning the PV system started to generate power with an increasing trend. Between 09:30 h and 15:00 h the power output of the PV was highly fluctuating due to scattered clouds. For the use-cases presented below the aggregated power output of the PV systems was scaled to meet the considered PV size.

As stated in chapter 1, the penetration of renewable energy has reached critical levels in Germany and challenges the grid capacity. Especially in the northern part of Germany with a high penetration of wind energy, the generated power cannot be distributed at times with high wind and low demand. In this regard, the power output of the wind farms needs to be reduced at certain times. In 2011 the

aggregated loss of production caused by grid congestion was 420.6 GWh and approximately 98% of these losses relate to wind farms installed at the distribution level (Bundesnetzagentur 2014). Hence, there is an increasing need to establish more flexible electricity grids which are able to locally manage the energy flow. In this context, the capability of buildings to be an active partner in the low voltage grid is considered in the use-cases as well. It is assumed that a DSR signal, the smart grid message, is provided from a smart grid operator. This message is composed of a Boolean variable to activate the smart grid mode and of the power reference signal at the PCC. For the simulation study the frequency of smart grid interaction was derived from a report presented by Börmer (2011). He stated that on 107 days in 2010 the power output of wind farms was actively manipulated by the grid operator. Since the wind penetration is higher during the winter season in northern Germany, the generated annual smart grid message profile shows activity during the winter, spring and autumn at 55 days. It has to be noticed that this profile is purely artificial and it is not based on proper analyses of the electrical grid condition of the considered location (Wolfenbüttel, Germany) and year (2013); its sole purpose is to demonstrate the principal response of the building-integrated HRES to a DSR signal.

### 6.1.2 Definition of the performance indices

The evaluation of the simulation scenarios was conducted by calculating a certain number of indices, which assess the performance of the components and the whole building-integrated HRES. At component level the AC energy efficiency was calculated as outlined in Chapter 4 for each energy system.

Regarding the electrolyser and the fuel cell, the overall annual energy efficiency was calculated as follows:

$$\eta_{ele,annual} = \frac{E_{H_2,HHV} + E_{ele,useable\ Heat}}{E_{ele,AC}} \quad \textbf{(6-1)}$$

$$\eta_{FC,annual} = \frac{E_{FC,AC} + E_{FC,useable\ Heat}}{E_{H_2,LHV}} \quad \textbf{(6-2)}$$

where, the $E_{H_2,HHV}$ is the accumulated energy of the generated hydrogen (HHV) transferred to the storage (kWh), $E_{ele/FC,useable\ Heat}$ is amount of utilised heat (kWh), $E_{ele/FC,AC}$ is accumulated AC energy and $E_{H_2,LHV}$ is the accumulated energy content of the hydrogen (LHV) supplied to the fuel cell (kWh).

To assess how the locally generated PV energy matches the current demand, two performance indices, the supply cover factor $\gamma_{supply}$ and the load cover factor $\gamma_{load}$, can be defined.

The first index, $\gamma_{supply}$, describes the proportion of the on-site generated renewable energy that is used by the building (Salom et al. 2013). High energy export rates are characterised by a low supply cover factor. The second index, $\gamma_{load}$, describes the degree of autonomy of the dwelling. It represents the proportion of the self-consumed renewable energy to the electric demand (Salom et al. 2013). A supply cover factor equal to one indicates that the on-site generation completely satisfies the local demand and the building becomes self-sufficient.

Both indices can be calculated for different time intervals ($t_1$ and $t_2$). In the analysis presented in the next section a time period of one day was chosen to illustrate seasonal effects. The on-site consumed renewable energy $E_{self}$ (Wh) can be calculated by applying the following energy balance:

$$E_{self} = \int_{t_1}^{t_2} \left(P_{gen} - \left(P_{store,charge} - P_{store,discharge}\right) - P_{ex}\right) dt, \qquad \textbf{(6-3)}$$

where, $P_{gen}$ is the on-site generated renewable power (W), $P_{store,charge}$ is the electric power to charge the storage system (W), $P_{store,discharge}$ is the electric power supplied by the storage system (W), $P_{ex}$ is the exported power (W).

In this thesis $\gamma_{supply}$ was calculated by the following formula, which also takes into account the energy balance of the electrical storage.

$$\gamma_{supply} = \frac{min\left[E_{self}, \int_{t_1}^{t_2} P_{load} dt\right]}{\int_{t_1}^{t_2} \left(P_{gen} - \left(P_{store,charge} - P_{store,discharge}\right)\right) dt}, \qquad \textbf{(6-4)}$$

where, $P_{load}$ is the electric load (W).

The following equation was applied to calculate $\gamma_{load}$:

$$\gamma_{load} = \frac{min\left[E_{self}, \int_{t_1}^{t_2} P_{load} dt\right]}{\int_{t_1}^{t_2} P_{load}\, dt} \qquad \textbf{(6-5)}$$

The third index, the fluctuation suppression factor $\gamma_{FS}$, describes the reduction of power fluctuations at the grid connection of the building. It is also known as grid interaction index and is defined by the ratio of the grid power to the annual maximum of the grid power (Voss et al. 2010):

$$\gamma_{FS} = \frac{\int_{t_1}^{t_2}(P_{load} - P_{gen} \pm P_{store})dt}{max_{annual}\left(abs(\int_{t_1}^{t_2}(P_{load} - P_{gen} \pm P_{store})\,dt)\right)} \quad \textbf{(6-6)}$$

This index can also be calculated for different time periods ($t_1$ and $t_2$), e.g. monthly, daily or minutely. In the next section the grid interaction index is calculated on basis of the minutely sampled data. The annual grid interaction index, $\gamma_{FS,annual}$ is defined as the standard deviation of the minutely calculated values (Voss et al. 2010). High fluctuations are characterised by a high value of $\gamma_{FS,annual}$.

## 6.2 Introduction of the use-cases

To assess the application of a building-integrated hydrogen loop and VRFB two simulation use-cases were designed. Basis of the scenarios were the validated system models and the energy management strategy as described in chapter 5. Thus, the system size of the electrolyser, fuel cell and VRFB applied in the simulations were equal to the real systems installed at the HREP to compare the simulation results with the experimental and modelling work carried out in the previous chapters. In both use-cases the considered building is equipped with a PV system and it is connected to the public electricity grid as depicted in Figure 6-3. Residential PV systems are typically sized with a power output ≤ 10 $kW_p$. For the simulation study, the rated power of the PV system was initially set to 8 $kW_P$, which is a typical size for new installed residential systems in Germany (Seel, Barbose & Wiser 2014). Issues related to optimal system configuration are beyond the scope of this thesis. Three different simulation scenarios were considered in each use-case. More details are outlined in the following sections.

The simulations were carried out on a standard personal computer with MATLAB/Simulink 2012b. All PI-controllers (local control level of the system models) were discrete controllers with a sample time of one second. For the analyses the simulation output data were stored minutely. Energy values were continuously integrated and stored on a daily basis (24*3600 s).

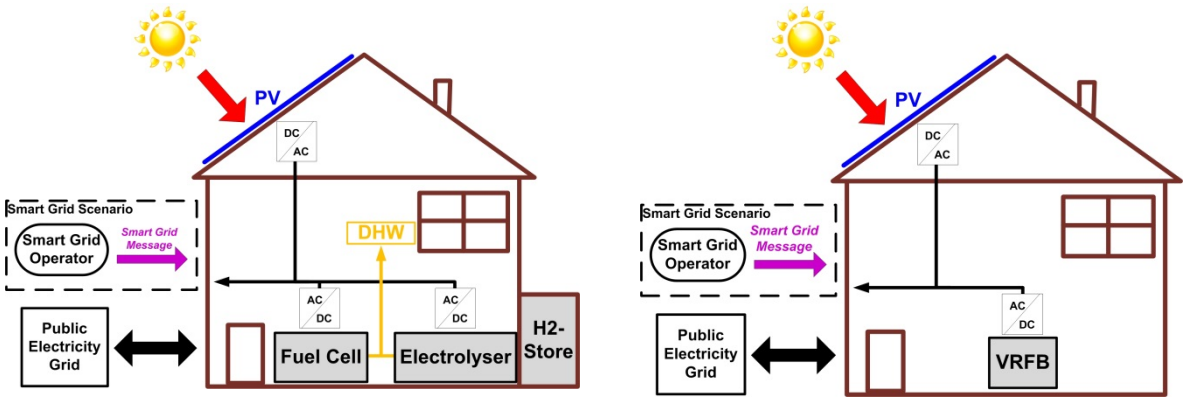


**Figure 6-3: Simulation use-cases: Hydrogen system (left) and VRFB system (right).**

### 6.2.1 Use-Case 1: Building-integrated hydrogen system

Three different scenarios of building-integrated HRES with hydrogen loop are presented in this section. The first scenario, $H_2$-I, analyses the installation of the hydrogen loop in a dwelling equipped with a typically sized PV array. Additionally, a second scenario, $H_2$-II, was defined to investigate the influence of the PV system size on the performance of the hydrogen loop and the grid interaction. Finally, a third scenario, $H_2$-III, was introduced to discuss the possibility of the building to response to DSR signal in a smart grid environment. The system configuration of each scenario is summarised in Table 6-1. As can be seen from the table, the system configuration of scenario $H_2$-I and $H_2$-III were identical and that they differ only in terms of the DSR signal.

Simulation input variables were the scaled minutely averaged measured PV data of the year 2013 and the generated electric load profile for a 4-person dwelling. The generated hydrogen is stored in a compressed gas cylinder with maximum pressure of 30 bar. The storage pressure was initially set to 25 bar.

The main decision variable is the power difference $P_{diff}$ (5-42) between the electric load and the generated PV power. Based on this variable the strategic supervisory level decides whether the fuel cell or the electrolyser can be switched on. In addition, the strategic supervisory level generates the power reference signal for the local control level of the fuel cell and electrolyser.

A sensitivity analysis was conducted beforehand to investigate the influence of the control parameters on the performance and to determine the threshold values of the strategic supervisory level for both the fuel cell and electrolyser. The reader is referred to Appendix A-4-4 for detailed information. The finally applied values of the control parameters in the strategic supervisory level and local control level are listed in Table 6-2. The effectiveness of the energy management strategy, in particular of the demand forecast, is briefly discussed in the following. In the Appendix A-4-5 the results of a simulation with and without demand forecast are presented. It was found that the

demand forecast algorithm effectively prevents the electrolyser from unnecessary start-ups. Without demand forecast the number of start-ups was increased by 54% and the average operational duration was decreased by 22%. In addition, the electricity imported from the grid was slightly increased by 5% as a reason of the unnecessary start-ups. Thus, the developed energy management strategy helps to operate the energy systems more efficiently.

**Table 6-1: System configuration for the case studies with the hydrogen loop.**

| Scenario | PV system (kWp) | Electrolyser system ($kW_{max}$) | Hydrogen storage ($m^3$/bar) | Fuel Cell system ($kW_{max}$) | DSR |
|---|---|---|---|---|---|
| **$H_2$-I** | 8kWp | 7 kW (AC) | 0.6 $m^3$/30 bar $p_{initial}$=25 bar | 1.2 kW (AC) | - |
| **$H_2$-II** | 10kWp | 7 kW (AC) | 1.2 $m^3$/30 bar $p_{initial}$=25 bar | 1.2 kW (AC) | - |
| **$H_2$-III** | 8kWp | 7 kW (AC) | 0.6 $m^3$/30 bar $p_{initial}$=25 bar | 1.2 kW (AC) | X |

**Table 6-2: Parameters of the energy management.**

| | *Strategic supervisory level* | | | *Local control level* | | |
|---|---|---|---|---|---|---|
| **System** | **Minimum start-up power** $P_{diff}$ | **Time constant** | **Maximum power** | **Minimum operating power** $P_{min,Ele/FC}$ | **Hysteresis power** | **Standby time** |
| **Electrolyser** | -2500 W | 3.2 s | 7000 W | 2500 W | 2700 W | 1800 s |
| **Fuel Cell** | 150 W | 6.4 s | 900 W | 120 W | 150 W | 1800 s |

Table 6-3 provides the annual results of the building, electrolyser, fuel cell and grid to assess the performance. A summary of annual performance indices are listed at the bottom of the table. For comparison the last three rows of the table show the annual grid interaction index, the annual grid import and export without hydrogen loop. The introduction of the hydrogen loop significantly reduced the grid interaction for all three scenarios. Although, there was a surplus of PV energy for all simulation scenarios, the building depended on the grid and imported energy on an annual basis. Only a small fraction of the PV energy was directly used by the local demand at the time it was generated, most of the excess PV energy was converted into hydrogen, stored and finally reconverted into electric energy using the fuel cell. The overall electric AC efficiency of the conversion process was for all simulations less than 20%, meaning that over 80% of the electric energy supplied to the hydrogen loop was lost; most of it was dissipated as unused heat. The AC

efficiency of the electrolyser varies between 38.6% (scenario $H_2$-I) and 40.2% (scenario $H_2$-II). The results of the fuel cell showed nearly a constant AC efficiency of greater than 45%.

In the following the three scenarios are discussed in more detail; the first scenario $H_2$-I provides insight about the daily supply and load cover factor, the grid interaction and the utilisation of the waste heat of the hydrogen loop to substitute conventional generated heat to supply domestic hot water. The influence of the PV capacity is discussed in scenario $H_2$-II and the smart grid interaction is presented in scenario $H_2$-III.

**Table 6-3: Results of the annual simulation.**

| Scenario | | $H_2$-I | $H_2$-II | $H_2$-III |
|---|---|---|---|---|
| **Parameter** | | **Annual Results** | | |
| **Building:** | Electric demand (kWh) | **4707.4** | **4707.4** | **4707.4** |
| | PV generation (kWh) | **7089.5** | **8861.9** | **7089.5** |
| | Domestic hot water demand (m³) | **73** | **73** | **73** |
| **Electrolyser:** | Energy supplied to the electrolyser (kWh) | **3981.1** | **5488.2** | **5030.4** |
| | On/Off cycles of the electrolyser (-) | **278** | **300** | **329** |
| | Operating hour of the electrolyser (h) | **837.2** | **1029.5** | **1048,3** |
| | Standby time of the electrolyser (h) | **300.9** | **298.4** | **321.1** |
| | Generated hydrogen (kWh) / (Nm³) | **1536.3/434** | **2204.6/622.8** | **1955.8/552.5** |
| | Generated heat of the electrolyser (kWh) | **1071.5** | **1540.9** | **1354.4** |
| | Removed heat by cooling system (kWh) | **536.7** | **850.1** | **679.4** |
| | Cooling water supplied to DHW > 40°C (m³) | **13.3** | **21.1** | **16.9** |
| **Fuel Cell:** | Energy supplied by the fuel cell (kWh) | **621.6** | **898.2** | **787.1** |
| | On/Off cycles of the fuel cell (-) | **437** | **692** | **613** |
| | Operating hour of the fuel cell (h) | **945.3** | **1386.3** | **1237.6** |
| | Standby time of the fuel cell (h) | **254.3** | **465.1** | **376.1** |
| | Consumed hydrogen (kWh) / (m³) | **1334.3/444.8** | **1933.2/644.4** | **1688.9/563** |
| | Generated heat of the fuel cell (kWh) | **619.1** | **894.6** | **779.7** |
| | Removed heat at stack temperature > 45°C (kWh) | **593.6** | **850.1** | **742.2** |
| **Grid exchange:** | Smart grid contribution (kWh) | **-** | **-** | **1070.7** |
| | Grid import (kWh) | **3076.5** | **2731.7** | **3956.7** |
| | Grid export (kWh) | **2099.1** | **2296.2** | **2095.6** |
| **Annual performance indices** | | **Annual Results** | | |
| | Electrolyser efficiency $\eta_{AC,HHV}$ (%) | **38.6** | **40.2** | **38.9** |
| | Electrolyser overall efficiency including waste heat (%) | **52** | **55.7** | **52.4** |
| | Fuel Cell efficiency $\eta_{AC,LHV}$ (%) | **46.7** | **46.5** | **46.6** |
| | Fuel cell overall efficiency (50 % heat can be used) (%) | **68.8** | **68.4** | **68.6** |
| | Annual grid interaction index (%) | **12.3** | **9.6** | **14.8** |
| | Annual grid balance (kWh) | **976.8 (imp.)** | **435.5 (imp.)** | **790.4 (imp.)** |
| ***Without $H_2$-loop:*** | *Annual grid interaction index (%)* | ***20.8*** | ***20.4*** | ***20.8*** |
| | *Annual grid import (kWh)* | ***3541*** | ***3473.9*** | ***3541*** |
| | *Annual grid export (kWh)* | ***5923.1*** | ***7628.4*** | ***5923.1*** |

### *6.2.1.1 Results of scenario $H_2$-I*

The annual PV generation was 7089.5 kWh, 3981.1 kWh was supplied to the electrolyser and 621.6 kWh was supplied by the fuel cell. The import of electricity from the grid was reduced by 13% compared to the result of the simulation without storage. Seasonal effects on the supply and load cover factor are illustrated in Figure 6-4. The daily supply and load cover factor were calculated by applying equations (6-4) and (6-5), respectively. If the renewable energy can be completely utilised to satisfy the electric demand, the supply cover factor is equal to one as it can be seen in winter due the low daily solar energy yield. During the spring, summer and autumn the index varied between 0.39 and 1. A high supply cover factor indicates that less renewable energy is exported to grid. The annual mean values for supply cover factor with and without hydrogen loop was 0.48 and 0.31, respectively. Complementary to this, the load cover factor shows the opposite trend with low values during winter, spring and autumn and high values during the summer. In other words, during the summer months the electric demand was almost covered by on-site generated renewable energy. The annual mean load cover factor was 0.36 and 0.25 for the simulation with and without hydrogen loop, respectively.

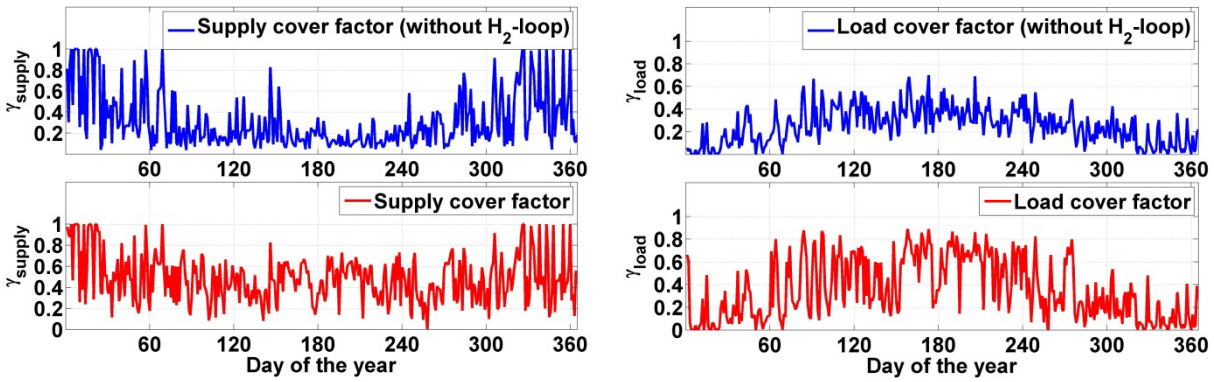


**Figure 6-4: Daily supply cover factor (left) and load cover factor (right) of the building. The upper diagram shows the corresponding index without hydrogen loop.**

As summarised in Table 6-3 the introduction of the hydrogen loop significantly reduces the grid interaction of the building. How the hydrogen loop contributes to limit the grid interaction can clearly be seen by comparing the two carpet plots presented in Figure 6-5 showing the minutely sampled power difference without (top) and with (bottom) electric storage at the PCC. The different colours indicate the magnitude of the power imported from the grid (positive values) and exported to the grid (negative values). The top graph illustrates the typical grid interaction of a dwelling equipped with PV. During the summer most of the generated electricity is injected into the grid. A completely different characteristic can be seen in the lower graph. At hours with high PV activity, the

electrolyser was able to follow the supply profile of the PV and significantly reduced the power injection into the grid. The fuel cell was in operation during the early morning and the evening lowering the power level by a maximum of 900 W. In total the electrolyser and the fuel cell were in operation for 837.1 h and 945.3 h, respectively. The start-up of the electrolyser can be identified at days where first power was exported and then, over a short time period, increased power consumption can be registered due to the start-up process of the electrolyser. The electrolyser and the fuel cell performed 278 and 437 on/off cycles, respectively.

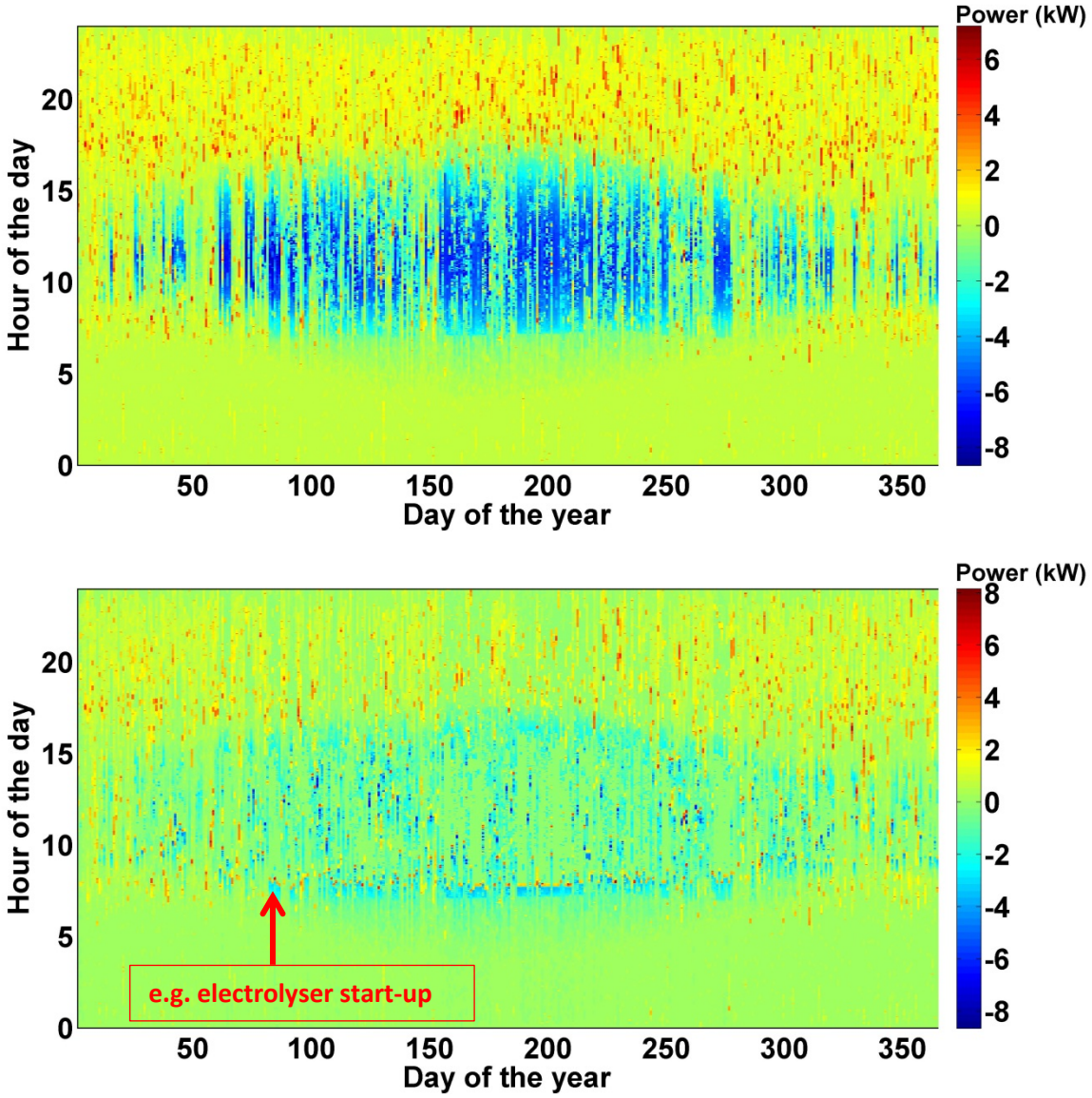


**Figure 6-5: Carpet plot of the power at the grid connection without (top) and with hydrogen loop (bottom).**

The performance of the building is illustrated in Figure 6-6 and Figure 6-7 for the day 201 (20$^{th}$ July 2013). As shown in Figure 6-6, the PV power evolution was highly fluctuating due to partly

overcast conditions. On basis of the operational arrangements listed in Table 6-2, the developed demand predictor, see section 5.4.2, of the strategic supervisory level decided to start the electrolyser around 9:30 h which is marked in Figure 6-7. The operation of the electrolyser was very intermittent with longer standby periods as it can be noticed during the time interval from minutes 600 to 800. The respective hydrogen storage pressure evolution is reported subsequently.

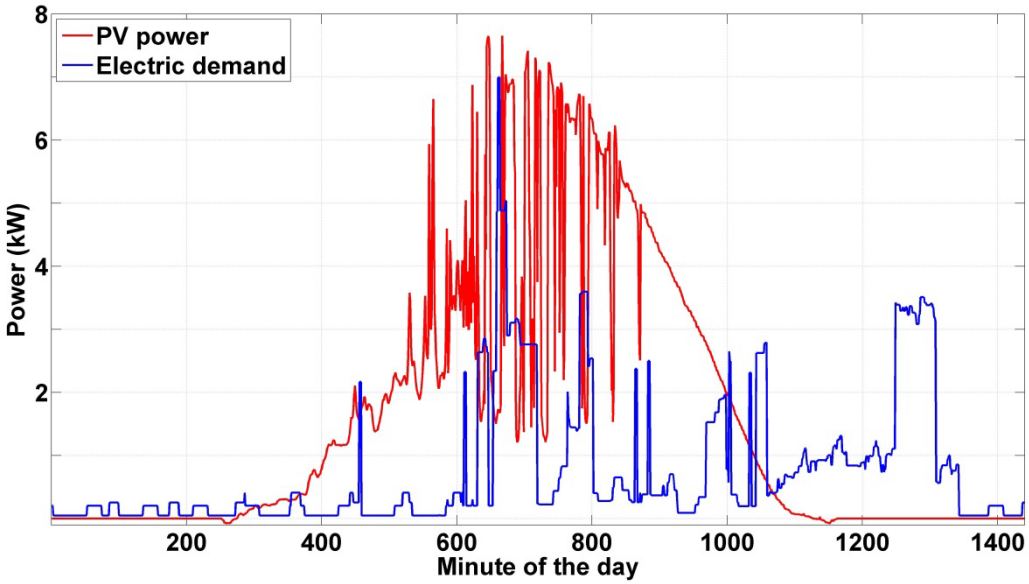


**Figure 6-6: PV and load profile for the simulation day 201 (20th July 2013).**

As Figure 6-7 shows, the electrolyser responded quickly and there is only a small mismatch between the power difference and the power consumption of the electrolyser. The implemented frequency decoupling protected the electrolyser for rapid power changes as it happened, for example shortly before minute 800. The main activity of the fuel cell was during the evening hours and it operated most of the time at maximum power. The overall electric efficiency of the hydrogen loop with values less than 20% is sobering compared to conventional lead acid batteries with a typical round-trip efficiency (AC) of values of greater than 75%. The inefficiency of the hydrogen loop is mainly due to the two stage energy converting process. A considerable amount of the losses are manifested in heat for both the electrolyser and the fuel cell. In total, the annual heat generated by the electrolyser and the fuel was 1071.5 kWh and 619.1 kWh, respectively. Capturing this waste heat of the hydrogen loop and making use of it, would improve the overall system performance.

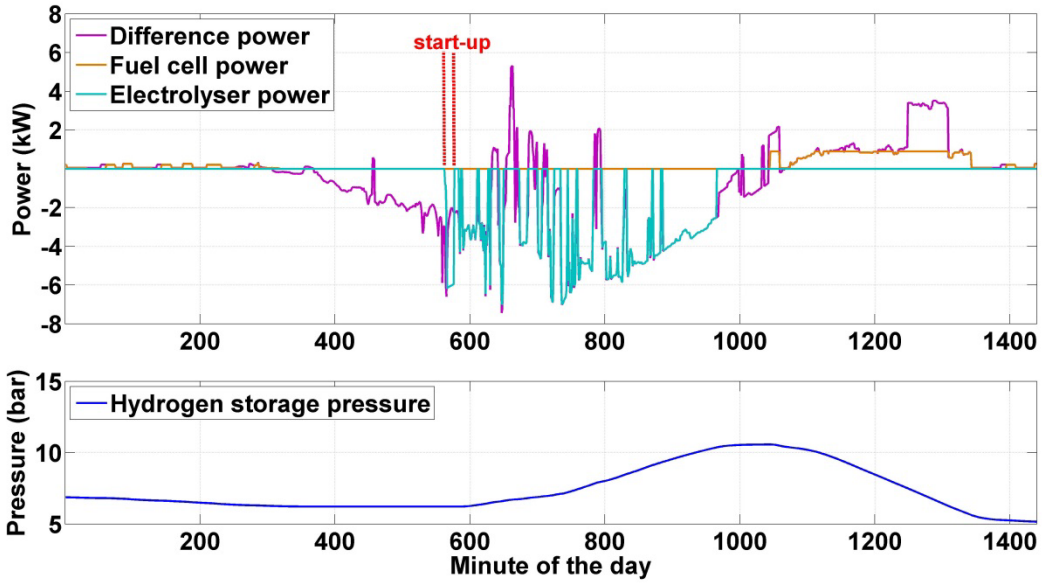


**Figure 6-7: Simulated fuel cell and electrolyser response to the difference power (top) and hydrogen storage evolution (bottom) for the simulation day 201 (20th July 2013).**

Considering residential application, the utilisation of heat for DHW would be a reasonable application. Especially, during the main operational period during the summer, the waste heat can be used to substitute heat conventionally generated, for example, by a gas boiler. This would be beneficial in terms of lowering the primary energy demand and reducing the carbon dioxide emission of the building. Figure 6-8 illustrates the DHW consumption of the building for the simulated time period and the amount of cooling water leaving the electrolyser with a temperature of about 40°C. The annual DHW demand was 73 m³ and the cooling water consumption 13.3 m³, which is equal to approximately 2550 kWh and 455 kWh of thermal energy[1], respectively. Approximately 18% of the annual DHW demand can be substituted by the electrolyser, leading to an overall electrolyser system efficiency of 52%. Regarding the fuel cell, it was assumed that 50% of the removed heat can be captured, resulting in an overall fuel cell system efficiency of 68.8%. Based on these figures the overall efficiency of the hydrogen loop is increased from less than 20% to approximately 35%. Although not explored in depth, it can be concluded that the utilisation of the waste heat, especially of the electrolyser, significantly improves the performance of the hydrogen system. This contribution can be further developed by optimising the thermal management of the electrolyser. For instance, the electrolyte vessels, the cell stack and the piping system are not insulated, see Figure 3-6. Thermal lagging would minimise the heat losses to the surrounding environment, it would reduce the warm-

[1] Calculation based on the assumption that the inlet temperature is 10°C and the average DHW temperature is 40°C.

up period and it would help to maintain the electrolyte temperature in phases of high intermittent operation, which will finally lead to an improvement of both the electric and thermal efficiency.

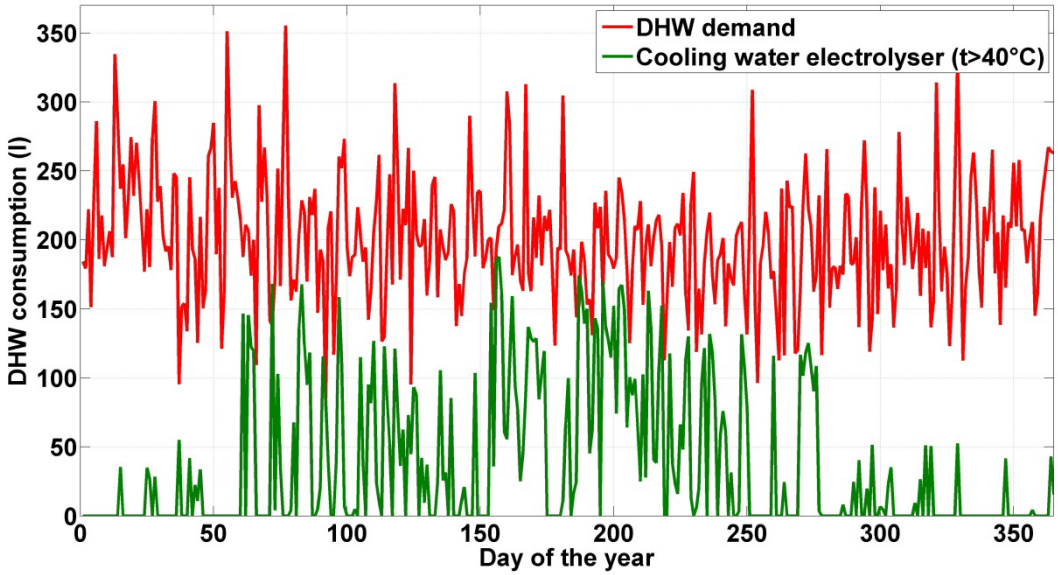


**Figure 6-8: Comparison of the DHW demand and cooling water of the electrolyser.**

### *6.2.1.2 Results of scenario $H_2$-II*

The second scenario investigates the same building, but equipped with a 10 $kW_p$ PV system. The annual PV energy yield was 8861.9 kWh, the electrolyser consumed 5488.2 kWh and the fuel cell generated 898.2 kWh. Compared to scenario $H_2$-I the average operating power of the electrolyser increased from 4755 kW to 5331 kW. Consequently, the electrolyser was operated at higher power levels, which led to an AC system efficiency of 40.2%. In addition, the electrolyser's overall performance including the thermal energy increased from 52% to 55.7%.

The efficiency of the fuel cell was not affected and remained at a level >46%. Interestingly, the annual grid interaction decreased from 12.3% to 9.6%. Although the PV capacity was increased by 2 $kW_p$, the electrolyser was able to smooth out more power peaks compared to scenario $H_2$-I. Sensitivity analysis was carried out to establish the impact of the PV system size on the annual performance. The reader is referred to AppendixA-4-6 for further details. The main outcome of the sensitivity analysis is illustrated in Figure 6-9. With increasing PV power the annual grid interaction index first decreases due to the better ratio of PV power and electrolyser power, but, at PV sizes greater than 12 $kW_p$ it starts to increase again because of the high difference between the power rate of the electrolyser and the PV system. From the results it can be concluded that the PV system size should be in a range between 10 $kW_p$ and 12 $kW_p$ to achieve an overall good performance of the installed 7 kW electrolyser system.

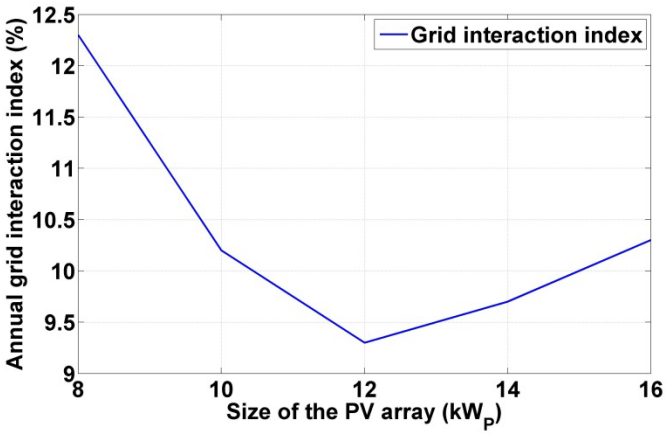


**Figure 6-9: Grid interaction index for different PV sizes.**

### *6.2.1.3 Results of scenario $H_2$-III*

The last application scenario is based on the same system configuration as presented in scenario $H_2$-I, but, the building can respond to a DSR signal provided by a grid operator. As noted before, this signal contains a Boolean variable to activate the smart grid operation and a power reference signal for the building's PCC. According to this information the strategic supervisory level coordinates the hydrogen loop.

The results of the third scenario are also listed in Table 6-3. Compared to scenario $H_2$-I, the operational hours of the electrolyser were increased from 837.2 h to 1048.3 h. The annual electric energy imported from the grid increased from 3076.5 kWh to 3956.7 kWh. However, 1070.7 kWh can be contributed to the forced energy consumption of the electrolyser due to the smart grid message. Considering this, the annual grid balance can be reduced from 976.8 kWh (import) to 790.4 kWh (import). The substitution of conventionally produced DHW can be increased by 3.6 m³ (144.6 kWh of thermal energy). Due to the increased hydrogen production, the fuel cell was in operation for 1237.6 h and supplied 787.1 kWh of electric energy. Figure 6-10 illustrates the annual smart grid message profile (upper diagrams) and the response of the building at day 35 (lower diagram). The strategic supervisory level activated the electrolyser according to the smart grid message. After the electrolyser was transited into normal operation, the power imported from the grid was stabilised at 5200 W for nearly 5 hours.

The conclusion from this simulation scenario is that, there is only a small improvement in terms of energy efficiency if the building-integrated hybrid systems responses to a smart grid signal. From a grid operator perspective, the introduction of electric storage and advanced communication would offer the possibility to manage the grid usage and to improve the overall grid performance, which would finally help to integrate a higher share of renewable energy sources without necessarily

expand the grid capacity. Nevertheless, the application of electrical storage would be only feasible if a business model exists. For example, the introduction of time varying tariffs, which consider peaks and valleys of the electricity grid or that the electricity supplier reward the building owner to remotely control the storage at certain times.

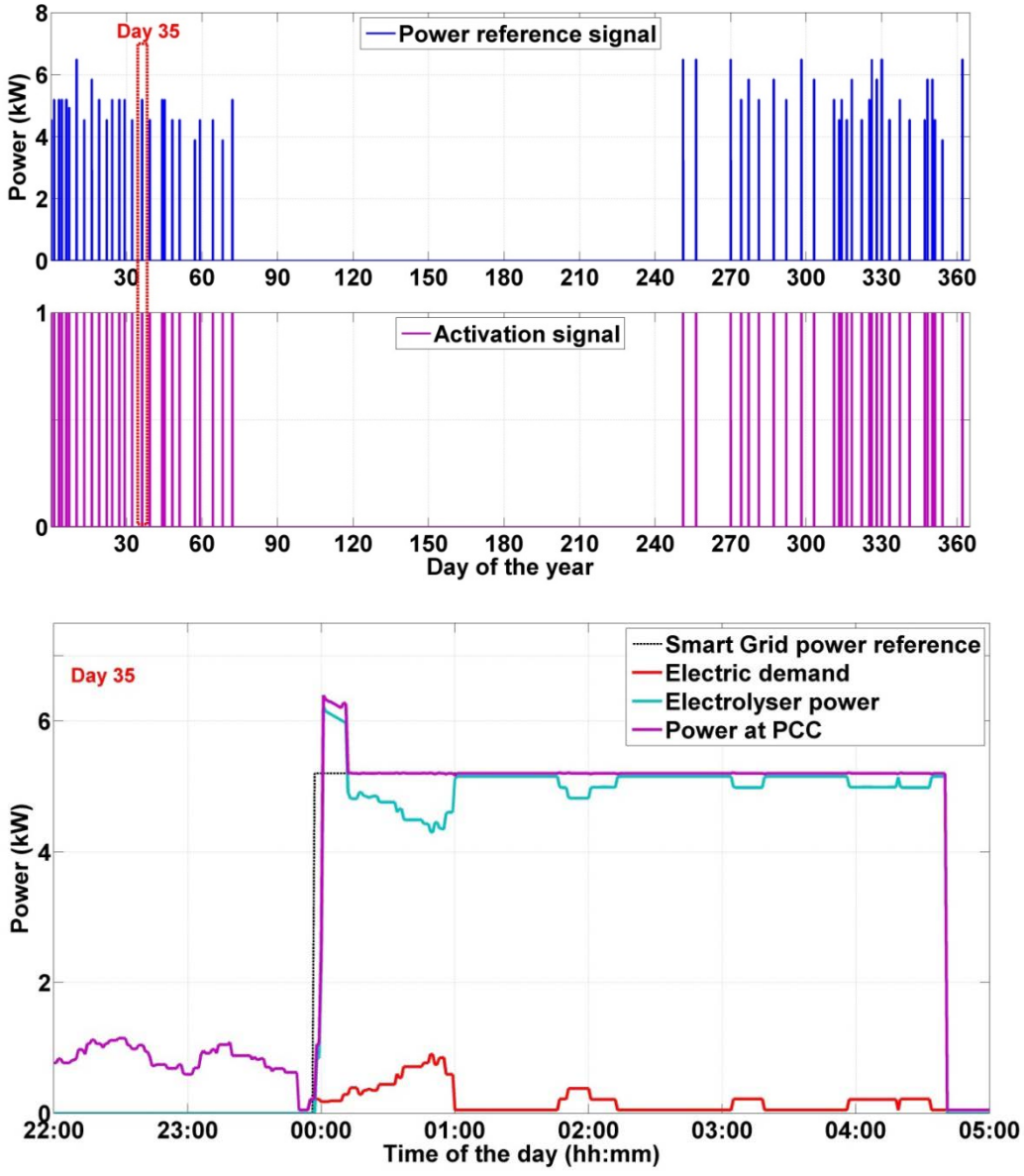


**Figure 6-10: Smart grid message profile (top) and the response of the building at day 35 (bottom).**

#### *6.2.1.4 Summary and conclusions of the $H_2$ simulation scenarios*

In the previous section the application of a building-integrated hydrogen loop was analysed by applying the proposed energy management strategy presented in section 5.4 and the developed system models introduced in section 5.2. Three different scenarios were designed to evaluate the annual performance and the grid interaction of the building.

A sensitivity analysis was performed to assess the effectiveness of the developed energy management strategy. The number of start-ups of the electrolyser was reduced by 54% and the average operational duration was increased by 22% compared to a simulation without demand forecast. The electrolyser and the fuel cell were only activated if the defined criteria in the demand forecast sub-model were fulfilled. In addition, both the electrolyser and the fuel cell were protected against rapid power changes by the frequency decoupling sub-model. Furthermore, based on a parameter analysis threshold values of the control parameters were determined to improve the efficiency. Moreover, it was shown that the introduction of the hydrogen loop significantly reduces the grid interaction of the building. However, the overall electric efficiency of the hydrogen loop with values below 20% is poor compared to conventional lead acid batteries with a typical round-trip efficiency (AC) of values greater than 75%.

In scenario $H_2$-I it was shown that a considerable amount of the losses is manifested in heat for both the electrolyser and the fuel cell. Capturing the waste heat of the hydrogen loop and making use of it, would improve the overall system efficiency from less than 20% to approximately 35%. In addition, the utilisation of waste heat of the electrolyser can be used to satisfy 18% of the annual DHW demand in the building. This contribution can be further developed by optimising the thermal management of the electrolyser.

In scenario $H_2$-II it was found that the performance of the electrolyser is affected by the PV system size. Of course, the higher the available PV power, the higher the average operating power of the electrolyser leading to an improved AC system efficiency. However, from a sensitivity analysis it was found that the installed PV power also affects the grid interaction. For the considered 7 kW electrolyser system the optimal size of the PV system should be in a range from 10 $kW_p$ to 12 $kW_p$ to achieve an good performance and low grid interaction.

Scenario $H_2$-III investigated the smart grid interaction of the building-integrated hybrid system. It was shown that the electrolyser can be used to store available energy from the public grid if needed. However, only from a grid operator perspective this option would be beneficial. The introduction of electric storage and advanced communication would offer the possibility to manage the grid usage and to improve the overall grid performance, which would finally help to integrate a higher share

renewable energy sources. Regarding the annual performance of the HRES, the smart grid application would not lead to an improvement. This highlights the need to introduce a business model that considers, for example, time varying tariffs or that the electricity suppliers reward the building owner to remotely control the storage at certain times.

### 6.2.2 Use-case 2: Building-integrated VRFB system

To analyse the application of building-integrated VRFB systems, three different simulation scenarios were defined. The differences between the three scenarios are listed in Table 6-4. As for the hydrogen use-case, the first scenario, VRFB-I, analyses the installation of the VRFB into a dwelling equipped with a typically sized PV array. The second scenario, VRFB-II, investigates the influence of the electric demand on the performance of the VRFB and SOC utilisation. Finally, the third scenario, VRFB-III, analyses the possibility of the building to respond to DSR signal.

Simulation input variables were the scaled minutely averaged measured PV data of the year 2013 and the generated annual load profile. In scenario VRFB-I and VRFB-III the VRFB is installed in a detached house with 4 occupants. In scenario II the application of the VRFB was considered in a semi-detached house with in total 7 occupants. The additional annual electric demand of the second family was 4334.6 kWh. The initial SOC of the battery was set to 32%.

**Table 6-4: System configuration for the case studies with the VRFB.**

| Scenario | PV system (kWp) | VRFB-System (kW/kWh) | Electric demand (kWh) | DSR |
|---|---|---|---|---|
| **VRFB-I** | 8 kWp | 6 kW/20 kWh | 4707.4 | - |
| **VRFB-II** | 8 kWp | 6 kW/20 kWh | 4707.4+4334.6 | - |
| **VRFB-III** | 8 kWp | 6 kW/20 kWh | 4707.4 | X |

A sensitivity analysis was conducted to examine the impact of the different control parameters (e.g. minimum charge power) on the performance of the VRFB. Details of the performed analysis can be found in the Appendix A-4-7. Table 6-5 presents the finally applied control parameters for both the strategic supervisory level and the local control level.

**Table 6-5: Parameters of the energy management.**

| | ***Strategic supervisory level*** | | | ***Local control level*** | | |
|---|---|---|---|---|---|---|
| **System** | **Minimum start-up power** $P_{diff}$ | **Time constant** | **Maximum power** | **Minimum charge power** | **Minimum discharge power** | **Standby time** |
| **VRFB** | -1100 W | 6.4 s | 6500 W | 1100 W | 300 W | 600 s |

Table 6-6 outlines the results of the three performed case studies. A summary of annual performance indices is listed at the bottom of the table. The last three rows show the annual grid interaction index, annual grid import and the annual grid export without VRFB system. The introduction of the VRFB significantly reduced the grid interaction for all three scenarios. On an annual basis, energy was exported in scenario VRFB-I and VRFB-III, whereas energy was imported in scenario VRFB-II because of the increased electrical demand. The round-trip AC energy efficiency showed values around 46% for scenario VRFB-I and VRFB-III. In scenario VRFB-II the AC efficiency slightly rose to 48.8%.

In the following sections the three scenarios are discussed in more detail.

**Table 6-6: Annual simulation results of three case studies.**

| **Scenario** | | **VRFB-I** | **VRFB-II** | **VRFB-III** |
|---|---|---|---|---|
| **Parameter** | | **Annual Results** | | |
| **Building:** | Electric demand (kWh) | **4707.4** | **9042** | **4707.4** |
| | PV generation (kWh) | **7089.5** | **7089.5** | **7089.5** |
| | Operating hours PV | **3550** | **3550** | **3550** |
| | Number of hours for which $P_{diff}$<-1100 W | **1560** | **1357** | **1560** |
| | Number of hours for which $P_{diff}$>300 W | **3028** | **4502** | **3028** |
| **VRFB:** | | | | |
| | Discharged AC electricity (kWh) | **1539.1** | **1873.6** | **1850.1** |
| | Charged AC electricity (kWh) | **3333.6** | **3839.1** | **3982.9** |
| | Discharged stack electric charge (Ah) | **41406** | **48878** | **49849** |
| | Charged stack electric charge (Ah) | **47551** | **55555** | **57225** |
| | On/off cycles | **2064** | **1930** | **2261** |
| | Operational hours | **2777.9** | **2457.8** | **3300.4** |
| | Standby hours | **288.1** | **195.2** | **352** |
| **Grid exchange:** | Smart grid contribution (kWh) | **-** | **-** | **798.8** |
| | Grid import (kWh) | **2027.9** | **5105.5** | **2521.8** |
| | Grid export (kWh) | **2615.5** | **1187.4** | **2771.2** |
| **Annual performance indices** | | **Annual Results** | | |
| | Efficiency $\eta_{energy,AC}$ (%) | **46.2** | **48.8** | **46.5** |
| | Annual grid interaction index (%) | **13.7** | **12.6** | **15.9** |
| | Annual grid balance (kWh) | **587.6 (exp.)** | **3918.1 (imp.)** | **1048.2 (exp.)** |
| ***Without VRFB:*** | *Annual grid interaction index (%)* | ***20.8*** | ***19.8*** | ***20.8*** |
| | *Annual grid import (kWh)* | ***3541*** | ***6937.8*** | ***3541*** |
| | *Annual grid export (kWh)* | ***5923.1*** | ***4985.3*** | ***5923.1*** |

### *6.2.2.1 Results of scenario VRFB-I*

The energy harvest of the PV system was 7089.5 kWh and the load demand was 4707.4 kWh. The amount of electric energy supplied to the VRFB and supplied by the VRFB was 3333.1 kWh and 1539.1 kWh, respectively. The building imported 2027.9 kWh from the public electric grid. Compared to the simulation without VRFB, the import was significantly reduced by 43%. Figure 6-11 compares the daily supply cover factor and the daily load cover factor of the building with and without VRFB. The presence of the VRFB was mostly visible in the time period between the days 60 to 300. The supply cover factor significantly increased, thus, less energy was exported to the grid. The annual values of the supply cover factor with and without VRFB were 0.61 and 0.31, respectively. In addition, the load cover factor was noticeably increased. During the summer the building became almost self-sufficient ($\gamma_{load} = 1$). The annual load cover factor was 0.58 and 0.25 for the simulation with and without VRFB, respectively.

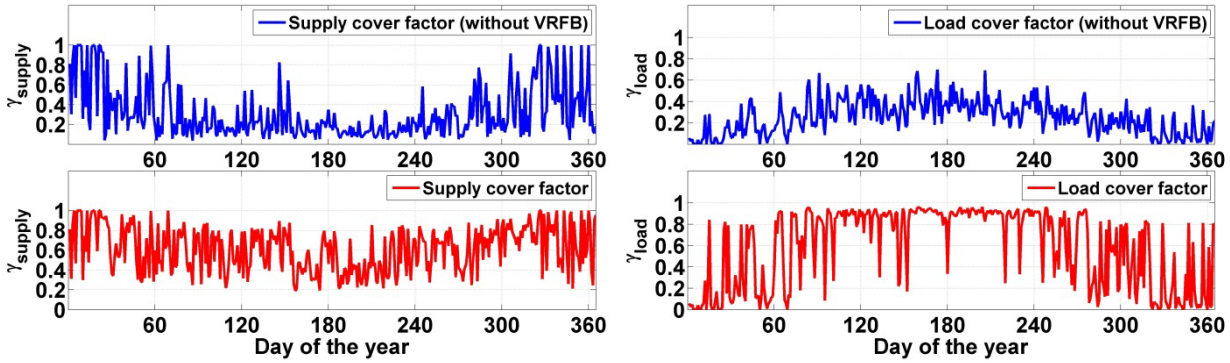


**Figure 6-11: Daily supply cover factor (left) and load cover factor (right) of the building. The upper diagram shows the corresponding index without VRFB.**

The annual grid interaction index was reduced from 20.8% to 13.7% by introducing the VRFB. Compared to scenario $H_2$-I, this improvement is slightly lower because of the smaller energy capacity of the VRFB compared to the hydrogen system. Figure 6-12 shows the grid interaction of the building with (bottom) and without (top) VRFB system. High activity of the VRFB can be registered during the spring, summer and autumn season. From the lower carpet plot it can be seen that the VRFB was most of the time in operation between morning and early afternoon storing surplus energy from the PV. In the evening hours the VRFB was discharged and high energy peaks were compensated, which can be noticed by a more uniform colour distribution. Throughout the year the VRFB performed 2064 on/off cycles, operated in total 2777.9 h and was 288.1 h in standby.

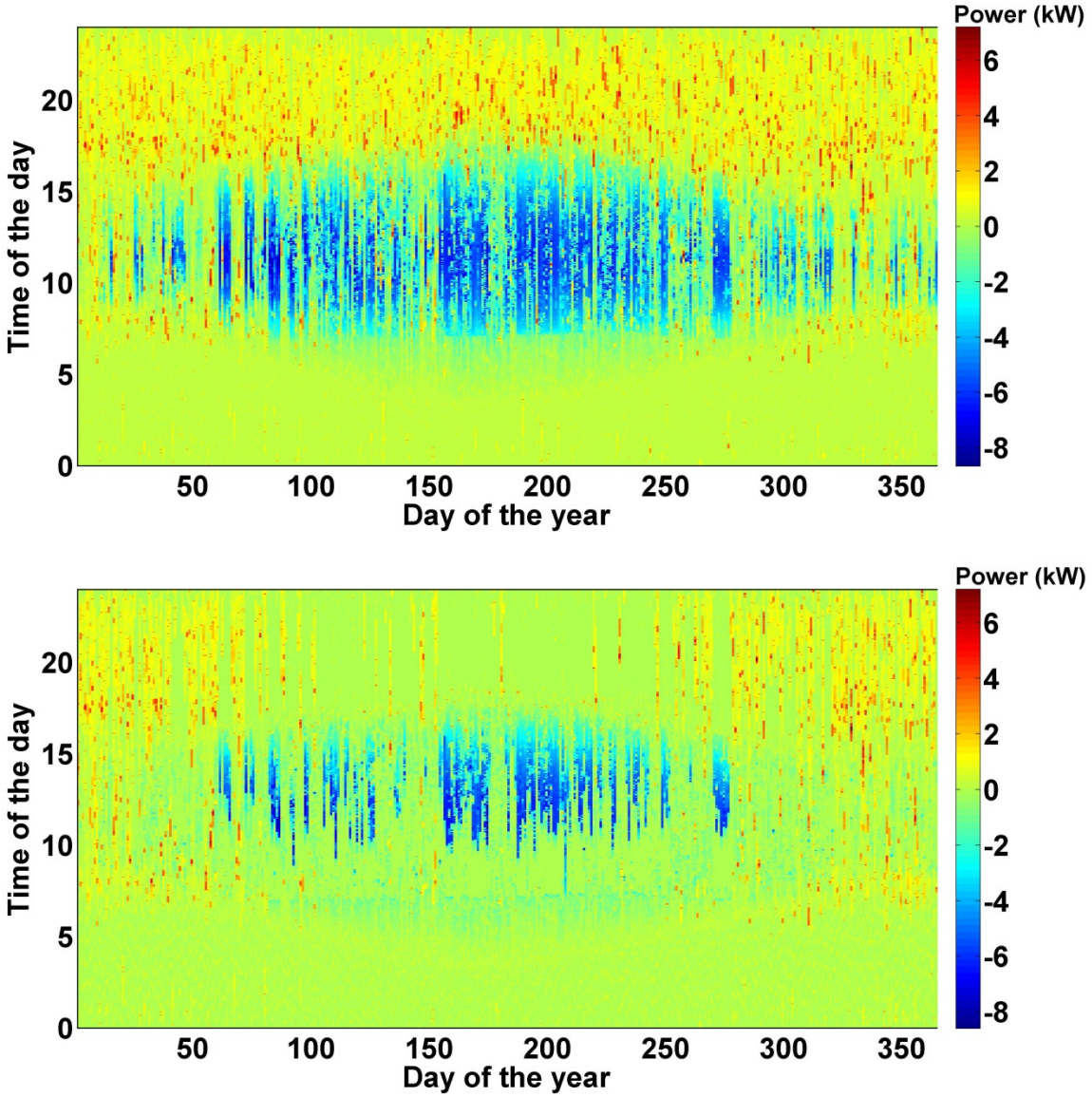


**Figure 6-12: Carpet plot of the power at the grid connection without (top) and with VRFB (bottom).**

The daily performance of the building is illustrated in Figure 6-6 and Figure 6-13 for the day 201 (20$^{th}$ July 2013). The sky was partly cloudy as can be seen from the highly fluctuating PV generation. On basis of the operational arrangements listed in Table 6-5, the developed demand predictor, see 5.4.2, of the strategic supervisory level decided to start the VRFB in the morning around 7:00 h (marked with "A" in the upper diagram of Figure 6-13). The first hour of operation was very intermittent; the VRFB was transited between charge, standby and discharge. Later, the VRFB was charged along with the increasing PV power. After 10:00 h the cloud cover approached and the VRFB followed the highly fluctuating power difference (5-42), see "B" in the upper diagram of Figure 6-13.

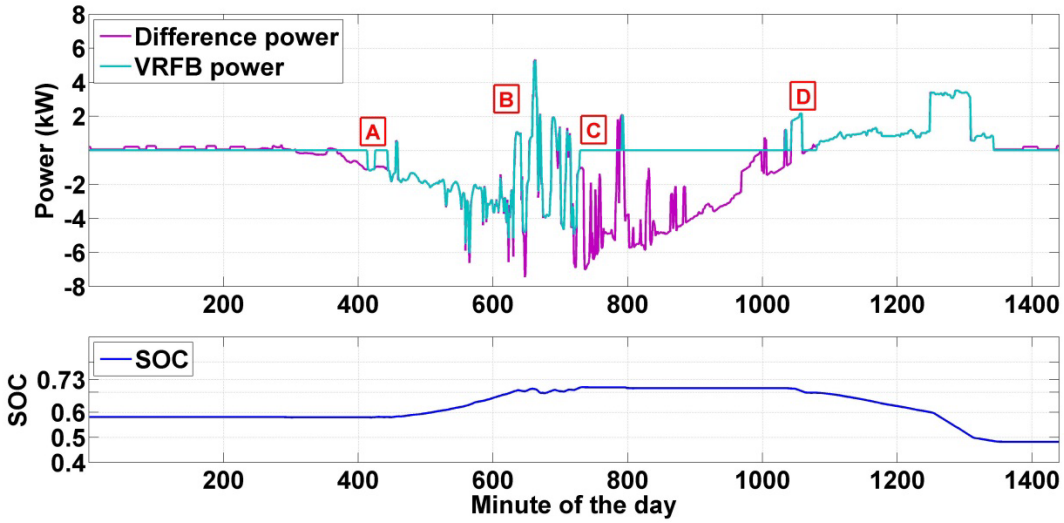


**Figure 6-13: Simulated response of VRFB to the difference power (top) and hydrogen storage evolution (bottom) for the simulation day 201 (20th July 2013).**

Subsequently, SOC evolution is reported in Figure 6-13. The SOC was at a relatively high level of 58%. During the day the SOC rose to 68% (see, "C" in the upper diagram) and further charging was restricted by the local supervisory controller of the VRFB (charging inhibited). The VRFB entered the off mode and the surplus PV was injected into the grid. During the afternoon the PV power decreased and the electric demand increased. At point "D" the VRFB was activated and the electric demand was fully served by the VRFB. It can be noticed that the VRFB was discharged mostly at low power values. At the end of the day, the SOC was at 49%.

The annual AC energy efficiency of the VRFB system was 46.2 %. One reason for this low efficiency can be found in the low average charge/discharge power of 2.9 kW and 1 kW, respectively. Especially, the low discharge power leads to inefficiencies caused by the high energy demand of the two electrolyte pumps. Furthermore, the low electric demand forced the VRFB to operate at high SOC level, which accelerates component degradation. Only a small fraction of the total capacity was utilised on a daily basis. A sensitivity analysis was performed to investigate the impact of the PV array size and the load profile on the annual performance. It was found that the VRFB was affected by both the installed PV capacity and the demand. To increase the overall performance, the VRFB should operate at high charge and discharge power rate. Based on these findings, the scenario VRFB-II was defined. More details can be found in the Appendix A-4-8.

### *6.2.2.2 Results of scenario VRFB-II*

The second scenario investigates the performance of the 6 kW/ 20 kWh VRFB system integrated into a semi-detached house (consequently with a higher demand) powered by a 8 $kW_p$ PV system. The annual PV energy yield was 8861.9 kWh, the VRFB consumed 3839.1 kWh and released 1873.6 kWh. The energy imported from the grid was 5105.5 kWh. Compared to simulation without VRFB, the energy import was reduced by 26%. The average charge/discharge power was 3.3 kW and 1.5 kW, respectively. As can be seen from Table 6-6, the AC energy efficiency rose from 46.2% to 48.8%. In addition, compared to scenario I the VRFB performed less on/off cycles (1930), the operational duration decreased from 2777.9 h to 2457.8 h and the standby time reduced from 288.1 h to 195.2 h. Moreover, the annual grid interaction index decreased from 13.7% to 12.6%. Compared to scenario VRFB-I, the installation of the VRFB in a semi-detached house with increased electrical demand, led to an improved overall utilisation as illustrated in Figure 6-14.

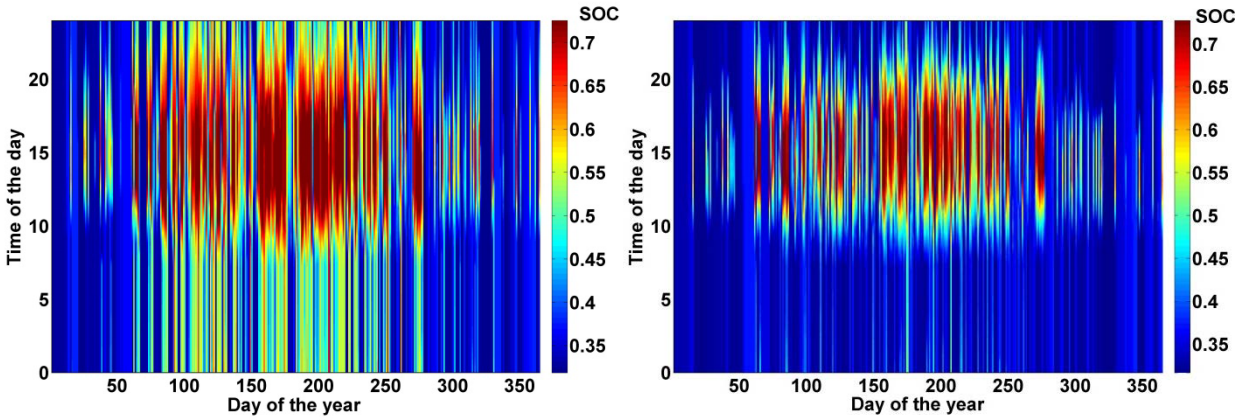


**Figure 6-14: Annual evolution of the SOC of the 6 kW/20 kWh VRFB system installed in a single house (left) and semi-detached house with higher demand (right) both equipped with 8 $kW_p$ PV system.**

The VRFB performed almost a complete charge/discharge cycle at each operational day. Figure 6-15 presents the annual power profile of the VRFB. During the day most of the available PV power was absorbed at high power rates. It can also be recognised from the carpet-plot, the VRFB was transited between charge and discharge during midday at certain days. The main activity in the building was during the evening and the VRFB was discharged at higher power levels as it can be seen from yellow to red coloured areas between 15:00 h and 24:00 h.

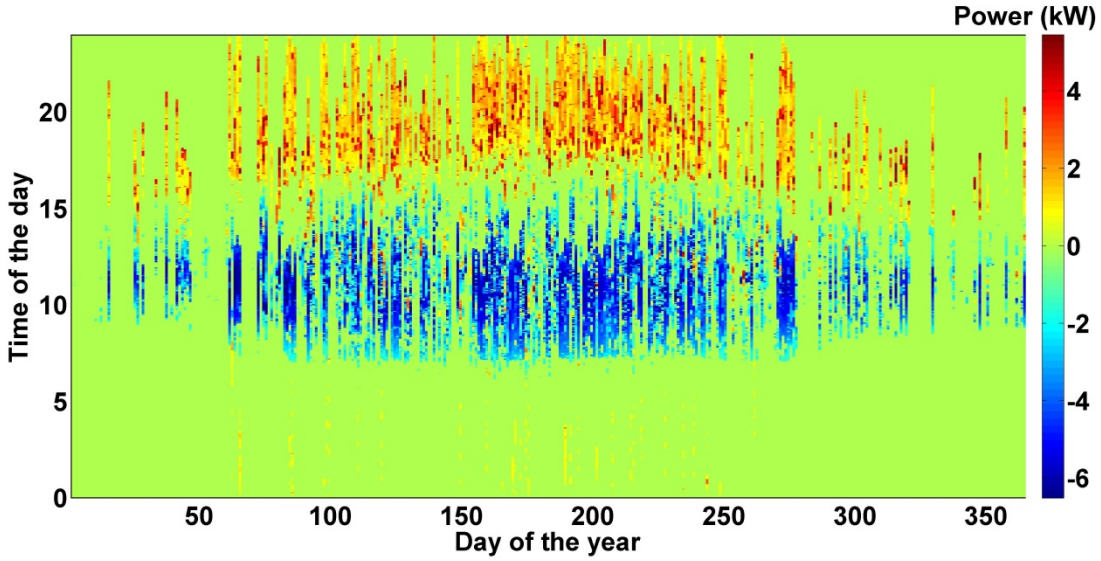


**Figure 6-15: VRFB power profile during the year.**

#### *6.2.2.3 Results of scenario VRFB-III*

The last scenario investigates the possibility of the smart grid interaction of a building-integrated VRFB system. Similar to the scenario $H_2$-III, an artificial DSR was applied. In addition to storing energy it was considered that the building can release power or can stabilise the power injected into the grid. This application is different to the scenario $H_2$-III as it accounts for the higher degree of operational flexibility of the VRFB in terms of switching between charge and discharge. Figure 6-16 presents the generated smart grid message composed of the power reference signal and the activation signal. The building's response to the signal for day 222 (middle) and 270 (bottom) are reported subsequently.

At day 222 the smart grid signal contained a negative power reference signal, meaning that the building should inject power into the grid. Shortly before 10:00 h the smart grid message was transmitted and the VRFB was forced to operate. The power output of the PV was relatively low and intermittent. The electrical demand was also low except shortly after noon, where a small peak occurred. As can be seen in the middle diagram, the VRFB was able to stabilise the power injected into the grid most of the time. At point "A" the demand suddenly increased and the VRFB reached its maximum discharge current, thus, it was not able to compensate the demand. As a result, the power injected into the grid decreased for a short period. After 14:00 h the smart grid signal was set back to zero.

The day 270 illustrates the case if the building is forced to store energy from the grid. After 23:00 h the smart grid signal was sent to the building and the VRFB transited into the charge mode. As can be

seen in the lower diagram, the power absorbed from the grid was stabilised at 5 kW. In the region at point “B”, shortly before 2:00 h, the maximum charge voltage was reached and the local control loop of the VRFB reduced the charge power. In general, the open circuit voltage of the VRFB increases with increasing SOC, consequently the magnitude of the charge power is also a function of the SOC. The lower the SOC value, the higher the maximum charge power, with respect to the system constraints such as maximum DC current, can be. A limitation of VRFB systems, in common with all battery systems, is the dependence of charge/discharge power on SOC.

Regarding the annual performance, the results show only a small improvement compared to scenario VRFB-I. The operational hours were increased from 2777.9 h to 3300.4 h. The annual electric energy imported from the grid increased from 2027.9 kWh to 2521.8 kWh. However, 798.8 kWh can be attributed to the forced operation of the VRFB according to the smart grid message. Considering this, the annual grid balance was increased from 587.6 kWh (export) to 1048.2 kWh (export). From these results a similar conclusion as for the hydrogen system can be drawn: only the introduction of an incentive for building owners to participate within a smart grid would justify this application.

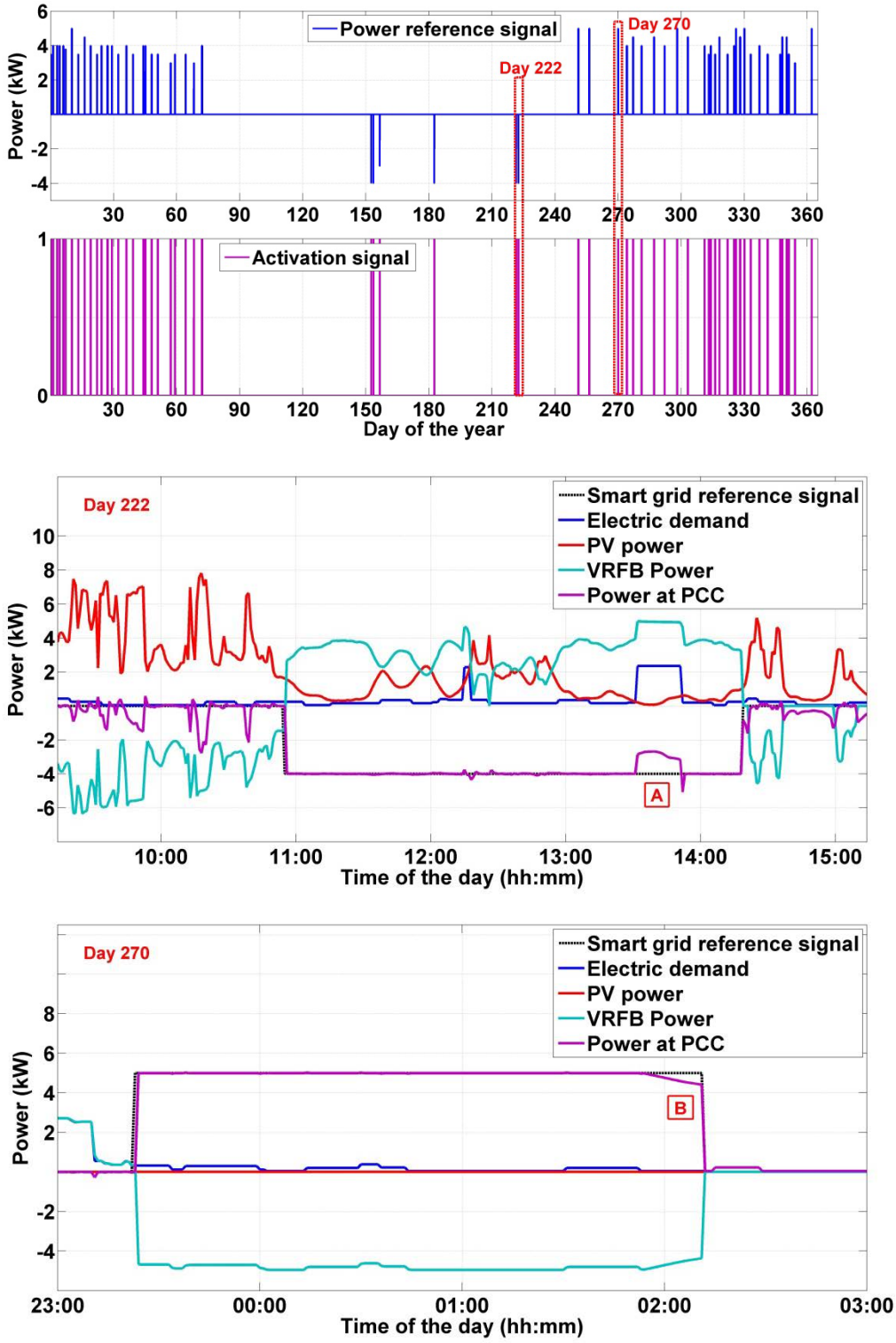


**Figure 6-16: Smart grid message profile (top), the response of the building at day 222 (middle) and at day 270 (bottom).**

#### *6.2.2.4 Summary and conclusions of the VRFB simulation scenarios*

Three different scenarios were designed to assess the annual performance and the grid interaction of a building-integrated VRFB system applying the energy management strategy presented in section 5.4 and the system model developed in section 5.3. From a sensitivity analysis threshold values of control parameters of the strategic supervisory level were derived and finally applied in all three scenarios. It was found that the minimum charge and discharge power should be -1100 W and 300 W, respectively. These threshold values provide a high degree of operational flexibility to serve high and low power demands, which are typical for domestic application. In all three scenarios the round-trip efficiency of the VRFB was greater than 46%. The results clearly show that the introduction of the VRFB significantly reduces the grid interaction of the building.

Scenario VRFB-I discussed the application of 6 kW VRFB system integrated in a four-person dwelling equipped with a 8 $kW_p$ PV system. The results indicate that the VRFB is sensitive to both the available PV power and the electric demand. Especially, the electric demand should be high enough to operate the VRFB at higher discharge power rates so as to increase the round-trip efficiency. Furthermore, it can be seen that the capacity of the VRFB was not fully utilised and that the SOC was kept at high levels during the summer which might accelerate component degradation.

In scenario VRFB-II it was shown that the performance of the VRFB can be improved by increasing the electric demand. In addition, the SOC of the VRFB was better utilised and almost a complete charge/discharge cycle was performed at each operational day.

In scenario VRFB-III the smart grid interaction of a building-integrated VRFB system was discussed. In comparison to scenario $H_2$-III the VRFB offers a high degree of operational flexibility. The maximum charge/discharge power has a similar magnitude and the VRFB can be switched between charge and discharge almost instantaneously. It was shown that the VRFB can be applied to stabilise the power injected into the public grid at the PCC of the building. Furthermore, the VRFB can be used to store excess energy from the grid if needed. However, in common with all batteries system, the VRFB charge/discharge power depends on the SOC of the electrolyte. This characteristic limits the capability, for instance, to absorb a constant high power over longer time periods from the public grid as shown in this scenario.

### 6.2.3 Comparison of the application of hydrogen and VRFB in buildings

Hydrogen systems and VRFB are not directly comparable, however, in this section the attempt is made to find the key merits and shortcomings between both technologies based on the discussed simulation scenarios.

From the annual results it is evident that the VRFB outperforms the hydrogen loop in terms of the overall efficiency. The AC round-trip efficiency of the hydrogen loop is approximately one third of the VRFB's efficiency. However, the hydrogen loop can be better adapted to the application due to the independent scalability of the electrolyser and fuel cell. The electrolyser can be sized to meet the PV power which is typically in the range of several kWs and the fuel cell can be sized to serve the low to mid power demands, which are more likely in a domestic load profile. On the other hand, the VRFB system should be placed into an application with high PV power and high electric demand. The AC efficiency can be slightly improved by operating the VRFB at high average charge/discharge power. However, more importantly a high electric demand leads to a better utilisation of the SOC during the summer months. Thus, a stagnation of the electrolyte at high SOC levels can be avoided and the system life time can be improved.

Both scenarios, H2-I and VRFB-I, were based on the same load and PV profile. Hence operational differences can be identified by comparing Figure 6-4 and Figure 6-11. Due to its higher overall efficiency and the higher degree of operational flexibility, the application of the VRFB results in higher annual values for the supply and load cover factor. This is most evident by comparing the load cover factor during the summer. The VRFB system reaches almost a value of one, meaning that the building becomes nearly self-sufficient. This can be also identified by comparing Figure 6-5 and Figure 6-12 showing the grid interaction of the building.

Comparing the two discussed smart grid scenarios an advantage of the hydrogen loop over the VRFB was found. The electrolyser can be charged at maximum power until the storage is completely full, whereas the VRFB reaches its voltage limit at higher SOC values due to the increasing voltage potential between the anolyte and catholyte leading to a charge power reduction.

## 6.3 Experimental demonstration

Figure 6-17 illustrates the hardware setup used to carry out the experiments presented in the sections below. As outlined in section 5.4 the strategic supervisory level is implemented in MATLAB/Simulink®/Stateflow® and it can be directly connected to the LON communication network, see section 3.6, via the Simulink® OPC toolbox (OPC Toolbox 2012). A cross communication among the LON subnets, see section 3.3, are achieved by network interfaces (AS) via LON over IP.

In general, the communication among LON devices (nodes) is established by exchanging network variables. Each device has a set of network input variables (nvi's) and network output variables (nvo's). The data exchange rate is driven by the COV mechanism, meaning that only data messages between the network nodes will be exchanged if the value of the network variable has changed by a certain magnitude.

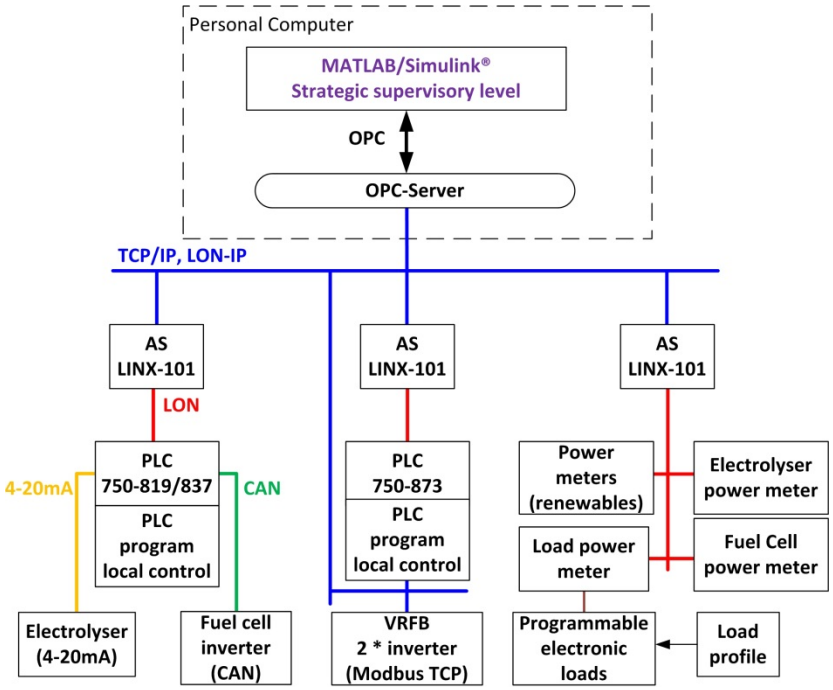


**Figure 6-17: Experimental set-up for real-time operation.**

As an example how the LON nodes interact with each other, Figure 6-18 illustrates the involved network variables to control the AC power consumption of the electrolyser system. The AC power output of the renewable energy sources, the electrolyser and the electric loads is separately measured by LON power meters. The information about the actual power supply and demand is sent to the strategic supervisory level, see section 5.4. If the condition of demand predictor, see section 5.4.2, is fulfilled, a message ("nvo_Ele_activate") is sent to the local LON PLC of the electrolyser. At this time instant the LON PLC activates the electrolyser via the analogue signal (4-20 mA). As soon as

the electrolyser enters the operational state, a message (“nvo_Ele_State”) is sent from the LON PLC to the strategic supervisory level and the filtered power reference signal (“nvo_P_Ref”) will be periodically sent from the strategic supervisory level to the LON PLC of the electrolyser. Within the developed PLC program, the control derivation is calculated by subtracting the measured AC power of the electrolyser (“nvo_P_Ele”) from the power reference signal. The PI controller implemented in the PLC regulates the AC power by adjusting the 4-20 mA analogue input signal of the electrolyser’s internal control system.

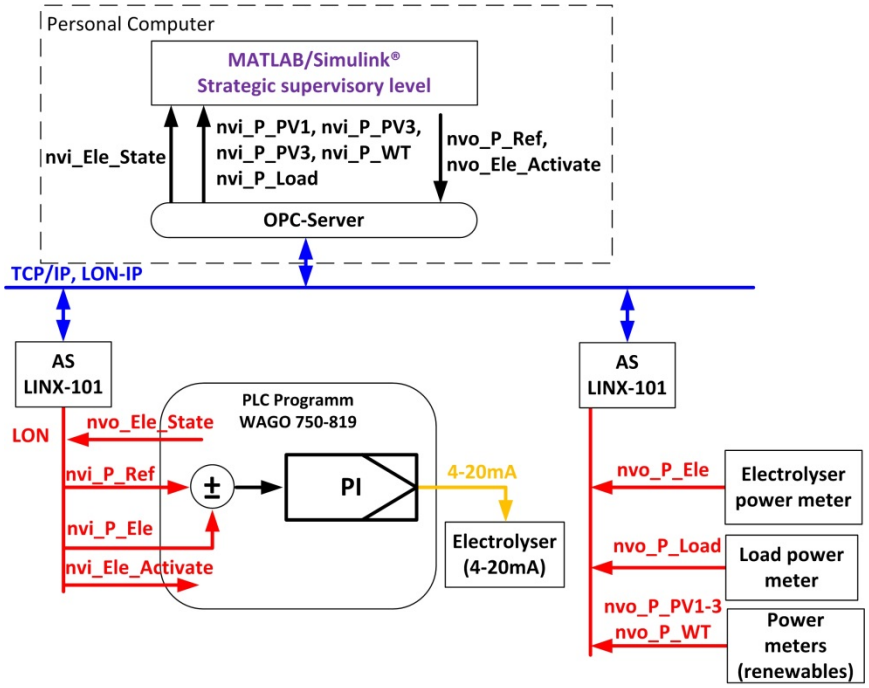


**Figure 6-18: Control loop to regulate the power consumption of the electrolyser.**

In the following sections the experimental results of two different system configurations of the HREP are presented. The first experiment demonstrates the dynamic performance of a building-integrated hydrogen loop and the second one demonstrates the operation of the HREP configured as hybrid storage system. As shown in the simulation study, a suitable PV system capacity for the electrolyser and the VRFB would be 8 $kW_P$. Therefore, it was decided to scale the sum of measured power of the three PV systems (in total 6.12 $kW_P$) by 8/6.12 to emulate 8 $kW_P$. The electric load profile was generated by using the aforementioned electric load model and was utilised by the three programmable AC loads, see Chapter 3.7.

### 6.3.1 Experimental demonstration: Hydrogen system

The first experimental case-study was set up based on a domestic electric load profile for a dwelling where a hybrid energy system composed of PV, electrolyser and fuel cell is employed to utilise the renewable energy locally. Figure 6-19 illustrates the measured electric power consumed by the AC loads and the scaled measured PV power on 3rd of September 2014 at Ostfalia University. The electric demand was characterised by a low base load and rapid power changes during midday and an increased demand after 18:00 h. The generated PV power was highly fluctuating over the day due to scattered clouds. It is evident that without electrical storage most of the on-site generated PV power would have been injected into the grid.

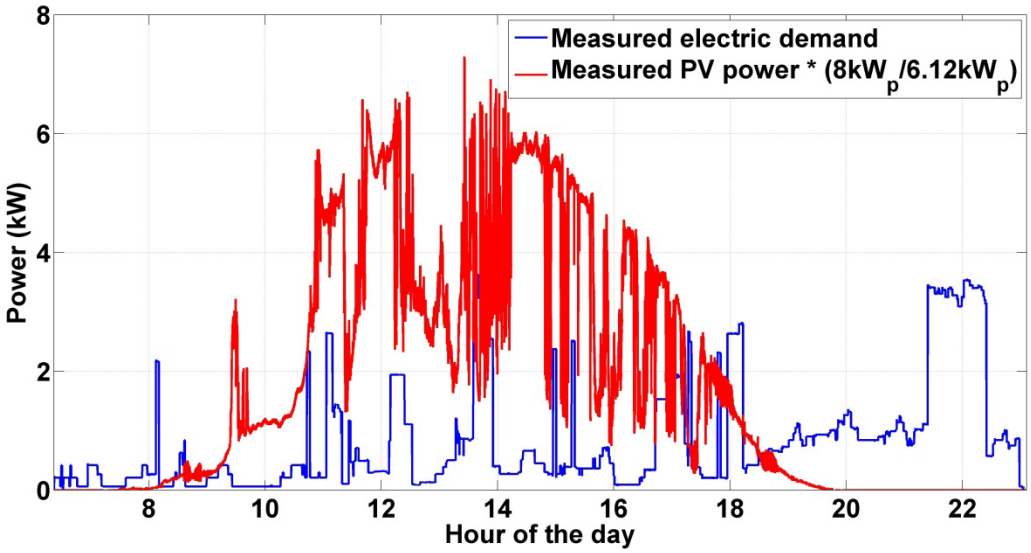


**Figure 6-19: Electricity generation by the PV and the electric demand on the 3rd Sept. 2014.**

Figure 6-20 shows in the upper graph the calculated power difference (5-42), the measured fuel cell power and the measured electrolyser power. The evolution of the hydrogen storage is illustrated subsequently. The PV system generated 28.96 kWh and the electrical demand was 13.77 kWh, whereby 3.77 kWh were supplied by the fuel cell. The electrolyser consumed 17.95 kWh electrical energy to produce 1.7 m³ (NTP) hydrogen.

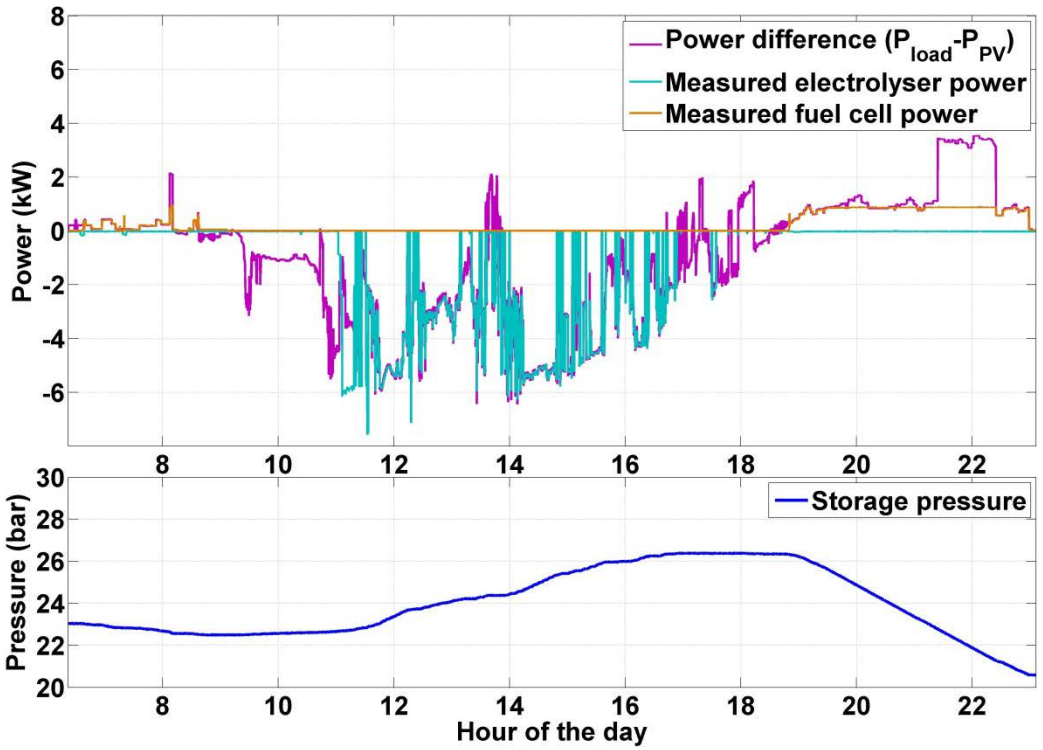


**Figure 6-20: The calculated power difference, the measured power of the electrolyser and of the fuel cell (top diagram). The measured pressure of the hydrogen tank (lower diagram).**

Considering only time intervals at which the electrolyser consumed energy and the fuel cell released energy, the average operating AC power of the electrolyser and the fuel cell was approximately 4 kW (320 mA/cm²) and 540 W, respectively. The calculated AC energy efficiency of the electrolyser and fuel cell was 33.2% and 41.2%, respectively. Furthermore, the overall efficiency of the hydrogen results in 14%. Comparing these calculated AC efficiencies with the results of the steady state experiments, presented in Figure 4-4 for the electrolyser and Figure 4-14 for the fuel cell, reveals that the efficiency is affected by the transient operation. Especially, the efficiency of the electrolyser is approximately 7% below the steady state value. The fuel cell efficiency is slightly affected by the transient operation and is approximately 2% below the steady state value.

The ability of both the electrolyser and the fuel cell to deal with the highly fluctuating electric power profile is reported below. As explained in chapter 6.1, the main decision variable of the strategic supervisory level is the power difference between the electric demand and the PV power. Based on this information decisions are made by the energy management system whether to activate the energy systems and the power reference signal is generated with respect to the dynamic performance for the corresponding component. If the energy system was able to respond instantaneously to this signal, the energy system would reach its maximum dynamic performance. Considering the power reference signals for the electrolyser and fuel cell, the ideal power exchanged

with the grid would be as shown in the upper diagram of Figure 6-21. The lower diagram shows the calculated grid power (5-43) based on the measured response of the electrolyser and fuel cell. It can be seen that especially during transient operation the measured profile shows wider fluctuations than the ideal course of the power.

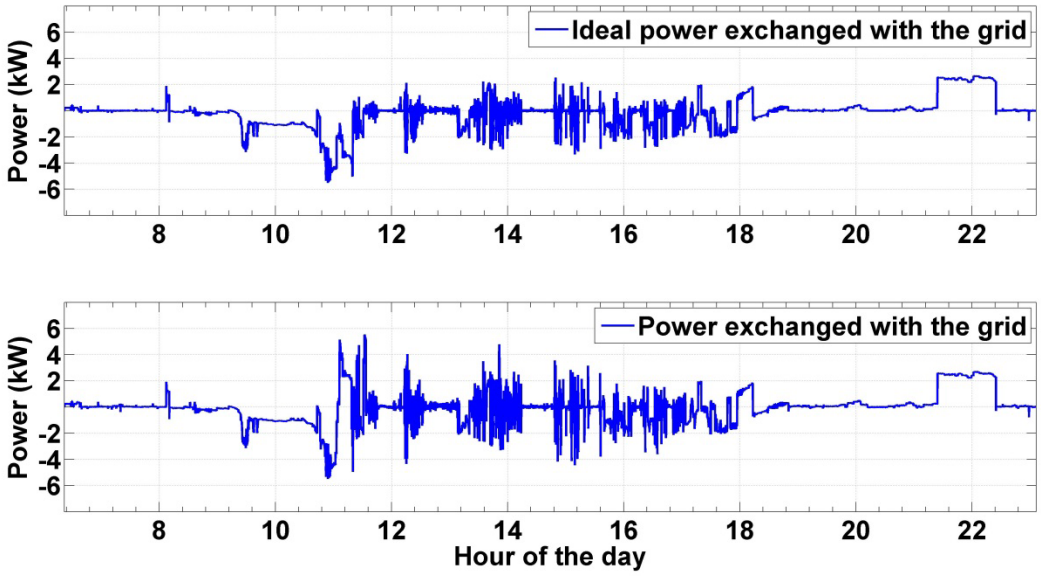


**Figure 6-21: The top graph shows the ideal grid power. The lower graph depicts the exchanged power with grid based on the measurements.**

The functionality of the demand predictor, see section 5.4.2, is illustrated in Figure 6-22. The calculated power difference (5-42), the estimated 10-minute forecast (5-46) and the 10-minute trend (5-45) of the power difference are illustrated in the upper diagram. Subsequently, the activation signal and the operational states of the electrolyser are reported. At approximately 11:00 h the calculated forecast value was above the threshold value and the strategic supervisory level sent the activation signal to the electrolyser. The electrolyser was transited from state 1 (off) to 2 (start-up). Furthermore, from the lower diagram it can be seen that the electrolyser was transferred several times from operation (state 3) into the standby (state 4). Around 19:00 h the electrolyser entered the blow down mode (state 5) and was finally transited back into the off mode.

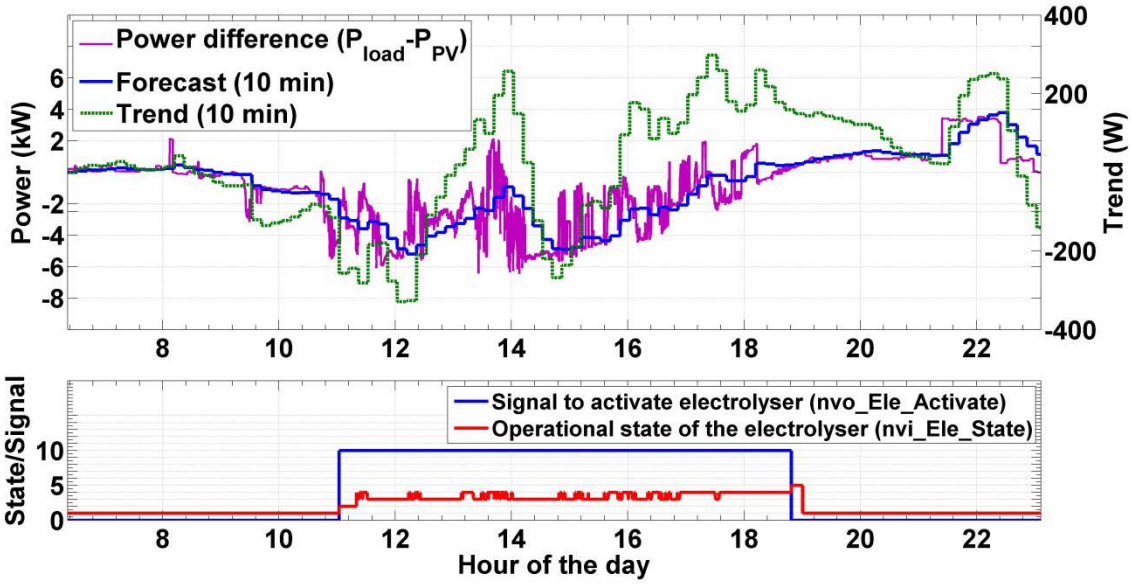


**Figure 6-22: The top graph depicts the power difference, the 10-minute forecast of the power difference and the trend of the forecast. The lower graph shows the activation signal (scaled by 1/10) and the operational state of the electrolyser.**

Figure 6-23 reports the dynamic response of the electrolyser system. The upper diagram shows the power difference, the reference power signal and the measured electrolyser power throughout the day. The start-up period is marked and highlights the increased power demand of the electrolyser to pressurise itself. The middle graph shows an enlargement of the red frame marked with "1" in the upper diagram. Here the dynamic response of the system is illustrated over time period of 15 minutes. The electrolyser was forced into standby several times; however, it was able to response quickly to the power changes. A zoom into the red frame "2" is presented at the bottom. This graph shows the response of the system over a time period of one minute. As shown in the diagram, the electrolyser system can follow sudden power changes of the power reference signal with a time delay of three to four seconds. Furthermore, the power control loop was able to stabilise the power consumption of the electrolyser quickly.

The effectiveness of the demand predictor to activate the fuel cell is illustrated in Figure 6-24. The upper diagram reports the calculated power difference, the 2-minute forecast and the 2-minute trend of the power difference. The top graph is similar to the top graph of Figure 6-22, however, the estimation time of the forecast and trend are shorter. Consequently, the evolution of the forecast and trend are less smoothed compared to Figure 6-22. Below, the activation signal and the operational states of the fuel cell are illustrated. The fuel cell was activated twice, in the morning and in the evening.

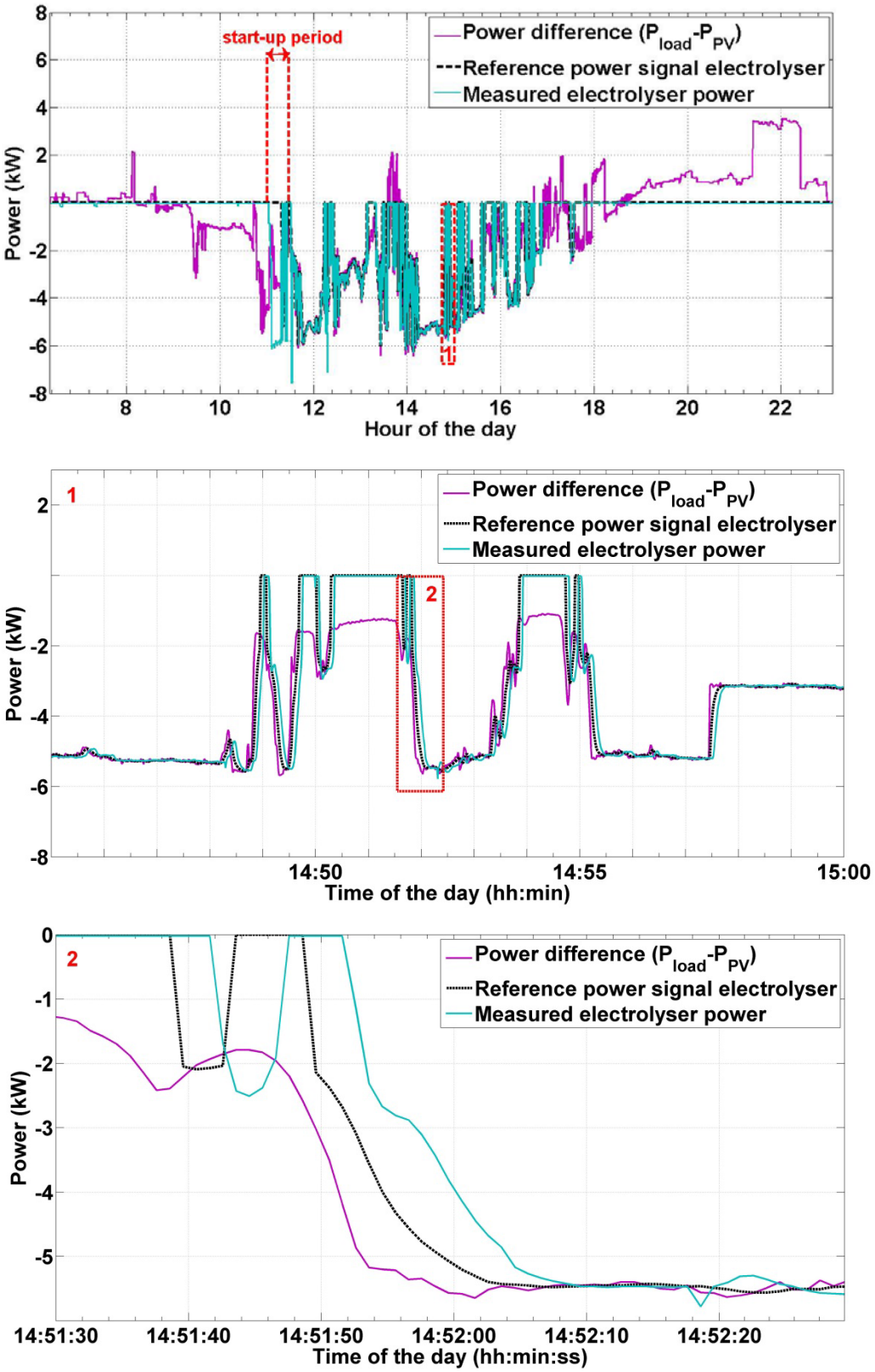


**Figure 6-23: Electrolyser characteristic: Top diagram shows the complete test. The middle diagram depicts the supply following capability. The bottom diagram illustrates the response characteristic.**

At approximately 6:25 h the calculated forecast value was above the threshold value and the strategic supervisory level sent the activation signal to the fuel cell. The fuel cell was transferred from operational state 1 (off) to 2 (start-up) and finally to 3 (operation). Furthermore, as can be seen from the lower diagram, the fuel cell was transited several times into standby (state 4).

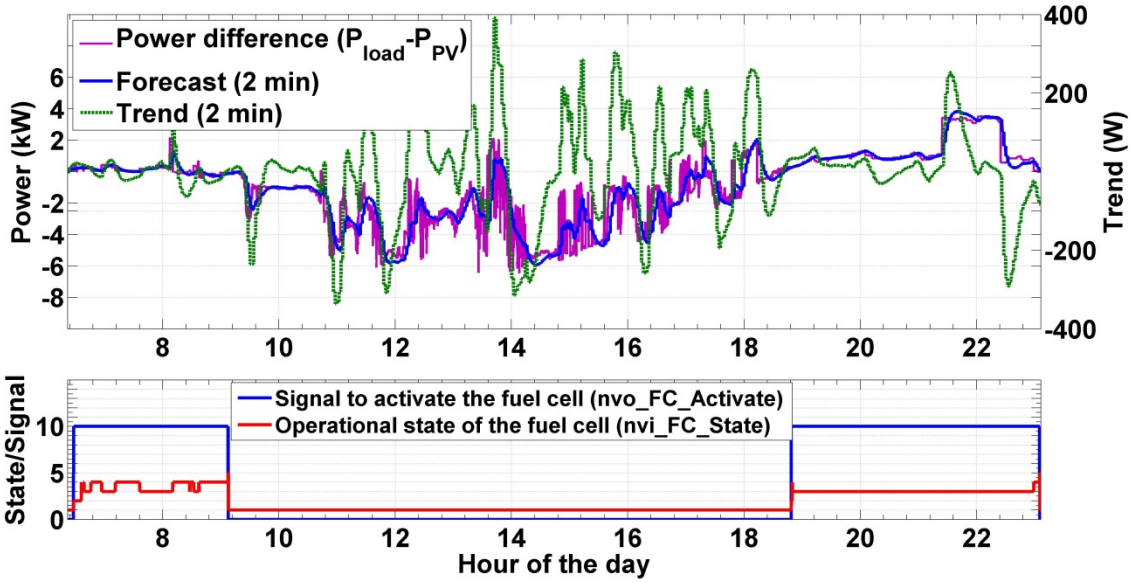


**Figure 6-24: The top graph depicts the power difference, the 2-minute forecast of the power difference and the trend of the forecast. The lower graph shows the activation signal (scaled by 1/10) and the operational state of the fuel cell.**

Figure 6-25 illustrates the dynamic behaviour of the fuel cell system. The upper diagram shows the power difference, the reference power signal and the measured fuel cell power over the day. The red frame “1” marked the time period which is reported in more detail subsequently. The middle graph depicts the start-up process of the fuel cell and the dynamic response from 8:21 h to 8:37 h. At this time the PV started to generate electricity and influenced noticeable the power profile after 8:35 h. An enlargement of the red frame “2” is shown below. The diagram depicts the response of the fuel cell over a period of about 1.5 minutes. The power difference was highly volatile due to the PV power. The power control loop implemented into the PLC of the fuel cell controlled quite quickly the power output. Furthermore, the filtered reference signal provided by the strategic supervisory level reduced noticeable the dynamic stress on the fuel cell.

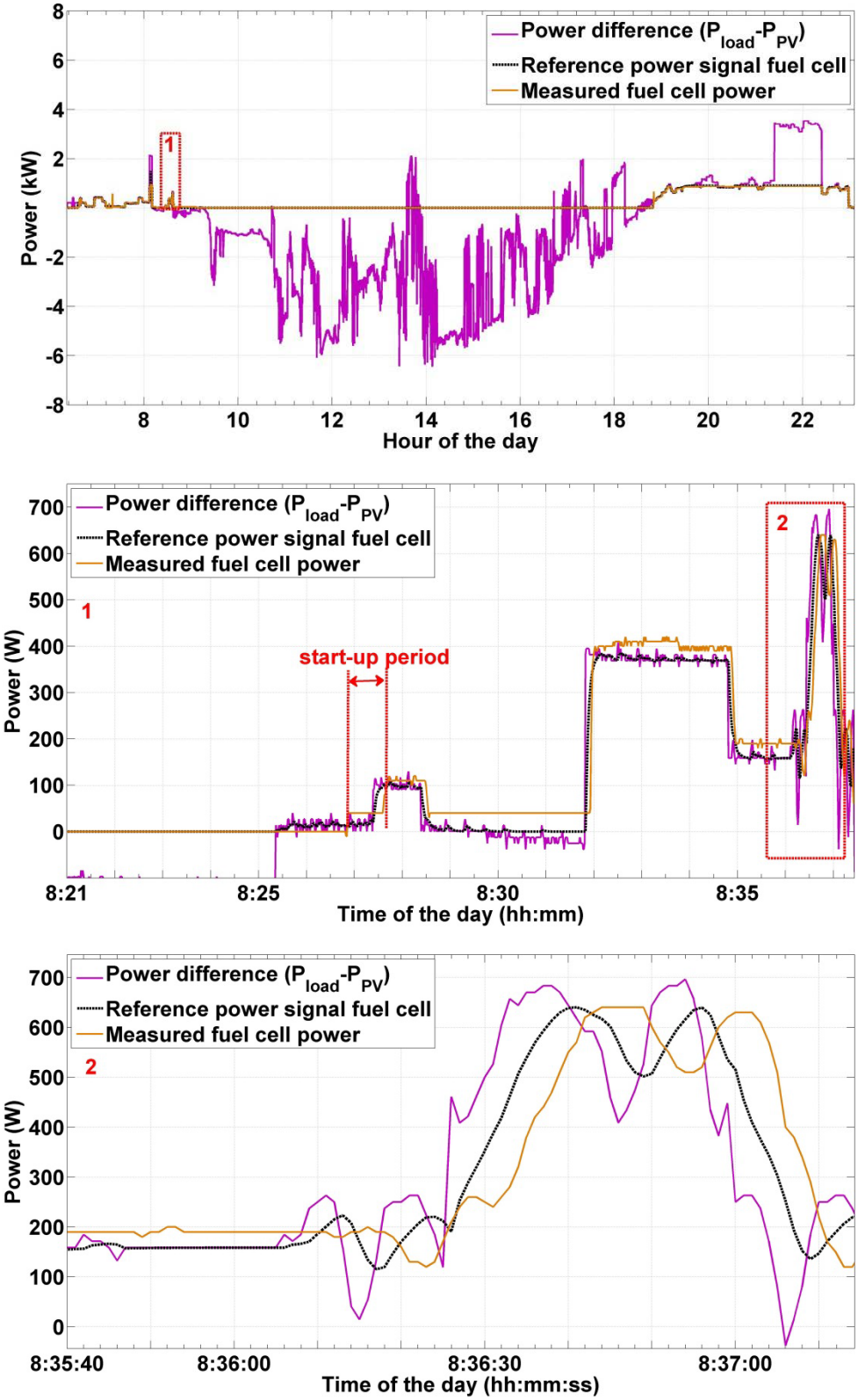


**Figure 6-25: Fuel cell behaviour: Top diagram shows the complete test. The middle diagram depicts the activation and load following capability. The bottom diagram illustrates the response characteristic.**

### 6.3.2 Experimental demonstration: Hybrid storage system

The second experimental case-study considered a domestic electric load profile for a dwelling and the HREP was configured as a hybrid energy system composed of PV, VRFB, electrolyser and fuel cell. As described in section 5.4.1, in case of a hybrid storage system, the energy management strategy prefers the VRFB to store/release energy before the hydrogen system is activated.

Figure 6-26 illustrates the measured electric power consumed by the AC loads and the scaled measured PV power on 17th September 2014 at Ostfalia University. The electric demand was characterised by a low base load, rapid power changes during morning hours and an increased demand after 16:00 h. Daily electricity demand was 15.78 kWh. The sky on this day was hazy with some cloud interruptions during the day. The daily PV energy yield was 31.92 kWh.

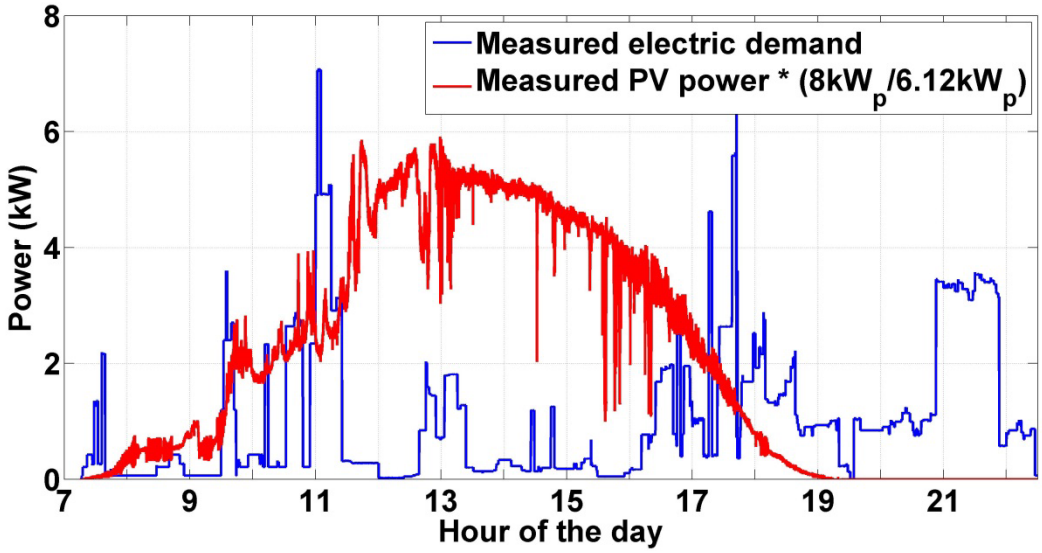


**Figure 6-26: Electricity generation by the PV arrays and the electric demand on the 17th Sept. 2014.**

Figure 6-27 reports in the upper graph the calculated power difference (5-42), the measured VRFB power, the measured fuel cell power and the measured electrolyser power. The evolution of both the SOC of the VRFB and the hydrogen storage are illustrated subsequently. It has to be noticed that the SOC range of the VRFB was restricted due to unexpected system degradation. The reasons for this are currently under investigation by the manufacturer and out of scope of this thesis. Therefore, the SOC was limited between 40% and 64% for this demonstration. The initial SOC of the VRFB was at 53% and the hydrogen storage pressure was at 24.6 bar. The noticeable pressure variations at moments at which the electrolyser and the fuel cell were switched off were caused by ambient temperature variations. The VRFB supplied 5.9 kWh to the electrical demand and consumed 10.8 kWh. To estimate the AC system efficiency of the VRFB only the charge and discharge energy within the time period between 11:30 h to 13:00 h and 18:00 h to 20:00 h and between an SOC of

48% to 60% were considered. The calculated charge and discharge energy were 9.68 kWh and 3.98 kWh, respectively. The calculated AC system efficiency of the VRFB was 41%. The electrolyser consumed 11.51 kWh electric energy to produce 1.12 m³ (NTP) of hydrogen. The fuel cell supplied 0.83 kWh electric energy and consumed 0.67 m³ (NTP) of hydrogen. The AC energy efficiency of the electrolyser and the fuel cell was 34.4 % and 41.5%, respectively. The overall efficiency of the hydrogen loop was 14.3%.

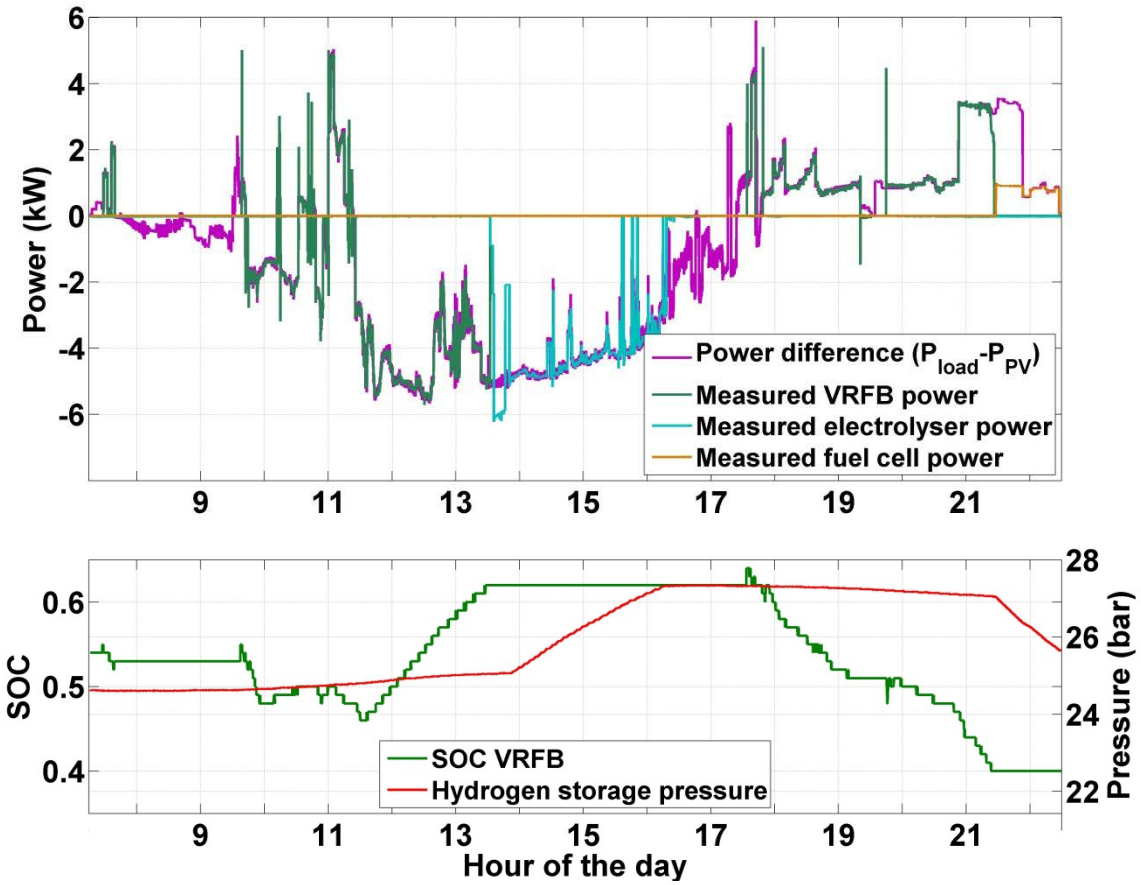


**Figure 6-27: The calculated power difference, the measured power of the, VRFB, electrolyser and of the fuel cell (top diagram). The SOC of the VRFB and the measured pressure of the hydrogen tank (lower diagram).**

The operation of the hybrid storage system with a particular focus on the ability of the VRFB to response to the fluctuating electric power profile is reported below. As aforementioned, the main decision variable of the strategic supervisory level is the power difference between the electric demand and the PV power. In addition, the VRFB system is preferred in the hybrid storage configuration due to its higher overall efficiency. Based on the power difference the decision is made to activate the energy systems and the power reference signal is generated regarding the dynamic performance for the corresponding component. If the energy systems were able to respond instantaneously to the reference signals, the maximum dynamic performance of the HRES is reached. Considering the power reference signals for the VRFB, electrolyser and fuel cell, the optimal power

exchanged with the grid would be as shown in the upper diagram of Figure 6-28. The lower diagram shows the calculated grid power (5-43) based on the real response of the VRFB, electrolyser and fuel cell. It can be seen that especially during transient operation the real profile shows a higher degree of variability in comparison to the ideal course of the power.

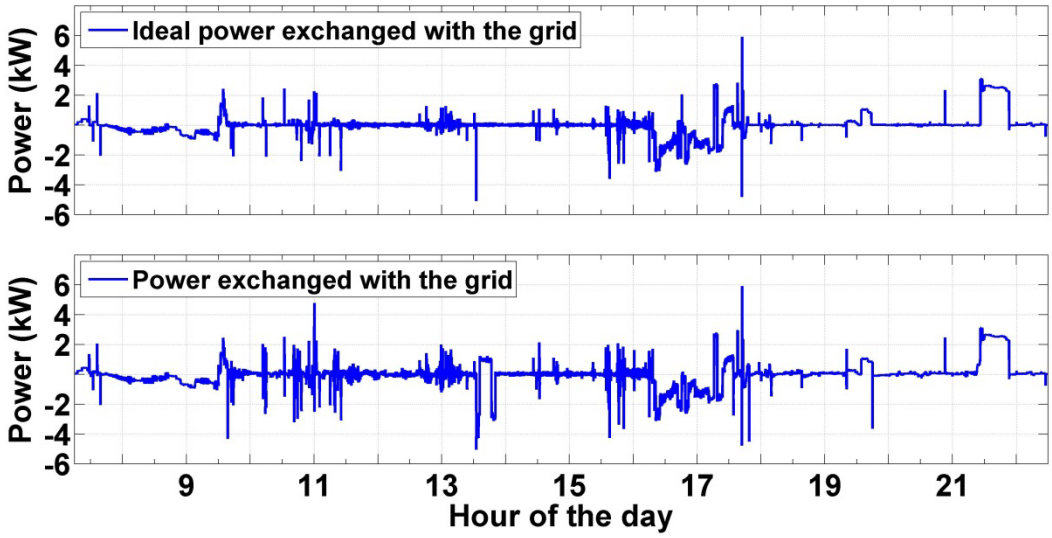


**Figure 6-28: The top graph shows the ideal grid power considering the power reference signals. The lower graph depicts the exchanged power with the grid based on the measurements.**

The effectiveness of the strategic supervisory level, see section 5.4, to coordinate the hybrid storage configuration of the HREP is illustrated in Figure 6-29. The upper diagram illustrates the power difference (5-42), the 2-minute forecast (5-46) and the 2-minute trend (5-45) of the power difference. Below, the activation signals of the VRFB, electrolyser and fuel cell are reported. The lower diagram illustrates the operational state of the energy systems. At approximately 7:15 h the calculated forecast was above the threshold value to discharge the VRFB and the supervisory level sent the activation signal. The VRFB was transited from state 6 (off) to 1 (start-up) as shown in the lower diagram. In total the VRFB performed five start-ups during the day. Furthermore, it can be seen that the VRFB was transferred several times from operation (state 2) into the standby (state 3). After 9:30 h the surplus PV energy was supplied to the VRFB. Around 13:30 h the supervisory level decided to activate the electrolyser before the VRFB would reach its SOC limited. The VRFB was activated again at approximately 17:30 h to supply electrical energy to the loads. At 21:30 h the lower SOC limit is reached and the fuel cell was activated to serve the electrical demand.

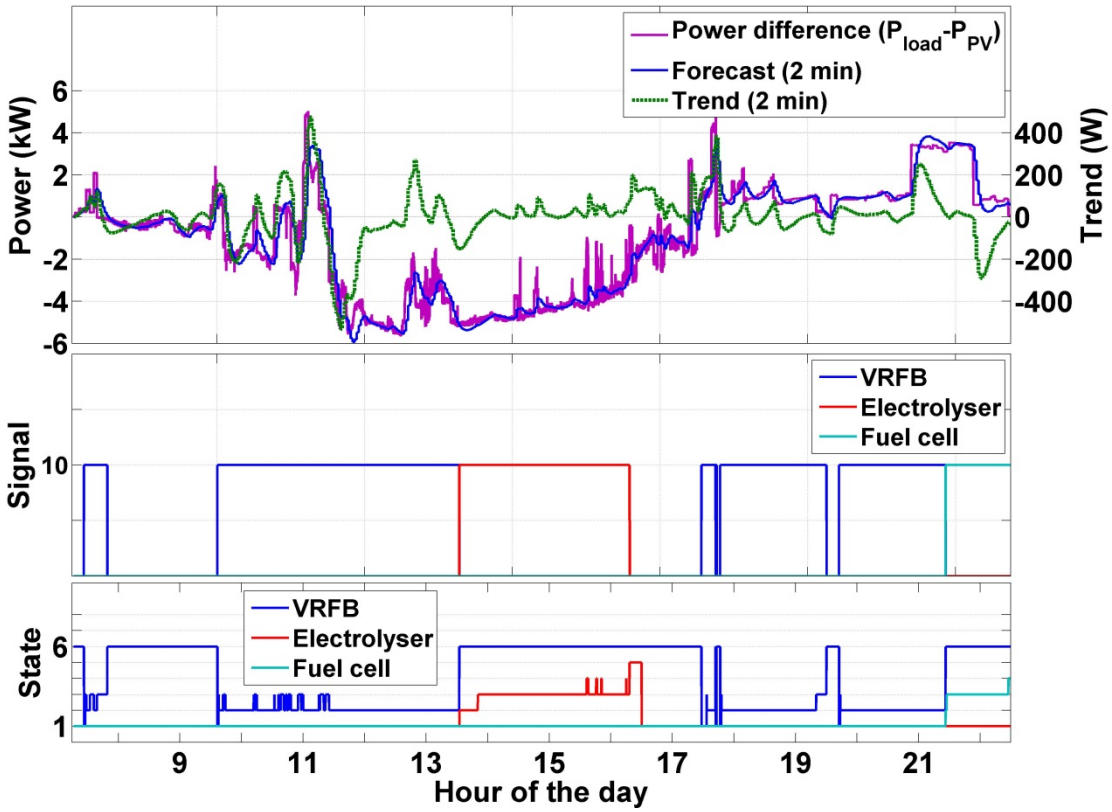


**Figure 6-29: The top graph depicts the power difference, the 2-minute forecast of the power difference and the trend of the forecast. The middle graph shows the activation signal (scaled by 1/10) generated in the supervisory level. The lower graph illustrates the operational state of the VRFB, electrolyser and fuel cell.**

Figure 6-30 and Figure 6-31 report the dynamic response of the VRFB system. The upper diagram in Figure 6-30 shows the power difference, the reference power signal and the measured VRFB power over the day. Subsequently, the area “1” of the upper diagram is illustrated. The start-up period of the VRFB is marked. Interesting here is the short high power peak caused by the internal control system of the inverters before the VRFB followed the demand. Another interesting area is marked with “A”. At this instant the VRFB system switched from discharge to charge. Similar to the activation of the inverter, the switching caused a short high power peak before the charge power was stabilised again.

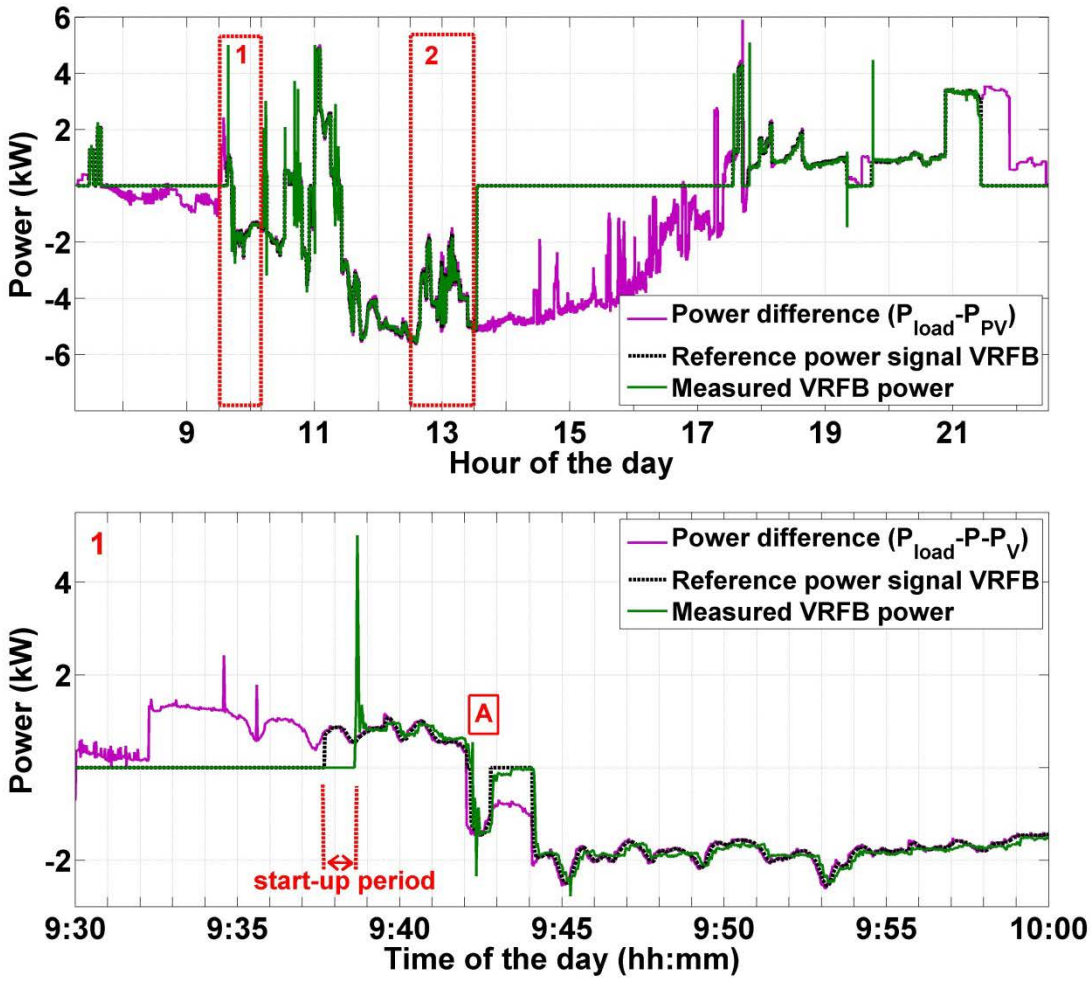


**Figure 6-30: VRFB characteristic: Top diagram reports the complete test. The lower diagram, an enlargement of frame "1", shows the start-up of the VRFB and the transition between discharge and charge.**

A zoom into the red frame "2" of Figure 6-30 is presented in the upper diagram of Figure 6-31. This graph shows the response of the VRFB over a time period of one hour. As shown in the diagram, the VRFB system can follow the sudden power changes of the power reference signal. Furthermore, the power control loop was able to stabilise the charge power quickly. To investigate the dynamic performance in more detail, the area "3" is presented in the lower diagram over a time period of two minutes. It can be seen that the response of the PI controller was fairly acceptable and the VRFB power output followed with a time delay of approximately 4-5 seconds.

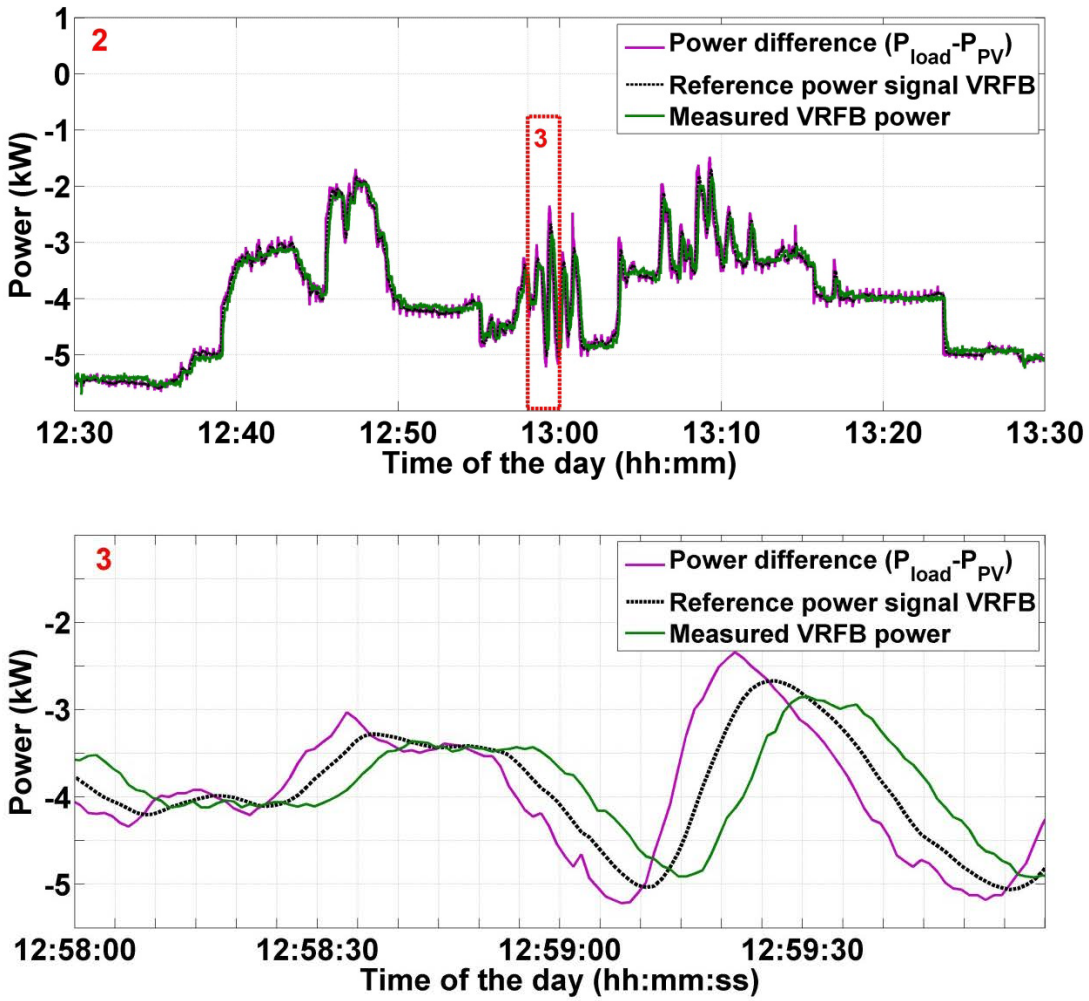


**Figure 6-31: VRFB characteristic: Top diagram shows the area 2 of the upper diagram in Figure 6-30. Lower diagram illustrates the area 3.**

### 6.3.3 Summary and conclusions of the experimental demonstration

The experimental results provided in this section, validate the developed energy management system as described in section 5.4 for single and hybrid storage configuration of the HREP.

From the results it can be concluded that the dynamic operation influences the performance of the hydrogen loop. Especially, the electrolyser showed a 7% lower AC efficiency compared to steady state results presented in section 4.1.1. This was caused by the start-up and warm-up period of the electrolyser. The fuel cell was less sensitive to the dynamic operation. The efficiency was only 2% below the steady state results presented in section 4.2.1. The dynamic results of the VRFB presented in this section are not comparable to the experimental results shown in section 4.3.1 because of unexpected component degradation. However, the first impression is that the performance is only slightly affected by the dynamic operation.

The load following capability of the hydrogen loop and the VRFB integrated into a building automation system were additionally presented in this section. Compared to the multiple dynamic event experiments presented in section 4.1.3, 4.2.3 and 4.3.3, the time before the energy starts to follow the reference power signal increased due to the communication between the energy management system and the local control units. The response time of the energy systems varied between 3-6 seconds. Such variations limit the capability of the components to compensate high power fluctuations, which can be noticed by comparing the ideal grid power and the calculated grid power as shown in Figure 6-20 and Figure 6-27. However, the power control implemented into the corresponding PLCs can follow such a volatile profile and can relatively quickly stabilise the power input/output.

# 7 Conclusions and perspective

This research aimed to investigate the impact of operational conditions and dynamic transitions on the performance of an alkaline electrolyser, a proton exchange membrane (PEM) fuel cell and a vanadium-redox-flow-battery (VRFB) integrated into a hybrid-renewable-energy-system (HRES) to satisfy a domestic demand. In the following a brief overview of the thesis is outlined in section 7.1, followed by presenting the outcomes in section 7.2. Recommendation for improvements and a suggestion of possible future routes for developments as the continuation of this research are presented in section 7.3. Finally, the main contributions are highlighted in section 7.4.

## 7.1 Overview of the thesis

It is expected that buildings will evolve into an active unit integrated in an electricity grid in which the electricity is generated, distributed and locally consumed. The introduction of electric storage technologies at this level can be applied to temporarily decouple the volatile renewable power generation from the electric demand. Various energy storage technologies have been discussed in the literature to store energy from renewable sources; however, each storage technology has its own merits and shortcomings. Two promising technologies, which can be applied at residential level, are hydrogen systems and VRFB. Although both technologies are commercially available in power rates and applicable for buildings, no existing literature was found to describe experimental studies that show how hydrogen systems and VRFB would response to a volatile power profile, if they are integrated in a building automation system. In simulation studies, on the other hand, hydrogen systems are often considered to be part of a residential scale HRES. A common simplification in such studies applied is that operational transitions such as start-up, standby and shutdowns are neglected and it is assumed that the energy systems can almost instantaneously respond to load variations. This thesis has sought to cover this research gap by combining theoretical and operational aspects into an integrated system model based on detailed experimental analysis of each energy system.

The research was carried out by means of a literature review (chapter 2), further development and the set-up of an experimental platform (chapter 3) and systematic experimental characterisation of the energy systems (chapter 4). In addition, system models have been developed and validated. Furthermore, an energy management strategy has been defined and implemented (chapter 5). Several simulation case-studies were designed to determine the annual performance, local utilisation of the renewable energy and the grid interaction of the building (chapter 6). Moreover, the developed energy management strategy has been applied to control the experimental platform and the dynamic interaction of the energy systems was presented in detail.

## 7.2 Conclusions

In the following sections the main achievements and findings in the light of the three research objectives are reviewed.

### 7.2.1 System integration and experimental characterisation of the energy storage technologies

The development of an experimental platform, the hybrid renewable energy park of the Ostfalia University Wolfenbüttel, has been outlined in detail. The technical focus was on the integration of an alkaline electrolyser, a PEM fuel cell and a VRFB system into the experimental platform. Although all applied technologies are commercially available, several integration issues were encountered and have been addressed. The most challenging task was the communicational integration into a building automation system (local operating network - LON) because of the diversity of the components, and the development of a control structure. Different communication protocols have been integrated and additional programmable logical controllers (PLC) installed and programmed. The achievement of a unified communication channel among all energy systems, the renewable energy sources and the electric storage technologies, was of utmost importance to establish data acquisition and to develop an overall energy management strategy.

To investigate the steady-state and dynamic behaviour of the energy systems an experimental method has been introduced, which can generally be applied to characterise energy systems. The first set of experiments was designed to identify operational aspects such as start-up and to determine the steady-state performance. The second set, the step-response experiments, revealed unfavourable operating conditions of the energy systems, which can lead to component degradation. The last set of experiments was carried out to determine the load following capability of the electrolyser, fuel cell and VRFB, which is the most likely event in a HRES. This experiment involved not only the energy system itself and the corresponding power conditioning unit, but also the installed PLC.

Each energy system follows a similar start-up routine before the power input/output can be finally controlled and has similar operational states. In addition, the time period to transfer the energy systems into normal operation varies from 2 minutes of the fuel cell and VRFB to 15 minutes of the electrolyser. Furthermore, the hydrogen systems are significantly influenced by the operating temperature. The electrolyser needs approximately 80 minutes at maximum power to reach its operating temperature. Bearing in mind that the daily average operating time is 4 to 6 hours at

variable power rate, it is clear that the performance of the hydrogen systems is affected by the dynamic operation.

The dynamic test has shown that considering only a step-response experiment would overestimate the dynamic performance. Thus, the multiple dynamic event experiment has been applied to determine the load following capability of each energy system. For instance, the VRFB can properly follow a load variation of approximately 5% of its rated power per second. This is an interesting finding because it is commonly assumed that VRFB can follow with a much larger slew rate, which may apply for individual systems or large scale applications with specialised equipment.

Furthermore, from the outlined results it can be concluded when operating HRES it is important to analyse the dynamic performance of the energy systems not only at component level, but also at a combined system level. Considering only the response times quoted in the literature would lead to an overestimation of the load following capability. This is in particular valid for distributed systems linked via a communication channel with several interacting control units. The presented experimental characterisation method can be applied to identify dynamic limitations and to define appropriate control strategies for multivendor HRES.

To summarise, the first research objective was motivated by the need to provide an experimental platform to investigate, document and report the performance of two emerging energy storage technologies, the hydrogen system and the VRFB, and to provide an environment to develop suitable control strategies for HRES. The main achievements are:

- Development of a fully instrumented, integrated and modular hybrid renewable energy system to analyse the performance of energy storage systems and to test different control strategies.
- Detailed performance characterisation of an alkaline electrolyser, a PEM fuel cell system and vanadium-redox-flow-battery at system level and the identification of system limitations to satisfy a volatile power profile.
- The developed method to characterise the energy systems helps to identify transient limitation not only at component level, but also at system level.

### 7.2.2 Development of integrated system models and an energy management strategy

A generic model layout for energy systems has been presented. The model layout has a modular structure composed of individual sub-models to describe the electrical and thermal (if required) behaviour, the energy capacity, the operational modes and the local power control. From the experimental analysis it has been identified that each energy system has different operating modes,

for example, initialisation, start-up or standby. Such discrete states of a system can be described by applying the statechart formalism. The MATLAB®/Simulink®/Stateflow® software has been used for the modelling process. Although the presented models are tailored to the physical systems installed at Ostfalia University, the experimental methods developed in this thesis to extract the empirical parameters of the models can be applied to other electrolysers, fuel cells or VRFB.

The experimental characterisation has shown that the electrolyser's performance is significantly affected by the temperature. It is therefore important to consider the impact of the dynamic operation associated with the intermittent power output of renewables on the temperature. A commonly applied approach to model the thermal behaviour of electrolysers for system level simulations was not effective in predicting the operating temperature of the installed electrolyser in low power regions. An experimental method has been developed to investigate the impact of the DC current on the warm-up sequence of the electrolyser. Based on these results two empirical functions have been defined aiming to take into account the findings without increasing the complexity of the thermal model. The validation against measured data has shown that the thermal model accurately predicts the temperature evolution at different DC currents. As aforementioned the temperature is an important factor which has significant impact on the system's performance. In particular when considering the utilisation of the waste heat, the prediction of the temperature evolution becomes even more important. Therefore, the developed system model can be applied to evaluate both the electrical and thermal performance of an electrolyser integrated into HRES.

The presented electrical model of the fuel cell is based on an existing semi-empirical model approach. However, the experimental analysis of the fuel cell system has shown that the internal resistance depends on temperature and the water content of the membrane, which is not considered in the initially applied model approach. To take this dependence into account the internal resistance has been modelled by an empirical function, which considers the impact of the temperature and the DC current. In addition, a thermal model has been developed that predicts the temperature based on the load dependence of the temperature control system. The overall heat loss of the fuel cell system has been modelled as a function of the DC current. Furthermore, parasitic losses of the BOP are incorporated in the system model.

From the experimental analysis of the VRFB it has been found that the equivalent internal resistance of the battery stack depends on the SOC of the electrolyte and magnitude of the charge/discharge current. A nonlinear regression analysis has been employed to model the equivalent internal resistance as a function of the SOC and the DC current rate. In addition, Coulombic losses have been considered by a shunt resistance in parallel with the voltage model. An experimental method has been designed to find an empirical function to calculate the shunt resistance in dependence of the

DC current. The developed electrical model of the VRFB is an improvement compared to other models applied for system level simulations, since it takes into account voltage and Coulombic losses, which depend on the SOC and/or DC current. In addition, the designed experimental methods can be applied to extract the parameters from other VRFB systems.

Each system model has been validated against measured data with a temporal resolution of seconds by means of the cross validation technique. The predicted values of the system models show a good correlation with the measured data; the mean absolute percentage error is less than 3%.

Different energy management approaches have been reviewed, among which deterministic methods have been broadly applied for HRES due to their simplicity and robustness. Another advantage of such methods is that they can be applied in real-time. Thus, the approach chosen uses three well known mechanisms, but their combination forms an advanced energy management strategy. The statecharts formalism is used to establish an overall coordination of the systems. The double exponential smoothing is implemented because no external weather data or large sets of historical data are required to calculate the forecast and the trend. In addition, low pass filter have been considered to smooth the power reference signal for the corresponding energy systems according to their dynamic limitations. These three mechanisms can be easily implemented into the simulation software or the PLCs. Moreover, the results show that the combined approach can effectively manage the HRES.

To summarise, the second objective was motivated by the need to develop system models which reflect the real operational behaviour of the energy storage technologies, which can easily be integrated in system level simulations to design HRES and to define operating strategies. The main achievements are:

- Development of combined system models of an alkaline electrolyser, a PEM fuel cell and a VRFB. System specific operational states and internal losses have been incorporated. Experimental methods have been designed to extract the empirical coefficients from the measured data. Each developed system model shows a good accuracy with a mean absolute percentage error of less than 3%.
- Development of an advanced energy management strategy to coordinate and to control the HRES. Three mechanisms, the statechart formalism, the double exponential smoothing and the frequency decoupling have been combined to manage the HRES and to analyse the performance of building-integrated HRES by means of simulation and real-time tests with the experimental platform.

### 7.2.3 Performance evaluation of the building-integrated energy storage technologies

Various simulation scenarios have been defined to assess the application of building-integrated hydrogen systems and VRFB and to determine the local utilisation of on-site generated PV energy and the grid interaction of a building. A domestic load model has been applied to generate a load profile that reflects the typical stochastic behaviour of the electric demand. Simulation inputs were the generated load profile and measured data of the installed PV systems at Ostfalia University with a temporal resolution of one minute. Applying high temporal resolution data is one advantage of this thesis compared to other simulation studies which typically use data with a resolution of minutes to 1 hour to perform annual simulations.

A sensitivity analysis has been performed to optimise the threshold values of the control parameters (the minimum and maximum power input/output) included in the strategic supervisory level. The power output of the fuel cell should be restricted to 75% of the maximum power output to achieve high overall system efficiency. The efficacy of the developed strategic supervisory level has been demonstrated by comparing a simulation with and without demand forecast. It has been shown that the developed forecast algorithm to activate the energy systems reduced the number of start-ups of the electrolyser by 54% and that its average operational duration was increased by 22%. As a result, the electrolyser was operated more efficiently.

The simulations of a building-integrated hydrogen system have shown that more on-site generated renewable energy was utilised to meet the building's electrical demand and that the grid interaction of the building was significantly reduced. The value of the AC energy efficiency of the hydrogen system was less than 20%. A considerable proportion of the losses were manifested in heat for both the electrolyser and the fuel cell. Therefore, the possibility to capture the waste heat of the hydrogen system and making use of it in a domestic application has been investigated. The results have shown that the overall energy efficiency can be improved from less than 20% to approximately 35%. Furthermore, it has been found that the utilisation of waste heat of the electrolyser can be used to satisfy 18% of the annual domestic hot water demand. This important outcome underlines the utilisation of the waste heat from both the electrolyser and the fuel cell, which has not gained much attention so far. Only a few simulation studies have been found (Lacko et al. 2014; Sossan et al. 2014), whereby both studies applied simplified models without analysing the temperature regime of the utilised heat. In this thesis the utilisation of the waste heat has been quantified by using a validated system model. Only the proportion of the removed heat with a reasonable temperature level of greater than 40°C has been considered.

A sensitivity analysis was conducted to establish the impact of the ratio of the PV size to the electrolyser size on the annual performance and the grid interaction. The results show that if the electrolyser is sized to meet the maximum PV power, the annual efficiency will be lower and the grid interaction will increase. With increasing PV size the utilisation of the electrolyser and thus the performance slightly increases; however, at a certain ratio the grid interaction starts to increase again. From the results obtained, it can be suggested that the electrolyser should have a power capacity of approximately 70% of the PV size to achieve a good performance and a low grid interaction. This result is interesting because a commonly applied sizing method for an electrolyser is to calculate the difference between the rated power of the renewable sources and the minimum load, and to reduce the calculated value by 50% to get a high utilisation (Gazey 2014). The capability of the electrolyser to reduce the power fluctuations is not considered. In addition, this result is relevant for stand-alone applications in which the power fluctuations not met by the electrolyser would need to be compensated by a short-term storage such as lead-acid batteries to guarantee grid stability. This outcome also underlines the need to apply high resolution data to assess the performance of energy storages associated with volatile power profiles.

Similar simulations have been carried out with the VRFB system model. The annual simulations have shown that the electricity grid import and the grid interaction of the building were significantly reduced. A sensitivity analyses has been performed to investigate the impact of the PV size and the electric demand on the annual performance of the VRFB. It has been found that the electrical demand should be high enough to operate the VRFB at higher discharge power rates to achieve a higher overall AC energy efficiency. Furthermore, a low electric demand leads to a poor utilisation of the VRFB's SOC during the summer months. The SOC was kept at high average levels which may accelerate component degradation (Schreiber 2011). A simulation scenario with an increased demand has been conducted and the results showed that the annual AC efficiency of the VRFB was slightly increased from 46.2% to 48.8%. Even more importantly, cycling of the electrolyte at high SOC levels was avoided.

In addition, simulations have been carried out to assess the application of building-integrated hydrogen systems and VRFB in a smart grid scenario. A demand response signal was provided from a smart grid operator. The results demonstrate that both the electrolyser and the VRFB can be used to store excess electric energy from the grid. Especially, during the winter season where the energy storage system is most of the time unused and at low SOC levels because of the low available PV power. The shared use of the energy storage system could be beneficial for both the building owner and the smart grid operator. Compared to lead-acid batteries, which have to be kept at high SOC

levels, both storage technologies may have a high potential to be applied as deferrable load in a future smart grid.

Based on the results of the annual simulations of both, the hydrogen systems and VRFB, a method to compare their performance in a domestic application has been described and applied. Considering only the AC energy efficiency the VRFB outperforms the hydrogen system. The AC round-trip efficiency of the hydrogen system is approximately one third of the VRFB's efficiency. Regarding the system design it can be suggested that the VRFB should be placed in buildings with a high average demand, whereas the hydrogen system can be better adapted to the installed PV size and the electric demand due to the independent scalability of the electrolyser and fuel cell.

The last part of this thesis dealt with the experimental investigation of the dynamic performance of the hydrogen system and the VRFB. The developed energy management strategy has been tested for both single storage and hybrid storage configuration of the experimental platform. It has been demonstrated that the developed energy management strategy can effectively coordinate and manage the power flow among the energy systems. Furthermore, the load following capability of the hydrogen system and the VRFB integrated into building automation system has been deeply analysed. Compared to the multiple dynamic event experiments, the results show that the response time of the energy systems was slightly increased. Reasons for this can be attributed to the communication among the strategic supervisory level, energy meters and the local control units. Such effects are often overlooked and limit the capability of the energy systems to compensate high power fluctuations within very short timescales. However, the presented results have demonstrated that the applied building automation system has the potential to control the AC power of the energy systems quickly and that the volatile power injection of the PV can be reduced. This important fact supports the application of LON to be used as communication protocol for demand side management to deal with fast power fluctuations in the range of seconds.

Based on the results obtained the dynamic performance of the electrolyser, fuel cell and VRFB have been evaluated. It has been found that dynamic operation influences the performance of the electrolyser system. The AC energy efficiency was reduced from 40% to 33% compared to the steady-state experiments. Reasons for this can be found in the start-up process, gas losses, warm-up period and the intermittent operation. The fuel cell showed a better dynamic performance; the efficiency was only 2% below the steady state results. The performance of the VRFB was only slightly affected by the dynamic operation.

To summarise, the third objective was motivated by the need to evaluate the application of building-integrated hydrogen systems and VRFB in the light of the developed systems models. In addition, to

investigate the dynamic performance of the hydrogen systems and VRFB integrated into building automation system. The main outcomes are:

- Using the advanced energy management strategy the number of unnecessary start-ups of the electrolyser can be significantly reduced and the average operating time can be increased.
- The application of high temporal resolution has revealed important insights of the energy systems regarding their dynamic performance and how they can be used to reduce the grid interaction of the building.
- When designing building-integrated HRES, the grid interaction index should be considered for an overall optimisation to determine the system sizes. Again, high temporal resolution data is required to reveal high power peaks, which affects both the performance and the grid interaction.
- The utilisation of the waste heat of the electrolyser and the fuel cell can increase the overall efficiency. An increase from 20% to 35% has been demonstrated by annual simulations.
- Hydrogen systems and VRFB have a high potential as a deferrable load in the smart grid context. During seasons with low PV energy yield the storage capacity of both remains unused. A shared usage of the storage could be beneficial for the building owner and the smart grid operator.
- The real-time demonstration of the energy management strategy to coordinate and to control the experimental platform. The dynamic performance of an alkaline electrolyser, PEM fuel cell and VRFB system integrated into LON based building automation system to equalise PV power and a domestic demand has been analysed and documented.
- The dynamic operation influences negatively the performance of energy storage systems, in particular of the electrolyser.
- Integrated in HRES the dynamic performance of the energy storages is limited by the communication among the distributed energy systems and by the interaction of different control units.

## 7.3 Recommendations and future work

The focus of this thesis was to perform system level simulations and thus to adequately model the electrical and thermal behaviour rather than to model in detail the processes which occur inside the components. The presented models could be further improved by additional experimental investigations. In the following recommendations are proposed to enhance the models.

Especially, ageing processes should be considered in long term simulations over a period of several years. The durability is an important factor to assess the performance, economics or to compare different technologies. A first order approach would be the introduction of linear coefficients to take into account the performance degradation as it has been already reported for PEM fuel cells (Miller & Bazylak 2011) and different types of batteries (Lemaire et al. 2008). Similar factors could be defined for electrolyser and VRFB based on further experimental analysis.

Although the simplifications made to predict the operating temperature of the electrolyser are in good agreement with measured data, an overall validation including the cooling cycle has not been performed due to warranty limitations. A more complex experimental set-up could be realised to investigate the temperature distribution and the flow pattern of the electrolyte. These findings could be used for a more detailed simulation study, for instance, to introduce a two-dimensional model that considers the natural circulation of the electrolyte.

In addition, rather than extending the component models there are many opportunities to use the existing fully validated system models and the developed experimental platform to carry out further research in the following areas:

- Apply the generic model layout to the other energy systems of the experimental platform such as the lead acid battery and the combined heat and power unit.
- Testing the applicability and capability of the developed system models as well as the empirical methods on other brands.
- A centralised deterministic approach has been applied to control HRES, alternatively a decentralised self-organising approach, for example, a multi-agent system could be implemented and its performance could be analysed by means of simulations and experiments. Another focus could be on the implementation of an advanced demand and supply forecast algorithm. Data from a weather forecast or day-ahead electricity tariffs could be processed to schedule the operation of the energy systems.
- As proposed in this thesis, it is worthwhile to have a holistic view on the application when introducing hydrogen systems into buildings. Utilisation of the waste heat could be beneficial in terms of reducing the heat supplied by conventional heat sources and finally help to

reduce the carbon emissions of the building. The presented models could be used to develop a complete building model that considers the electrical and thermal energy. A first attempted has already been made in this research direction (D'Agostino et al. 2014) where a VRFB is integrated in a residential PV heat pump system.

- Electric vehicles could be considered as an additional electric storage. Several new challenging issues arise in this research avenue. The electric vehicle can be used as mobile storage that provides an additional degree of freedom to optimise the energy flow within buildings. Therefore, integrated energy management strategies are needed to optimise the charging of the electric vehicle with respect to the energy needs of its environment. A charging station has already been integrated into experimental platform at Ostfalia and could be used for further developments.
- The placement of electrical storage in non-domestic buildings would be also interesting. The developed system models could be scaled up to be used in medium to large commercial and industrial environments. Based on standard load profiles, for instance provided from the BDEW (German Association of Energy and Water Industries), simulation studies could be carried out to assess the value of the application of hydrogen systems or VRFB in this area. Both technologies can be used to lower the peak power, which is often a cost driver in industry.
- A techno-economic analysis could be carried out based on the developed models. Additional simulation inputs (e.g. investment costs, time varying electricity tariffs, fuel costs, component ageing and operating costs) could be considered and a model based optimisation could be performed to define operational strategies, to reduce the operating costs, to compare different storage technologies or to develop a business case where the application of storage could be justified.

## 7.4 Concluding words

The overall aim of this thesis was firstly to provide a better understanding of the impact of operational aspects and dynamic operation on hydrogen systems and VRFB integrated in a domestic building equipped with renewable energy sources and secondly to show how theoretical and operational aspects can be combined to an integrated system model applicable for annual simulations with a high temporal resolution.

A recently started project initiated by the International Energy Agency has underlined the research need to investigate the technical potential and the performance of all kind of energy storage systems for buildings associated with renewable energy systems (IEA-ECES 2014). In addition, computer

models are required to develop control strategies for the operation of the whole building and to assess the performance.

This thesis was also motivated by these needs and it can provide the following contributions to knowledge:

- The development of an experimental platform composed of renewable energy sources, alkaline electrolyser, PEM fuel cell and VRFB to investigate the performance of the energy storage systems integrated into building automation system and to test control strategies.
- The dynamic performance of an alkaline electrolyser, PEM fuel cell and VRFB has been experimentally investigated not only at individual component level, but also at a combined system level with particular focus on domestic application.
- The development of three novel system models of an alkaline electrolyser, a PEM fuel cell and VRFB, which combine theoretical and operational aspects. In addition, experimental methods have been designed and empirical functions have been developed. All system models are fully validated with measured data.
- The performance of building-integrated hydrogen systems and VRFB has been assessed by means of annual simulations with a high temporal resolution. In addition, suggestions have been made to improve the performance of the energy systems.

The presented findings provide a rich data pool and validated models to further develop the understanding of the dynamic behaviour of alkaline electrolyser, PEM fuel cell and VRFB at system level. Furthermore, the presented research exposes the current state of the employed technologies and its findings can be used to further improve their performance with respect to the dynamic operation. Moreover, the presented findings provide important insights, which are valuable for component developers, system designers, system integrators and control engineers.

# 8 References


Abd El-Aal, AEMMA (2005), *Modelling and simulation of a photovoltaic fuel cell hybrid system*. PhD-Thesis, University of Kassel, Kassel, Germany. Available from: http://nbn-resolving.de/urn:nbn:de:hebis:34-2242.

Accagen SA (2011), *Hydrogen generation plant Operating Manual*.

Agarwal, Y, Weng, T & Gupta, RK (2011), 'Understanding the role of buildings in a smart microgrid'. *Design, Automation & Test in Europe Conference & Exhibition (DATE), 2011. 14 - 18 March 2011, Grenoble, France ; proceedings,* IEEE, Piscataway, NJ, pp. 1–6.

Agbli, KS, Péra, MC, Hissel, D, Rallières, O, Turpin, C & Doumbia, I (2011), 'Multiphysics simulation of a PEM electrolyser: Energetic Macroscopic Representation approach', *International Journal of Hydrogen Energy*, vol. 36, no. 2, pp. 1382–1398.

AG-En (2014), *Stromerzeugung nach Energieträgern 1990 - 2013*. Available from: http://www.ag-energiebilanzen.de/#quartalsbericht_q4_2013_23012014 [23 October 2014].

Al-Alawi, A, M Al-Alawi, S & M Islam, S (2007), 'Predictive control of an integrated PV-diesel water and power supply system using an artificial neural network', *Renewable Energy*, vol. 32, no. 8, pp. 1426–1439.

Alotto, P, Guarnieri, M & Moro, F (2014), 'Redox flow batteries for the storage of renewable energy: A review', *Renewable and Sustainable Energy Reviews*, vol. 29, pp. 325–335.

Ashok, S (2007), 'Optimised model for community-based hybrid energy system', *Renewable Energy*, vol. 32, no. 7, pp. 1155–1164.

Åström, KJ & Hägglund, T (1995), *PID controllers,* International Society for Measurement and Control, Research Triangle Park, N.C.

Bajpai, P & Dash, V (2012), 'Hybrid renewable energy systems for power generation in stand-alone applications: A review', *Renewable and Sustainable Energy Reviews*, vol. 16, no. 5, pp. 2926–2939.

Ball, M & Wietschel, M (2009), 'The future of hydrogen – opportunities and challenges', *International Journal of Hydrogen Energy*, vol. 34, no. 2, pp. 615–627.

Balta-Ozkan, N, Davidson, R, Bicket, M & Whitmarsh, L (2013), 'The development of smart homes market in the UK', *Energy*, vol. 60, pp. 361–372.

Barote, L, Marinescu, C & Georgescu, M (2009), 'VRB modeling for storage in stand-alone wind energy systems'. *PowerTech, 2009 IEEE Bucharest.* PowerTech, 2009 IEEE Bucharest, pp. 1–6.

Barthels, H, Brocke, W, Bonhoff, K, Groehn, HG, Heuts, G, Lennartz, M, Mai, H, Mergel, J, Schmid, L & Ritzenhoff, P (1998), 'Phoebus-Jülich: An autonomous energy supply system comprising photovoltaics, electrolytic hydrogen, fuel cell', *International Journal of Hydrogen Energy*, vol. 23, 23 // 4, pp. 295–301.

Bergen, A, Pitt, L, Rowe, A, Wild, P & Djilali, N (2009), 'Experimental assessment of a residential scale renewable–regenerative energy system', *Journal of Power Sources*, vol. 186, no. 1, pp. 158–166.

Bergen, A, Schmeister, T, Pitt, L, Rowe, A, Djilali, N & Wild, P (2007), 'Development of a dynamic regenerative fuel cell system', *Journal of Power Sources*, vol. 164, no. 2, pp. 624–630.

Bernal-Agustín, JL & Dufo-López, R (2009), 'Simulation and optimization of stand-alone hybrid renewable energy systems', *Renewable and Sustainable Energy Reviews*, vol. 13, no. 8, pp. 2111–2118.

Bhuiyan, FA & Yazdani, A (2012), 'Energy storage technologies for grid-connected and off-grid power system applications'. *2012 IEEE Electrical Power and Energy Conference. Took place 10-12 October 2012 in London, Canada,* IEEE, Piscataway, NJ, pp. 303–310.

Bilodeau, A & Agbossou, K (2006), 'Control analysis of renewable energy system with hydrogen storage for residential applications', *Journal of Power Sources*, vol. 162, no. 2, pp. 757–764.

Bindner, H, Ekman, C, Gehrke, O & Isleifsson, F (2011), *Characterization of vanadium flow battery. Revised,* Risø-DTU, Roskilde, Denmark.

Blanc, C (2009), *Modeling of a vanadium redox flow battery electricity storage system*. PhD-Thesis, EPFL, Ecole Polytechnique Fédérale de Lausanne, Lausanne, Switzerland.

Blanc, C & Rufer, A (2009), 'Optimization of the operating point of a vanadium redox flow battery'. *IEEE Energy Conversion Congress and Exposition, 2009. ECCE 2009 ; 20 - 24 Sept. 2009, San Jose, California, USA,* IEEE, Piscataway, NJ, pp. 2600–2605.

Blanc, C & Rufer, A (2010), *Understanding the Vanadium Redox Flow Batteries*. *Paths to Sustainable Energy, Dr Artie Ng (Ed.)*. Available from: http://www.intechopen.com/books/paths-to-sustainable-energy/understanding-the-vanadium-redox-flow-batteries [24 January 2014].

Bocklisch, T, Böttiger, M & Paulitschke, M (2014), 'Multi-storage Hybrid System Approach and Experimental Investigations', *Energy Procedia*, vol. 46, pp. 186–193.

Börmer, J (2011), *Abschätzung der Bedeutung des Einspeisemanagements nach EEG 2009 Auswirkungen auf die Windenergieerzeugung in den Jahren 2009 und 2010*. Available from: www.wind-energie.de/ [09 September 2014].

Bundesnetzagentur (2014), *Monitoringbericht 2013*. Available from: http://www.bundesnetzagentur.de/SharedDocs/Downloads/DE/Allgemeines/Bundesnetzagentur/Publikationen/Berichte/2013/131217_Monitoringbericht2013.pdf?__blob=publicationFile&v=15 [09 September 2014].

Cau, G, Cocco, D & Petrollese, M (2014), 'Modeling and Simulation of an Isolated Hybrid Micro-grid with Hydrogen Production and Storage', *Energy Procedia*, vol. 45, pp. 12–21.

Caux, S, Hankache, W, Fadel, M & Hissel, D (2010), 'On-line fuzzy energy management for hybrid fuel cell systems', *International Journal of Hydrogen Energy*, vol. 35, no. 5, pp. 2134–2143.

Çengel, YA (2003), *Heat transfer*. *A practical approach,* McGraw-Hill, Boston.

Cerbe, G & Wilhelms, G (2013), *Technische Thermodynamik*. *Theoretische Grundlagen und praktische Anwendung,* Carl Hanser Verlag, München.

Chahwan, J, Abbey, C & Joos, G (2007), 'VRB Modelling for the Study of Output Terminal Voltages, Internal Losses and Performance'. *2007 IEEE Canada Electrical Power Conference, Montreal, QC, Canada, 25-26 October 2007,* IEEE, New York, pp. 387–392.

Chatzivasileiadi, A, Ampatzi, E & Knight, I (2013), 'Characteristics of electrical energy storage technologies and their applications in buildings', *Renewable and Sustainable Energy Reviews*, vol. 25, pp. 814–830.

Cheddie, D & Munroe, N (2005), 'Review and comparison of approaches to proton exchange membrane fuel cell modeling', *Journal of Power Sources*, vol. 147, 1-2, pp. 72–84.

Chedid, R & Rahman, S (1997), 'Unit sizing and control of hybrid wind-solar power systems', *IEEE Transactions on Energy Conversion*, vol. 12, no. 1, pp. 79–85.

Chen, D, Hickner, MA, Agar, E & Kumbur, EC (2013a), 'Selective anion exchange membranes for high coulombic efficiency vanadium redox flow batteries', *Electrochemistry Communications*, vol. 26, pp. 37–40.

Chen, W, Jiyun Zhao, Tseng, KJ, Kian Wee Ng, Lip, WTW & Rao Yimin (2013b), 'Optimization of the VRB-ESS integrated hybrid power system for building applications'. *PEDS 2013. 2013 IEEE 10th International Conference on Power Electronics and Drive Systems (PEDS), Program, April 22-25, 2013, Kitakyushu, Japan,* pp. 1219–1224.

CoDeSys (2014), *CODESYS – industrial IEC 61131-3 PLC programming*. Available from: http://www.codesys.com/ [22 May 2014].

Cooper, DJ (2008), *Practical Process Control*. *Proven Methods and Best Practices for Automatic PID Control.* e-textbook published on www.controlguru.com. Available from: http://www.controlguru.com/pages/table.html [04 August 2014].

Courtecuisse, V, Sprooten, J, Robyns, B, Petit, M, Francois, B & Deuse, J (2010), 'A methodology to design a fuzzy logic based supervision of Hybrid Renewable Energy Systems', *Mathematics and Computers in Simulation*, vol. 81, no. 2, pp. 208–224.

D'Agostino, R, Baumann, L, Damiano, A & Boggasch, E (2014), 'A Vanadium-Redox-Flow-Battery Model for Evaluation of Distributed Storage Implementation in Residential Energy Systems', *IEEE Transactions on Energy Conversion*, no. 99, pp. 1–10.

Dall'ara, R (2009), *Electrolyser for producing substances*. *EP Patent App. EP20,070,405,328*. Available from: http://worldwide.espacenet.com/publicationDetails/biblio?FT=D&date=20090520&DB=EPODOC&locale=de_EP&CC=EP&NR=2060661A1&KC=A1&ND=4 [30 November 2014].

Darras, C, Muselli, M, Poggi, P, Voyant, C, Hoguet, J & Montignac, F (2012), 'PV output power fluctuations smoothing: The MYRTE platform experience', *International Journal of Hydrogen Energy*, vol. 37, no. 19, pp. 14015–14025.

DE-BMWIU (2012), *Erster Monitoring-Bericht "Energie der Zukunft"*. Bundesministerium für Wirtschaft und Technologie (BMWI), Bundesministerium für Umwelt, Naturschutz und Reaktorsicherheit (BMU). Available from: http://www.bmwi.de/BMWi/Redaktion/PDF/Publikationen/erster-monitoring-bericht-energie-der-zukunft,property=pdf,bereich=bmwi2012,sprache=de,rwb=true.pdf [23 October 2014].

DECC (2014b), *Energy trends section 6: renewables*. *Renewables statistics*. Available from: https://www.gov.uk/government/uploads/system/uploads/attachment_data/file/357505/6_Renewables.pdf [24 October 2014].

DECC (2014a), *Solar photovoltaics deployment*. Available from: https://www.gov.uk/government/statistics/solar-photovoltaics-deployment [24 October 2014].

DECE (2009), *The UK Low Carbon Transition Plan*. *National strategy for climate and energy*. Available from: https://www.gov.uk/government/publications/the-uk-low-carbon-transition-plan-national-strategy-for-climate-and-energy [23 October 2014].

Deshmukh, M & Deshmukh, S (2008), 'Modeling of hybrid renewable energy systems', *Renewable and Sustainable Energy Reviews*, vol. 12, no. 1, pp. 235–249.

DEW (2008), *Nichtrostender austenitischer Stahl 1.4404*. Available from: http://www.dew-stahl.com/fileadmin/files/dew-stahl.com/documents/Publikationen/Werkstoffdatenblaetter/RSH/1.4404_de.pdf [21 March 2014].

Dieguez, P, Ursua, A, Sanchis, P, Sopena, C, Guelbenzu, E & Gandia, L (2008), 'Thermal performance of a commercial alkaline water electrolyzer: Experimental study and mathematical modeling', *International Journal of Hydrogen Energy*, vol. 33, no. 24, pp. 7338–7354.

DIN EN 61131 (2004), *DIN EN 61131-1: Speicherprogrammierbare Steuerungen,* Beuth Verlag, Berlin.

DIN EN ISO 16484-2 (2004), *DIN EN ISO 16484-2 Systeme der Gebäudeautomation (GA),* Beuth Verlag, Berlin.

Dursun, E & Kilic, O (2012), 'Comparative evaluation of different power management strategies of a stand-alone PV/Wind/PEMFC hybrid power system', *International Journal of Electrical Power & Energy Systems*, vol. 34, no. 1, pp. 81–89.

EeB (2010), 'Energy-efficient buildings PPP. Multi-Annual Roadmap and longer term strategy'. Directorate-General for Research and Innovation, European Commission, vol. 24283.

Eftekharnejad, S, Vittal, V, Heydt, Keel, B & Loehr, J (2013), 'Impact of increased penetration of photovoltaic generation on power systems', *IEEE Transactions on Power Systems*, vol. 28, no. 2, pp. 893–901.

EN 14908 (2005), *DIN EN 14908-1:2005 Firmenneutrale Datenkommunikation für die Gebäudeautomation und Gebäudemanagement - Gebäudedatennetzprotokoll - Teil 1: Datenprotokollschichtenmodell,* Beuth Verlag, Berlin.

EN 50090 (2005), *DIN EN 50090-5-1:2005-06 Elektrische Systemtechnik für Heim und Gebäude (ESHG) - Teil 5-1: Medien und medienabhängige Schichten - Signalübertragung auf elektrischen Niederspannungsnetzen für ESHG Klasse 1;,* Beuth Verlag, Berlin.

ENA/EnergyUK (2012), *Smart Demand Response: A Discussion Paper*. Available from: http://www.energynetworks.org/news/publications/reports.html [08 November 2014].

Erdinc, O, Elma, O, Uzunoglu, M, Selamogullari, US, Vural, B, Ugur, E, Boynuegri, AR & Dusmez, S (2012), 'Experimental performance assessment of an online energy management strategy for varying renewable power production suppression', *International Journal of Hydrogen Energy*, vol. 37, no. 6, pp. 4737–4748.

Erdinc, O & Uzunoglu, M (2010), 'Recent trends in PEM fuel cell-powered hybrid systems: Investigation of application areas, design architectures and energy management approaches', *Renewable and Sustainable Energy Reviews*, vol. 14, no. 9, pp. 2874–2884.

Erdinc, O & Uzunoglu, M (2011), 'The importance of detailed data utilization on the performance evaluation of a grid-independent hybrid renewable energy system', *International Journal of Hydrogen Energy*, vol. 36, no. 20, pp. 12664–12677.

ETG Task Force DSM (2012), *Demand Side Integration*. *Lastverschiebungspotenziale in Deutschland*. VDE VERBAND DER ELEKTROTECHNIK ELEKTRONIK INFORMATIONSTECHNIK e.V., Frankfurt.

ETG Task Force ES (2009), *Energiespeicher in Stromversorgungssystemen mit hohem Anteil erneuerbarer Energieträger*. *Bedeutung, Stand der Technik, Handlungsbedarf*. VDE VERBAND DER ELEKTROTECHNIK ELEKTRONIK INFORMATIONSTECHNIK e.V. Available from: www.vde.com/de/InfoCenter/Seiten/Details.aspx?eslShopItemID=b631a513-35fa-4587-b396-5c897827551c.

Etxeberria, A, Vechiu, I, Camblong, H & Vinassa, JM (2010), 'Hybrid Energy Storage Systems for renewable Energy Sources Integration in microgrids: A review', *IPEC, 2010 Conference Proceedings*, 27-29 Oct. 2010, pp. 532–537.

EU-DGE (2011), *Energy Roadmap 2050*, European Commission. Available from: http://ec.europa.eu/energy/energy2020/roadmap/index_en.htm [04 November 2014].

EU-DGE (2013), *The future role and challenges of Energy Storage*. *DG ENER Working Paper*, European Commission. Directrorate-General for Energy. Available from: http://ec.europa.eu/energy/infrastructure/doc/energy-storage/2013/energy_storage.pdf [04 July 2014].

EU-DGR (2006), *European SmartGrids Technology Platform*. *Vision and strategy for Europe's electricity networks of the future*, European Commission Directorate-General for Research, Information and Communication Unit. Available from: http://bookshop.europa.eu/en/european-smartgrids-technology-platform-pbKINA22040/ [23 October 2014].

EU-Directive (2010), *Directive 2010/31/EU of the European Parliament and of the Council of 19 May 2010 on the energy performance of buildings*, European Commission. Available from: http://eur-lex.europa.eu/LexUriServ/LexUriServ.do?uri=OJ:L:2010:153:0013:0035:EN:PDF [03 July 2014].

EU-EC (2008), *Communication from the Commission to the European Parliament, the Council, the European Economic and Social Committee and the Committee of the Regions - 20 20 by 2020 - Europe's climate change opportunity*, European Commission. Available from: http://eur-lex.europa.eu/legal-content/EN/TXT/?uri=CELEX:52008DC0030 [24 October 2014].

EU-ECO (2014), *Conclusions on 2030 Climate and Energy Policy Framewor*. *Note: European Council (23 and 24 October 2014)*. Available from: http://www.consilium.europa.eu/uedocs/cms_data/docs/pressdata/en/ec/145356.pdf [24 October 2014].

Fan, Z, Kulkarni, P, Gormus, S, Efthymiou, C, Kalogridis, G, Sooriyabandara, M, Zhu, Z, Lambotharan, S & Chin, WH (2013), 'Smart Grid Communications: Overview of Research Challenges, Solutions, and Standardization Activities', *IEEE Communications Surveys & Tutorials*, vol. 15, no. 1, pp. 21–38.

Figueiredo, J & Martins, J (2010), 'Energy Production System Management – Renewable energy power supply integration with Building Automation System', *Energy Conversion and Management*, vol. 51, no. 6, pp. 1120–1126.

Gahleitner, G (2013), 'Hydrogen from renewable electricity: An international review of power-to-gas pilot plants for stationary applications', *International Journal of Hydrogen Energy*, vol. 38, no. 5, pp. 2039–2061.

Gammon, R, Roy, A, Barton, J & Little, M (2006), *Hydrogen and renewables integration (HARI). Report of the project*. Available from: http://www.ieahia.org/pdfs/HARI.pdf [11 July 2014].

Gazey, RN (2014), *Sizing Hybrid Green Hydrogen Energy generation and Storage systems (HGHES) to enable an increase in renewable penetration for stabilising the grid*. PhD Thesis, Robert Gordon University, Aberdeen, UK. Available from: http://openair.rgu.ac.uk.

Greer, C, Wollman, DA, Prochaska, DE, Boynton, PA, Mazer, JA, Nguyen, CT, FitzPatrick, GJ, Nelson, TL, Koepke, GH, Hefner Jr, AR, Pillitteri, VY, Brewer, TL, Golmie, NT, Su, DH, Eustis, AC, Holmberg, DG & Bushby, ST (2014), *NIST Framework and Roadmap for Smart Grid Interoperability Standards, Release 3.0*. Available from: http://www.nist.gov/smartgrid/framework3.cfm [09 November 2014].

Gupta, A, Saini, R & Sharma, M (2011), 'Modelling of hybrid energy system—Part I: Problem formulation and model development', *Renewable Energy*, vol. 36, no. 2, pp. 459–465.

H2SusBuild (2010), *H2SusBuild project*. Available from: http://www.h2susbuild.ntua.gr/ [27 January 2013].

Hamada, Y, Takeda, K, Goto, R & Kubota, H (2011), 'Hybrid utilization of renewable energy and fuel cells for residential energy systems', *Energy and Buildings*, vol. 43, no. 12, pp. 3680–3684.

Harel, D (1987), 'Statecharts: a visual formalism for complex systems', *Science of Computer Programming*, vol. 8, no. 3, pp. 231–274.

Harrison, KW, Ramsden, T, Martin, G & Saur, G (2009), *Renewable Electrolysis Integrated System Development and Testing*. *DOE Hydrogen Program FY 2009 Annual Progress Report*, National Renewable Energy Laboratory. Available from: http://hydrogen.energy.gov/pdfs/progress09/ii_e_4_harrison.pdf [12 November 2014].

Harrison, KW, Remick, R & Martin, GD (2010), *Hydrogen Production: Fundamentals and Case Study Summaries*. Available from: http://www.nrel.gov/hydrogen/pdfs/47302.pdf [05 May 2013].

Hatti, M, Meharrar, A & Tioursi, M (2011), 'Power management strategy in the alternative energy photovoltaic/PEM Fuel Cell hybrid system', *Renewable and Sustainable Energy Reviews*, vol. 15, no. 9, pp. 5104–5110.

Haubrock, J (2007), *Parametrierung elektrischer Äquivalentschaltbilder von PEM Brennstoffzellen*. PhD-Thesis, Otto-von-Guericke-Universität, Magdeburg, Germany.

Henao, C, Agbossou, K, Hammoudi, M, Dubé, Y & Cardenas, A (2014), 'Simulation tool based on a physics model and an electrical analogy for an alkaline electrolyser', *Journal of Power Sources*, vol. 250, pp. 58–67.

Hollinger, R, Wille-Haussmann, B, Erge, T, Sönnichsen, J, Stillahn, T & Kreifels, N (2013), *SPEICHERSTUDIE 2013*. *Kurzgutachten zur Abschätzung und Einordnung energiewirtschaftlicher, ökonomischer und anderer Effekte bei Förderung von objektgebunden elektrochemischen Speichern*. Fraunhofer-Institut für Solare Energiesysteme ISE. Available from: http://www.ise.fraunhofer.de/de/veroeffentlichungen/veroeffentlichungen-pdf-dateien/studien-und-konzeptpapiere/speicherstudie-2013.pdf [10 July 2014].

Hollmuller, P, Joubert, J, Lachal, B & Yvon, K (2000), 'Evaluation of a 5 kWp photovoltaic hydrogen production and storage installation for a residential home in Switzerland', *International Journal of Hydrogen Energy*, vol. 25, no. 2, pp. 97–109.

Holt, CC (2004), 'Forecasting seasonals and trends by exponentially weighted moving averages', *International Journal of Forecasting*, vol. 20, no. 1, pp. 5–10.

Hongfeng Li & Hennessy, T (2013), 'European town microgrid and energy storage application study'. *ISGT. Fourth Conference on Innovative Smart Grid Technologies,* IEEE, Piscataway, N.J., pp. 1–6.

Ibrahim, H, Ilinca, A & Perron, J (2008), 'Energy storage systems—Characteristics and comparisons', *Renewable and Sustainable Energy Reviews*, vol. 12, no. 5, pp. 1221–1250.

IEA (2014), *Technology Roadmap Energy storage*, International Energy Agency. Available from: http://www.iea.org/publications/freepublications/publication/technology-roadmap-energy-storage-.html [14 November 2014].

IEA-ECES (2014), *Annex 31 Energy Storage with Energy Efficient Buildings and Districts: Optimization and Automation*, International Energy Agency. Available from: http://www.iea-eces.org/annexes/ongoing-annexes/annex-31.html [23 November 2014].

IEA-HIA (2010), *TASK FINAL REPORT Annex-18, Phase 2 "Evaluation of Integrated Systems"*, International Energy Agency. Available from: http://ieahia.org/page.php?s=publications&p=technical [14 November 2014].

IEC (2011), *Electrical energy storage*. *White Paper*. International Electrotechnical Commission. Available from: http://www.iec.ch/whitepaper/energystorage/?ref=extfooter [08 July 2014].

Ipsakis, D, Voutetakis, S, Seferlis, P, Stergiopoulos, F & Elmasides, C (2009), 'Power management strategies for a stand-alone power system using renewable energy sources and hydrogen storage', *International Journal of Hydrogen Energy*, vol. 34, no. 16, pp. 7081–7095.

Isermann, R (2008), *Mechatronische Systeme*. *Grundlagen,* Springer Berlin Heidelberg, Berlin, Heidelberg.

Jiao, K & Li, X (2011), 'Water transport in polymer electrolyte membrane fuel cells', *Progress in Energy and Combustion Science*, vol. 37, no. 3, pp. 221–291.

Jordan, U & Vajen, K (2005), 'Programm to generate domestic hot water profiles with statistical means for user defined conditions'. *ISES 2005 Solar World Congress. Proceedings of 30th National Passive Solar Conference,* American Solar Energy Society, Orlando, Florida USA.

Jun, Z, Junfeng, L, Jie, W & Ngan, HW (2011), 'A multi-agent solution to energy management in hybrid renewable energy generation system', *Renewable Energy*, vol. 36, no. 5, pp. 1352–1363.

Kanchev, H, Di Lu, Colas, F, Lazarov, V & Francois, B (2011), 'Energy Management and Operational Planning of a Microgrid With a PV-Based Active Generator for Smart Grid Applications', *IEEE Transactions on Industrial Electronics*, vol. 58, no. 10, pp. 4583–4592.

Kastner, W, Neugschwandtner, G, Soucek, S & Newmann, H (2005), 'Communication Systems for Building Automation and Control', *Proceedings of the IEEE*, vol. 93, no. 6, pp. 1178–1203.

Kaundinya, DP, Balachandra, P & Ravindranath, NH (2009), 'Grid-connected versus stand-alone energy systems for decentralized power—A review of literature', *Renewable and Sustainable Energy Reviews*, vol. 13, no. 8, pp. 2041–2050.

Kélouwani, S, Agbossou, K & Chahine, R (2005), 'Model for energy conversion in renewable energy system with hydrogen storage', *Journal of Power Sources*, vol. 140, no. 2, pp. 392–399.

Khan, M & Iqbal, M (2009), 'Analysis of a small wind-hydrogen stand-alone hybrid energy system', *Applied Energy*, vol. 86, no. 11, pp. 2429–2442.

Kim, H, Cho, CY, Nam, JH, Shin, D & Chung, T (2010), 'A simple dynamic model for polymer electrolyte membrane fuel cell (PEMFC) power modules: Parameter estimation and model prediction', *International Journal of Hydrogen Energy*, vol. 35, no. 8, pp. 3656–3663.

Kim, J, Lee, S, Srinivasan, S & Chamberlin, C (1995), 'Modeling of Proton Exchange Membrane Fuel Cell Performance with an Empirical Equation', *Journal of The Electrochemical Society*, vol. 142, no. 8, p. 2670.

KNX-Assoc (2014), *KNX Association*. Available from: http://www.knx.org/knx-en/index.php [22 May 2014].

Kolokotsa, D, Rovas, D, Kosmatopoulos, E & Kalaitzakis, K (2011), 'A roadmap towards intelligent net zero- and positive-energy buildings', *Solar Energy*, vol. 85, no. 12, pp. 3067–3084.

LabERT (2014), *Labor für Elektrotechnik und regenerative Energietechnik*, Laboratory of Electrical and Renewable Energy Engineering, Ostfalia University. Available from: http://www.ostfalia.de/cms/de/v/wir_ueber_uns/Institute_Labor/EOS/E-Technik.html [10 November 2014].

Lacko, R, Drobnič, B, Mori, M, Sekavčnik, M & Vidmar, M (2014), 'Stand-alone renewable combined heat and power system with hydrogen technologies for household application', *Energy*, vol. 77, pp. 164–170.

Lagorse, J, Paire, D & Miraoui, A (2010), 'A multi-agent system for energy management of distributed power sources', *Renewable Energy*, vol. 35, no. 1, pp. 174–182.

Larminie, J & Dicks, A (2003), *Fuel cell systems explained,* John Wiley & Sons Ltd, Chichester, West Sussex.

Le Canut, J, Latham, R, Mérida, W & Harrington, DA (2009), 'Impedance study of membrane dehydration and compression in proton exchange membrane fuel cells', *Journal of Power Sources*, vol. 192, no. 2, pp. 457–466.

Lemaire, E, Mattera, F, Delaille, A & Malbranche, P (2008), 'Assessment of Storage Ageing in Different Types of PV Systems: Technical and Economical Aspects'. *23rd European Photovoltaic Solar Energy Conference. Proceedings of the international conference held in Valencia, Spain, 1-5 September 2008,* WIP-Renewable Energies, München, Germany.

LeRoy, R, Bowen, C & LeRoy, D (1980), 'The Thermodynamics of Aqueous Water Electrolysis', *Journal of The Electrochemical Society,* pp. 1954–1962.

Lide, DR (ed.) (2006), *CRC Handbook of chemistry and physics*. *2005-2006 : a ready-reference book of chemical and physical data,* CRC Press; Taylor & Francis Group, Boca Raton, New York, Washington.

Little, M, Thomson, M & Infield, D (2007), 'Electrical integration of renewable energy into stand-alone power supplies incorporating hydrogen storage', *International Journal of Hydrogen Energy*, vol. 32, 10-11, pp. 1582–1588.

Livingstone, D (2009), *A Practical Guide to Scientific Data Analysis,* John Wiley & Sons, Ltd.

LonMark (2014), *LonMark International*. Available from: http://www.lonmark.org/ [22 May 2014].

Lopes, LAC, Katiaraei, F, Mauch, K & Arribas, L (2012), *PV Hybrid Mini-Grids: Applicable Control Methods for Various Situations*. *IEA PVPS T11-07:2012*. Available from: http://www.iea-pvps-task11.org/id40.htm [08 April 2013].

Lu, D, Fakham, H, Zhou, T & François, B (2010), 'Application of Petri nets for the energy management of a photovoltaic based power station including storage units', *Renewable Energy*, vol. 35, no. 6, pp. 1117–1124.

Lutz, A, Stewart E., Busquet S., Ewan M. & Rocheleau R. (2010), *Case Study: The Hawaii Hydrogen Power Park Demonstration at Kahua Ranch*. Sandia National Laboratories. Available from: http://ieahia.org/pdfs/Task18_Kahua_Ranch_Case_Study%28USA%29.pdf [02 February 2013].

Ma, X, Zhang, H, Sun, C, Zou, Y & Zhang, T (2012), 'An optimal strategy of electrolyte flow rate for vanadium redox flow battery', *Journal of Power Sources*, vol. 203, pp. 153–158.

Maclay, J, Brouwer, J & Samuelsen, GS (2006), 'Dynamic analyses of regenerative fuel cell power for potential use in renewable residential applications', *International Journal of Hydrogen Energy*, vol. 31, no. 8, pp. 994–1009.

Maclay, JD, Brouwer, J & Samuelsen, GS (2011), 'Experimental results for hybrid energy storage systems coupled to photovoltaic generation in residential applications', *International Journal of Hydrogen Energy*, vol. 36, no. 19, pp. 12130–12140.

Manwell, JF (2004), 'Hybrid Energy Systems', *Encyclopedia of Energy*, no. 3, pp. 215–229.

MATLAB (2012), *MATLAB Documentation - MathWorks United Kingdom*. Available from: http://www.mathworks.co.uk/help/releases/R2012b/matlab/index.html [07 February 2014].

MESSIB (2014), *Multi-source energy storage system integrated in buildings*. *Vanadium Redoy Flow Battery for the solar house*. Poster. Available from: http://www.messib.eu/assets/files/docs/MESSIB_Poster_Tech_VRB_Fin-Vanadium%20Redox%20Flow%20Battery%20for%20the%20solar%20house.pdf [15 July 2014].

Miller, M & Bazylak, A (2011), 'A review of polymer electrolyte membrane fuel cell stack testing', *Journal of Power Sources*, vol. 196, no. 2, pp. 601–613.

Milo, A, Gaztañaga, H, Etxeberria-Otadui, I, Bacha, S & Rodríguez, P (2011), 'Optimal economic exploitation of hydrogen based grid-friendly zero energy buildings', *Renewable Energy*, vol. 36, no. 1, pp. 197–205.

Mohamed, MR, Ahmad, H & Abu Seman, MN (2012), 'State-of-the-Art of Vanadium Redox Flow Battery: a Review on Research Prospects', *International Review of Electrical Engineering*, no. 5, pp. 5610–5622.

Muhando, B & Johnson, T (2012), *Characterisation and Assessment of the Flow Battery Concept for Energy Storage and Ancillary Services in Isolated Wind-Diesel Power Networks in Alaska*. *Report*, University of Alaska. Available from: http://acep.uaf.edu/media/95969/Prudent-Energy-Final-Report.pdf [15 July 2014].

Nair, NC & Garimella, N (2010), 'Battery energy storage systems: Assessment for small-scale renewable energy integration', *Energy and Buildings*, vol. 42, no. 11, pp. 2124–2130.

Nehrir, MH, Wang, C, Strunz, K, Aki, H, Ramakumar, R, Bing, J, Miao, Z & Salameh, Z (2011), 'A Review of Hybrid Renewable/Alternative Energy Systems for Electric Power Generation: Configurations, Control, and Applications', *IEEE Transactions on Sustainable Energy*, vol. 2, no. 4, pp. 392–403.

Nema, P, Nema, RK & Rangnekar, S (2009), 'A current and future state of art development of hybrid energy system using wind and PV-solar: A review', *Renewable and Sustainable Energy Reviews*, vol. 13, no. 8, pp. 2096–2103.

Neusser, L & Canha, LN (2013), 'Real-time load forecasting for demand side management with only a few days of history available'. *Proceedings of 2013 Fourth International Conference on Power Engineering, Energy and Electrical Drives (POWERENG). Istanbul, Turkey, 13-17 May 2013,* IEEE, Piscataway, N.J, pp. 911–914.

NEXA (2011), *Nexa® 1200 Bedienungsanleitung*. *Heliocentris GmbH*.

Nguyen, TA, Qiu, X, Gamage, TT, Crow, ML, McMillin, BM & Elmore, AC (2011), 'Microgrid application with computer models and power management integrated using PSCAD/EMTDC'. *2011 North American Power Symposium (NAPS). 4 - 6 Aug. 2011, Boston, Massachusetts, USA,* IEEE, Piscataway, NJ, pp. 1–7.

Noga, M, Ożadowicz, A, Grela, J & Hayduk, G (2013), 'Active Consumers in Smart Grid Systems - Applications of the Building Automation Technologies', *Przeglad Elektrotechniczny*, vol. 2013, no. 89, pp. 227–233.

Onda, K, Kyakuno, T, Hattori, K & Ito, K (2004), 'Prediction of production power for high-pressure hydrogen by high-pressure water electrolysis', *Journal of Power Sources*, vol. 132, 1-2, pp. 64–70.

Ontiveros, LJ & Mercado, PE (2014), 'Modeling of a Vanadium Redox Flow Battery for power system dynamic studies', *International Journal of Hydrogen Energy*, vol. 39, no. 16, pp. 8720–8727.

OPC (2014), *OPC Foundation*. Available from: https://opcfoundation.org/ [22 May 2014].

OPC Toolbox (2012), *OPC Toolbox Documentation - MathWorks Deutschland*. Available from: http://www.mathworks.de/de/help/opc/index.html [03 September 2014].

OpenADR (2010), *The OpenADR Primer*. *An introduction to Automated Demand Response and the OpenADR Standard*, OpenADR Alliance. Available from: http://www.openadr.org/assets/docs/openadr_primer.pdf [09 November 2014].

Optimization Toolbox (2012), *Solve nonlinear curve-fitting (data-fitting) problems in least-squares sense - MATLAB - MathWorks United Kingdom*. Available from: http://www.mathworks.co.uk/help/releases/R2012b/optim/ug/lsqcurvefit.html [07 February 2014].

Paolo, B, Labanca, N & Hirl, B (2012), *Energy efficiency status report 2012*. *Electricity consumption and efficiency trends in the EU -27*, Joint Research Centre, Institute for Energy and Transport. Available from: http://bookshop.europa.eu/is-bin/INTERSHOP.enfinity/WFS/EU-Bookshop-Site/en_GB/-/EUR/ViewPublication-Start?PublicationKey=LBNA25405 [28 October 2014].

Parra, D, Gillott, M & Walker, GS (2014b), 'The role of hydrogen in achieving the decarbonization targets for the UK domestic sector', *International Journal of Hydrogen Energy*, vol. 39, no. 9, pp. 4158–4169.

Parra, D, Walker, GS & Gillott, M (2014a), 'Modeling of PV generation, battery and hydrogen storage to investigate the benefits of energy storage for single dwelling', *Sustainable Cities and Society*, vol. 10, pp. 1–10.

Paspaliaris, I, Taxiarchou, M, Peppas, A, Bernados, PG, Carosio, S, Urbano, G, Monero, A & Laurentiis, R de (2013), *Application of a hybrid energy system combining RES and hydrogen in an office building in Lavrion Greece*. International Conference on Renewable Energies and Power Quality (ICREPQ'13), Bilbao, Spain, 20.-22. March 2013. Available from: http://www.icrepq.com/icrepq%2713/450-paspaliaris.pdf [11 July 2014].

Pérez, D, Cervantes V., Báez, MJ & Domínguez, FT (2013), *PV Grid Parity Monitor*. *Residential Sector*. Available from: http://www.eclareon.com [23 October 2014].

Poling, BE (2008), *Physical and chemical data,* McGraw-Hill, New York.

Prins, J (2012), *Process or Product Monitoring and Control*. *NIST/SEMATECH e-Handbook of Statistical Methods*. Available from: http://www.itl.nist.gov/div898/handbook/.

Prudent (2010), *VRB-ESS kW Class VRB Operation Manual*.

PVMD (2014), *pv magazine Deutschland: Produktdaten 2014*. Available from: http://www.pv-magazine.de/marktubersichten/batteriespeichersysteme/produktdaten-2014/ [08 July 2014].

Qiu, X, Nguyen, TA, Guggenberger, JD & Crow, ML (2014), 'A Field Validated Model of a Vanadium Redox Flow Battery for Microgrids', *IEEE Transactions on Smart Grid*, vol. 5, no. 4, pp. 1592–1601.

Renau, J, Domenech, L, García, V, Real, A, Montés, N & Sánchez, F (2014), 'Proposal of a nearly zero energy building electrical power generator with an optimal temporary generation–consumption correlation', *Energy and Buildings*, vol. 83, pp. 140–148.

Richardson, I & Thomson, M (2010), *Domestic electricity demand model - simulation example*, Loughborough University Institutional Repository. Available from: https://dspace.lboro.ac.uk/dspace-jspui/handle/2134/5786 [18 August 2014].

Richardson, I, Thomson, M, Infield, D & Clifford, C (2010), 'Domestic electricity use: A high-resolution energy demand model', *Energy and Buildings*, vol. 42, no. 10, pp. 1878–1887.

Riffonneau, Y, Bacha, S, Barruel, F & Ploix, S (2011), 'Optimal Power Flow Management for Grid Connected PV Systems With Batteries', *IEEE Transactions on Sustainable Energy*, vol. 2, no. 3, pp. 309–320.

Robyns, B, Davigny, A & Saudemont, C (2013), 'Methodologies for supervision of Hybrid Energy Sources based on Storage Systems – A survey', *Mathematics and Computers in Simulation*, vol. 91, pp. 52–71.

Roy, A (2006), *Dynamic and transient modeling of electrolysers powered by renewable energy sources and cost analysis of electric hydrogen*. PhD-Thesis, Loughborough University, Loughborough, UK.

Saadi, A, Becherif, M, Aboubou, A & Ayad, MY (2013), 'Comparison of proton exchange membrane fuel cell static models', *Renewable Energy*, vol. 56, pp. 64–71.

Salmasi, FR (2007), 'Control Strategies for Hybrid Electric Vehicles: Evolution, Classification, Comparison, and Future Trends', *IEEE Transactions on Vehicular Technology*, vol. 56, no. 5, pp. 2393–2404.

Salom, J, Marszal, AJ, Candanedo, J, Widén, J, Byskov-Lindberg, K & Sartori, I (2013), *Analysis Of Load Match and Grid Interaction Indicators in NZEB with High-Resolution Data*. *A report of Subtask A IEA Task 40/Annex 52 Towards Net Zero Energy Solar Buildings*. Available from: http://www.nachhaltigwirtschaften.at/iea_pdf/endbericht_201417_iea_shc_task40_ebc_annex_52_anhang05.pdf [19 August 2014].

San Martín, I, Ursúa, A & Sanchis, P (2014), 'Modelling of PEM Fuel Cell Performance: Steady-State and Dynamic Experimental Validation', *Energies*, vol. 7, no. 2, pp. 670–700.

Schaft, A. J. van der & Schumacher, JM (2000), *An introduction to hybrid dynamical systems,* Springer, London, New York.

Schreiber, M (2011), *Lifetime of Vanadium Redox Flow Battery*. *The Electrical Energy Storage Applications and Technologies (EESAT) Conference 2011, Oct. 16-19, San Diego, USA*. Available from: http://www.sandia.gov/eesat/2011/papers/Wednesday/02_Schreiber_Abstract.pdf.

Schreiber, M, Harrer, M, Whitehead, A, Bucsich, H, Dragschitz, M, Seifert, E & Tymciw, P (2012), 'Practical and commercial issues in the design and manufacture of vanadium flow batteries', *Journal of Power Sources*, vol. 206, pp. 483–489.

Schreiber, M, Whitehead, AH, Harrer, M & Moser, R (2005), 'The vanadium redox battery - an energy reservoir for stand-alone ITS applications along motor- and expressways'. *ITSC '05. 8th International Conference on Intelligent Transportation Systems, 13-15 September, 2005,* IEEE, Piscataway New Jersey, pp. 936–940.

Sechilariu, M, Wang, B & Locment, F (2013), 'Building Integrated Photovoltaic System With Energy Storage and Smart Grid Communication', *IEEE Transactions on Industrial Electronics*, vol. 60, no. 4, pp. 1607–1618.

Seel, J, Barbose, GL & Wiser, RH (2014), 'An analysis of residential PV system price differences between the United States and Germany', *Energy Policy*, vol. 69, pp. 216–226.

Shigematsu T. (2011), 'Redox flow batteries for energy storage', *SEI Technical Review*, vol. 2011, no. 75, pp. 4–13.

Simulink (2012), *Simulink Documentation - MathWorks United Kingdom*. Available from: http://www.mathworks.co.uk/help/releases/R2012b/simulink/index.html [07 February 2014].

Skyllas-Kazacos, M & Kazacos, M (2011), 'State of charge monitoring methods for vanadium redox flow battery control', *Journal of Power Sources*, vol. 196, no. 20, pp. 8822–8827.

SMA AG (2009), 'Hydro Boy HB1124 Inverter for Supplementary Grid-Feeding Preliminary Version'.

SMA AG (2011), *SUNNY ISLAND 5048 - Technical Description*.

Sossan, F, Bindner, H, Madsen, H, Torregrossa, D, Chamorro, LR & Paolone, M (2014), 'A model predictive control strategy for the space heating of a smart building including cogeneration of a fuel cell-electrolyzer system', *International Journal of Electrical Power & Energy Systems*, vol. 62, pp. 879–889.

Staffell, I (2009), *Fuel cells for domestic heat and power: are they worth it?* PhD-Thesis, University of Birmingham, UK.

Stateflow (2012), *Stateflow Documentation - MathWorks United Kingdom*. Available from: http://www.mathworks.co.uk/help/releases/R2012b/stateflow/index.html [07 February 2014].

Sterrer, R & Prüggler, W (2013), 'Multifunktionales Batteriespeichersystem', *e & i Elektrotechnik und Informationstechnik*, vol. 130, no. 6, pp. 161–168.

Stewart, EM, Lutz, AE, Schoenung, S, Chiesa, M, Keller, JO, Fletcher, J, Ault, G, McDonald, J & Cruden, A (2009), 'Modeling, analysis and control system development for the Italian hydrogen house', *International Journal of Hydrogen Energy*, vol. 34, no. 4, pp. 1638–1646.

Strbac, G, Aunedi, M, Pudjianto, D, Djapic, P, Teng, T, Sturt, A, Jackravut, D, Sansom, R, Yufit, V & Brandon, N (2012), *Strategic Assessment of the Role and Value of Energy Storage in the UK*. Available from: http://www.carbontrust.com/resources/reports/technology/energy-storage-systems-strategic-assessment-role-and-value [23 October 2014].

Stumper, J & Stone, C (2008), 'Recent advances in fuel cell technology at Ballard', *Journal of Power Sources*, vol. 176, no. 2, pp. 468–476.

Sukkar, T & Skyllas-Kazacos, M (2003), 'Water transfer behaviour across cation exchange membranes in the vanadium redox battery', *Journal of Membrane Science*, vol. 222, 1-2, pp. 235–247.

Tang, A, Bao, J & Skyllas-Kazacos, M (2012), 'Thermal modelling of battery configuration and self-discharge reactions in vanadium redox flow battery', *Journal of Power Sources*, vol. 216, pp. 489–501.

Tang, A, Bao, J & Skyllas-Kazacos, M (2014), 'Studies on pressure losses and flow rate optimization in vanadium redox flow battery', *Journal of Power Sources*, vol. 248, pp. 154–162.

Tang, A, McCann, J, Bao, J & Skyllas-Kazacos, M (2013), 'Investigation of the effect of shunt current on battery efficiency and stack temperature in vanadium redox flow battery', *Journal of Power Sources*, vol. 242, pp. 349–356.

Tang, Y, Yuan, W, Pan, M, Li, Z, Chen, G & Li, Y (2010), 'Experimental investigation of dynamic performance and transient responses of a kW-class PEM fuel cell stack under various load changes', *Applied Energy*, vol. 87, no. 4, pp. 1410–1417.

Taylor, PG, Bolton, R, Stone, D & Upham, P (2013), 'Developing pathways for energy storage in the UK using a coevolutionary framework', *Energy Policy*, vol. 63, pp. 230–243.

Tesfahunegn, SG, Ulleberg, Ø, Vie, P & Undeland, TM (2011), 'Optimal shifting of Photovoltaic and load fluctuations from fuel cell and electrolyzer to lead acid battery in a Photovoltaic/hydrogen standalone power system for improved performance and life time', *Journal of Power Sources*, vol. 196, no. 23, pp. 10401–10414.

Turker, B, Arroyo Klein, S, Hammer, E, Lenz, B & Komsiyska, L (2013), 'Modeling a vanadium redox flow battery system for large scale applications', *Energy Conversion and Management*, vol. 66, pp. 26–32.

Ulleberg, Ø (1998), *Stand-alone power systems for the future: optimal design, operation & control of solar-hydrogen energy systems*. PhD-Thesis, Norwegian University of Science and Technology, Trondheim, Norway.

Ulleberg, Ø (2003), 'Modeling of advanced alkaline electrolyzers: a system simulation approach', *International Journal of Hydrogen Energy*, vol. 28, no. 1, pp. 21–33.

Ulleberg, Ø, Ito, H, Maak, MH, Ridell, B, Miles, S, Kelly, N, Iacobazzi, MP, Schoenung, S & Stewart, E (2007), *Hydrogen Demonstration Project Evaluations: Final Report*. *IEA – International Energy Agency HIA – Hydrogen Implementing Agreement*, International Energy Agency. Available from: http://ieahia.org/page.php?s=publications&p=technical [14 November 2014].

Ulleberg, Ø, Nakken, T & Eté, A (2010), 'The wind/hydrogen demonstration system at Utsira in Norway: Evaluation of system performance using operational data and updated hydrogen energy system modeling tools', *International Journal of Hydrogen Energy*, vol. 35, no. 5, pp. 1841–1852.

Ursua, A, Gandia, LM & Sanchis, P (2012), 'Hydrogen Production From Water Electrolysis: Current Status and Future Trends', *Proceedings of the IEEE*, vol. 100, no. 2, pp. 410–426.

Uzunoglu, M, Onar, OC & Alam, MS (2009), 'Modeling, control and simulation of a PV/FC/UC based hybrid power generation system for stand-alone applications', *Renewable Energy*, vol. 34, no. 3, pp. 509–520.

van Nguyen, T & Knobbe, MW (2003), 'A liquid water management strategy for PEM fuel cell stacks', *Journal of Power Sources*, vol. 114, no. 1, pp. 70–79.

VDE (2010), *Energieinformationsnetze und -systeme - Bestandsaufnahme und Entwicklungstendenzen*. Positionspapier, VDE VERBAND DER ELEKTROTECHNIK ELEKTRONIK INFORMATIONSTECHNIK e.V. Available from: http://www.vde.com/de/fg/ITG/Documents/ITG%20Positionspapier%20Energieinformationsnetze_Webversion.pdf [08 November 2014].

Voss, K, Goetzberger, A, Bopp, G, Haberle, A, Heinzel, A & Lehmberg, H (1996), 'The self-sufficient solar house Freiburg-Results of 3 year of operation', *Solar Energy*, vol. 58, pp. 17–23.

Voss, K, Sartori, I, Napolitano, A, Geier, S, Gonçalves, H, Hall, M, Heiselberg, P, Widén, J, Candanedo, J, Musall, E, Karlsson, B & Torcellini, P (2010), 'Load Matching and Grid Interaction of Net Zero Energy Buildings'. *Proceedings of the International Conference of Solar, Heating, Cooling and Buildings Eurosun 2010. International Conference of Solar, Heating, Cooling and Buildings*.

Wang, BP (2013), *Intelligent control and power flow optimization of microgrid : energy management strategies*. PhD Thesis, Universite de Technologie de Compiègne, France. Available from: www.theses.fr/2013COMP2122.pdf.

Wang, C, Nehrir, MH & Shaw, SR (2005), 'Dynamic models and model validation for PEM fuel cells using electrical circuits', *IEEE Transactions on Energy Conversion*, vol. 2005, no. 20, pp. 445–451.

Wasowicz, B (2012), 'SmartRegion Pellworm. 7th International Renewable Energy Storage Conference and Exhibition (IRES 2012)'. Proceedings. *7th International Renewable Energy Storage Conference and Exhibition (IRES 2012). Proceedings,* ed EUROSOLAR e.V., pp. 1561–1580.

Weber, AZ, Mench, MM, Meyers, JP, Ross, PN, Gostick, JT & Liu, Q (2011), 'Redox flow batteries: a review', *Journal of Applied Electrochemistry*, vol. 41, no. 10, pp. 1137–1164.

Wichert, B (1997), 'PV-diesel hybrid energy systems for remote area power generation — A review of current practice and future developments', *Renewable and Sustainable Energy Reviews*, vol. 1, no. 3, pp. 209–228.

Williams, MC (2004), *Fuel Cell Handbook (Seventh Edition)*.

Wissner, M (2011), 'The Smart Grid – A saucerful of secrets?', *Applied Energy*, vol. 88, no. 7, pp. 2509–2518.

Wright, A & Firth, S (2007), 'The nature of domestic electricity-loads and effects of time averaging on statistics and on-site generation calculations', *Applied Energy*, vol. 84, no. 4, pp. 389–403.

Xing, F, Zhang, H & Ma, X (2011), 'Shunt current loss of the vanadium redox flow battery', *Journal of Power Sources*, vol. 196, no. 24, pp. 10753–10757.

Yilanci, A, Dincer, I & Ozturk, H (2009), 'A review on solar-hydrogen/fuel cell hybrid energy systems for stationary applications', *Progress in Energy and Combustion Science*, vol. 35, no. 3, pp. 231–244.

You, D, Zhang, H & Chen, J (2009), 'A simple model for the vanadium redox battery', *Electrochimica Acta*, vol. 54, no. 27, pp. 6827–6836.

Zeng, Z, Zhao, R & Yang, H (2013), 'Micro-sources design of an intelligent building integrated with micro-grid', *Energy and Buildings*, vol. 57, pp. 261–267.

Zhao, P, Zhang, H, Wen, Y & YI, B (2007), 'Charge-Discharge Behaviors and Properties of a Lab-Scale All-Vanadium Redox-Flow Single Cell', *Journal of Electrochemistry*, vol. 13, no. 01, p. 12.

Zhao, P, Zhang, H, Zhou, H, Chen, J, Gao, S & Yi, B (2006), 'Characteristics and performance of 10kW class all-vanadium redox-flow battery stack', *Journal of Power Sources*, vol. 162, no. 2, pp. 1416–1420.

Ziogou, C, Ipsakis, D, Elmasides, C, Stergiopoulos, F, Papadopoulou, S, Seferlis, P & Voutetakis, S (2011), 'Automation infrastructure and operation control strategy in a stand-alone power system based on renewable energy sources', *Journal of Power Sources*, vol. 196, no. 22, pp. 9488–9499.

Ziogou, C, Ipsakis, D, Stergiopoulos, F, Papadopoulou, S, Bezergianni, S & Voutetakis, S (2012), 'Infrastructure, automation and model-based operation strategy in a stand-alone hydrolytic solar-hydrogen production unit', *International Journal of Hydrogen Energy*, vol. 37, no. 21, pp. 16591–16603.

# A Appendix

## A-1 List of publications

**Book chapters:**

L. Baumann, E. Boggasch und R. Vanhaelst, „Redox-Flow-Batterien und zukünftige Anwendungen“, Buchbeitrag im Fachbuch „Batterien als Energiespeicher für umweltverträgliche Anwendungen in den Bereichen Mobilität, Energieversorgung sowie Gesundheit und Sicherheit“ Beuth Verlag, ISBN 978-3-410-24478-3 (to be published)

**Journal Articles (peer-reviewed):**

R. D’Agostino, L. Baumann, A. Damiano, E. Boggasch, “A Vanadium-Redox-Flow-Battery Model for Evaluation of Distributed Storage Implementation in Residential Energy Systems," Energy Conversion, IEEE Transactions on , vol.PP, no.99, pp.1,10 doi: 10.1109/TEC.2014.2369437

**Conference contributions:**

L. Baumann, “Systemintegration von Stromspeichertechniken in einen Energieverbund“, WAGO Smart Grid Fachtagung 2014, 20.02.2014, Frankfurt (oral presentation)

L. Baumann, E. Boggasch, L. Kühl, „Experimental study of an alkaline electrolyser to store renewable energy“ Fuel Cell & Hydrogen 2013, 20.-21.03.2013, Birmingham, UK (poster)

L. Baumann, J. Grahn, A. Kluge, E. Boggasch, L. Kühl, „Integration of a Vanadium-Redox-Flow-Battery into a Hybrid Renewable Energy System“, 7th International Renewable Energy Storage Conference 12. - 14. November 2012 Berlin, (paper/poster)

L. Baumann, E. Boggasch, „Monitoring and management of a renewable energy system with hydrogen using a building automation system”, e-nova 2010 international conference “Sustainable Buildings”, 12.11.2010 Pinkafeld, ISBN 978-3-9502452-02-2 (oral presentation/paper)

L. Baumann, E. Boggasch, M. Rylatt, A. Wright, „Energy Management of a Hydrogen/PV/Wind/Battery Hybrid System“, IEEE Conference “Innovative Technology for an Efficient and Reliable Electricity Supply”, 27.-29.09.2010 Boston, USA, ISBN 978-1-4244-6077-9

L. Baumann, „Energy Flow Management of a Hybrid Renewable Energy System“, IESD Postgraduate Research Conference 2010, 21.05.2010, Leicester UK ISBN 978-185-721-4079 (short presentation/paper/poster)

E. Boggasch, L. Baumann , „Management eines Stromnetzwerkes aus überwiegend dezentralen regenerativen Energieerzeugern im kW Bereich“, Tagungsband zur Facility Management Kongress 2010, 09.03.2010 in Frankfurt (presentation/paper)

L. Baumann, E. Boggasch, M. Rylatt, A. Wright, „IGES Intelligent-Building-Energy-Systems: Energy Management of Hybrid Renewable Energy Systems“, 4th International Renewable Energy Storage Conference 24. - 25. November 2009 Berlin (poster presentation)

L. Baumann, E. Boggasch, M. Rylatt, A. Wright, „IGES Intelligent-Building-Energy-Systems: Preliminary Study on Hybrid Renewable Energy Systems for Residential Applications”, 3rd International Renewable Energy Storage Conference 24. - 25. November 2008 Berlin (poster presentation)

**Journal articles:**

L. Baumann, E. Boggasch, „Gebäude als intelligenter Netzknoten in der Versorgungsstruktur: Experimentelle Untersuchungen an einer Wasserstoffkette“ BTGA Almanach 2012

E. Boggasch, L. Baumann, „Energiemanagement von vernetzten regenerativen Energieerzeugern für Gebäudesysteme” BHKS Almanach 2009

L. Baumann, M. Heiser, S. Miehe, E. Boggasch, „Regenerativer Energieverbund: Energiemanagement mit LON“, LONMARK Magazin Deutschland, September 2008

# A-2 Appendix of chapter 3

## A-2-1 Technical data electrolyser

**Table A-1: Technical data electrolyser AccaGen AGE 1.1 (Accagen SA 2011).**

| Parameter | Value |
|---|---|
| Rated power | 6.3 kW (approx..) |
| Nominal voltage (DC) | 110 V |
| Maximum operating current (DC) | 56 A |
| Electrolyte | KOH 30 wt% |
| Production rate | 10-100% (18-56 A) |
| Hydrogen production rate | 1.1 $Nm^3/h$ |
| Gas purity | 99.99% |
| Number of cells | 50 |
| Cell area | 105.68 $cm^2$ |
| Operating pressure | max. 30 bar |
| Demi water conductivity | $<5*10^{-6}$ S/cm |
| Cooling water | >0.25 $m^3/h$ |
| Heat exchanger area | 2*0.94 $m^2$ |

## A-2-2 Technical data fuel cell

**Table A-2: Technical data NEXA® 1200 (NEXA 2011)**

| Parameter | Value |
|---|---|
| Rated power (DC) | 1200 W |
| Voltage (DC) | 20-36 V |
| Maximum operating current (DC) | 60 A |
| Hydrogen production consumption | 15 Nl/min |
| Gas purity | 99.99% |
| Number of cells | 36 |
| Hydrogen inlet pressure | 1-15 bar |
| Oxidant/Coolant | Air max. 335m³/h |

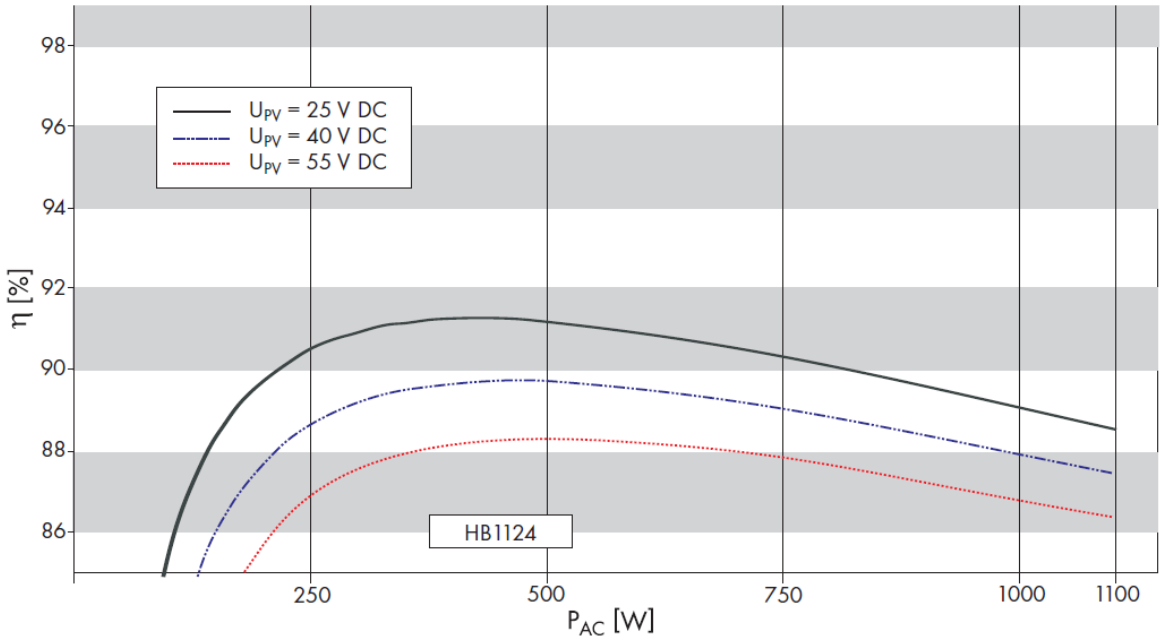


**Figure A-1: Efficiency curve of the SMA HydroBoy (SMA AG 2009)**

## A-2-3 Technical data VRFB

**Table A-3: Technical data Prudent Energy™ Vanadium-Redox-Flow-Battery (Prudent 2010)**

| Parameter | Value |
|---|---|
| Rated power (DC) | 5 kW |
| Open circuit voltage range (DC) | 47-54 V |
| Operating voltage | 42-55.8 V |
| Maximum charge current (DC) | 140 A |
| Maximum discharge current (DC) | 125 A |
| Number of cells | 36 |
| Electrolyte volume | 2*0.9 $m^3$ |

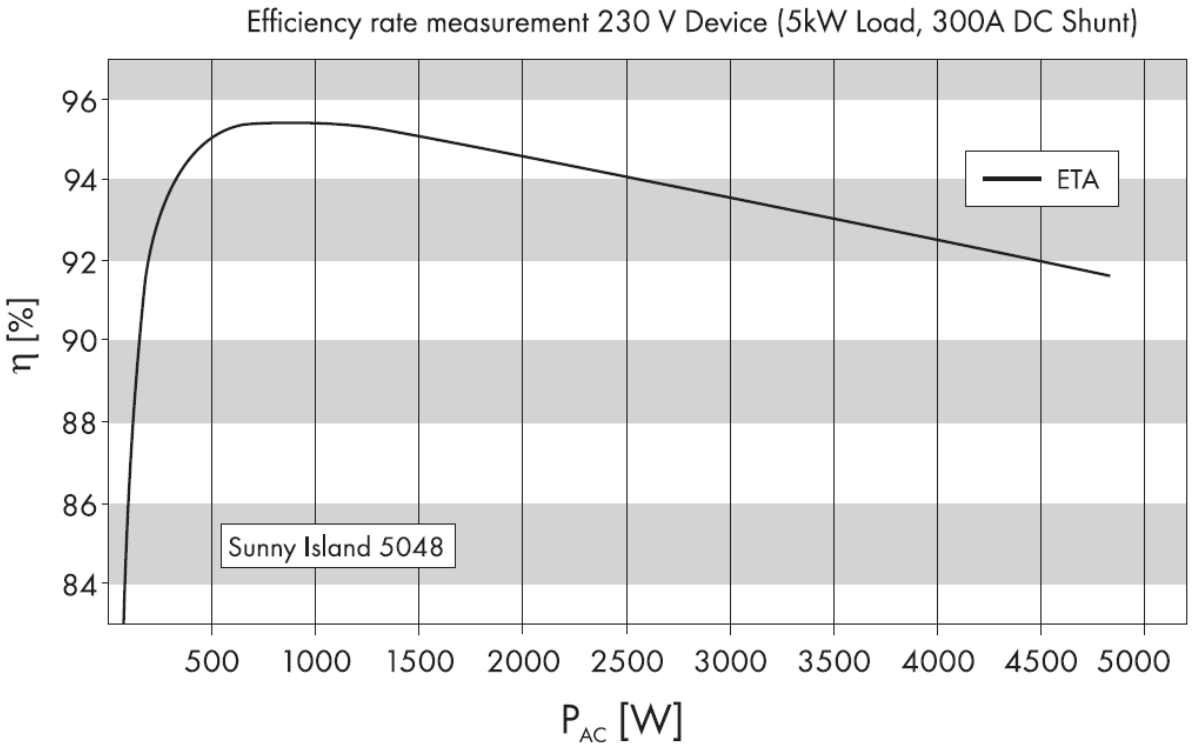


**Figure A-2: Efficiency curve of the SMA Sunny Island 5048 (SMA AG 2011)**

### A-2-4 Control parameters

All PLC programs were programed with the CoDeSys software environment version 2.3.9.40 (CoDeSys 2014) provided by the WAGO GmbH. Each PLC contains several sub-programs to process the field data, to control the power and to determine the operational state of the energy systems. Several libraries have been used to develop the programs, for example the "WAGO HVAC_Lib03" or the "OSCAT library". In the following the control parameters are listed for each energy system.

**Table A-4: Control parameters AC power control electrolyser**

| Parameter | Value |
|---|---|
| Library | WAGO HVAC_Lib03 |
| Functional block | PI-Controller |
| Proportional gain $k_{pr}$ | 1.7 |
| Reset time $T_N$ | 1 s |
| Dead band | 80 W |

**Table A-5: Control parameters AC power control fuel cell**

| Parameter | Value |
|---|---|
| Library | WAGO HVAC_Lib03 |
| Functional block | PI-Controller |
| Proportional gain $k_{pr}$ | 0.03 |
| Reset time $T_N$ | 1.5 s |
| Dead band | 50 W |

**Table A-6: Control parameters AC power control VRFB**

| Parameter | Value |
|---|---|
| Library | OSCAT 3.32 |
| Functional block | PI-Controller |
| Proportional gain $k_{pr}$ | $2.97*10^{-3}$ |
| Reset time $T_N$ | 2.85 s |
| Dead band | 80W |

### A-2-5 Lead acid battery system

The SMA Backup System™ consists of three bidirectional Sunny Backup™ inverters, an automatic switch box and a lead acid battery bank. The functionality of the system is comparable to an uninterruptible power supply (USV). In the event of a failure in the public electricity grid, the automatic switch box activates the island mode and the three inverters control the AC voltage and frequency. As shown in Figure 3-2, the SMA Backup System™ is the central component of the HREP. Every power source, storage device and load are electrically connected the automatic switch box. The system regulates itself; only data from the battery and the inverter can be gathered via Modbus-Gateway. In addition, a three phase energy meter is installed and connected to the LON communication network. Figure A-3 shows the installed system in the control room of the HREP.


**Figure A-3: SMA Backup System composed of the automatic switch box (orange) the three SMA Backup inverter (yellow) and the lead acid battery bank composed of 12 Hoppecke power.com SB 140 batteries (12 V, 142 Ah).**

The battery storage bank consists of 12 Hoppecke power.com SB 140 battery blocks. Each block has a nominal voltage of 12 V and a discharge capacity $C_{10h}$=142 Ah. Four battery blocks are wired in serial to one string with a voltage of 48 V and capacity of 142 Ah. In total three battery strings are connected in parallel. Accordingly, the nominal voltage of the battery bank is 48 V and has a total capacity of the 426 Ah, which gives 48 V*426 Ah= 20.448 kWh.

### A-2-6 Controllable power generators

Two controllable power generators are integrated into the HREP. Both generators are connected via a three-phase cable to the AC bus and the power flow is measured via LON power meters. The three

phase synchronous generator is used to emulate variable AC power sources. The maximum power output is 1 kW.

The second generator, a diesel powered CHP unit (manufactured by Fischer Panda GmbH), provides 6 kW electric power and 16 kW thermal power. The CHP can be used as constant power source to supply electricity to the HREP. The produced heat is utilised via a heat exchanger. Considering both electric and thermal power the total efficiency is about 85% (55% thermal and 30% electric efficiency).

### A-2-7 Electric vehicle charging point

Electric vehicles are likely to play an important role in our energy system in the near future. Many European governments have promoted the development and application of electric vehicles. With growing registration numbers of such vehicles, the need for a suitable infrastructure increased to provide a widespread availability of charging stations. This might lead to new challenges in terms of grid stability. To investigate the interaction between electric vehicles and the building environment, where firstly most of the electric vehicles will be charged, a charging point has been integrated into the HREP in 2012. Figure A-4 illustrates the charging station installed in front of the Faculty building. The charging station consist of two electric connections: a normal single phase power plug and an IEC 62196 Type 2 power plug. The charging station is equipped with a WAGO Pilot-Box and a PLC. The Pilot-Box controls the charging process conform to the IEC 61851-1 (Mode 3).


**Figure A-4: Electric charging station for electric vehicles set-up in front of the Faculty building. To the right the picture shows the PLC installed inside of the enclosure.**

The PLC is used to supervise the charging process and to communicate with the HREP over a Modbus TCP interface. Furthermore, the developed PLC program can be used to set maximum AC current (6 A, 10 A, 16 A or 32 A), which the electric vehicle can draw from the local electricity net. A smart charging mode has been implemented that calculates the maximum charge current based on the available renewable energy supplied by the HREP. Thus, the charge process is linked to the renewable energy; consequently, the charging process is time dependent related to the instantaneous availability of renewable power. The overall integration into the HREP can be found in Figure 3-2 and Figure 3-3.

# A-3 Appendix of chapter 5

## A-3-1 Thermodynamic properties

**Table A-7: Table of thermodynamic properties of the substances at STP (Lide 2006; Cerbe & Wilhelms 2013)**

| Substance | $\Delta_f H^0_{m,i}$ | $S^0_{m,i}$ | $C_{p,i}$ |
|---|---|---|---|
| $H_2O$ | 285.83 KJ/mol | 69.95 J/(mol*K) | 75.288 J/(mol*K) |
| $H_2$ | 0 | 130.68 J/(mol*K) | 28.836 J/(mol*K) |
| $O_2$ | 0 | 205.147 J/(mol*K) | 29.376 j/(mol*k) |

## A-3-2 Parameter estimation

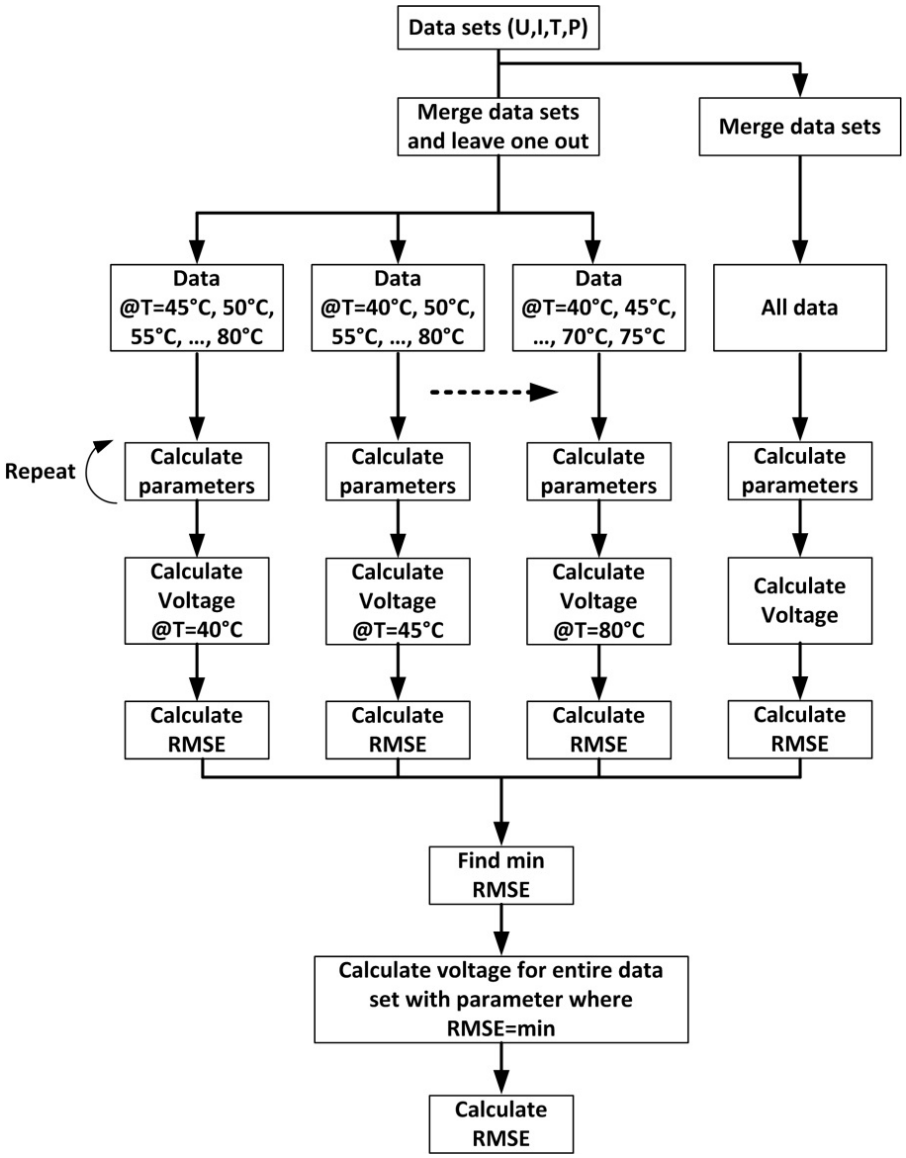


**Figure A-5: Flow-chart of the parameter estimation process.**

To assess the simulation results of the developed models the calculation of RMSE and MAPE is used:

$$RMSE = \sqrt{\frac{\sum_{i=1}^{n}(\hat{y}_i - y_i)^2}{(n-1)}} \quad \textbf{(A-1)}$$

$$MAPE = \frac{1}{n} * \sum_{i=1}^{n} \left| \frac{(\hat{y}_i - y_i)}{(\hat{y}_i)} \right| * 100\% \quad \textbf{(A-2)}$$

where $\hat{y}_i$ is the measured value, $y_i$ is the predicted value and *n* is the number samples.

### A-3-3 Stateflow® diagrams

Figure A-6: shows the Stateflow® chart of the electrolyser system operational model.

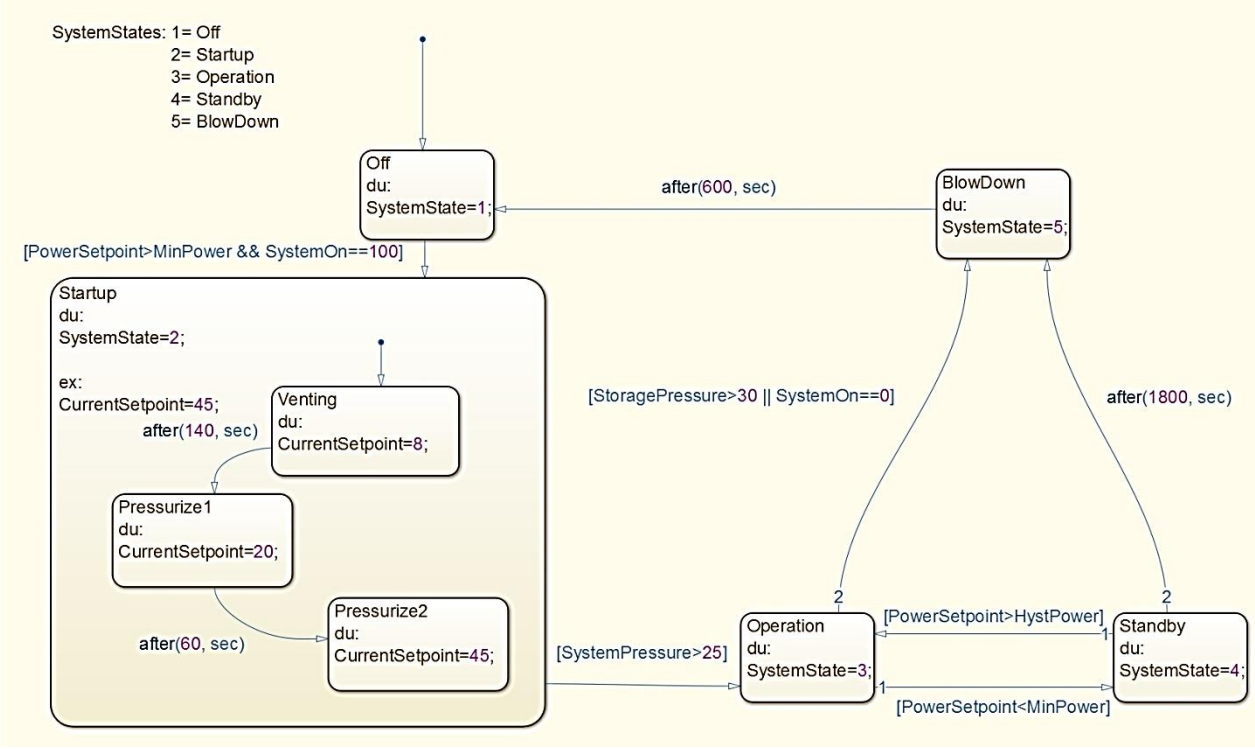


**Figure A-6: Stateflow chart of electrolyser operational control system.**

Figure A-7 illustrates the Stateflow® chart of the fuel cell system operational model.

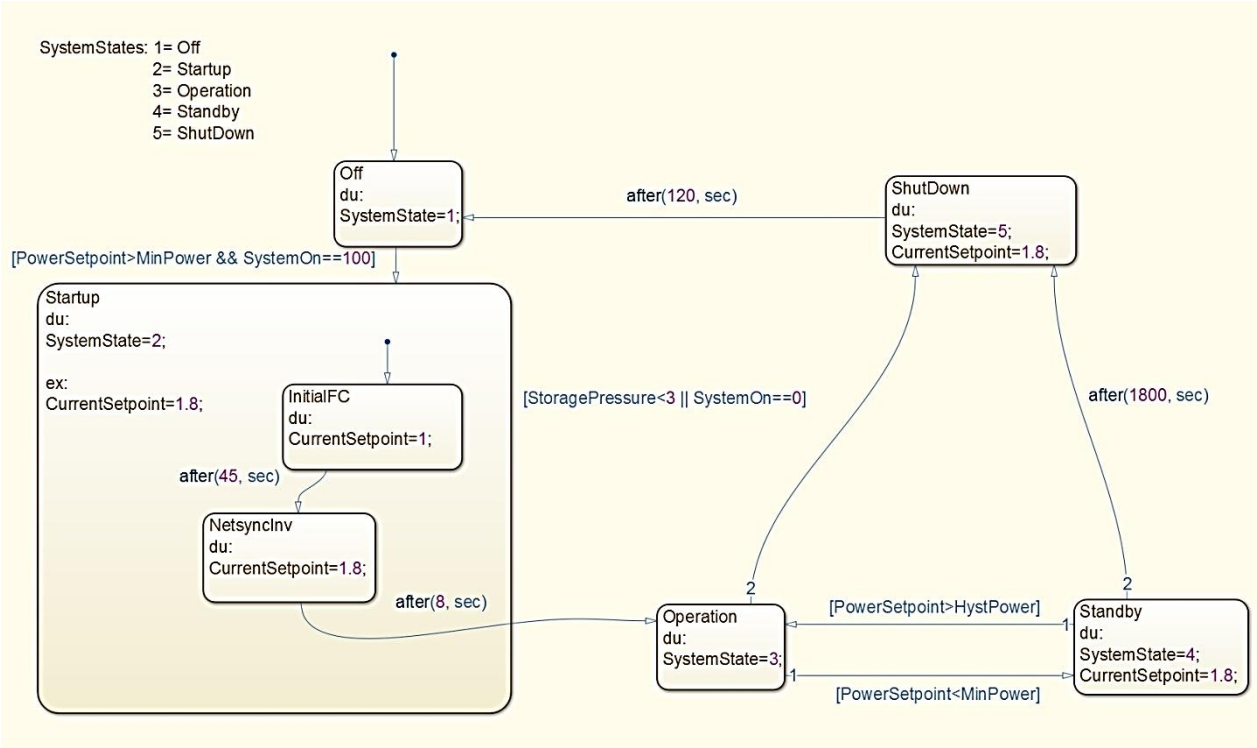


**Figure A-7: Stateflow chart of the fuel cell operational control system.**

Figure A-8 depicts the Statechart® digram of the VRFB operational model.

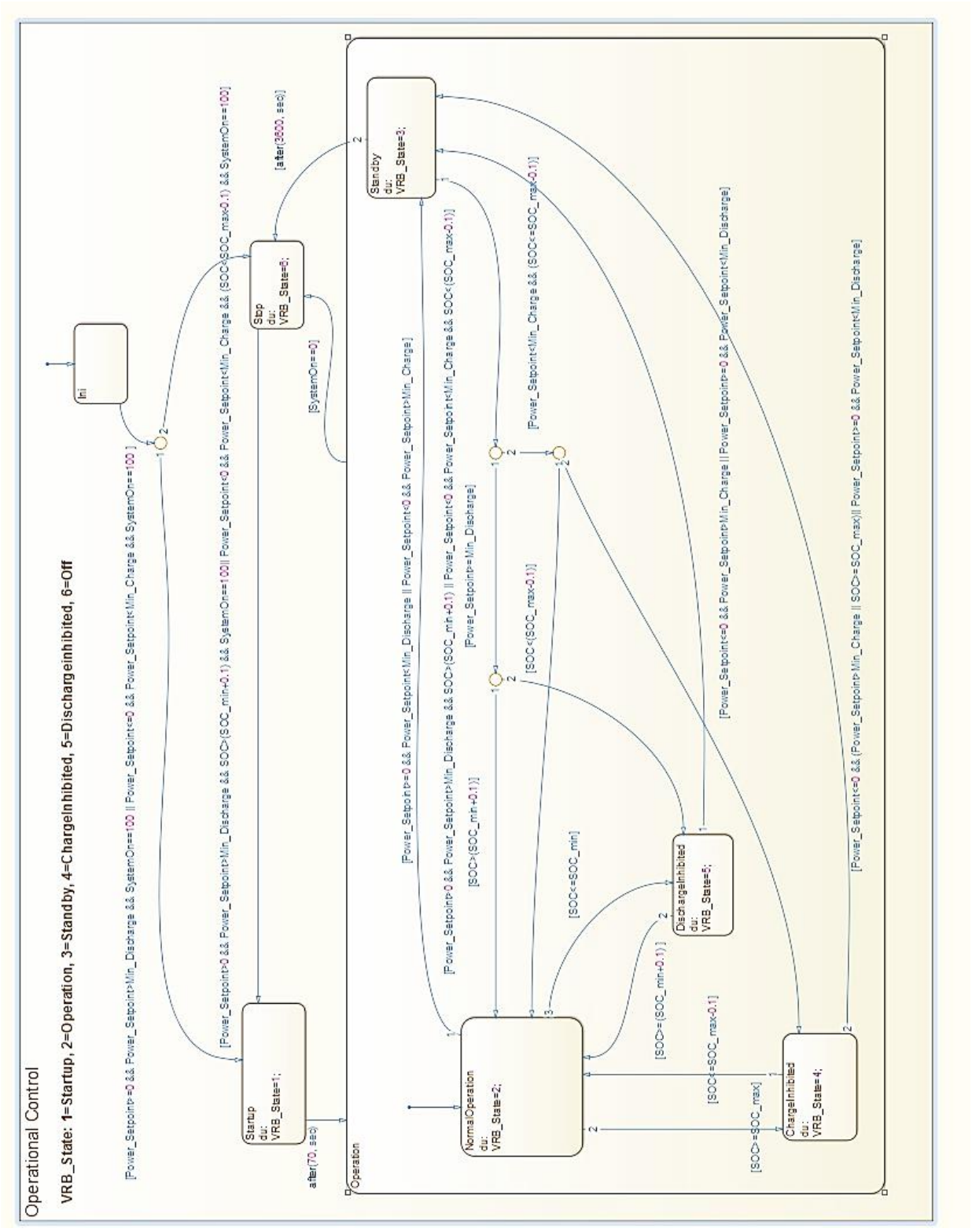


**Figure A-8: Statechart of the VRFB operational control system.**

In the following the hierarchical organised statechart diagram of the strategic supervisory level is illustrated. Figure A-9 shows the top level of the diagram. Figure A-10 illustrates the subchart "P_Excess/H2-loop" to coordinate the electrolyser. Figure A-11 graphs the subchart "P_Demand/VRFB" to coordinate the discharge of the VRFB.

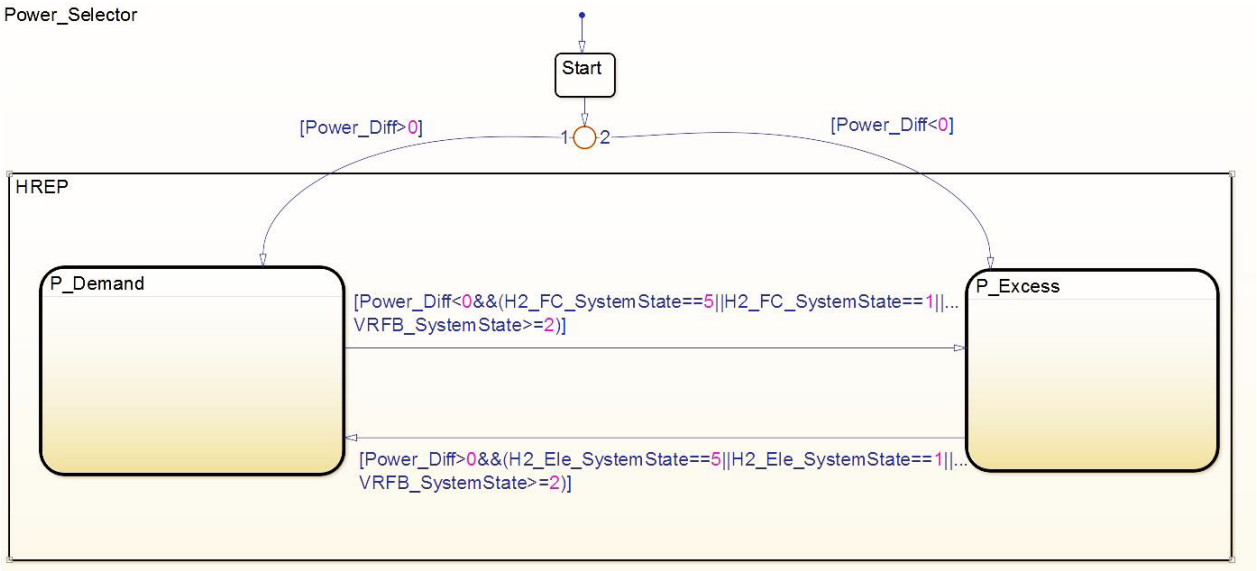


**Figure A-9: Top-level of the strategic supervisory level controller.**

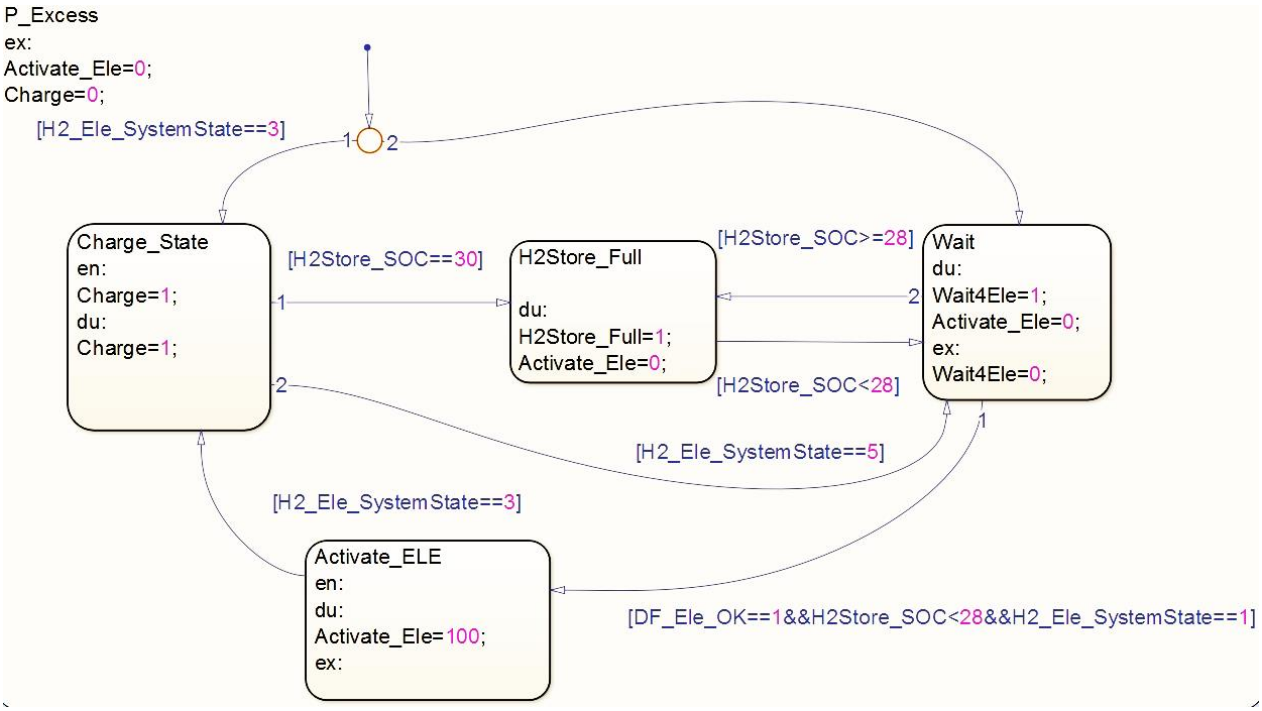


**Figure A-10: Subchart to coordinate the electrolyser system.**

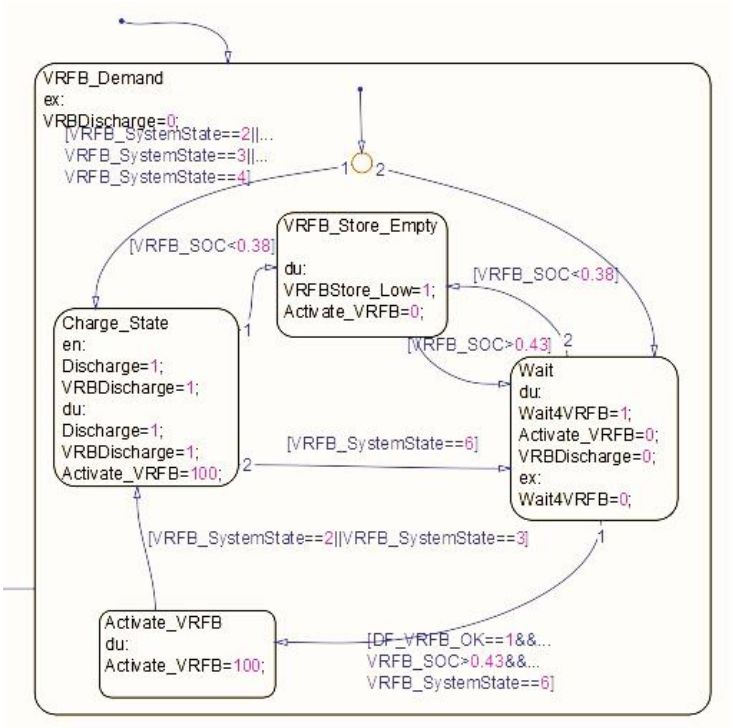


**Figure A-11: Subchart to coordinate the discharge of the VRFB.**

### A-3-4 Control Parameters

In the following the control parameter applied the simulations are listed. The Simulink® block "PID controller" is used in all three system models. All PI controllers are parameterised as discrete-controller with anti-windup.

**Table A-8: Control parameters electrolyser and fuel cell Simulink® model**

| Parameter | Value | Value |
|---|---|---|
| | **Electrolyser** | **Fuel cell** |
| Proportional gain (P) | 0.0125 | 0.05 |
| Integral gain (I) | 1.15 | 1.5 |
| Upper saturation limit | 56 | 62 |
| Lower saturation limit | 18 | 3 |

**Table A-9: Control parameters VRFB Simulink® model**

| Parameter | VRFB AC power control Value | VRFB charge voltage control Value |
|---|---|---|
| Proportional gain (P) | 0.0225 | 250 |
| Integral gain (I) | 1 | 4 |
| Upper saturation limit | 125 | 5000 |
| Lower saturation limit | -125 | 0 |

# A-4 Appendix of chapter 6

## A-4-1 Hydrogen loop system model

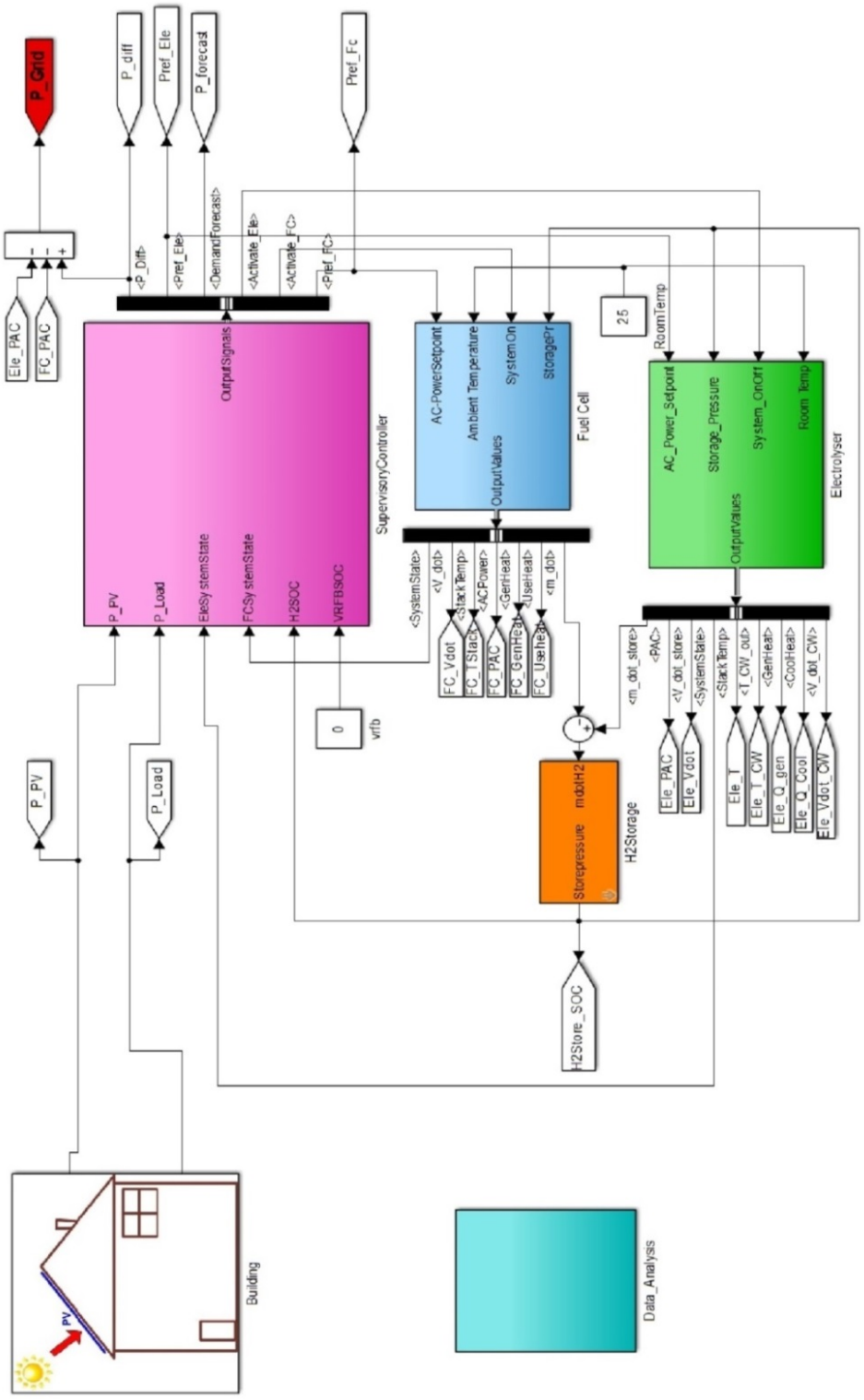


**Figure A-12: Overall system model including building data, supervisory controller, electrolyser, gas storage and fuel cell.**

## A-4-2 Electric load profile

The used load profiles were generated with a tool developed by (Richardson & Thomson 2010). The default values for the appliances were applied to generate the load profiles. Weather data were taken from the database of the HREP. Figure A-13 shows the in-house MATLAB program that was used to modify the EXCEL based model and to generate the annual load profile.

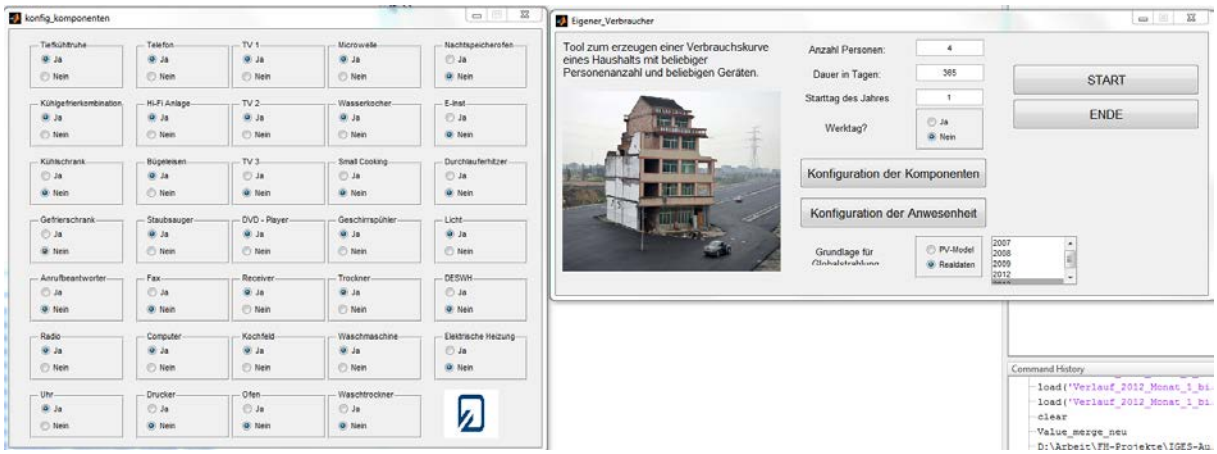


**Figure A-13: In-house MATLAB tool to generate annual load profiles using the CREST load model.**

## A-4-3 Domestic hot water profile:

Figure A-14 shows the DHW profile generated with the model developed by (Jordan & Vajen 2005).

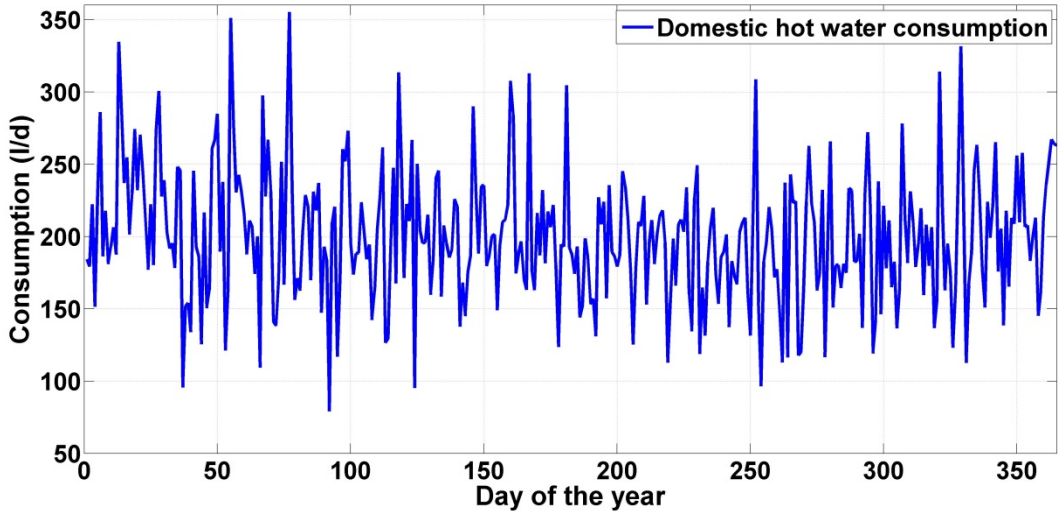


**Figure A-14: Generated DHW profile.**

### A-4-4 Sensitivity analysis of the control parameters of the hydrogen loop

A sensitivity analysis was carried out to find nearly optimal threshold values for the control parameters of the fuel cell and the electrolyser. First, the maximum fuel cell power was increased stepwise from 600 W to 1200 W. Second, with the previously determined maximum fuel cell power, the minimum operating and start-up power were varied from 2000 W to 4000 W and from -2000 W to -4000 W, respectively. Based on the efficiency values and the number of start-ups, the thresholds for the electrolyser were examined. The system configuration was the same as the basic scenario described in section 6.2.1. The simulation was performed for a time period of one week. Figure A-15 depicts the power output of the 8 $kW_p$ PV array and the electrical demand of the building.

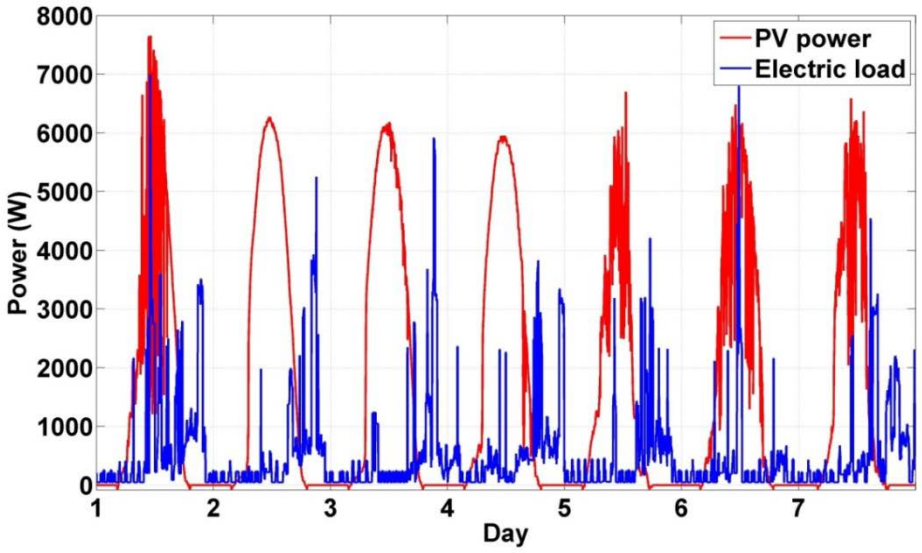


**Figure A-15: PV electricity generation (red) and simulated electric demand for period of one week in July 2013.**

The PV data used for the simulation study was based on the aggregated PV power of the HREP during the first week of July in 2013. The scaling factor was $8kW_p/6.12kW_p$. This week was characterised by three sunny days (day 2-4) and four cloudy days. Especially, the first day was shaped by rapid power spikes due to partly covered sky conditions. The data of the electrical demand was taken from the generated annual load profile for this certain time period. Figure A-16 shows the simulated behaviour of the fuel cell and the electrolyser based on the calculated power difference, which is the main decision variable of the strategic supervisory level. The parameters of the fuel cell were set to $P_{max}$=600 W and for the electrolyser $P_{min}$=2500 W and $P_{start\text{-}up}$=-2500 W. The operation of the electrolyser was highly dynamic during the day 1, 6 and 7 and relatively smooth during the other days. The fuel cell operated most of the time at its defined power limit of 600 W. In total 7 simulation

runs were conducted with incrementally increasing power threshold for the fuel cell. Table A-10 summarises the results of the parameter variation and highlights the effect of varying the maximum power output of the fuel cell system.

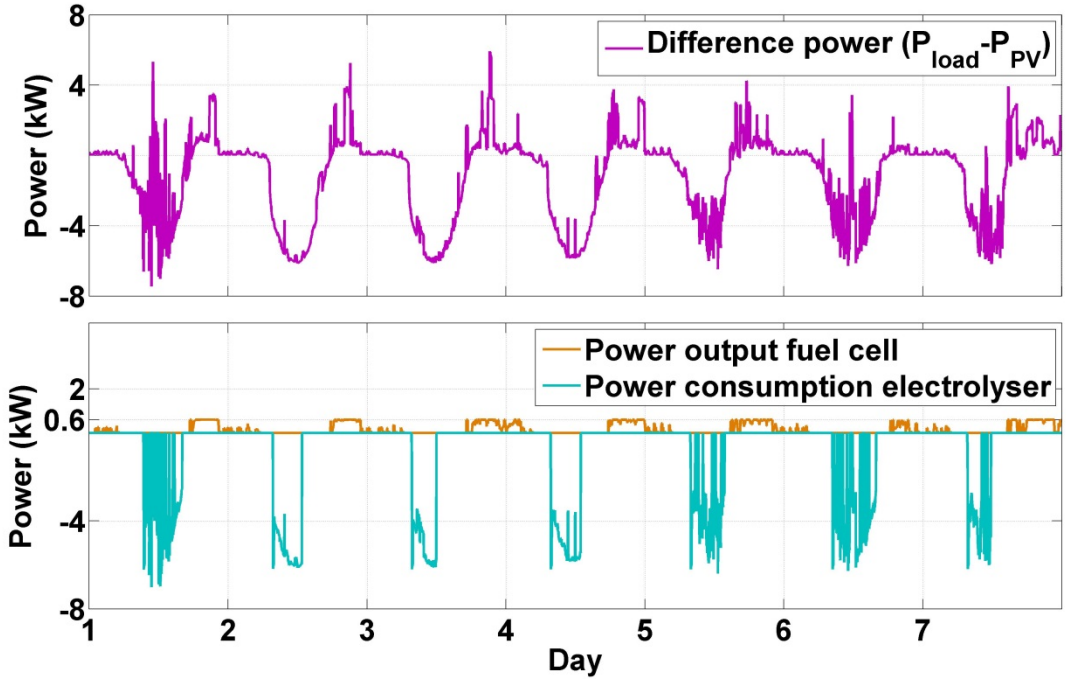


**Figure A-16: Result of the simulation with maximum fuel cell power output equal to 600 W. The top graph shows the difference power and the bottom graph illustrates the fuel cell and electrolyser power.**

During the simulation the fuel cell was in operation for 51.9 h and in standby for 22.9 h. This is applicable to all simulation runs regardless of the power threshold. The effect of varying the maximum power output can be evaluated by calculating the AC system efficiency of the fuel cell. This value decreases almost linear from 48.7% at 600 W to 43.2% at 1200 W. The conclusion of the sensitivity analysis presented in the table below, is that the maximum power output is set to 900 W. This facilitates a good AC system efficiency, a wide operational range and it increases the lifetime due to the modest current rates drawn from the fuel cell stack.

**Table A-10: Summarised results of varying the maximum power output of the fuel cell system.**

| Fuel cell $P_{max}$ (W) | 600 | 700 | 800 | 900 | 1000 | 1100 | 1200 |
|---|---|---|---|---|---|---|---|
| Generated electricity (kWh) | 25.2 | 27.6 | 29.5 | 31.2 | 32.6 | 33.8 | 33.9 |
| Consumed hydrogen (kWh/Nm³) | 51.7/17.2 | 57.3/19.1 | 62.4/20.8 | 67.2/22.4 | 71.9/24 | 77.3/25.8 | 78.4/26.1 |
| Efficiency $\eta_{AC,LHV}$ (%) | 48.7 | 48.1 | 47.3 | 46.4 | 45.3 | 43.7 | 43.2 |

The same simulation scenario was used to analyse the effect of the minimum start-up power and operating power of the electrolyser on its performance. The AC system efficiency shows only a small dependency on the variation of the two parameters, except the last two simulations revealed a decrease of the efficiency. This can be attributed to the increased number of start-ups and decreased operational time. Each start-up consumes electric energy to pressurise the system and electric energy is needed to heat up the electrolyser. Since the main purpose of the electrolyser is to store fluctuating renewable energy, the minimum power input and the minimum start-up power were set to 2500 W and to -2500 W, respectively.

**Table A-11: Summarised results of the effect of varying the minimum start-up power and minimum operating power of the electrolyser system.**

| $P_{start-up}$ (kW) | -2.5 | -3.0 | -2.5 | -3.0 | -3.0 | -3.5 | -4.0 | -4.5 | -5.0 |
|---|---|---|---|---|---|---|---|---|---|
| $P_{min}$ (kW) | 2.0 | 2.0 | 2.5 | 2.5 | 3.0 | 3.5 | 4.0 | 4.5 | 5.0 |
| Operational hours | 42.1 | 41.1 | 40.2 | 39.4 | 36.8 | 32.2 | 28.5 | 21.1 | 16.3 |
| On/off cycles | 7 | 7 | 7 | 7 | 7 | 8 | 8 | 10 | 9 |
| Consumed electricity (kWh) | 191.7 | 189.4 | 187.7 | 185.7 | 178.6 | 162.4 | 147.9 | 113.5 | 90.4 |
| Produced hydrogen (kWh) / (Nm³) | 76.8/ 21.7 | 76/ 21.5 | 75.4/ 21.3 | 74.7/ 21.1 | 72/ 22.3 | 65.1/ 18.4 | 59.1/ 16.7 | 43.7/ 12.3 | 34.3/ 9.7 |
| Efficiency $\eta_{AC,HHV}$ (%) | 40% | 40.1% | 40.2% | 40.2% | 40.3% | 40% | 40% | 38.5 | 37.9 |

### A-4-5 Evaluation of the energy management strategy

In order to evaluate the proposed energy management strategy a comparison between a simulation with and without demand forecast is presented in the following. The simulation inputs were the PV data (scaled with 8/6.12) of the year 2013 and the load profile of a 4-person household. The simulation time period was set to 31 days (day 100 to 130). The results of the analysis are summarised in Table A-12. As can be seen, the number of start-ups increased from 37 to 57 (+54%) if the demand forecast is deactivated. The total operational hours increased from 119.7 h to 139.9 h. However, the average operational hours per start-up reduced from 3.2 h to 2.5 h. In other words, the average operational duration was reduced by almost 22%.

From the simulation results without demand forecast it was also found, that the electrolyser was at three times directly transitioned from the start-up into the standby mode and then into the blow-down mode. Hence, no hydrogen was passed from the electrolyser to the gas storage. Furthermore, by comparing the electricity exchanged with the grid, it was found that the imported electricity increased by 5% when the demand forecast was deactivated because of the start-up process of the electrolyser.

From these results it can be concluded that the implemented demand forecast effectively prevents the electrolyser from unnecessary start-ups. This will help to increase the overall performance and it will help to increase the component life-time.

**Table A-12: Comparison of simulation with and without demand forecast.**

| Simulation: | with demand forecast | without demand forecast |
|---|---|---|
| Number of electrolyser start-ups: | 37 | 57 |
| Electrolyser operational hours: | 119.7 | 139.9 |
| Electricity import (kWh): | 159.1 | 167.4 |

### A-4-6 Sensitivity analysis of the PV array size to power the building-integrated hydrogen loop

To evaluate the impact of the PV array size a sensitivity analysis was performed aiming to maximise the hydrogen production and subsequently to increase the efficiency of the electrolyser by operating at higher power rates. The system configuration of the simulation study, except for the PV array, was the same as for the basic scenario described in section 6.2.1. The electrical annual demand was 4707.4 kWh and the annual domestic hot water demand was 72 m³. Based on the metered data of the 1 $kW_p$ PV system installed at the Ostfalia HREP, the PV size was stepwise scaled from 8 $kW_p$ to

16 $kW_p$. In addition, the volume of the hydrogen storage tank was increased with increasing PV size from 0.6 m³ to 3 m³. The storage pressure was initially set to 25 bar in each simulation run. The simulation was performed for a time period of one year.

Figure A-17 depicts in the top diagram the annual evolution of the pressure of the hydrogen tanks for the 8 $kW_p$/0.6 m³, 10 $kW_p$/1.2 m³ and 12 $kW_p$/1.8 m³ systems. The lower diagram shows the simulations with 14 $kW_p$/2.4 m³ and 16 $kW_p$/3 m³. It can be seen that the storage pressure of the system with 8 $kW_p$/0.6 m³ never reaches its upper limit of 30 bar. It is evident that the PV system was sized too small. As a consequence the electrolyser was operated less frequently and at lower power rates. On the other hand, the 16 $kW_p$/3 m³ shows a good hydrogen storage evolution during the year. Only at a few times in summer the upper threshold of the hydrogen storage tank was reached. Nevertheless, it can be seen that all system configurations hardly operate during the winter season, which of course is due to the geographical location (Wolfenbüttel, Germany) and the limitation of the PV size to reasonable values for grid connected buildings.

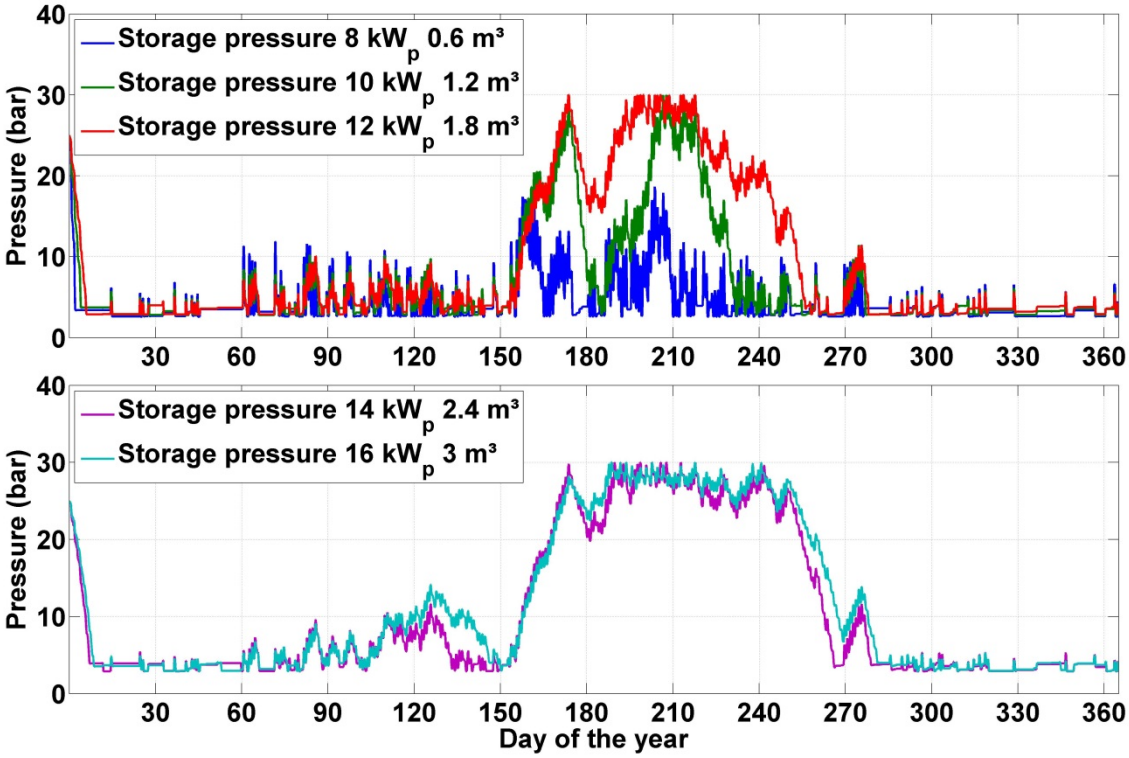


**Figure A-17: Evolution of the hydrogen storage tank pressure.**

Table A-13 and Table A-14 outline the results of varying the PV size providing the performance data of the PV, electrolyser and fuel cell. In addition, the hours of occurrence at which the power difference ($P_{load}$-$P_{renewables}$) was <-2500 W (minimum and start-up power of the electrolyser) are also listed.

**Table A-13: Simulation results of the parameter variation, continue with next page**

| PV size ($kW_p$) / Hydrogen store volume ($m^3$) | | 8 / 0.6 | 10 / 1.2 |
|---|---|---|---|
| **Parameter** | | **Annual Results** | |
| **Building:** | PV generation (kWh) | **7089.5** | **8861.9** |
| | Operating hours PV | **3550** | **3573** |
| | Number of hours for which $P_{diff}$<-2500 W | **970.5** | **1163** |
| **Electrolyser:** | Energy supplied to the electrolyser (kWh) | **3981.1** | **5488.2** |
| | On/Off cycles of the electrolyser (-) | **278** | **300** |
| | Operating hours of the electrolyser (h) | **837.2** | **992.9** |
| | Standby time of the electrolyser (h) | **300.9** | **298.4** |
| | Generated hydrogen (kWh)/($Nm^3$) | **1536.3/434** | **2204.6/622.8** |
| | Generated heat of the electrolyser (kWh) | **1071.5** | **1540.9** |
| | Removed heat by cooling system (kWh) | **536.7** | **850.1** |
| | Cooling water supplied to DHW > 40°C ($m^3$) | **13.3** | **21.1** |
| **Fuel Cell:** | Energy supplied by the fuel cell (kWh) | **621.6** | **898.2** |
| | On/Off cycles of the fuel cell (-) | **437** | **692** |
| | Operating hours of the fuel cell (h) | **945.3** | **1386.3** |
| | Standby time of the fuel cell (h) | **254.4** | **465.1** |
| | Consumed hydrogen (kWh)/($m^3$) | **1334.3/444.8** | **1933.2/644.4** |
| | Generated heat of the fuel cell (kWh) | **619.1** | **894.6** |
| | Removed heat at stack temperature > 45°C (kWh) | **593.6** | **850.1** |
| **Grid exchange:** | Grid import (kWh) | **3076.5.8** | **2731.7** |
| | Grid export (kWh) | **2099.1** | **2296.2** |
| **Annual performance indices** | | **Annual Results** | |
| | Electrolyser efficiency $\eta_{AC,HHV}$ (%) | **38.6** | **40.2** |
| | Electrolyser overall efficiency including waste heat (%) | **52.1** | **55.7** |
| | Fuel Cell efficiency $\eta_{AC,LHV}$ (%) | **46.6** | **46.4** |
| | Fuel cell overall efficiency assumed that 50 % heat can be used (%) | **68.8** | **68.4** |
| | Annual grid interaction index (%) | **12.3** | **9.6** |
| | Annual supply cover factor | **0.48** | **0.49** |
| | Annual load cover factor | **0.36** | **0.42** |
| | Annual grid balance (kWh) | **976.8 (imp.)** | **435.5 (imp.)** |

**Table A-14: Simulation results of the parameter variation**

| PV size ($kW_p$) / Hydrogen store volume ($m^3$) | | 12 / 1.8 | 14 / 2.4 | 16 / 3 |
|---|---|---|---|---|
| **Parameter** | | **Annual Results** | | |
| **Building:** | PV generation (kWh) | **10634.3** | **12406.7** | **14179** |
| | Operating hours PV | **3586** | **3595** | **3601** |
| | Number of hours for which $P_{diff}$<-2500 W | **1327** | **1460** | **1576** |
| **Electrolyser:** | Energy supplied to the electrolyser (kWh) | **6374.1** | **7064.1** | **7631.7** |
| | On/Off cycles of the electrolyser (-) | **312** | **304** | **313** |
| | Operating hours of the electrolyser (h) | **1135** | **1225.6** | **1305.4** |
| | Standby time of the electrolyser (h) | **289.2** | **277.4** | **275.3** |
| | Generated hydrogen (kWh)/($Nm^3$) | **2600.2/734.5** | **2914.8/823.4** | **3163.9/893.8** |
| | Generated heat of the electrolyser (kWh) | **1822.1** | **2033.8** | **2205.8** |
| | Removed heat by cooling system (kWh) | **1032.1** | **1177.4** | **1322.3** |
| | Cooling water supplied to DHW > 40°C ($m^3$) | **25.6** | **29.3** | **32** |
| **Fuel Cell:** | Energy supplied by the fuel cell (kWh) | **1066.1** | **1207.7** | **1283.1** |
| | On/Off cycles of the fuel cell (-) | **823** | **914** | **1033** |
| | Operating hours of the fuel cell (h) | **1663.1** | **1889.2** | **2077.1** |
| | Standby time of the fuel cell (h) | **594.8** | **677.6** | **759.2** |
| | Consumed hydrogen (kWh) / ($m^3$) | **2295.9/765.3** | **2600.8/866.9** | **2847.2/949.1** |
| | Generated heat of the fuel cell (kWh) | **1060.7** | **1201.2** | **1313.8** |
| | Removed heat at stack temperature > 45°C (kWh) | **1004.1** | **1136.6** | **1241.3** |
| **Grid exchange:** | Grid import (kWh) | **2513** | **2316.2** | **2170.1** |
| | Grid export (kWh) | **3131.2** | **4159.1** | **5332.4** |
| **Annual performance indices** | | **Annual Results** | | |
| | Electrolyser efficiency $\eta_{AC,HHV}$ (%) | **40.8** | **41.3** | **41.5** |
| | Electrolyser overall efficiency including waste heat (%) | **57** | **57.9** | **58.8** |
| | Fuel Cell efficiency $\eta_{AC,LHV}$ (%) | **46.4** | **46.4** | **46.4** |
| | Fuel cell overall efficiency assumed that 50 % heat can be used (%) | **68.3** | **68.2** | **66.9** |
| | Annual grid interaction index (%) | **9.3** | **9.7** | **10.4** |
| | Annual supply cover factor | **0.45** | **0.42** | **0.4** |
| | Annual load cover factor | **0.47** | **0.52** | **0.55** |
| | Annual grid balance (kWh) | **618.2 (exp.)** | **1842.9 (exp.)** | **3162.3 (exp.)** |

Only a small deviation of the performance of the electrolyser can be registered throughout the five simulations varying between 38.6% and 41.5% ($\eta_{AC,HHV}$). The fuel cell performance was almost

constant. Increasing the PV array from 8 $kW_p$ to 10 $kW_p$ improved the electrolyser's performance by 1.6%. This is the highest improvement for all five simulations. The average operating power increases from 4.74 kW to 5.53 kW leading to an increase of the AC efficiency, see Figure 4-4 for comparison. With respect to the energy exchanged with the grid, only simulations with a PV array >10 $kW_p$ achieved an annual grid export. Both, the 8 $kW_p$ and 10 $kW_p$ simulations needed energy from the grid on an annual basis. However, regarding the grid interaction Figure A-18 illustrates the annual grid interaction index versus the PV array size. The lower the grid interaction index, the lower the fluctuations are. First the index declines from 12.3% (8$kW_p$/0.6 $m^3$) to 9.3% (12 $kW_p$/1.8 $m^3$) and starts to increase again to finally 10.3% (16 $kW_p$/3 $m^3$). The best improvement of the index shows the simulation with 10$kW_p$/1.2 $m^3$. The reason why the index starts to increase again can be found in the ratio of the rated power of the electrolyser to the size of the PV array. At PV sizes greater than 12 $kW_p$ the electrolyser (rated power 7 kW) reaches its limit to adequately compensate the power fluctuations due to the increased PV power.

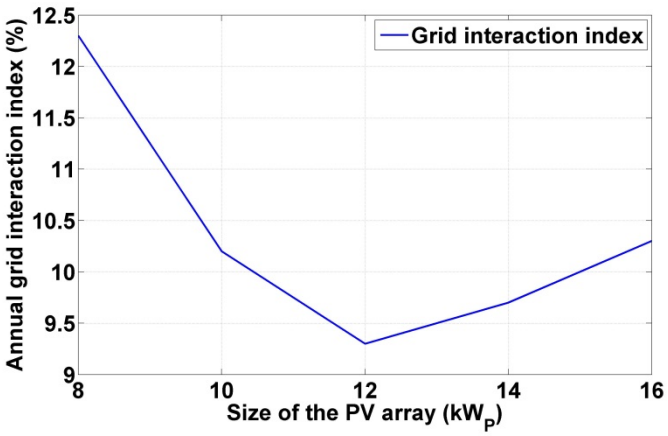


**Figure A-18: Grid interaction index for different PV sizes.**

From the results presented above it can be concluded that the lowest grid interaction index shows the simulation with 12$kW_p$/1.8 $m^3$. However, this PV size is not typical for residential application. Since the aim of this research was not to find the optimal system configuration of a building-integrated hybrid renewable energy, the system configuration used in this thesis was associated with the HREP installed at Ostfalia University and with reasonable PV system sizes which can be typically found on the roof of dwellings located in central Europe.

### A-4-7 Sensitivity analysis of the control parameters of the VRFB

A sensitivity analysis was carried out to find nearly optimal threshold values for the control parameters of the VRFB system. First, the impact of the maximum charge/discharge power was examined. Second, the minimum discharge power was increased stepwise from 300 W to 1000 W. Finally, the minimum charge power was varied from -800 W to -1500 W. The threshold of the minimum start-up power either for discharge or charge was the same as the minimum operation power. The system configuration was the identical to the basic scenario described in Chapter 6.2.2. The simulation was performed for a time period of one week. Figure A-15 illustrates the power output of the 8 $kW_p$ PV array and the electrical demand of the building. In Figure A-19 the power difference and the power of the VRFB is reported. As can be seen, the maximum charge/discharge power was limited to 3000 W.

As can be seen from the graph, the VRFB power was most of time at lower power levels during discharge and during charge almost at maximum power. How the thresholds affect the AC energy efficiency is shown in Table A-14. With increasing power threshold the efficiency slightly increases from values at 44% to 46%. However, at threshold values greater than ± 3500 W the efficiency stabilises at 46%. A second analysis was performed to assess the impact of the minimum charge and discharge power on the performance of the VRFB. The minimum charge power was increased from -800 W to -1500 W and the minimum discharge power varied from 300 W to 1000W. Table A- 15: outlines the results of the parameter variation.

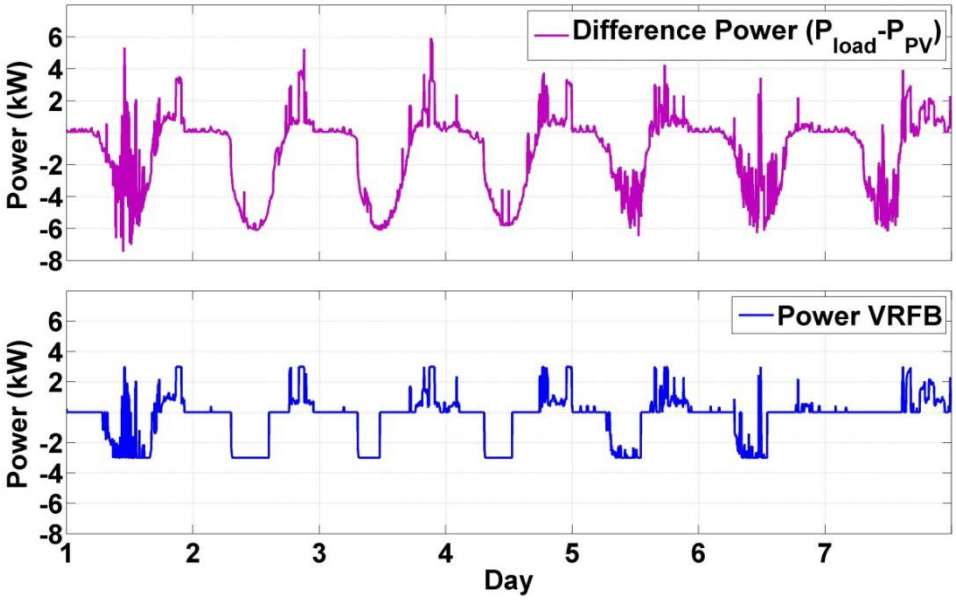


**Figure A-19: Result of the simulation with maximum 3000 W charge/discharge power. The top graph shows the difference power and the bottom graph illustrate the VRFB power.**

As can be seen from the graph, the VRFB power was most of time at lower power levels during discharge and during charge almost at maximum power. How the thresholds affect the AC energy efficiency is shown in Table A- 15. With increasing power threshold the efficiency slightly increases from values at 44% to 46%. However, at threshold values greater than ± 3500 W the efficiency stabilises at 46%. A second analysis was performed to assess the impact of the minimum charge and discharge power on the performance of the VRFB. The minimum charge power was increased from -800 W to -1500 W and the minimum discharge power varied from 300 W to 1000W. Table A- 16 outlines the results of the parameter variation.

**Table A- 15: Summarised results of effect of varying the maximum charge/discharge power of the VRFB system.**

| **VRFB $P_{max}$ (W)** | **±3000** | **±3500** | **±4000** | **±4500** | **±5000** | **±5500** | **±6000** | **±6500** |
|---|---|---|---|---|---|---|---|---|
| **Discharged electricity (kWh)** | 45.9 | 47.1 | 47.5 | 47.7 | 47.9 | 47.9 | 47.9 | 47.9 |
| **Charged electricity (kWh)** | 102.4 | 106.6 | 102.4 | 102.8 | 103.9 | 104 | 104 | 103.7 |
| **Efficiency $\eta_{energy,AC}$ (%)** | 44.8 | 44.2 | 46.4 | 46.4 | 46.1 | 46.1 | 46.1 | 46.2 |
| **On/off cycles** | 45 | 47 | 46 | 46 | 46 | 46 | 46 | 46 |
| **Operational hours** | 83.7 | 81 | 77.2 | 75.8 | 75.2 | 74.9 | 74.8 | 74.2 |
| **Standby hours** | 7.1 | 7 | 7 | 6.9 | 6.9 | 6.9 | 6.9 | 6.8 |

**Table A- 16: Summarised results of varying the minimum discharge and charge power of the VRFB system.**

| **VRFB $P_{min,\ charge}$ (W)** | **-800** | **-900** | **-1000** | **-1100** | **-1200** | **-1300** | **-1400** | **-1500** |
|---|---|---|---|---|---|---|---|---|
| **Discharged electricity (kWh)** | 46.9 | 46.9 | 46.9 | 46.9 | 46.6 | 46.4 | 46.4 | 46.6 |
| **Charged electricity (kWh)** | 102.3 | 102 | 101.6 | 101.3 | 101.3 | 100.7 | 100.4 | 101.3 |
| **Efficiency $\eta_{energy,AC}$ (%)** | 45.8 | 46 | 46.2 | 46.3 | 46 | 46.1 | 46.2 | 46 |
| **On/off cycles** | 41 | 41 | 43 | 44 | 42 | 42 | 42 | 40 |
| **Operational hours** | 72.6 | 72 | 71.3 | 70.7 | 70.5 | 69.7 | 69.1 | 70.4 |
| **Standby hours** | 7 | 6.9 | 7 | 7.1 | 7.3 | 7.1 | 6.8 | 7 |
| **VRFB $P_{min,\ discharge}$ (W)** | **300** | **400** | **500** | **600** | **700** | **800** | **900** | **1000** |
| **Discharged electricity (kWh)** | 47.9 | 46.6 | 44 | 41 | 37.7 | 34.8 | 32.2 | 30.1 |
| **Charged electricity (kWh)** | 103.7 | 101.4 | 97.2 | 92.3 | 86.1 | 81.3 | 77.3 | 73.8 |
| **Efficiency $\eta_{energy,AC}$ (%)** | 46.2 | 46 | 45.3 | 44.4 | 43.8 | 42.8 | 41.7 | 40.8 |
| **On/off cycles** | 46 | 44 | 41 | 45 | 47 | 45 | 44 | 42 |
| **Operational hours** | 74.2 | 70.7 | 65.2 | 59.6 | 53 | 49 | 44.5 | 40.8 |
| **Standby hours** | 6.8 | 7.1 | 7.6 | 8.1 | 7.7 | 7.9 | 7.4 | 6.6 |

The variation of the minimum charge power has a marginal effect on the energy efficiency. On the other hand, the efficiency shows a decreasing trend with increasing discharge power. Of course this can be contributed to the domestic load profile with a relatively low average power.

Based on the results it was concluded that the thresholds of the maximum charge/discharge power, minimum charge power and minimum discharge power should be set to ±6500 W, -1100 W and 300, respectively. This provides a high degree of flexibility and the VRFB can serve high power and low power demands, which are typical in domestic load profiles.

### A-4-8 Sensitivity analysis of the PV array size and the electric demand

In order to analyse the effect of the system configuration, two sensitivity analyses were performed varying the PV array size and the electric demand. The simulations were carried out for a time period of one year. First, the PV size was increased stepwise from 6 $kW_p$ to 12 $kW_p$. The annual electric demand was 4707.4 kWh. Table A-17 presents the result of the analyses.

**Table A-17: Summarised results of increasing the PV array size.**

| PV size ($kW_p$) | 6 | 8 | 10 | 12 |
|---|---|---|---|---|
| **Parameter** | **Annual Results** | | | |
| **Building:** | | | | |
| PV generation (kWh) | **5317.2** | **7089.5** | **8861.9** | **10634.3** |
| Operating hours PV | **3470** | **3550** | **3573** | **3586** |
| Number of hours for which $P_{diff}$<-1100 W | **1309** | **1560** | **1757** | **1916** |
| Number of hours for which $P_{diff}$>300 W | **3087** | **3028** | **2989** | **2960** |
| **VRFB:** | | | | |
| Discharged AC electricity (kWh) | **1318.4** | **1539.1** | **1690.7** | **1784.9** |
| Charged AC electricity (kWh) | **2902.8** | **3333.6** | **3640.2** | **3829** |
| Discharged stack electric charge (Ah) | **35756** | **41406** | **45249** | **47659** |
| Charged stack electric charge (Ah) | **41175** | **47551** | **51977** | **54729** |
| On/off cycles | **2099** | **2064** | **2054** | **2012** |
| Operational hours | **2555.1** | **2777.9** | **2964.4** | **3070.2** |
| Standby hours | **282.2** | **288.1** | **309** | **309.4** |
| **Grid exchange:** | | | | |
| Grid import (kWh) | **2334.1** | **2027.9** | **1814.3** | **1671.7** |
| Grid export (kWh) | **1359.5** | **2615.5** | **4019.3** | **5554.5** |
| **Annual performance indices** | **Annual Results** | | | |
| Efficiency $\eta_{energy,AC}$ (%) | **45.4** | **46.2** | **46.4** | **46.6** |
| Annual grid interaction index (%) | **11.4** | **13.7** | **14.5** | **15** |
| Annual grid balance (kWh) | **974.6 (imp.)** | **587.6 (exp.)** | **2205 (exp.)** | **3882.8 (exp.)** |
| Annual supply cover factor | **0.67** | **0.61** | **0.57** | **0.52** |
| Annual load cover factor | **0.52** | **0.58** | **0.63** | **0.66** |
| **Without VRFB:** | **Annual Results** | | | |
| Annual grid balance (kWh) | **609.8 (exp.)** | **2382.1 (exp.)** | **4154.5 (exp.)** | **5927 (exp.)** |
| Annual grid interaction index (%) | **19.7** | **20.8** | **20** | **19.6** |
| Annual supply cover factor | **0.36** | **0.31** | **0.28** | **0.25** |
| Annual load cover factor | **0.23** | **0.25** | **0.26** | **0.27** |

The AC energy efficiency of the VRFB slightly rose from 45.4% (6 $kW_p$) to 46.6% (12 $kW_p$) because of the increased available charge power. The annual grid interaction index shows the lowest value for the 6 $kW_p$ PV system and increased with the installed PV capacity, whereas the lowest annual grid balance with 587.6 kWh (export) was calculated for the simulated scenario with a 8 $kW_p$ PV array. Table A-18 outlines the results of the second analysis.

**Table A-18: Summarised results of simulated semi-detached house with varying PV size.**

| PV size ($kW_p$) | | 6 | 8 | 10 | 12 |
|---|---|---|---|---|---|
| **Parameter** | | **Annual Result** | | | |
| **Building:** | Electric demand (kWh) | **9042** | **9042** | **9042** | **9042** |
| | PV generation (kWh) | **5317.2** | **7089.5** | **8861.9** | **10634.3** |
| | Operating hours PV | **3470** | **3550** | **3573** | **3586** |
| | Number of hours for which $P_{diff}$<-1100 W | **1094** | **1357** | **1555** | **1717** |
| | Number of hours for which $P_{diff}$>300 W | **4631** | **4502** | **4412** | **4340** |
| **VRFB:** | | | | | |
| | Discharged electricity (kWh) | **1334.7** | **1873.6** | **2175.6** | **2387.9** |
| | Charged electricity (kWh) | **2811.4** | **3839.1** | **4422.1** | **4846.8** |
| | Charged electric charge (Ah) | **35355** | **48878** | **56485** | **61796** |
| | Discharged electric charge (Ah) | **40325** | **55555** | **64091** | **70063** |
| | On/off cycles | **2061** | **1930** | **1932** | **1954** |
| | Operational hours | **2005.3** | **2457.8** | **2685.6** | **2859.9** |
| | Standby hours | **178.64** | **195.2** | **196.9** | **196.5** |
| **Grid exchange:** | | | | | |
| | Grid import (kWh) | **5826.6** | **5105.5** | **4666.6** | **4348** |
| | Grid export (kWh) | **625.1** | **1187.4** | **2240** | **3481.3** |
| **Annual performance indices** | | | | | |
| | Efficiency $\eta_{energy,AC}$ (%) | **47.5** | **48.8** | **49.2** | **49** |
| | Annual grid interaction index (%) | **11.6** | **12.6** | **13.6** | **13.4** |
| | Annual grid balance (kWh) | **5201.5 (imp.)** | **3918.1 (imp.)** | **2426.6 (imp.)** | **866.7 (imp.)** |
| | Annual supply cover factor | **0.83** | **0.8** | **0.75** | **0.70** |
| | Annual load cover factor | **0.37** | **0.45** | **0.50** | **0.54** |
| **Without VRFB:** | | | | | |
| | Annual grid balance (kWh) | **3724.8 (imp.)** | **1952.5 (imp.)** | **180.1 (imp.)** | **1592.2 (exp.)** |
| | Annual grid interaction index (%) | **16.6** | **19.8** | **21.8** | **20.9** |
| | Annual supply cover factor | **0.53** | **0.47** | **0.43** | **0.39** |
| | Annual load cover factor | **0.22** | **0.24** | **0.25** | **0.26** |

The second set of simulations considered a semi-detached dwelling. A second additional load profile was generated by using the CREST load model (Richardson & Thomson 2010) assuming 3 inhabitants. Both profiles were applied and the total annual electric demand was 9042 kWh for the semi-detached dwelling. Comparing the AC efficiency of 6 $kW_p$, 8 $kW_p$ and 10 $kW_p$ simulations listed in Table A-18, a small improvement can be noticed. Furthermore, the annual grid interaction was

slightly decreased for the 8 $kW_p$ and 10 $kW_p$ simulation. The reason can be found by analysing the supply cover factor. This value significantly increased in the second set of simulations due to the better utilisation of the VRFB. During the summer the VRFB operated most of the time at high SOC levels in the first set of simulation. On the other hand, the SOC varied between low and high values during the summer in the second set of simulations due to increased demand. Figure A-20 compares the SOC of the simulation of a single dwelling and a semi-detached dwelling, both equipped with 8 $kW_p$ PV.

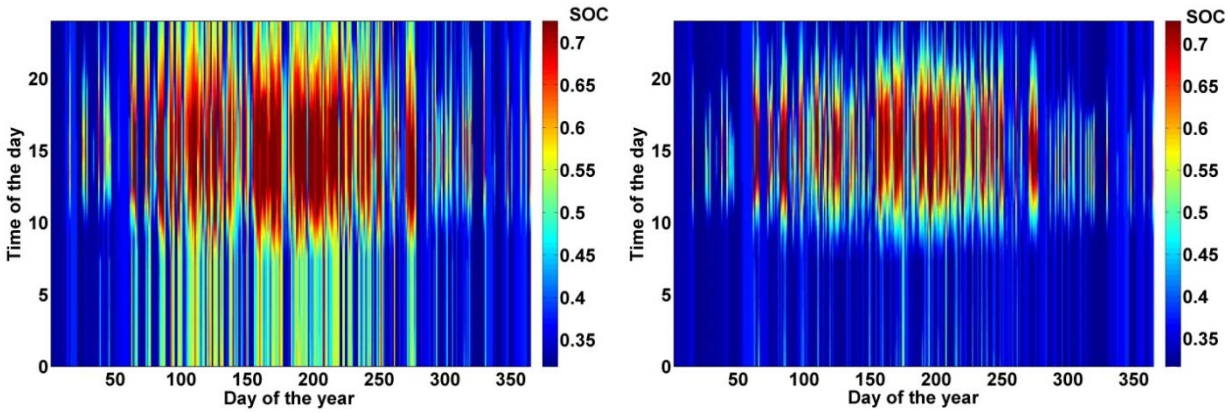


**Figure A-20: Annual evolution of the SOC of the 6 kW/20 kWh VRFB system installed in a single house (left) and semi-detached house (right) both equipped with 8 $kW_p$ PV system.**

The load cover factor indicates the degree of self-sufficiency. The higher the index, the higher the self-generation is. Of course this value tends to be higher at simulations of the single-dwelling due to the lower electric demand. However, compared to the values without VRFB, it can be seen that the value almost doubled for each simulation case. In addition, the grid interaction index decreases for the semi-detached dwelling equipped with PV systems >6 $kW_p$. For instance, the simulation with 12 $kW_p$ PV, the annual grid interaction index was reduced from 15% to 13.4%. The annual supply cover factor rose from 0.52 to 0.7 meaning that less energy was exported to the grid. The annual energy balance was almost equalised for this simulation scenario and was reduced from 3882.8 kWh (export) to 866.7 (import).

From the presented results it can be concluded that the VRFB system was affected by both the supply and load profile. The availability of either high charge or discharge power improves the overall efficiency. The simulation result of a single dwelling at different PV sizes showed that the VRFB operated at high SOC levels during the summer. Thus, only a small amount of the available capacity was utilised. Therefore, a second set of simulations was conducted for semi-detached dwelling with an increased demand. The results show, that the VRFB was better utilised, higher efficiency value was reached and that the grid interaction was reduced.